Etude des propriétés thermodynamiques des nouveaux fluides frigorigènes

Jamal El Abbadi

▶ **To cite this version:**

Jamal El Abbadi. Etude des propriétés thermodynamiques des nouveaux fluides frigorigènes. Génie chimique. Université Paris sciences et lettres, 2016. Français. ⟨NNT : 2016PSLEM089⟩. ⟨tel-01804996⟩

HAL Id: tel-01804996

https://pastel.hal.science/tel-01804996v1

Submitted on 1 Jun 2018

HAL is a multi-disciplinary open access archive for the deposit and dissemination of scientific research documents, whether they are published or not. The documents may come from teaching and research institutions in France or abroad, or from public or private research centers.

L'archive ouverte pluridisciplinaire **HAL**, est destinée au dépôt et à la diffusion de documents scientifiques de niveau recherche, publiés ou non, émanant des établissements d'enseignement et de recherche français ou étrangers, des laboratoires publics ou privés.

HAL Authorization

THÈSE DE DOCTORAT

de l'Université de recherche Paris Sciences et Lettres
PSL Research University

Préparée à MINES ParisTech

Etude des propriétés thermodynamiques des nouveaux fluides frigorigènes

Thermodynamic properties of new refrigerants

Ecole doctorale n°432

Sciences des Métiers de l'Ingénieur

Spécialité Energétique et Procédés

COMPOSITION DU JURY :

M. Pascal TOBALY
CNAM, Président

M. J.P. Martin TRUSLER
Imperial College London, Rapporteur

M. Romain PRIVAT
ENSIC - LRGP, Rapporteur

M. Bernard ROUSSEAU
Université Paris-Sud, Examinateur

M. Patrice PARICAUD
ENSTA ParisTech – Université Paris Saclay, Examinateur

M. Christophe COQUELET
Mines ParisTech – PSL Research University, Examinateur

Mme. Céline HOURIEZ
Mines ParisTech – PSL Research University, Examinateur

Soutenue par Jamal EL ABBADI
le 02 Décembre 2016

Dirigée par :
Christophe COQUELET
Céline HOURIEZ

To Mom and Dad

To my sisters Nadia and Ibtissam

To my family and friends

Acknowledgments

First, I would like to thank my *Directeur de thèse* Prof. Christophe Coquelet for according me this wonderful opportunity to do my PhD at the CTP, for his great supervision and guidance, for his great help and support all along my thesis, for the great discussions we had, and for constantly pushing me to reach my full potential and be a better scientist.
I would also like to thank my *Maître de thèse* Dr. Céline Houriez, for her great supervision and guidance, for her continuous support and help, for her precious advices and the great discussions we had, for always checking on me, and for continuously believing in me.
Then, I would like to thank Prof. J.P. Martin Trusler for welcoming me into his research group at Imperial College London, for his tremendous help and support, for his precious advices and guidance, for helping me with the experimental work, and for his hospitality.

I would like to thank the members of the jury: Prof. J.P. Martin Trusler and Dr. Romain Privat for accepting to review my manuscript and to evaluate my work, and for their precious advices and discussions; Dr. Patrice Paricaud, Prof. Bernard Rousseau, and Prof. Pascal Tobaly for accepting to evaluate my work, and for their advices and recommendations.
I would also like to thank Dr. Paolo Stringari and Dr. Elise El Ahmar for evaluating my work in the first and second year of my PhD, for all the advices, and for the discussions and exchanges we had.

I would like to thank the PREDIREF project's partners: Dr. Abdelatif Baba-Ahmed, Gilbert Fuchs, Olivier Baudouin, Dr. Patrice Paricaud and Dr. Jiri Janecek, for the tremendous work performed during this project, for the great discussions and exchanges.
Also, I would like to thank the French National Research Agency (ANR) for financing this project (ANR-13-CDII-0008), and for financing my thesis.
Related to my period abroad at Imperial College London, I would like to thank Prof. Christophe Coquelet and the CTP for the financial support, the "Fondation Mines ParisTech" for according me the mobility scholarship, and Prof. J.P. Martin Trusler for his financial support and for covering all the expenses related to the laboratory work.

My acknowledgments to my friends, colleagues and former colleagues from the CTP: Céline, Martha, Marco, Elise, Fan, Mauro, Eric A., Etienne, Alfonso, Hamadi, Charlie, Rémi, Alain, Elodie, David, Hervé, Jocelyne, Marie-Claude, Snaïde, Paolo, Christophe, Eric B., Pascal, Alain G., Arnaud, Yi, Mauro G., Stéfano, Giorgia, Alessia, Mahmoud, Jessy, Rohani, Mark, Marine, Pierre, Moussa, Nelly, Hakim, Lamine, Houda. Thank you all for your help and friendships, for the great working atmosphere inside the lab, for your encouragements, and for all the great moments we shared together inside and outside of the lab. You guys have been amazing and made me feel like home, thank you sincerely.

A special thanks to Alain and Elodie for helping me with the experimental work, David and Hervé for always helping me to fix the technical problems and David for organising the football games; Jocelyne and Marie-Claude for the great support and helping me with the paperwork and the administrative procedures, and for continuously checking on me; Céline (and Guillaume), Martha (and Jean), Elise, Marco (and Fabrizia), Mauro (and Elise) and Fan, for always being here for me, for their tremendous support during the tough moments, for always being ready to help, for their advices, for our discussions and exchanges, and for their precious friendships and hospitality. You guys are the best.

Many thanks to the IT guys Alain Q. and Christophe D., for their tremendous help, and always being able to bring quick solutions.

I would also like to thank all my friends and colleagues from the Thermophysics Laboratory at Imperial College London: Claudio, Julian, Benaiah, Sultan, Malami, Theodor, Lorena, Mihaela, Yolanda, Chidi, Hao, Rayane, Yanah, Geraldine, Carolina, Alejandro, Amos, Maria, and for their friendships and support, for their tremendous help with the experimental work, and for all the great moments we spent together inside and outside of the lab. You guys made my stay enjoyable, and I am truly grateful for that.

A special thanks to Claudio for teaching me everything about the lab work, for the precious advices, for the great moments and discussions shared together and for his hospitality (many thanks to Ilaria as well); Julian for helping me with the experiments and for all the great moments and discussions we had; Benaiah for always cheering me up, for the great moments and discussions, and for the fun we had together playing squash and tennis; Sultan for the great moments spent together and for helping me with the lab work; Malami for sharing his knowledge on the equipment, for answering my many questions and for his precious advices; Theodor, Lorena (and Henrique), Yolanda, Mihaela and Chidi for the great help and support,

for cheering me up, and for the great moments we spent together; and Yanah for carrying on the experimental work on the refrigerants.
My acknowledgments to Gavin for all the technical help, to Jessica for helping me with the administrative procedures; to my teammates from the Imperial United football team, especially Dan for organising the games and for accepting me in the team; we had a lot of fun playing together and battling for the victory.

Finally, I would like to thank my dear Mom and Dad, and my sisters Nadia and Ibtissam, for their permanent support and encouragements, for their unconditional love, and for always pushing me to be a better person. Many thanks to all my family here in France and Morocco for their tremendous support and help, and to all my friends around the world (especially Anvar, Elaine, Yassine A., Yassine AZ. and Fahd) for their help, support and encouragements.

I had a wonderful three years, with great experiences and memories, which I will always remember and this thanks to you all guys. I hope I didn't forget anyone, and I apologize if by mistake I forgot to thank anyone who has been involved in my thesis.
I am sincerely grateful to all of you, and I hope our paths will cross again soon.

Thank you all,
Jamal

Abstract

This thesis presents and describes the results obtained from the study of the thermodynamic properties of the new-generation refrigerants.

To fulfil the gap of experimental data concerning new fluorinated compounds such as HFO-1234yf and HCFO-1233zd(E), experimental measurements were carried out to achieve vapour-liquid equilibrium and density measurements of these systems (pure compounds and mixtures), along with viscosity measurements.

The vapour-liquid equilibrium measurements were performed using an equilibrium cell, while the density measurements were achieved using a vibrating-tube densimeter. For the viscosity measurements, a vibrating-wire viscometer-densimeter is used.

In addition to the experimental measurements, and in order to calculate accurately the thermodynamic properties of refrigerant fluids, a new three-parameter cubic equation of state was developed, based on the modification of the well-known Patel-Teja equation of state. The new equation of state is associated with the Mathias-Copeman alpha function.

By only knowing the acentric factor ω and the experimental critical compressibility factor Z_c of the pure compounds, it is possible to predict thermodynamic properties for both pure compounds and mixtures by means of the new equation of state. No binary interaction parameter k_{ij} is necessary for the prediction of mixture properties.

The results obtained with the new equation of state show a good agreement with experimental data for vapour-liquid equilibrium and density properties. The obtained results are particularly good for the liquid densities, and in the vicinity of the critical point, by comparison with the results obtained using the Peng-Robinson and the Patel-Teja equations of state.

In addition, new correlations dedicated to densities and surface tensions calculations were developed, based on the scaling laws (for densities) and the density-gradient theory (for surface tensions). The results obtained were in good agreement with the experimental data for the densities and the surface tensions.

Finally, a model based on the friction theory was developed to calculate the viscosities. This model is associated to the new equation of state, and the results obtained were in good agreement with the experimental measurements.

Cette thèse présente et décrit les résultats obtenus sur l'étude des propriétés thermos-physiques des réfrigérants de nouvelle génération.

Pour répondre au manque de données expérimentales des composés fluorés tels que le HFO-1234yf et le HCFO-1233zd(E), des mesures expérimentales ont été faites durant ce travail, couvrant les mesures des équilibres liquide-vapeur, les mesures de densités et les mesures de viscosités pour des systèmes de réfrigérants (corps purs et mélanges).

Les mesures d'équilibre liquide-vapeur ont été achevées au moyen d'une cellule d'équilibre, tandis que les mesures de densités ont faites en utilisant un densimètre à tube vibrant. Pour les mesures de viscosités, elles ont été faites au biais d'un viscomètre-densimètre à fil vibrant.

En plus des mesures expérimentales, et afin de calculer précisément les propriétés thermodynamiques des fluides frigorigènes, une nouvelle équation d'état cubique à trois paramètres a été développée, en se basant sur la modification de l'équation d'état de Patel-Teja. La nouvelle équation d'état est associée à la fonction alpha de Mathias-Copeman.

En connaissant uniquement le facteur acentrique ω et le facteur de compressibilité critique Z_c des corps purs, il est possible de prédire les propriétés thermodynamiques des corps purs et des mélanges, en utilisant cette nouvelle équation d'état, sans avoir à utiliser le paramètre d'interaction binaire k_{ij} pour les mélanges.

Les résultats obtenus avec la nouvelle équation d'état montrent sa très bonne capacité de prédiction des propriétés thermodynamiques, et les résultats obtenus correspondent aux données expérimentales. En particulier, les résultats sont meilleurs pour les densités liquides, et au voisinage du point critique, et aussi pour les isothermes supercritiques, en comparaison avec les résultats obtenus à partir des équations d'état de Peng-Robinson et Patel-Teja.

En plus, des corrélations destinées aux calculs des densités et des tensions superficielles à saturation ont été développées, basées sur les lois d'échelles (pour le calcul des densités), et sur la théorie du gradient-densité (pour les tensions de surface). Les résultats obtenus sont en très bon accord avec les données expérimentales des densités et des tensions superficielles.

Enfin, un modèle basé sur la théorie de la friction a été développé pour permettre le calcul des viscosités. Ce modèle a été associé à la nouvelle équation d'état, et les résultats obtenus étaient en très bon accord avec les mesures expérimentales de viscosités.

Contents

List of tables

List of tables

List of figures

Nomenclature

Definitions of commonly used notations are given below:

Symbols and abbreviations

a	Cohesive energy parameter ($J.m^3.mol^{-2}$)
ARD	Average relative deviation
b	Co-volume parameter ($m^3.mol^{-1}$)
EoS	Equation of state
CEoS	Cubic equation of state
F_{obj}	Objective function
k_{ij}	Binary interaction parameter
m_n	Alpha function parameter
NEoS	Our new equation of state
MC	Mathias-Copeman
P	Pressure (MPa) / (bar)
PR	Peng-Robinson
PT	Patel-Teja
SRK	Soave-Redlich-Kwong
T	Temperature (K) / (°C)
v	Molar volume ($m^3.mol^{-1}$)
x	Liquid mole fraction
y	Vapor mole fraction
Z	Compressibility factor
CFCs	Chlorofluorocarbons
HCFCs	Hydrochlorofluorocarbons
HFCs	Hydrofluorocarbons
HFOs	Hydrofluoroolefins
HCFOs	Hydrochlorofluoroolefins
GWP	Global warming potential
ODP	Ozone depletion potential

Greek letters

ω	Acentric factor
α	Alpha function
Ω_a, Ω_b, Ω_c	Substance depending factors
ρ	Molar density (mol.m^{-3}) / Density (kg. m^{-3})
σ	Surface tension (mN.m^{-1})
η	Viscosity (mPa.s)
κ	Empirical parameter of the wire
β	Dimensionless added mass
β'	Dimensionless viscous damping
Δ_0	Logarithmic decrement
Λ	Amplitude

Subscripts

c	Critical property
cal	Calculated property
exp	Experimental property
i,j	Molecular species
opt	Optimized property
r	Reduced property

Superscripts

V	Vapour phase
L	Liquid phase

1. Introduction

La connaissance des propriétés thermodynamiques et des diagrammes de phases des composés fluorés est essentielle pour la conception et l'optimisation des systèmes thermodynamiques. Lors du procédé de production de ces composés, des impuretés (telles que HCl, HF) peuvent apparaître après réaction chimique, d'où la nécessité de déterminer les diagrammes de phases impliquant ces espèces chimiques, pour bien dimensionner et optimiser les colonnes de distillation utilisées pour séparer ces impuretés du mélange. De plus, plusieurs applications requièrent de connaître précisément les propriétés thermodynamiques des composés fluorés pour leur fonctionnement, afin d'assurer de meilleures performances du point de vue énergétique et environnemental. A titre d'exemple, on peut citer: les systèmes de réfrigération, les cycles de Rankine, les pompes à chaleur, les systèmes de climatisation, etc.

Vis-à-vis des régulations environnementales imposées par l'Union Européenne (F-Gas (Lasserre et al. 2014)*) et dans le but de réduire l'émission globale des gaz à effets de serre, les fluides frigorigènes doivent avoir un très bas potentiel de déplétion ozonique (ODP) et un très bas potentiel de réchauffement global (GWP). Les chimistes sont donc appelés à développer de nouvelles solutions en matière de fluides frigorigènes, soit en synthétisant de nouveaux fluides respectant les contraintes mentionnées ci-dessus, soit en se basant sur des mélanges de fluides déjà existants.*

Les fluides de nouvelle génération comme les HFOs (hydrofluorooléfines), et les HCFOs (hydrochlorofluorooléfines) suscitent un vif intérêt, en particulier le R1234yf (2,3,3,3-tetrafluoropropène) qui présente un très bas GWP (= 4), et qui est un des fluides les plus étudiés actuellement.

L'objectif de cette thèse est d'étudier les propriétés thermo-physiques des fluides de nouvelle génération. Notre travail a été en particulier focalisé sur trois réfrigérants, à savoir le HFO R1234yf et les deux HCFOs R1233xf et R1233zd(E). Ces réfrigérants ont été étudiés comme corps purs mais aussi en mélange avec d'autres réfrigérants de nouvelle et d'ancienne génération. Les propriétés thermo-physiques principalement étudiées sont les équilibres liquide-vapeur (ELV), les densités et les viscosités.

Cette thèse fait partie du projet PREDIREF (Prediction of the physical properties of next-generation refrigerant fluids), financé par l'agence nationale de la recherche (ANR), et en collaboration avec des partenaires académiques (MINES ParisTech et ENSTA ParisTech), et des parteniares industriels (ARKEMA et PROSIM, France).

Cette thèse comporte deux principaux volets : la partie expérimentale et la partie modélisation. L'objectif de la partie expérimentale était de faire les mesures expérimentales des ELV et des

densités; travail fait au sein du Centre Thermodynamique des Procédés (CTP) à MINES ParisTech; et les mesures des viscosités ; travail fait au sein du Thermophysics Laboratory à l'Imperial College London, dans le cadre d'un séjour international.
L'objectif de la partie modélisation quant à elle était de développer un modèle thermodynamique basé sur une équation d'état cubique, en vue de calculer les différentes propriétés thermo-physiques des réfrigérants en corps purs et en mélanges.

Ce manuscrit présente les principaux résultats obtenus durant ce travail de thèse. Pour ce faire, nous commencerons par un chapitre introductif (le présent chapitre), en donnant des généralités sur les réfrigérants et les systèmes de réfrigération.
Dans le deuxième chapitre, nous présenterons et décrierons l'équipement expérimental utilisés pour les mesures d'ELV et de densités.
Le chapitre 3 sera consacré à la présentation des résultats expérimentaux obtenus lors de ce travail, pour les ELV et les densités des différents systèmes de réfrigérants étudiés, pour les corps purs ainsi que les mélanges.
Le chapitre 4 sera dédié à l'introduction et la présentation du modèle thermodynamique utilisé durant cette thèse, à savoir l'équation d'état cubique à trois paramètres développée et validée lors de cette thèse.
Dans le cinquième chapitre, nous présenterons les résultats de la modélisation obtenus en utilisant l'équation d'état cubique à trois paramètres pour les propriétés thermodynamiques des réfrigérants corps purs, en comparaison avec les résultats expérimentaux et avec d'autres modèles thermodynamiques.
Le chapitre 6 quant à lui fera objet de la présentation des résultats de la modélisation des propriétés thermodynamiques des mélanges de réfrigérants, en comparaison avec les données expérimentales et les autres modèles thermodynamiques.
Dans le chapitre 7, nous présenterons les corrélations développées pour le calcul des densités (basées sur les lois d'échelle) et des tensions superficielles (inspirée de la théorie du gradient et basée sur une loi de puissance), ainsi que les résultats de calcul obtenus.
Dans le chapitre 8, nous présenterons les résultats des mesures expérimentales des viscosités des réfrigérants, ainsi qu'un modèle dédié à leur calcul et basé sur la théorie de la friction. Les résultats expérimentaux sont comparés avec les résultats de la modélisation.

Enfin, dans le dernier chapitre de ce manuscrit, nous finirons par une conclusion générale, pour résumer l'ensemble des résultats obtenus lors de cette thèse, et donner des perspectives de travail dans la continuation de cette thèse.

For several years, new-generation refrigerants are proposed, in order to reduce the overall emission of greenhouse gases (Kyoto protocol, 1997) and to respect the environmental regulations issued by the European Union (F-gas regulations) (Lasserre et al. 2014). In particular, due to their low global warming potential (GWP), hydrofluoroolefins (HFOs), such as the R-1234yf (2,3,3,3-tetrafluoropropene) and the R-1234ze (trans-1,3,3,3-tetrafluoropropene), arouse interest and have been proposed as replacements for some previous-generation fluids such as the 1,1,1,2-tetrafluoroethane (R-134a) (Minor & Spatz 2008). However, the use of pure component fluid may not be suitable for some refrigeration applications, due to performance and safety concerns. Thus, blends of refrigerants are often considered, including for instance a HFO, a hydrofluorocarbon (HFC), and CO_2, such as the R-445A blend.

The knowledge of the thermophysical properties and phase diagrams of fluorinated compounds; such as HFCs, hydrofluoroolefins (HFOs) and hydrochlorofluoroolefins (HCFOs) is essential to the design and optimization of thermodynamic systems.

Moreover, many refrigeration applications need the thermodynamic properties (such as density, enthalpy, heat capacity…) of the refrigerant fluids to ensure better performances (coefficient of performance, energy consumption, environmentally friendly, etc). We can cite from the many applications: the refrigeration systems, the organic Rankine cycle, the heat pumps, the air conditioning systems, etc.

In addition, the transport properties (such as viscosity, thermal conductivity) are important for refrigeration applications. Viscosity for instance, has a great effect on heat transfer coefficients, which are important for heat exchangers. Viscosity data are also essential for calculating pressure drops, as for pump and piping (Smith et al. 2003).

The purpose of this thesis is to investigate and understand the thermophysical properties of the new-generation refrigerants. Our work will be in particular focused on three refrigerants: the HFO R1234yf, and the two HCFOs R1233xf and R1233zd(E). These refrigerants were studied as pure compounds, and in mixtures with other refrigerants (new and old-generation ones). The thermodynamic properties that we investigated are mainly the vapour-liquid equilibria (VLE), density and viscosity properties.

This thesis is part of PREDIREF (Prediction of the physical properties of next-generation refrigerant fluids) project, funded by the French National Research Agency (ANR), and in joint

collaboration with academic partners (MINES ParisTech and ENSTA ParisTech) and industrial partners (ARKEMA and PROSIM, France).

This thesis contains two main sides: the experimental work and the modelling work. The aim of the experimental work was to carry out experimental measurements of VLE and density properties; experimental measurements carried out at the Centre Thermodynamics of Processes (CTP); and viscosity properties; experimental measurements carried out at the Thermophysics Laboratory at Imperial College London, as part of an international stay.

The aim of the modelling work was to develop a thermodynamic model based on a cubic equation of state, in order to calculate the different thermodynamic properties for pure compounds and mixtures.

This manuscript summarises the main results obtained during this thesis. To do so, we will start first by giving generalities about refrigerants and refrigeration systems; this will be the purpose of the ongoing Chapter.

Chapter 2 will be dedicated to describe and present the experimental equipment used to achieve VLE and density measurements of the refrigerants studied.

In Chapter 3, we will present the experimental results obtained during this work for VLE and density properties, for the different systems studied, containing measurements of pure compounds, and for mixtures.

Chapter 4 will be dedicated to present the thermodynamic model used during this work for the prediction of the thermodynamic properties, consisting of a new three-parameter cubic equation of state developed and validated during this work.

In Chapter 5, we will present the results of the calculations for the properties of pure compounds refrigerants, obtained with our model, in comparison with the experimental data, and with other thermodynamic models.

Chapter 6 will extend the results of the prediction to the systems of mixtures, always by using our model of prediction, and in comparison to the experimental data, and to other thermodynamic models.

In Chapter 7, we will introduce developed correlations for density and surface tension properties. The correlations dedicated to densities are based on the scaling laws, while the surface tension correlations are inspired from the gradient theory, and based on a power law equation.

Chapter 8 deals with the work carried out during my short stay at Imperial College London, within the research group of Professor J.P. Martin Trusler, and presents the results of the experimental viscosities of refrigerants obtained, as well as a model based on the friction theory that was developed. The experimental results are compared to the modelling ones.
Finally, in Chapter 9, we will end this manuscript by general conclusions about the results obtained during this thesis and the future perspectives of work.

1.1. Brief history of refrigeration industry

The mechanical refrigeration, began in the 19th century when the physicist Jacob Perkins introduced the first practical refrigeration machine in 1834. This machine had the main components of a modern one, containing a compressor, a condenser, an evaporator, and an expansion valve. This machine used ethyl ether as a working fluid, which prevented the machine from being industrialized, due to several hazardous characteristics, in term of flammability and toxicity of this fluid (Ciotta 2010).
We have to wait for 30 years later that the first machine using CO_2 as a working fluid was introduced. The natural refrigerants were used until early of the 20th century, when alternative refrigerants such as dichloroethene ($C_2H_2Cl_2$) and dichloromethane (CH_2Cl_2) were introduced. However, these refrigerants as well had a high hazardous risk, causing a number of industrial accidents.
In 1926, the chemist Thomas Midgley focused his studies on the fluorinated compounds, with the aim of finding a non-flammable safe refrigerant, and successfully introduced the dichlorodifluoromethane (CCl_2F_2), commonly known nowadays as R12. Two years later, the company Frigidaire developed a new category of refrigerants known as halocarbons, and launched their industrial production (Ciotta 2010).
The halogenated compounds have been used all along the 20th century, due to their good thermodynamic properties and high flexibility, which make them suitable for different industrial applications. The halogenated compounds include several refrigerant families, such as chlorofluorocarbons (CFCs), hydrochlorofluorocarbons (HCFCs), and hydrofluorocarbons (HFCs).
However, due to the environmental regulations and protocols (Montreal protocol, Kyoto protocol, and F-gas regulations), most of these refrigerants had to be banned, phased out or limited.

The Montreal protocol that was agreed on 26 August 1987 and took effect on 26 August 1989, was designed to protect the ozone layer, by phasing out the production of number of compounds responsible of ozone depletion. Such compounds include number of the CFCs and HCFCs refrigerants.

The Kyoto protocol that was agreed on 11 December 1997, came to fight against the global warming, by reducing the greenhouse gas emissions.

Finally the F-gas regulations (Lasserre et al. 2014), issued by the European Union, came to control and reduce the emissions of fluorinated greenhouse gases including HFCs. The F-gas was adopted initially in 2006 and was replaced by a new regulation adopted in 2014, and took effect from 1 January 2015.

The harmfulness of the refrigerants is quantified by two potentials: the ozone depletion potential (ODP), which is related to the effect of the refrigerants on the ozone layer, and the global warming potential (GWP), which is related to the impact of the refrigerants on the global warming of the planet. The details about these two potentials will be given later in this Chapter.

All of these environmental constraints pushed the chemists to develop a new-generation of refrigerants (also designed as fourth generation refrigerants), which are harmless to the ozone layer, and with low impact on the global warming of the planet.

In addition to the safety and environmental concerns, these alternative fluids must have proper thermodynamic properties in order to be considered as efficient refrigerants. Their energetic properties must be equivalent to the previous fluids in order to be used to retrofit the existing equipments, and thus to avoid important modifications of the industrial systems and heavy investment costs.

Working with refrigerant blends is often preferable to pure component fluids for energy saving and flexibility of operation. In order to select the optimal mixture composition for the design and operation of a refrigeration process, it is necessary to know the phase diagram and thermodynamic properties of mixtures. Vapour-liquid equilibria (VLE) and the location of azeotropes must be accurately known (PREDIREF website 2016).

Hydrofluoroolefins (HFOs) such as HFO-1234yf and HFO-1234ze, and hydrochlorofluoroolefins such as HCFO-1233xf and HCFO-1233zd(E) have recently been considered as promising replacements for common refrigerants (such as HFC-134a and HFC -245fa), as they have a particularly low global warming potential (GWP) and a zero-ozone depletion potential (ODP). However experimental data are scarce for these compounds, in particular for mixtures.

The knowledge of the thermodynamic properties of these refrigerants is important at the production level where properties such as VLE and relative volatility are needed for the processes of synthesis and purification of a given product, and also at the application level, where properties such as densities, critical temperature and pressure and heat capacities are needed for the design and optimisation of refrigeration systems.

1.2. Working fluids

The refrigerant is the heat transfer media in the refrigeration systems, and should meet a number of requirements to be suitable for a designed application. These requirements are related to the thermodynamic properties, to the health and safety issues, and also to the environmental concerns (Ciotta 2010). In general, the criteria for choosing a refrigerant are (but not limited to):

- Non-flammability
- Low toxicity
- Compatibility with construction materials and lubricants
- High coefficient of performance
- High evaporating enthalpy
- Convenient working pressure
- Low global warming potential (GWP)
- Zero ozone depletion potential (ODP)

1.2.1. Refrigerants nomenclature

We often use a label instead of the full name, to simplify the designation of the refrigerants, designed as Rnxyz, where:

- R: stands for refrigerant.
- n: indicates the number of double bonds (omitted if zero).
- x: indicates the number of carbon atoms minus one (omitted if zero): $x = n(C) - 1$.
- y: is the number of hydrogen atoms plus one: $y = n(H) + 1$.
- z: is the number of fluorine atoms: $z = n(F)$.

The number of chlorine atoms (if present) is given by: $n(Cl) = 2 \times n(C) + 2 - n(H) + n(F)$.

If bromine atoms are present, their number is given after a prefix “B”. For the cyclic compounds, we add the letter “C” after “R”.

For some refrigerants, the digits are followed by letters, indicating the structure of the molecule. For example, the two compounds R1234yf and R1234ze have the same chemical formula ($C_3H_2F_4$), but two different molecule structures:

- R1234yf: $CF_3CF=CH_2$
- R1234ze: $CHF=CHCF_3$

1.2.2. GWP and ODP

The global warming potential (GWP) is a relative measure of the amount of heat trapped by a certain mass of gas in comparison to the amount of heat trapped in the same mass of CO_2. The GWP is expressed as a factor of CO_2 (whose GWP is taken as a reference and equal to 1). The GWP is calculated over a specific time period, usually 100 years.

The ozone depletion potential (ODP) is defined as the ratio of global loss of ozone due to a specific compound over the global loss of ozone due to the same mass of trichlorofluoromethane (R11) (the reference fluid R11 has thus a ODP value equal to 1).

The different environmental protocols have regulated the use of the refrigerants, in order to have refrigerants with low GWP and zero ODP.

In *Table 1.1*, we summarize the most common refrigerants used, and the new generation refrigerants, along with their GWP and ODP. The values of the GWP may differ from one assessment to another, and depending on the organisation giving the evaluation. Here the values given are mainly to illustrate.

Table 1.1 Characteristics of some common refrigerants (Ciotta 2010; IPCC report 2016).

Family	*Label*	*Chemical formula*	*GWP*	*ODP*
CFC	R11	CCl_3F	4000	1
	R12	CCl_2F_2	10300	1
	R13	$CClF_3$	11700	1
	R113	$C_2F_3Cl_3$	5000	0.8
	R114	$C_2F_4Cl_2$	9300	1
	R115	C_2F_5Cl	9300	0.6
HCFC	R22	CHF_2Cl	1780	0.055
	R123	$C_2HF_3Cl_2$	79	0.02
	R124	C_2HF_4Cl	527	0.022
	R141b	$C_2H_3FCl_2$	630	0.11
	R142b	$C_2H_3F_2Cl$	2070	0.065
HFC	R23	CHF_3	12500	0
	R32	CH_2F_2	704	0
	R41	CH_3F	97	0
	R125	CHF_2CF_3	3450	0
	R134	CHF_2CHF_2	1100	0
	R134a	CH_2FCF_3	1360	0
	R143	CHF_2CH_2F	300	0
	R143a	CH_3CF_3	5080	0
	R152a	CH_3CHF_2	148	0
	R227ea	CF_3CHFCF_3	3500	0
	R236fa	$CF_3CH_2CF_3$	9400	0
	R236ea	CHF_2CHFCF_3	1200	0
	R245ca	$CH_2FCF_2CHF_2$	640	0
	R245fa	$CHF_2CH_2CF_3$	950	0
Natural refrigerants	R170 (Ethane)	C_2H_6	3	0
	R290 (Propane)	C_3H_8	5	0
	R600a (iso-Butane)	C_4H_{10}	3	0
	R1270 (Propylene)	C_3H_6	3	0
	R717 (Ammonia)	NH_3	0	0
	R744 (Carbon dioxide)	CO_2	1	0
HFO	R1234yf	$C_3H_2F_4$	<1	0
	R1234ze(E)	$C_3H_2F_4$	<1	0
HCFO	R1233xf	$C_3F_3H_2Cl$	<5	0
	R1233zd(E)	$C_3F_3H_2Cl$	<5	0

1.2.3. Synthesis of fluorinated compounds

Knowing the thermodynamic properties of the refrigerant (in particular phase diagrams and relative volatility) is essential in the production process, during the synthesis and purification of a desired fluorinated component. The phase diagrams and relative volatility give us information about the difficulty of separating the compounds contained in the mixture, and the location of the azeotrope (if dealing with an azeotropic system), and also used to determine the number of stages of a distillation column in a distillation process for instance.

In the production process, we need to go through several steps of reaction, separation and distillation in order to separate the desired product from the impurities and reach a high purity of the product.

For instance, during the production of the refrigerant R134a, we need to go through the following series of reactions:

$$\begin{aligned} 3HF + TCE^{1}\ (HC_2Cl_3) &\rightarrow R133a\ (H_2C_2ClF_3) + 2HCl \\ R133a\ (H_2C_2ClF_3) + \ HF &\rightarrow R134a\ (H_2C_2F_4) + HCl \end{aligned} \tag{1.1}$$

We can see from these reactions that in addition to the R134a, we have other by-products such as R133a and undesired impurities that we need to separate from the R134a, such as HF and HCl.

The production process of the R134a can be summarized by the following simplified block flow diagram, displayed in *Figure 1.1*, with two main sections: the reaction section, where the chemical reactions occur, and the separation section, where we go through the processes of separation and distillation, in order to obtain pure R134a.

[1] TCE: Trichloroethene

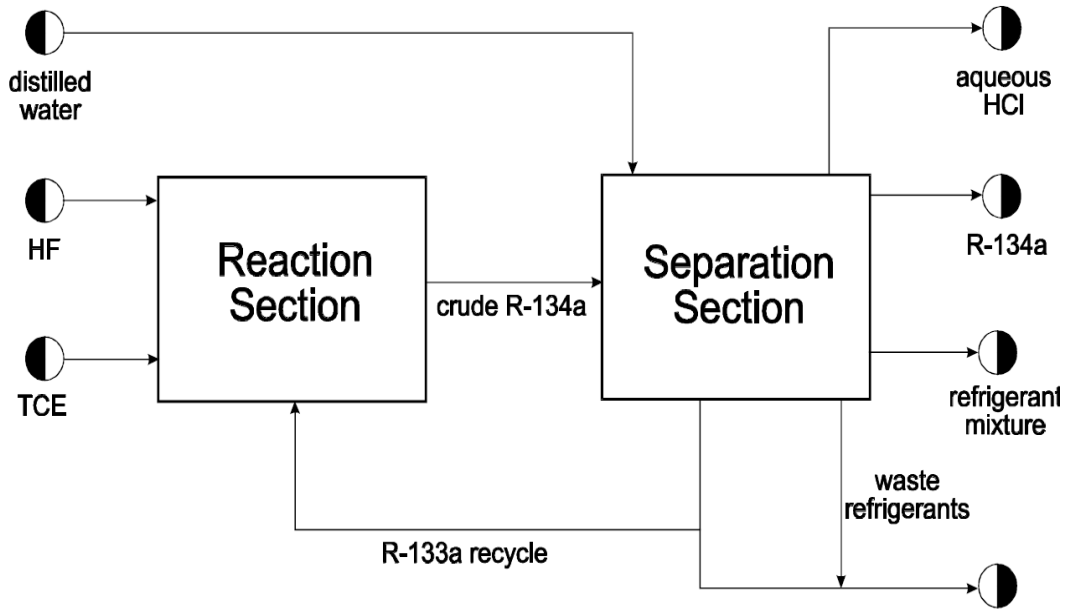

Figure 1.1 Block flow diagram of the R134a production (Scott & Steven 1993).

1.2.4. Applications aspect

In parallel to the production aspect, we have the "application aspects", for which the users of working fluids, need to know the thermodynamic properties, such as the critical properties, densities, enthalpies, heat capacities, etc.

The knowledge of these properties is important for many industrial applications: the refrigeration systems, the organic Rankine cycle, the heat pumps, the air conditioning systems, etc., in order to choose the best working fluid for the desired application, and ensure better performances of the system (coefficient of performance, energy consumption, environmentally friendly, etc), and also to design and optimize thermodynamic systems.

The air conditioner is an example of the many applications encountered, where a refrigerant is used as a heat transfer media. The schematic of the air conditioning cycle is displayed in *Figure 1.2*.

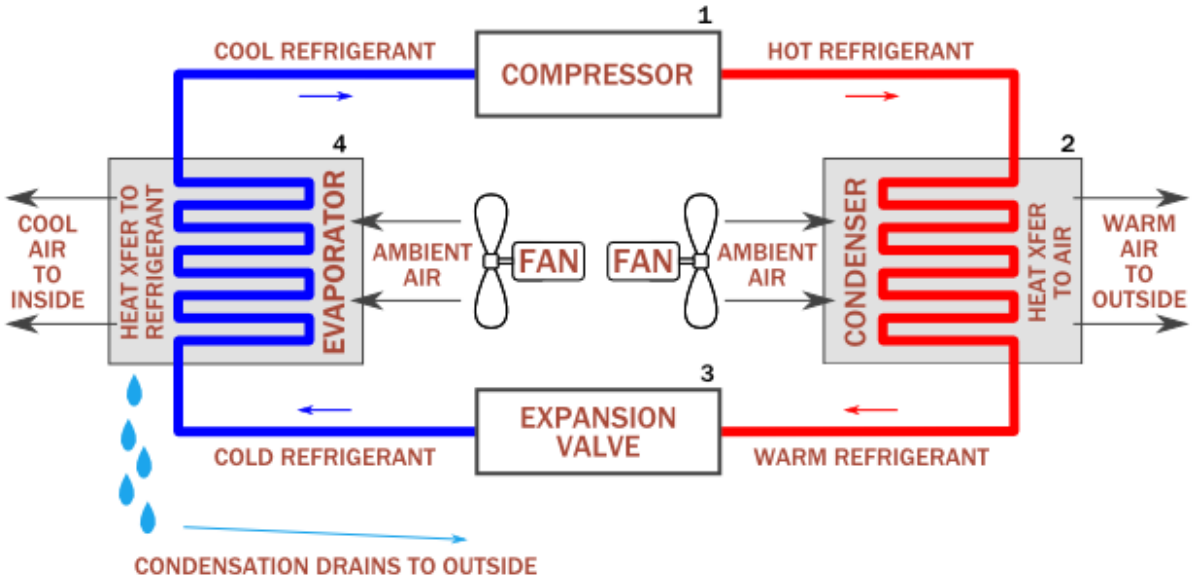

Figure 1.2 Schematic of the air conditioning cycle (Website 1 2016).

The purpose of a refrigeration cycle is to transfer heat from a cold source to a hot well, following different cycles, depending on the needs and the operation conditions (Ciotta 2010). An example of the cycles used is the vapour compression refrigeration cycle.

In this cycle, we find the four main components:

- Compressor: where the refrigerant vapour is compressed following an adiabatic transformation.
- Condenser: where the hot compressed refrigerant vapour is cooled and liquefied following an isobaric transformation.
- Expansion valve: where the liquid refrigerant is expanded irreversibly.
- Evaporator: where the refrigerant is evaporated following an isobaric transformation.

The schematic of the vapour compression refrigeration cycle, along with its T-s (Temperature - entropy) diagram, are displayed in *Figure 1.3*.

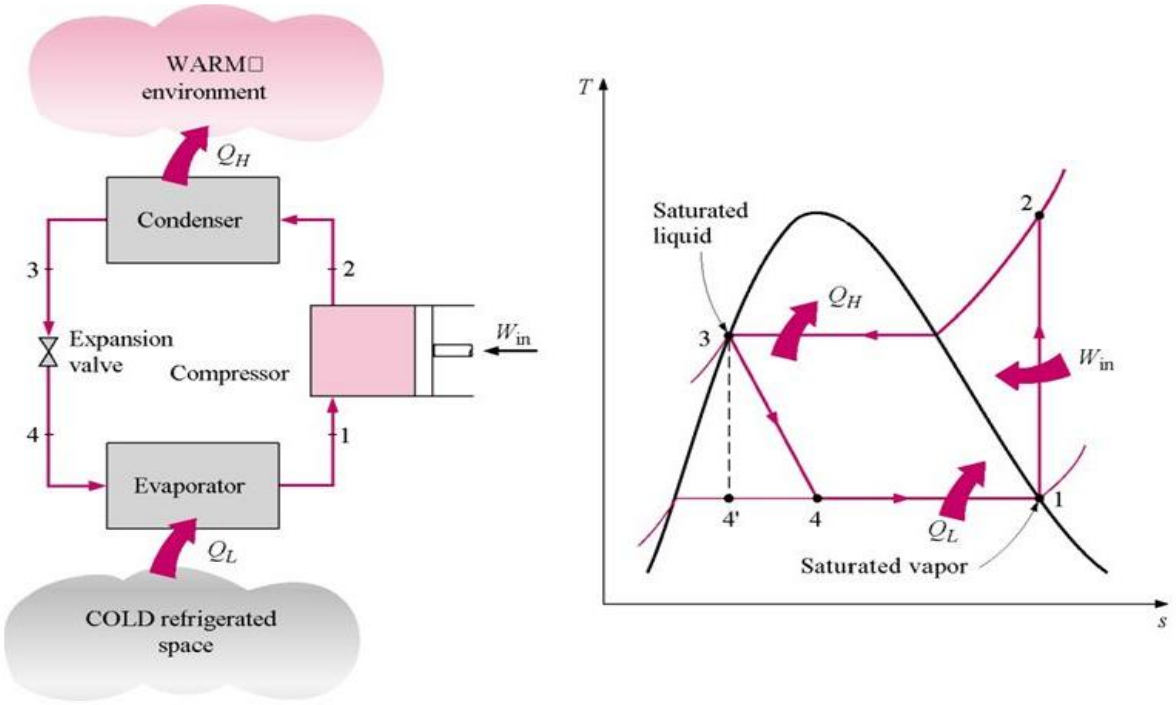

Figure 1.3 Schematic of a vapour compression refrigeration cycle and its associated T-s diagram (Website 2 2016).

To evaluate the performance of a system, we use the coefficient of performance (COP), defined as the ratio between the useful heat (Q_L), and the work supplied to drive the system (W), according to the following expression:

$$COP = \frac{Q_L}{W} \tag{1.2}$$

For a refrigeration system, the expression becomes:

$$COP = \frac{Q_L}{Q_H - Q_L} \tag{1.3}$$

where Q_H is the heat released and Q_L the heat absorbed.

For a heat pump, the expression is obtained by replacing Q_L in the numerator of Eq. (1.3) by Q_H:

$$COP = \frac{Q_H}{Q_H - Q_L} \tag{1.4}$$

1.3. Literature review of available data

To gather the thermodynamic properties of refrigerants needed for the different refrigeration applications, a literature review has been carried out, to investigate the different systems with publicly available data.

In *Table 1.2* we present the pure fluorinated compounds refrigerants with available data in the literature (the data concern mainly VLE and densities properties), and contains the refrigerants from different families.

This table with the references for these data can be found in Appendix A.

Table 1.2 Pure fluorinated compounds refrigerants with available data (Last updated 01/10/2016).

PFC	*CFC*	*HCFC*	*HFC*	*HCFO*	*HFO*
RC318	R11	R21	R23	R1233xf	R1225ye(E)
R14	R12	R22	R32	R1233zd(E)	R1225ye(z)
R116	R13	R123	R41	--	R1225zc
R218	R113	R124	R125	--	R1234ye(E)
--	R114	R141b	R134a	--	R1234yf
--	R115	R142b	R143a	--	R1234ze(E)-trans
--	--	R244bb	R152a	--	R1234ze (trans)
--	--	--	R161	--	R1234ze(Z)-cis
--	--	--	R227ea	--	R1243zf
--	--	--	R236ea	--	R1216
--	--	--	R236fa	--	--
--	--	--	R245ca	--	--
--	--	--	R245fa	--	--
--	--	--	R365mfc	--	--

For the refrigerants, we use not only pure compounds, but also systems of mixtures. In *Table 1.3*, we present the mixtures with available data, that we have found in public literature (the data concern mainly VLE and densities properties). The table contains the mixtures of refrigerants from different families.

This table with the references for these data can be found in Appendix A.

Table 1.3 Mixtures of refrigerants with available data (Last updated 01/10/2016).

Systems			
R14 - R13	R161 - R227ea	R32 - R290	R23 - Propane
R116 - R134a	R236ea - R32	R41 - CO_2	R23 - nButane
R116 - R143a	R236ea - R125	R125 - R134a	Isopentane - R365mfc
R116 - CO_2	HFP - R123	R125 - R143a	Isopentane - R245fa
R12 - R22	HFPO - R123	R125 - R152a	CO_2 - R1233zd(E)
R22 - R114	CO_2 - R32	R125 - R236fa	R134a - R1233zd(E)
R22 - R134a	CO_2 - R134a	R125 - R1234yf	R152a - R1233zd(E)
R22 - R152a	CO_2 - R152a	R134a - R12	R161 - R125 - R143a
R23 - R11	CO_2 - R227ea	R134a - R142b	R161 - R125 - R32
R23 - R13	CO_2 - R1234yf	R134a - R227ea	R32 - R290 - R227ea
R23 - R32	CO_2 - R1234ze(E)	R134a - R236fa	R32 - R125 - R134a
R23 - R125	CO_2 - HFP	R134a - R245fa	R125 - R143a - R134a
R23 - R134a	CO_2 - HFPO	R134a - R1234yf	R22 - R152a - R142b
R23 - R143a	R290 - R227ea	R134a - R1234ze(E)	R290 - R600a - R32
R23 - R152a	R3110 - R365mfc	R143a - R134a	R404A
R23 - R227ea	R161 - R1234yf	R143a - R161	R421A
R32 - R125	R1234yf - R227ea	R143a - R1234yf	R421B
R32 - R134a	R1234yf - R152a	R134a - R152a	R508A
R32 - R143a	R1234yf - R600a	R152a - R227ea	R410A
R32 - R227ea	R1234yf - R244bb	R152a - R1234ze(E)	R410B
R32 - R236fa	R152a - R134	R161 - R32	
R32 - R1234yf	R23 - R116	R161 - R125	
R161 - R134a	R152a - R245fa	R32 - SO_2	

In this work, we focus mainly on the new-generation refrigerants, especially the HFO R1234yf, and the two HCFOs R1233xf and R1233zd(E) (pure compounds and mixtures containing at least one of these refrigerants).

From analysing the data gathered, we can summarize the systems of the new-generation refrigerants with data found in the literature along with the references, in *Table 1.4* (for the pure compounds), and in *Table 1.5* (for the mixtures).

Table 1.4 New-generation pure compounds refrigerants with available data.

HFO	*HCFO*
R1234yf (Lemmon et al. 2010; Di Nicola et al. 2010; Yang et al. 2014; Brown et al. 2010a; Hu, L.-X. Chen, et al. 2013; Tanaka & Higashi 2010a; Klomfar et al. 2012)	R1233xf (Zhang et al. 2013) R1233zd(E) (Hulse et al. 2012)

Table 1.5 Mixtures containing new-generation refrigerants with available data.

	R1234yf
R125	(Kamiaka et al. 2013)
R32	(Kamiaka et al. 2013
R143a	(Hu, L.-X. Chen, et al. 2013)
R134a	(Kamiaka et al. 2013)
R1216	(Klomfar et al. 2012)
CO_2	(G. Di Nicola et al. 2012; Juntarachat et al. 2014)

We can see from these two tables, that the data about these new refrigerants are very scarce (as pure compounds or in mixtures), especially for the two HCFOs, which make a proper investigation and study of these compounds mandatory, in order to have a good understanding of their thermodynamic properties.

2. Experimental equipments

Dans ce chapitre, nous nous intéressons à la description des équipements expérimentaux utilisés dans ce travail, pour les mesures des équilibres liquide-vapeur et des densités. Dans un premier temps, nous donnons la classification des différentes techniques de mesures expérimentales selon la classification de (Dohrn et al. 2010).

Dans un second temps, nous présentons l'appareil utilisé pour les mesures des équilibres liquide-vapeur (ELV), à savoir la cellule d'équilibre. Les mesures ELV se font par méthode statique-analytique à température constante. La cellule d'équilibre est immergée dans un bain liquide permettant le contrôle de la température à l'intérieur de la cellule. Le prélèvement des échantillons se fait au moyen d'échantillonneurs capillaires ROLSI™. L'analyse des échantillons se fait via chromatographie gazeuse au moyen d'un TCD, qui est relié à une unité d'acquisition des données. La mesure des températures et des pressions se fait respectivement par des sondes de température et des capteurs de pression, pour des températures allant jusqu'à 470 K et des pressions allant jusqu'à 300 bar.

En plus de la description de l'appareil de mesure, nous donnons la liste des réfrigérants utilisés pour les mesures d'ELV, avec leur pureté et d'autres informations sur les produits. Aussi, les méthodes d'étalonnage des sondes de température, des capteurs de pression et du TCD sont décrites, en plus de la procédure expérimentale suivie.

Dans un troisième temps l'appareil expérimental utilisé pour les mesures de densités à savoir le densimètre à tube vibrant. Les mesures se font par méthode synthétique-dynamique à température constante. Le densimètre est équipé de deux bains liquides permettant le contrôle des températures du circuit de mesure et du tube vibrant. La mesure des températures et des pressions se fait respectivement par des sondes de température et des capteurs de pression, pour des températures allant jusqu'à 423 K et des pressions allant jusqu'à 700 bar.

En plus de la description du densimètre, nous donnons la liste des réfrigérants utilisés pour les mesures de densités, avec leur pureté et d'autres informations sur les produits. Aussi, les méthodes d'étalonnage des sondes de température, des capteurs de pression et du densimètre sont décrites, en plus de la procédure expérimentale suivie, et la méthode de préparation des mélanges.

Introduction

This Chapter presents and describes the experimental equipment used to perform the vapour-liquid equilibrium (VLE) measurements, and the density measurements during this thesis.
The description and details are given about the materials used, the apparatus specifications, the calibration method, and the experimental procedure followed in order to achieve accurate measurements. Before describing the equipment, a brief review of the experimental phase equilibria techniques available for is given.

2.1. Experimental techniques review

Before describing the equipment used for our experiments, it is of interest to give a brief review about the existing experimental techniques used for phase equilibria, and the classifications used in general to design them.
An example of the classifications is given in *Figure 2.1*, for high-pressure phase equilibria techniques. According to this classification (Dohrn et al. 2010), the different phase equilibria techniques are ranked under two main methods: "Analytical methods" and "Synthetic methods".

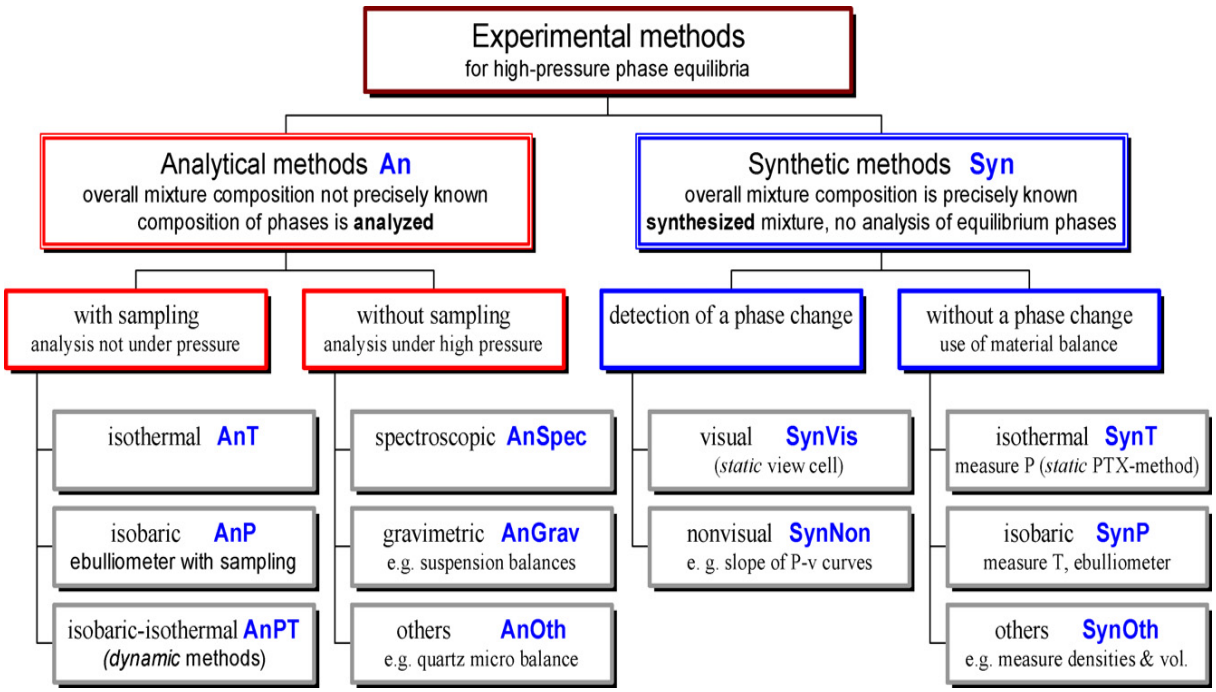

Figure 2.1 Experimental methods classifications for high-pressure phase equilibria (Dohrn et al. 2010)

2.1.1. Analytical methods

For the “analytical methods”, we usually work without knowing the overall mixture composition, and through the method, we determine “analyse” the composition of the phases, hence the designation “analytical methods”. Under this category, different techniques can be found, classified under two main classes: “with sampling” and “without sampling”.

For the “analytical methods with sampling”, the phase composition analysis is carried out not under pressure. Under this category, we find several techniques such as the “isothermal techniques” in which the measure is achieved at fixed temperature; the “isobaric techniques” where the working pressure is fixed (an example of these techniques is the ebulliometer with sampling) and the “isobaric-isothermal” techniques.

For the “analytical methods without sampling”, the analysis of the phase composition is performed under high pressure. Under this category, different techniques can be found, like the “spectroscopic techniques”, and the “gravimetric techniques” (e.g. the suspension balances).

The full details and description of these different techniques can be found in (Dohrn et al. 2010; Fonseca et al. 2011) papers.

2.1.2. Synthetic methods

For the synthetic methods, the overall mixture composition is exactly known in advance, and no analysis of the equilibrium phase is performed. The synthetic methods can mainly be classified under two main families: “methods with a phase change” and “methods without a phase change”.

For the “synthetic methods with a phase change”, the detection of the phase change can be “visual”, like when using a static view cell, or “non-visual”, such as determining the phase change from the slope of the P-V curves.

Under the “synthetic methods without a phase change” category, we find “isothermal techniques”, such as static PTx method, allowing one to measure the pressure while the temperature is constant. We also find “isobaric techniques” where the pressure is fixed, while we measure the temperature (e.g. the ebulliometer). In addition, we can find other synthetic techniques, such as the techniques involving the measurement of the densities.

The full details and description concerning these different techniques can be found in (Dohrn et al. 2010; Fonseca et al. 2011) papers.

2.2. VLE equipment

2.2.1. Materials

Nine refrigerants were used to achieve VLE measurements, to study pure compounds vapour pressures, and binary mixtures phase behaviour.

The refrigerants used for the VLE experiments, along with their ASHRAE number, chemical formula, CAS number, the name of the supplier and the purity of the product, are reported in *Table 2.1*.

Table 2.1 Refrigerants used in VLE measurements

Compound	*ASHRAE Number*	*Formula*	*CAS Number*	*Supplier*	*Purity*
Carbon dioxide	R744	CO_2	124-38-9	Air liquide	>99.995%
2,3,3,3-Tetrafluoropropene	R1234yf	$C_3H_2F_4$	754-12-1	Honeywell	>99.5%
1,1,1,2-Tetrafluoroethane	R134a	$C_2H_2F_4$	811-97-2	Climalife	>99%
1,1-Difluoroethane	R152a	$C_2H_4F_2$	75-37-6	Dehon	>99%
Trans-1-chloro,3,3,3-trifluoropropene	R1233zd(E)	$C_3F_3H_2Cl$	102687-65-0	Synquest	>97%[a]
2-chloro-3,3,3 -trifluoropropene	R1233xf	$C_3F_3H_2Cl$	2730-62-3	Synquest	>99%
1,1,1,3,3-pentafluoropropane	R245fa	$C_3H_3F_5$	460-73-1	Honeywell	>99%
Trifluoroethane	R23	$C_2H_3F_3$	420-46-2	Climalife	> 99.5%
n-Propane	R290	C_3H_8	74-98-6	Messer	> 99.995%

[a] The purities given by the suppliers were verified by chromatographic analysis. For the R1233zd(E) we found a purity different to the one announced by the supplier (purity verified is estimated to be 93%).

2.2.2. Apparatus

The equipment used for the VLE measurements is based on a static-analytic method with liquid and vapour phase sampling using a capillary sampler ROLSI™. The equipment can be categorized under "Analytical technique, with sampling, isothermal AnT" according to (Dohrn et al. 2010) classification.

The main part of the apparatus is the equilibrium cell, where the two-phase equilibrium takes place. The flow diagram of the apparatus is displayed in *Figure 2.2* below.

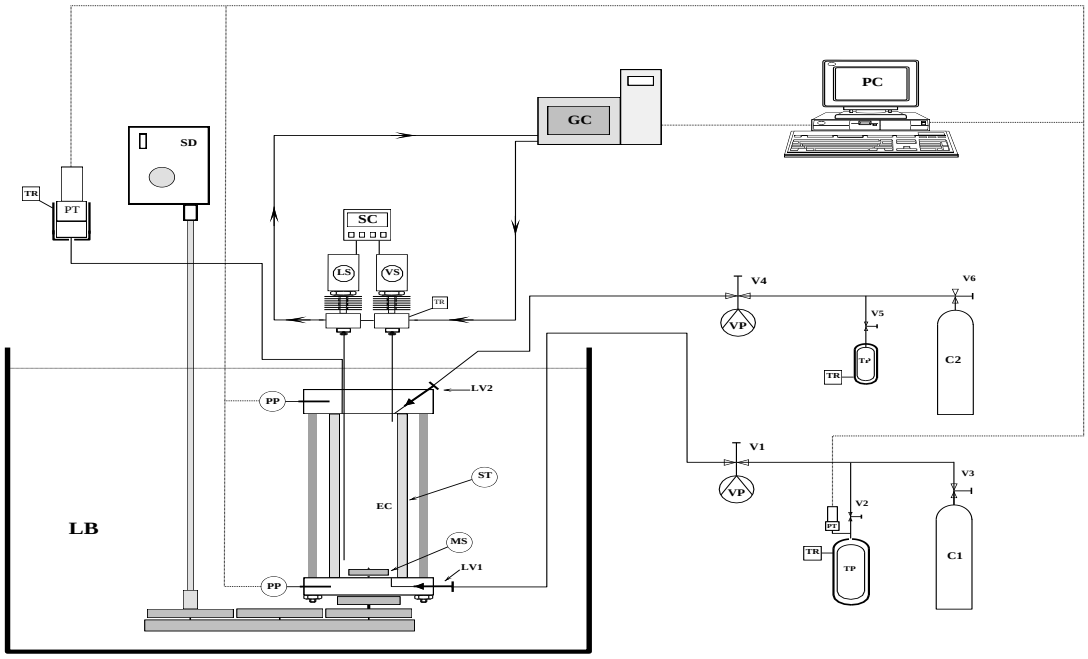

Figure 2.2 Flow diagram of the static-analytic apparatus (Juntarachat et al. 2014).
EC: equilibrium cell; LV: loading valve; MS: magnetic stirrer; PP: platinum resistance thermometer probe; PT: pressure transducer; RT: temperature regulator; LB: liquid bath; TP: thermal press; C1: more volatile compound; C2: less volatile compound; V: valve; GC: gas chromatograph; LS: liquid sampler; VS: vapor sampler; SC: sample controlling; PC: personal computer; VP: vacuum pump.

The apparatus is equipped with a thermo-regulated liquid bath where the equilibrium cell is immersed. The bath ensures the control of the temperature within 0.01 K.

The temperature measurements inside the equilibrium cell is performed using two platinum resistance thermometer probes (Pt100) (Valtz et al. 2003), one to measure the temperature at the top of the cell, and the other for the temperature at the bottom of the cell. Two other

temperature probes are used to control the temperature inside the thermal presses used to load the chemical products into the equilibrium cell.

The Pt100 probes are connected to a data acquisition unit (HP34970A). The Pt100 probes are calibrated against a 25 Ω reference platinum resistance thermometer (Pt25 - Hart Scientific). The Pt25 reference probe was calibrated by the "Laboratoire National d'Essais de Paris" based on the 1990 International Temperature Scale (ITS 90). The temperature accuracy is estimated to be within ± 0.03 K.

The pressure is measured using two pressure transducers, one for low pressures (DRUCK, 0 – 30 bar), and another for high pressures (DRUCK, 0 – 300 bar) connected to the same data acquisition unit (HP34970A). The pressure transducers are calibrated against a pressure automated calibrator (GE Sensing, model PACE 5000). The pressure accuracy is estimated to be within ± 0.004 bar.

The analytical work is performed using a gas chromatograph (VARIAN, model CP-3800) equipped with a thermal conductivity detector (TCD). The analytical column used for most of the measurements is a RESTEK, 1% RT-1000 on Carboblack B, 60/80 mesh (length: 2.4m, diameter: 2mm from Restek, ID Silcosteel).

The TCD is calibrated by introducing manually known amounts of each pure compound (for the system studied) through an automatic syringe in the injector of the gas chromatograph.

2.2.3. Sensors Calibrations

2.2.3.1. Temperature probes calibration

As mentioned before, the calibration of the Pt100 probes is performed using a 25 Ω reference platinum resistance thermometer (Pt25 - Hart Scientific).

The corrected values (T_{cal}) are obtained from the polynomial relation (1^{st} or 2^{nd} order) relating the values read through the temperature probes (T_{read}) to the values obtained with the reference probe (T_{ref}).

Example of the calibration is given in *Figure 2.3*, representing the calibration of the temperature probe at the bottom of the cell, where we have the representation of T_{ref} as a function of T_{read} and the representation of the deviation between T_{ref} and T_{cal} as a function of T_{ref}.

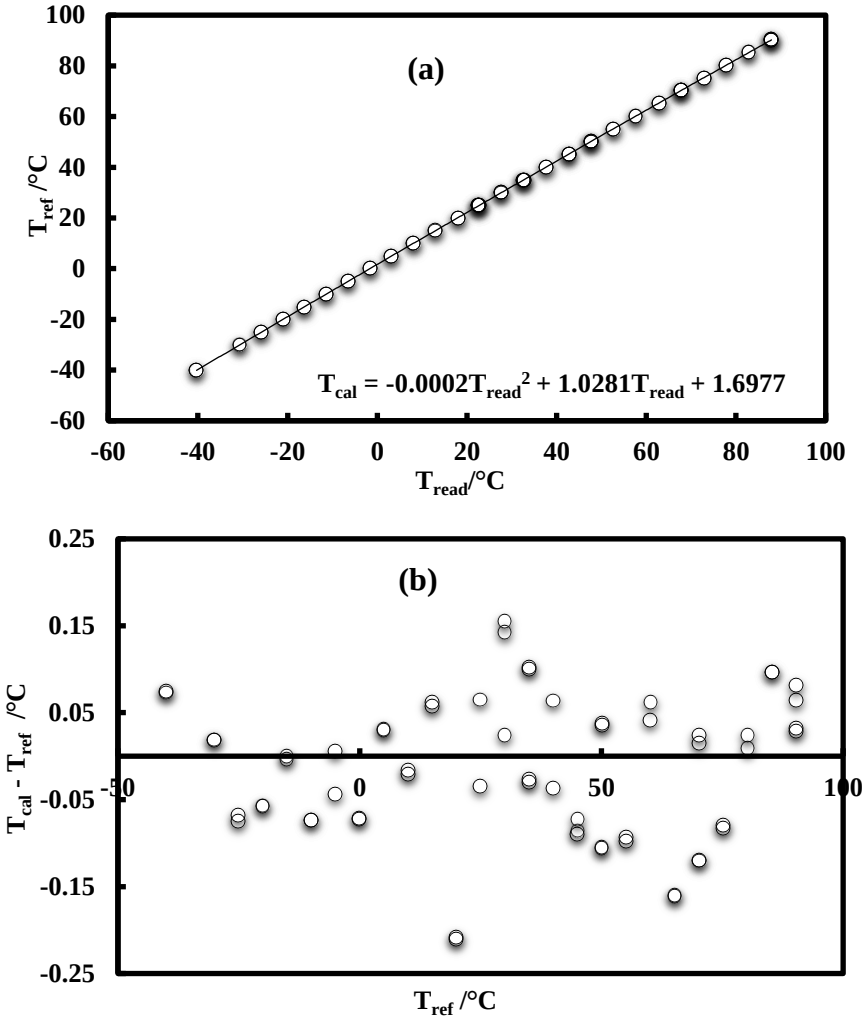

Figure 2.3 Calibration of the temperature probe. (a): Second-order relation between the read and reference temperatures. (b): Deviations from the reference temperature, resulting from the use of a second-order relation.

2.2.3.2. Pressure transducers calibration

As mentioned before, the pressure transducers are calibrated against a pressure automated calibrator (GE Sensing, model PACE 5000).

The corrected value (P_{cal}) are obtained from the polynomial relation (1st or 2nd order) relating the values read through the temperature probes (P_{read}) to the values obtained with the reference probe (P_{ref}).

Example of the calibration is given in *Figure 2.4*, representing the calibration of the low-pressure transducer (DRUCK, 0 – 30 bar), where we have the representation of P_{ref} as a function of P_{read}, and the representation of the deviation between P_{ref} and P_{cal} as a function of P_{ref}.

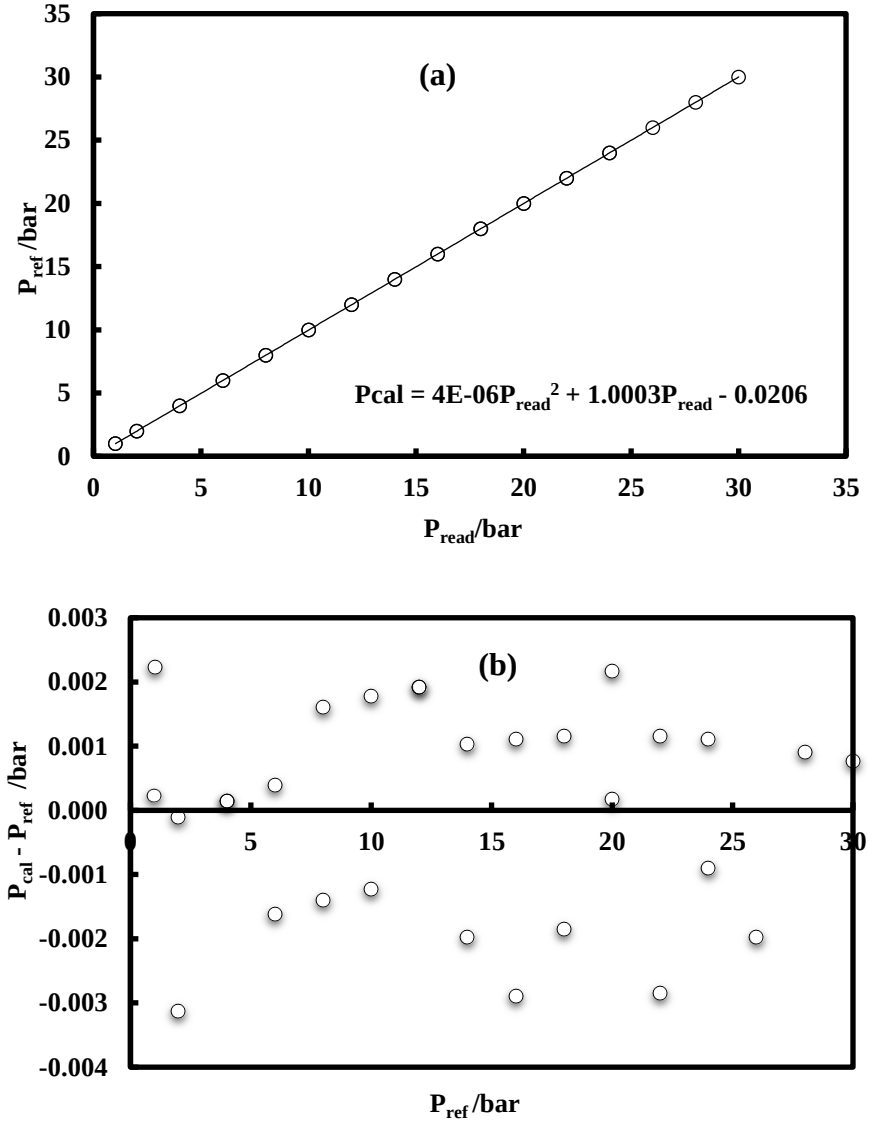

Figure 2.4. Calibration of the pressure transducer DRUCK (0 – 30 bar). (a): Second-order relation between the experimental and reference pressures. (b): Deviations from the reference pressure, resulting from the use of a second-order relation.

2.2.3.3. TCD calibration

As mentioned before, the TCD is calibrated by introducing known amounts of each pure compound (for the system studied) through an automatic syringe (allowing more precise injections) in the injector of the gas chromatograph.

The calibration of the gas chromatograph consists in establishing a polynomial expression (usually second order, for more precision) between the surface area of the peak obtained (S) and the number of moles injected n_{inj}. The number of moles injected is obtained through the

volume injected using the automatic syringe (which has a total volume of 500µl). The number of moles calculated n_{cal} is obtained through the polynomial relation determined.

Example of the calibration is given in *Figure 2.5*, where we have the representation of n_{inj} as function of the surface peak area (S), and the representation of the relative deviation between n_{inj} and n_{cal} as a function of (S).

The relative deviation relatively low (less than 1%) can be explained by the fact of using an automatic syringe (allowing more precise injections), and also due to the fact of using the refrigerants at gas state during the calibration.

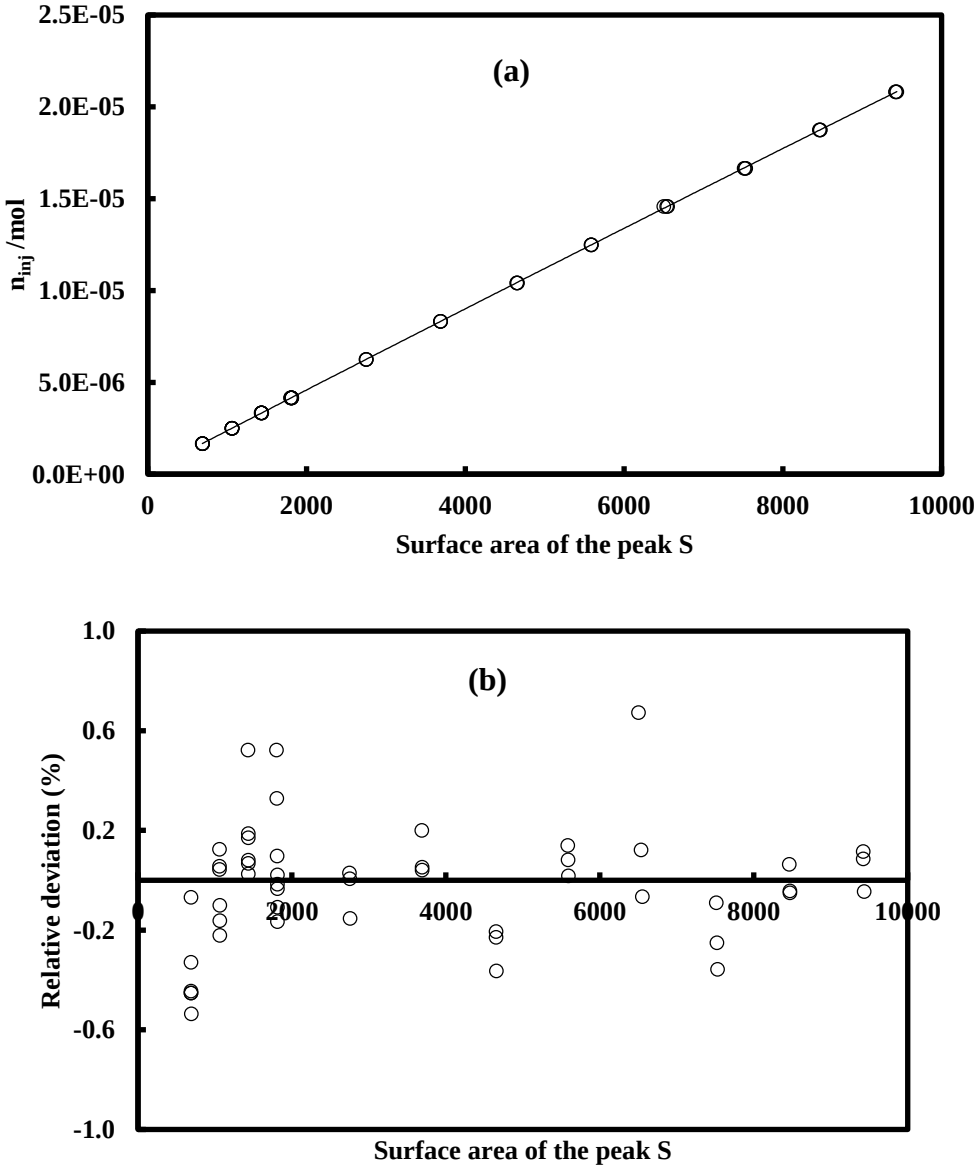

Figure 2.5. Calibration of the TCD. (a): Second-order relation between the peak surface area S and the number of moles injected n_{inj}. (b): Relative deviation between n_{inj} and n_{cal}.

2.2.4. Experimental procedure

At ambient temperature, the equilibrium cell and its loading lines are made under vacuum. A first thermal press is loaded with one of the compounds, the second press with the other compound.

The liquid bath is set to the temperature desired. When the equilibrium temperature is reached (the equilibrium temperature is reached when the Pt100 probes give the same temperature value within their temperature uncertainty for at least 10 minutes), an amount of about 5 cm^3 of the heavier component (the component with the lower vapour pressure) is introduced into the equilibrium cell. Its vapour pressure is then measured at this temperature (Valtz et al. 2003).

Then, given amount of the lightest component (the component with the higher vapour pressure) is introduced step by step in order to increase the pressure inside the cell, leading to successive equilibrium mixtures, in order to have enough points to cover the two-phase envelope.

The equilibrium inside the cell is assumed to be reached when the pressure does not change during a period of 10 minutes within ±0.01 bar under continuous stirring (Valtz et al. 2003).

For each equilibrium condition, six or more samples of both vapour and liquid phases are taken using the capillary sampler ROLSI^{TM} and analysed in order to verify the repeatability of the measurement.

2.3. Vibrating tube densimeter (VTD)

2.3.1. Materials

Five refrigerants were used for density measurements, aiming to study the density of two pure compounds, two binary mixtures, and one ternary mixture.

In *Table 2.2* are reported the refrigerants used for density measurements, with the details about their ASHRAE number, chemical formula, CAS number, along with the name of the supplier and the purity of the product.

Table 2.2 Refrigerants used for density measurements

Compound	*ASHRAE Number*	*Formula*	*CAS Number*	*Supplier*	*Purity*
1,1,1,2-Tetrafluoroethane	R134a	$C_2H_2F_4$	811-97-2	Climalife	>99%
1,1-Difluoroethane	R152a	$C_2H_4F_2$	75-37-6	Dehon	>99%
2,3,3,3-Tetrafluoropropene	R1234yf	$C_3H_2F_4$	754-12-1	Honeywell	>99.5%
Trans-1-chloro,3,3,3-trifluoropropene	R1233zd(E)	$C_3F_3H_2Cl$	102687-65-0	Synquest	>97%[a]
2-chloro-3,3,3 -trifluoropropene	R1233xf	$C_3F_3H_2Cl$	2730-62-3	Synquest	>99%

[a] The purities given by the suppliers were verified by chromatographic analysis. For the R1233zd(E) we found a purity different to the one announced by the supplier (purity verified is estimated to be 93%).

2.3.2. Apparatus

The measurements are based on an indirect synthetic method, by means of a vibrating tube densimeter (VTD). The measurements are performed in a dynamic way, at isothermal conditions.

The method is based on the relation between the vibrating period of a dimensional resonator and its vibrating mass. The density of a system is determined by measuring the period of vibration as a function of temperature and pressure (Dicko, Belaribi-Boukais, et al. 2011).

The simplified equation modelling the vibrating tube densimeter is given as follows (Bouchot & Richon 1998a):

$$\rho = \left(\frac{M_0}{V_i}\right)\left(\left(\frac{K\tau^2}{K_0{\tau_0}^2}\right) - 1\right) \tag{2.1}$$

where ρ is the density of the fluid inside the tube; M_0 is the mass of the tube under vacuum; V_i is the internal volume of the densimeter tube; K ($kg.m^{-3}.s^{-2}$) is the natural transversal stiffness of the vibrating tube; τ is the period of vibration of the tube; K_0 ($kg.m^{-3}.s^{-2}$) is the transversal stiffness of the tube under vacuum; τ_0 is the vibrating period of the tube under vacuum. The detailed equations of the VTD can be found in Appendix B.

The main part of the apparatus is the densimeter cell DMA-512P (Anton Paar KG). The vibrating tube is made of stainless steel and can support pressures up to 400 bar (Coquelet et al. 2010).

The flow diagram of the vibrating tube densimeter is displayed in *Figure 2.6*.

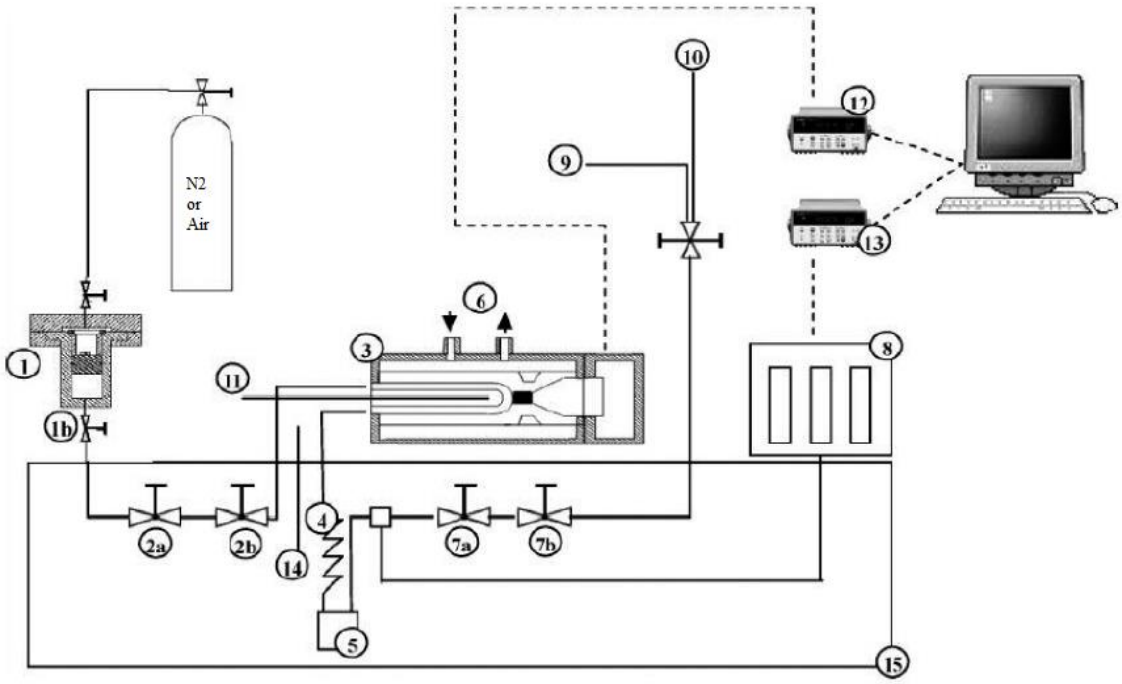

Figure 2.6 Flow diagram of the vibrating-tube densimeter. (Khalil et al. 2007; Khalil 2006).
(1): loading cell; (2a) and (2b): regulating and shut-off valves; (3): DMA-512P densimeter; (4): heat exchanger; (5): bursting disk; (6): inlet of the temperature regulating fluid; (7a) and (7b): regulating and shut-off valves; (8): pressure transducers; (9): vacuum pump; (10): vent; (11): vibrating cell temperature probe; (12): HP 53131A data acquisition unit; (13): HP34970A data acquisition unit; (14): bath temperature probe; (15): principal liquid bath.

The pressure is measured using three pressure transducers (DRUCK, 0 – 50 bar, 0 – 300 bar, 0 – 700 bar) depending on the interval of study concerned (in our measurements, we work in the range of pressure up to 200 bar, and thus we need only the first two transducers).
The three transducers are connected to the same data acquisition unit (HP34970A). They are calibrated against a reference pressure automated calibrator (GE Sensing, model PACE 5000). The resulting accuracy is estimated to be ±0.002 bar for the "0 – 50 bar" transducer and ±0.015 bar for the "0 – 300 bar" transducer.
The temperature of the vibrating tube is controlled by a regulated liquid bath (Lauda RE206) with a stability within ±0.01 K. The temperature of the remaining parts of the circuit is regulated by a liquid bath (West P6100) (Bouchot & Richon 1998a).
The temperatures of the vibrating tube and of the principal liquid bath are measured by two platinum resistance thermometer probes (Pt100), respectively PT1 and PT2. The Pt100 probes are connected to the data acquisition unit (HP34970A). The Pt100 probes are calibrated against a 25Ω reference platinum resistance thermometer (Hart Scientific).
For the liquid phase, and in order to reach the bubble point, the temperature of the principal liquid bath is set to a value between 0.2 and 0.5 K lower than the vibrating tube temperature (in this way, the vibrating tube will be the place where the first vapour bubble appears). For the vapour phase, the temperature of the principal liquid bath should be higher by the same value than the temperature of the vibrating tube in order to reach the dew point (in this way, the vibrating tube will be the place where the first liquid drop appears).

2.3.3. Mixture preparation

A variable volume cell is used for preparing the mixture and loading it into the measurement circuit.
The volume of the cell is variable through a piston separating the pressurized nitrogen from the fluid inside the cell (Bouchot & Richon 1998a). The cell has a total volume of 100 cm^3.
For the pure compounds, we can either use a variable volume cell or a thermal press. When using a thermal press, the pressure is increased by increasing the temperature of the press (by heating for instance). However, this method is only possible for pure compounds, and also if the domain of pressure is not very high (around 100 bar in our case).
For the mixtures, the variable volume cell was used to prepare the mixture with the desired composition. The cell is first made under vacuum along with its loading lines for couple of

minutes in order to reach a good vacuum. The cell is then weighed using an electronic mass balance with four digits degree precision.
The less volatile component (with the lowest vapour pressure) is introduced first into the cell while controlling the amount introduced with the mass balance.
The more volatile compound is then introduced into the cell following the same procedure.
Mixtures are homogenized and pressurized to pressures higher than their bubble pressures to be in the monophasic domain.

2.3.4. Sensors calibration

In this section, the procedures followed to calibrate the temperature probes, the pressures transducers and the densimeter itself, are described.

2.3.4.1. Temperature probes calibration

As mentioned before, the calibration of the Pt100 probes is performed using a 25 Ω reference platinum resistance thermometer (Pt25 - Hart Scientific), which was calibrated by the "Laboratoire National d'Essais de Paris" based on the 1990 International Temperature Scale (ITS 90).
The corrected value (T_{cal}) are obtained from the polynomial relation (1^{st} or 2^{nd} order) relating the values read through the temperature probes (T_{read}) to the values obtained with the reference probe (T_{ref}).
Example of the calibration is given in *Figure 2.7*, representing the calibration of the temperature probe of the vibrating tube, where we have the representation of T_{ref} as a function of T_{read} and the representation of the deviation between T_{ref} and T_{cal} as a function of T_{ref}.

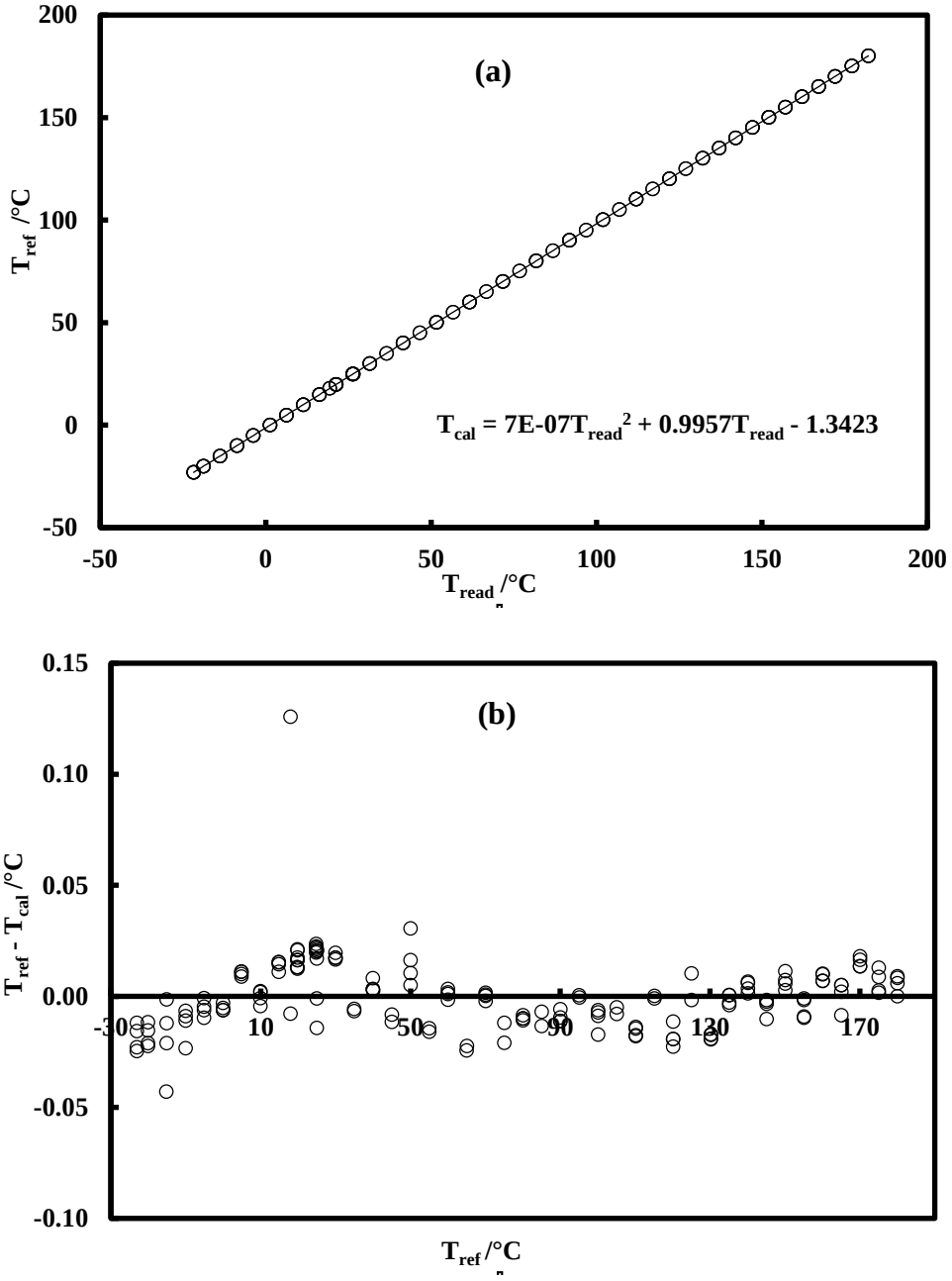

Figure 2.7 Calibration of the VTD temperature probe. (a): Second-order relation between the read and reference temperatures. (b): Deviations from the reference temperature, resulting from the use of a second-order relation.

2.3.4.2. Pressure transducers calibration

As mentioned before, the pressure transducers are calibrated against a reference pressure automated calibrator (GE Sensing, model PACE 5000).

The resulting accuracy is estimated to be ±0.002 bar for the "0 – 50 bar" transducer and ±0.015 bar for the "0 – 300 bar" transducer.

The corrected value (P_{cal}) are obtained from the polynomial relation (1^{st} or 2^{nd} order) relating the values read through the temperature probes (P_{read}) to the values obtained with the reference probe (P_{ref}).

An example of the calibration is given in *Figure 2.8*, representing the calibration of the low-pressure transducer (DRUCK, 0 – 50 bar), where we have the representation of P_{ref} as a function of P_{read}, and the representation of the deviation between P_{ref} and P_{cal} as a function of P_{ref}.

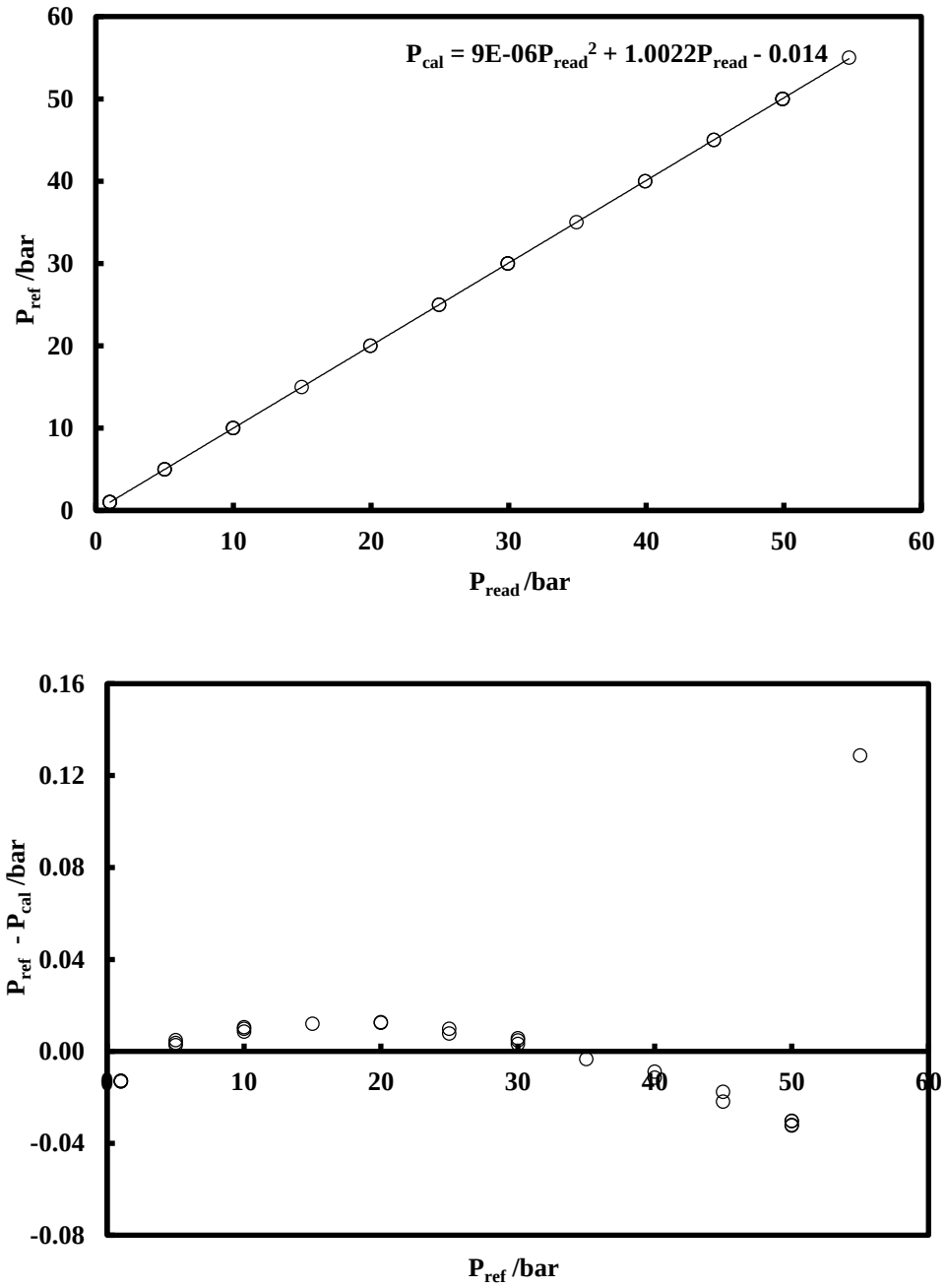

Figure 2.8 Calibration of the low-pressure transducer DRUCK (0 – 50 bar). (a): Second-order relation between the experimental and reference pressures. (b): Deviations from the reference pressure, resulting from the use of a second-order relation.

2.3.4.3. Densimeter calibration

To proceed to the densimeter calibration, the tube is made first under vacuum at the measurement temperature and its vibrating period τ_0 is measured and used for the calibration of the densimeter, in order to determine the optimal mechanical parameters of Eq. (2.1).

The measurements are started with a reference fluid for the calibration. This fluid may differ depending on the system under study. Indeed, there are various constraints on the choice of the reference fluid. Its density should be well known as a function of T and P, and its compressibility should be sufficient. The reference fluid should have a neutral behaviour so it does not cause any adsorption or desorption effects or mechanical damages to the material of the tube. And it should be easy to remove from the tube after each calibration (Bouchot & Richon 1998a).

For the systems of refrigerants studied, we used the R134a (1,1,1,2-tetrafluoroethane) as a reference fluid for the calibration of the densimeter. Data concerning density, pressure and temperature of this fluid are very well known, and are available on REFPROP 9.0 (Lemmon et al. 2010).

The calibration at a given temperature consists of the determination of the value of the vibrating period under vacuum (τ_0) and the description of the corresponding isothermal P-ρ curve of R134a. The period measured by the VTD is converted into density using the parameters of Eq. (2.1). The calibration of the densimeter is achieved using the forced path mechanical calibration model (FPMC) (Bouchot & Richon 1998a). It consists in determining the mechanical parameters of the densimeter by minimizing the difference between the density calculated and the density obtained from REFPROP 9.0.

Example of the calibration with the refrigerant R134a (reference fluid) at T = 278.15 K, is displayed in *Figure 2.9*, representing the deviations between the reference density ρ_{ref} (obtained from REFPROP 9.0), and the calculated density ρ_{cal} as a function of the reference density ρ_{ref}.

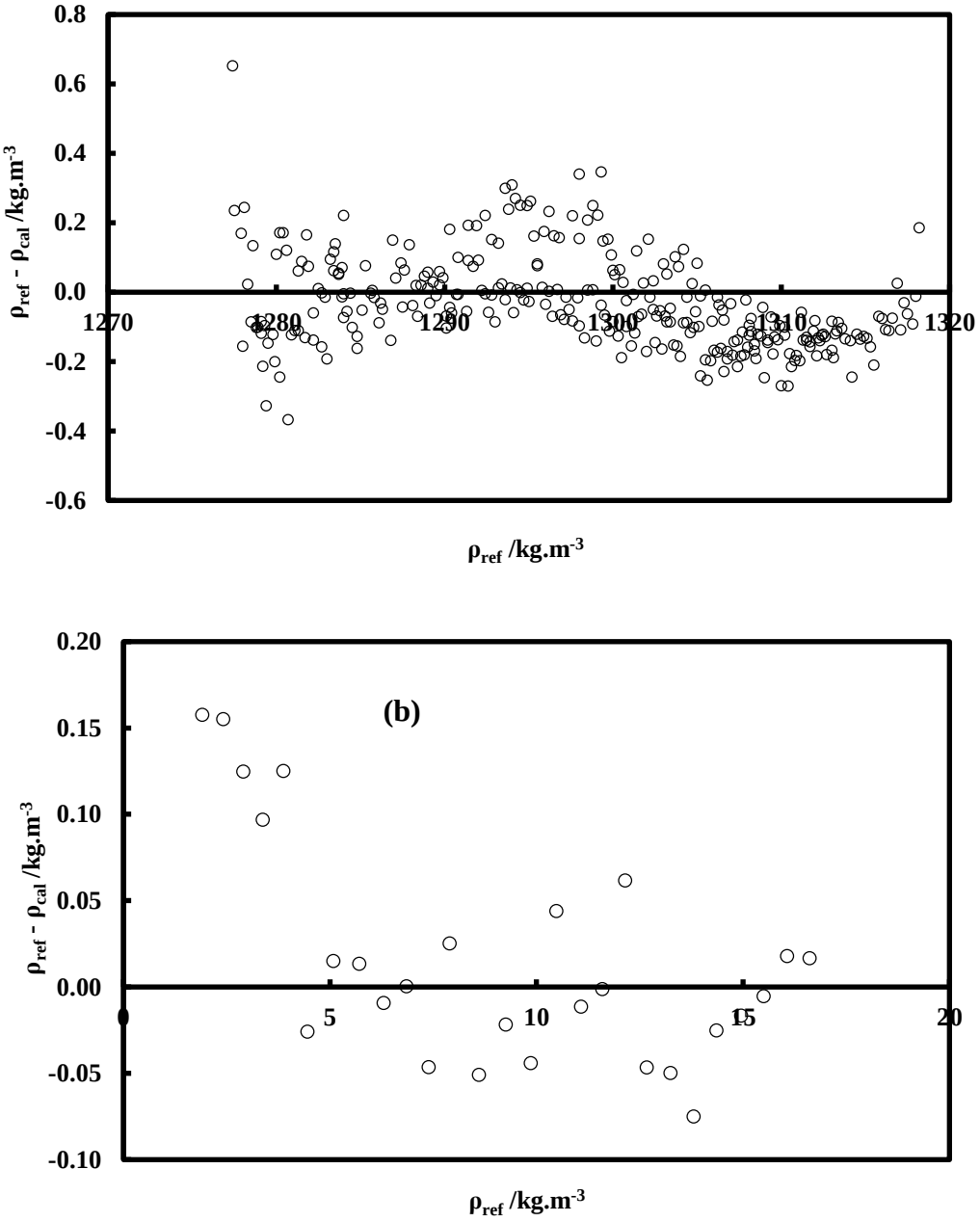

Figure 2.9 Calibration of the vibrating tube densimeter. (a): Liquid phase. (b): Vapour phase.

2.3.5. Experimental procedure

Once the calibration phase is completed, the reference fluid R134a is removed from the measurement circuit, the vacuum conditions are made, and an isothermal measurement of the studied fluid can be started (Bouchot & Richon 1998a).

The fluid under study is kept in a pressure higher than its bubble point pressure (to be in a monophasic state). Small amounts of the fluid are continuously introduced into the vibrating tube in order to increase the pressure. The pressure is increased gradually until reaching the dew point, determined from the drastic change in the slope of the P-τ curve. The fluid is then condensed by increasing gradually the pressure until reaching the highest pressure desired (for our case around 100 - 120 bar).

When the fluid is in the liquid phase we should pay attention to purge the circuit by introducing a fresh fluid from the loading cell into the circuit (particularly when working with mixtures) (Khalil et al. 2007) to make sure to have the right composition inside the circuit. When reaching the maximum pressure, we start by decreasing the pressure until reaching the bubble point (determined from the drastic change in the slope of the P-τ curve), and we continue until reaching the lowest pressure possible. The pressure, temperature and period are recorded every 3 s. The pressure increase and decrease are controlled using a regulating valve with a rate of 0.03 bar/s approximately.

Concluding remarks

In this Chapter, a review of the experimental techniques available for phase equilibria measurements and its classification were given. A detailed description of the equipment used for VLE and density measurements was carried out, along with the description of the materials and the apparatus used, the experimental procedure and the calibration.

The equipments described in this section were used to achieve the experimental VLE and density measurements that will be presented in Chapter 3.

3. Experimental results

Dans ce chapitre, nous présentons les résultats expérimentaux obtenus pour les mesures d'ELV et les mesures de densités pour les systèmes de réfrigérants étudiés (corps purs et mélanges).

La méthodologie utilisée pour le choix des systèmes étudiés repose sur plusieurs facteurs. Comme mentionné précédemment dans l'étude bibliographique établie, les données concernant les réfrigérants R1234yf, R1233xf et R1233zd(E) et les mélanges les contenant sont très rares. Les systèmes étudiés contiennent au moins un de ces réfrigérants.

Pour les mesures ELV, en plus des pressions de vapeur de ces trois réfrigérants et des deux réfrigérants d'ancienne génération R134a et R152a, nous avons aussi étudié les mélanges binaires contenant une combinaison de ces trois réfrigérants à savoir (R1234yf/R1233xf, R1234yf/R1233zd(E) and R1233zd(E)/R1233xf). En plus de ces systèmes nous avons aussi étudié des systèmes binaires contenant au moins un de ces trois nouveaux réfrigérants. Certains des réfrigérants étudiés sont supposés être remplacés par les nouveaux réfrigérants, comme le R134a destiné à être remplacé par le R1234yf, ou le R245fa destiné à être remplacé par le R1233zd(E). En plus, plusieurs des systèmes étudiés contiennent un azéotrope, ce qui les rend intéressant d'un point de vue d'application industrielle.

Nous avons aussi étudié des systèmes contenant ces nouveaux réfrigérants et le dioxyde de carbone (CO_2/R1234yf, CO_2/R1233zd(E)), puisque ces types de systèmes sont très intéressants d'un point de vue pratique pour les systèmes trans-critiques. Enfin, d'autres systèmes font partie de collaborations académiques comme le système (R23/Propane).

Pour les mesures de densités, nous nous sommes concentrés sur l'étude des réfrigérants corps purs R1233xf et R1233zd(E), comme il n'y a pas de données disponibles sur les densités de ces composés. Pour les mélanges, nous avons étudié des systèmes contenant le R1234yf avec d'autres fluides d'ancienne génération comme le R134a et le R152a (ces systèmes ont été aussi étudiés dans les mesures ELV), car ces systèmes ont une (P, T) enveloppe très étroite ; similaire à celle d'un corps pur ; et un glissement de température très faible, ce qui les rend très intéressant du point de vue d'application dans des systèmes de réfrigération.

Dans une première partie de ce chapitre, les mesures d'ELV sont présentées, tout d'abord pour les réfrigérants corps purs, et ensuite pour les mélanges étudiés.

Dans la seconde partie de ce chapitre, les mesures de densités sont présentées, tout d'abord pour les réfrigérants corps purs, et ensuite pour les mélanges binaires et ternaires.

En plus des résultats expérimentaux présentés, les incertitudes sur les mesures sont reportées, notamment les incertitudes sur les températures, les pressions, les compositions molaires et les densités.

Introduction

In this Chapter, the experimental results for VLE and density measurements of the refrigerants systems studied are presented.

The methodology followed to choose the systems studied was based on several factors. As we mentioned earlier in the literature review, data and information about the new-generation refrigerants R1234yf, R1233xf and R1233zd(E), are scarce. Thus, the systems studied experimentally contain at least one of these refrigerants.

For the VLE measurements, in addition to the vapour pressures of the three new-generation and two old-generation refrigerants (R152a and R245fa), we have studied binary systems containing combinations of these three new refrigerants (R1234yf/R1233xf, R1234yf/R1233zd(E) and R1233zd(E)/R1233xf), in addition to systems containing one of these refrigerants with other common refrigerants. Some of these refrigerants are supposed to be replaced by the new refrigerants (such as the R1234yf for the R134a, or the R1233zd(E) for the R245fa). Plus, these systems are azeotropic and thus would be very interesting in refrigeration applications.

Also, we studied combinations of new refrigerants with CO_2 (CO_2/R1234yf, CO_2/R1233zd(E)), as this would be very interesting for the trans-critical cycles. Then there is other systems that are part of academic collaborations (R23/Propane).

For the density measurements, we focused on the study of the pure compounds R1233xf and R1233zd(E), as no data are available on their densities. For the mixtures, we studied the binary and ternary mixtures containing R1234yf with other old-generation refrigerants such as R134a and R152a (these systems were also studied for VLE measurements), as these systems have a very narrow (P, T) envelope similar to a pure compound and a low temperature glide, and would be very interesting from an industrial perspective for refrigeration applications.

In a first section, the VLE results are presented, first the pure compounds; by presenting the results of the vapour pressures obtained; then for the binary mixtures, by presenting the results of the phase diagrams obtained, within the relative volatility calculated.

In a second section, the density measurements are presented, first for the pure compounds, then for the binary and ternary mixtures.

Along with the results presented, the experimental uncertainties on the temperature, the pressure, the molar composition, and the density are reported.

3.1. VLE results

3.1.1. Pure compounds vapour pressures

The vapour pressures of the pure compounds R152a, R1234yf, R1233zd(E), R1233xf and R245fa were measured, for different ranges of temperature, as reported in *Table 3.1*.
The results of the vapour pressures obtained for each compound are presented below in this section, along with the expanded uncertainties on the temperature and the pressure (denoted by U(X) = u(X, k=2), with a coverage factor k = 2).

Table 3.1 Pure compounds studied.

Pure compounds	*T/K*
R152a	275 - 336
R1234yf	275 - 336
R1233zd(E)	276 - 340
R1233xf	237 - 308
R245fa	280 - 340

3.1.1.1. Pure compound R152a

The vapour pressures of the pure compound R152a were measured for temperatures between 275 K and 336 K.

The experimental data obtained are displayed in *Figure 3.1*, with the graphical representation of the (P-T) diagram, and the (lnP - 1/T) diagram, along with the expanded experimental uncertainties on the temperature and the pressure. We can notice that the (lnP - 1/T) curve shows a linear trend.

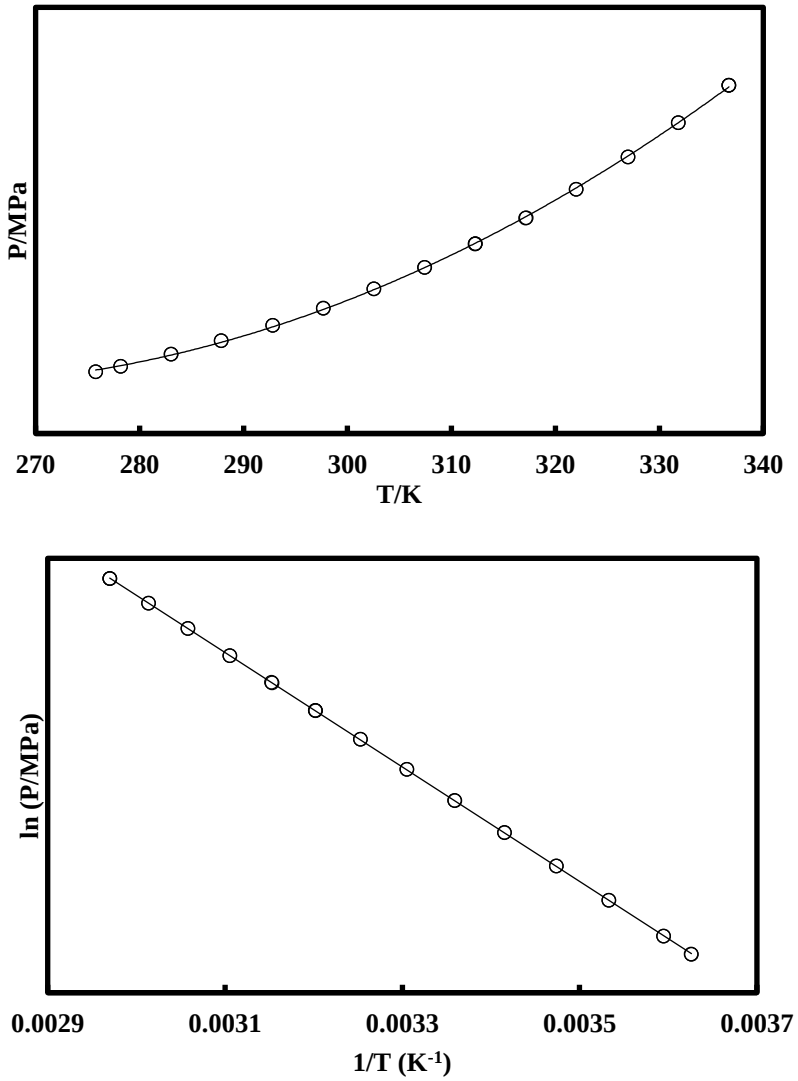

Figure 3.1 Vapour pressures of the pure compound R152a. U(T) = 0.08 K; U(P) = 0.0004 MPa.

3.1.1.2. Pure compound R1234yf

The vapour pressures of the pure compound R1234yf were measured for temperatures between 275 K and 336 K. The experimental data obtained are displayed in *Figure 3.2*, showing the graphical representation of the (P-T) diagram, and the (lnP - 1/T) diagram, along with the expanded experimental uncertainties on the temperature and the pressure.

As we can see from the (lnP - 1/T) representation, a linear trend is obtained.

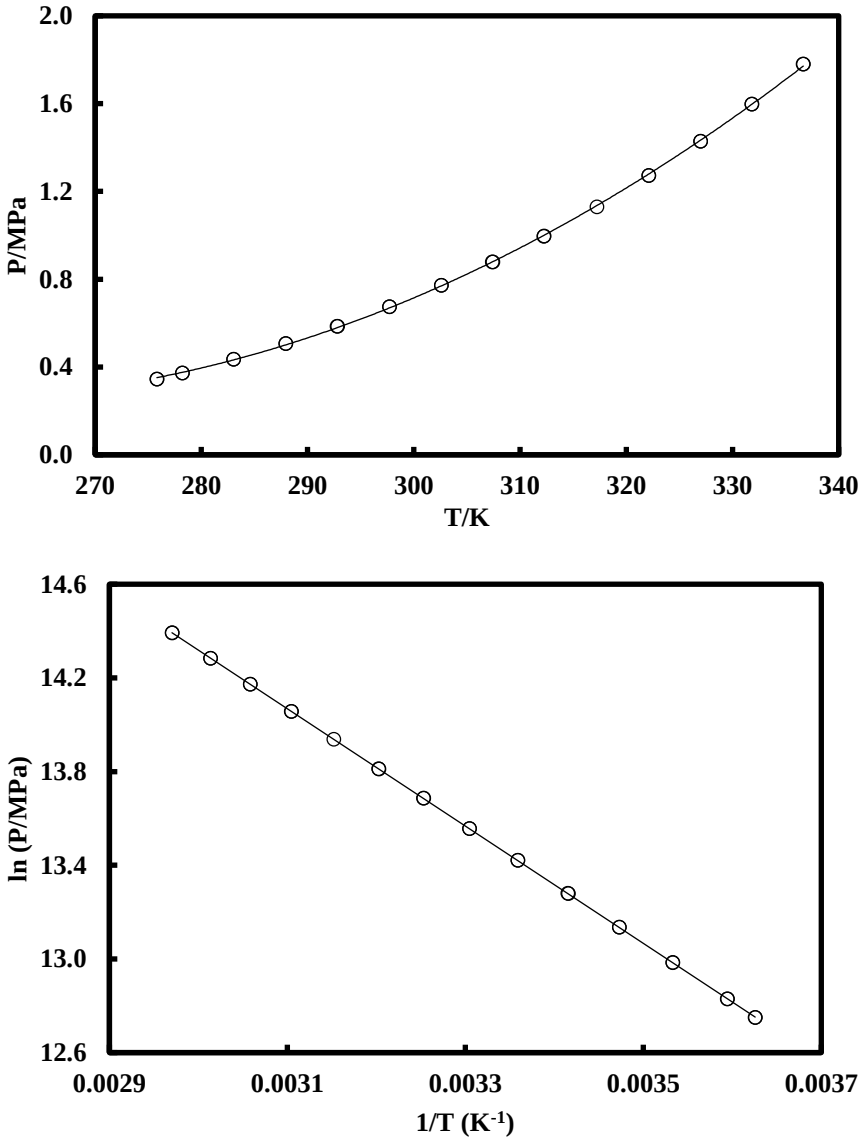

Figure 3.2 Vapour pressures of the pure compound R1234yf. U(T) = 0.08 K; U(P) = 0.0004 MPa.

3.1.1.3. Pure compound R1233zd(E)

The vapour pressures of R1233zd(E) were measured for temperatures between 276 K and 340 K. The experimental data obtained are displayed in *Figure 3.3*, showing the graphical representation of the (P-T) diagram, and (lnP - 1/T) diagram, along with the expanded experimental uncertainties on the temperature and the pressure.

The (lnP - 1/T) representation shows a linear trend.

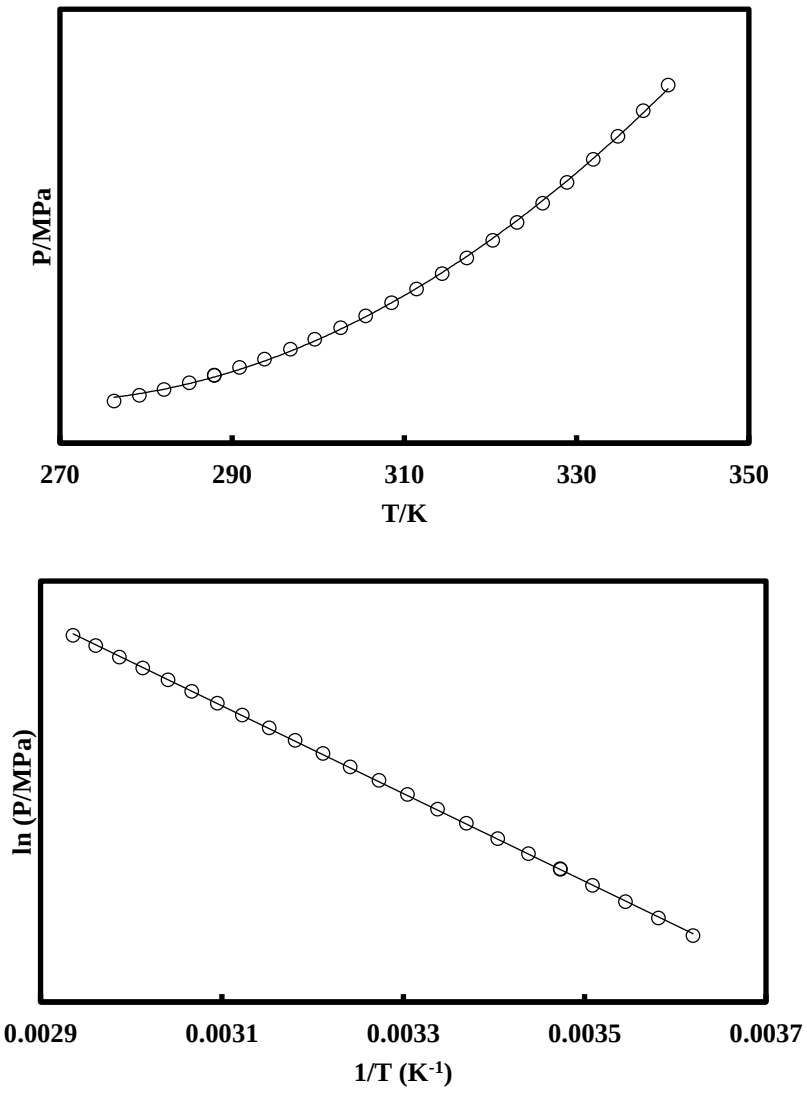

Figure 3.3 Vapour pressures of the pure compound R1233zd(E). U(T) = 0.08 K; U(P) = 0.0004 MPa.

3.1.1.4. Pure compound R1233xf

The vapour pressures of the pure compound R1233xf were measured for temperatures between 237 K and 308 K. The experimental data obtained are displayed in *Figure 3.4*, with the graphical representation of the (P-T) diagram, and (lnP - 1/T) diagram, along with the expanded experimental uncertainties on the temperature and the pressure.

As seen from the (lnP - 1/T) representation, a linear trend is obtained.

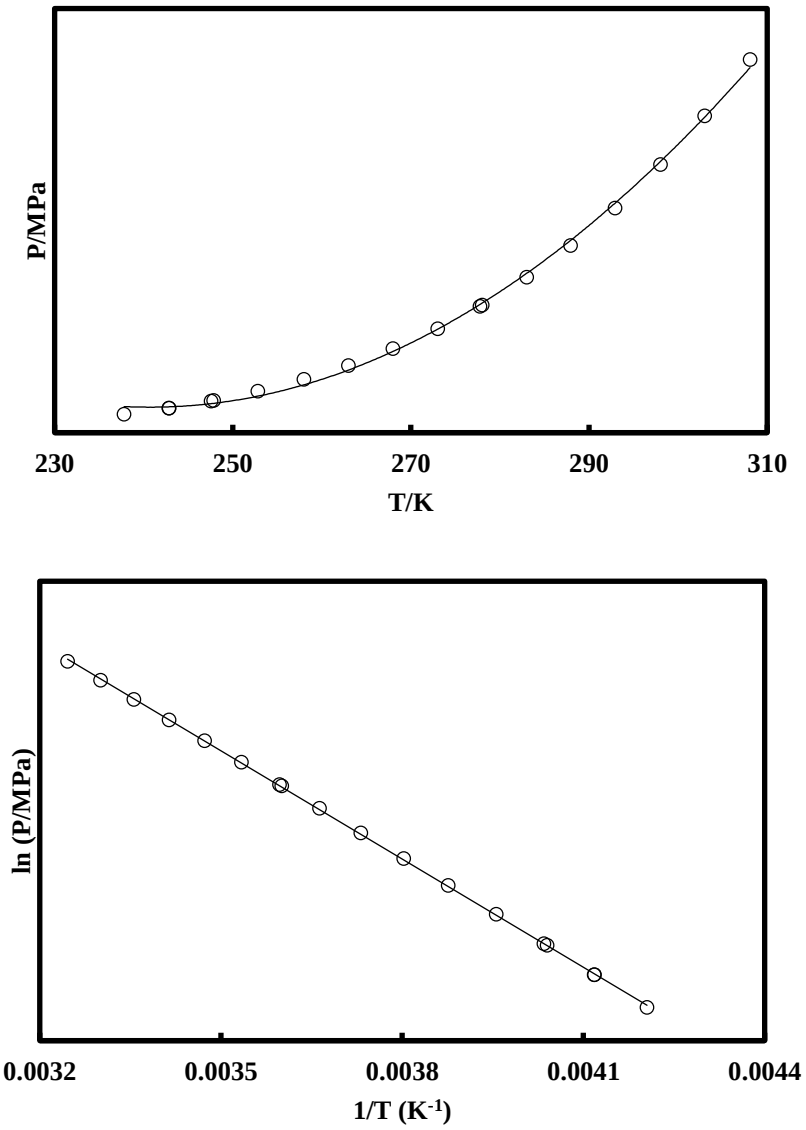

Figure 3.4 Vapour pressures of the pure compound R1233xf. U(T) = 0.08 K; U(P) = 0.0004 MPa.

3.1.1.5. Pure compound R245fa

The vapour pressures of the pure compound R245fa were measured for temperatures between 280 K and 340 K. The experimental data obtained are displayed in *Figure 3.5*, with the graphical representation of the (P-T) diagram, and (lnP - 1/T) diagram, along with the expanded experimental uncertainties on the temperature and the pressure.

The (lnP - 1/T) representation shows a linear trend.

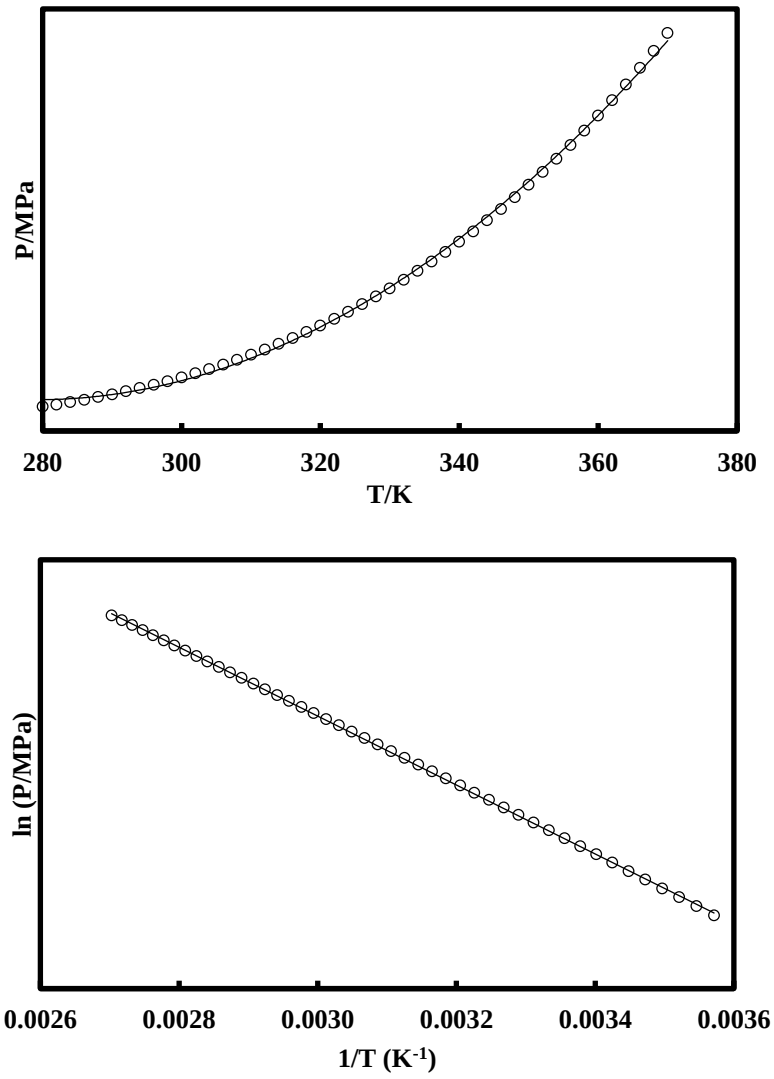

Figure 3.5 Vapour pressures of the pure compound R245fa. U(T) = 0.08 K; U(P) = 0.0004 MPa

3.1.2. VLE measurements for mixtures

Twelve binary mixtures of refrigerants were measured for VLE experiments. Ten systems were studied as part of the PREDIREF project, and two systems were measured as part of academic collaborations with other research groups.

The range of the temperatures covered for the VLE measurements are between 278.17 K and 353.25 K.

The details about the mixtures studied and the conditions of the measurements are reported in *Table 3.2*.

Table 3.2 Systems studied for VLE measurements.

Systems	*T/K*	*Analytical Column*
R134a + R1233zd(E)	303.07, 333.23	
R152a + R1233zd(E)	303.10, 333.23	
R1234yf + R1233zd(E)	303.22, 333.27	
R134a + R1233xf	298.30, 323.38, 348.27	
R1234yf + R1233xf	298.31, 323.27, 348.25	
CO_2 + R1234yf	283.21, 293.18, 298.11, 308.20, 323.18, 338.24, 353.25	1% RT-1000 on Carbo Black B 60/80 mesh 1/8" × 2.4 m Silcosteel tube RESTEK
CO_2 + R1233zd(E)	278.28, 302.59, 333.17	
R1234yf + R134a	278.17, 303.16, 333.17	
R1234yf + R152a	278.18, 303.16, 333.29	
R245fa + R1233xf	323.40, 353.27	
R245fa + R1233zd(E)	323.23, 353.27	
R23 + Propane	293.18, 298.15, 313.15, 323.15, 353.15	

The experimental results for each of the systems studied are presented in the following section, with the calculated relative volatility and the expanded experimental uncertainties (denoted by U(X), with a coverage factor k = 2).

3.1.2.1. Quasi-ideal systems

In this section, we present the systems having a quasi-ideal phase diagrams representation. Among the systems studied, five systems have this kind of behaviour. According to Van Konynenburg and Scott classification (Konynenburg & Scott 1980; Scott & van Konynenburg 1970), the phase diagrams of these systems are of type I.

3.1.2.1.1. Binary mixture (R134a + R1233zd(E))

The binary mixture (R134a + R1233zd(E)) was studied at two different isotherms T = 303.07 K and 333.23 K.

The critical temperatures of R134a and R1233zd(E) are respectively 374.21 K (Lemmon et al. 2010) and 438.75 K (Hulse et al. 2012).

The experimental results for this system are displayed in *Figure 3.6*, representing the pressure in function of the molar fraction, and the relative volatility as function of the molar fraction.

The expression of the relative volatility for binary mixtures is given by Eq. (3.1) below. This expression will be used for all the calculations of the relative volatility in this work.

$$\alpha_{12} = \frac{K_1}{K_2} = \frac{\frac{y_1}{x_1}}{\frac{y_2}{x_2}} \tag{3.1}$$

We can see from the graphical representation that the relative volatility for this system follows a linear trend in the range of the experimental error.

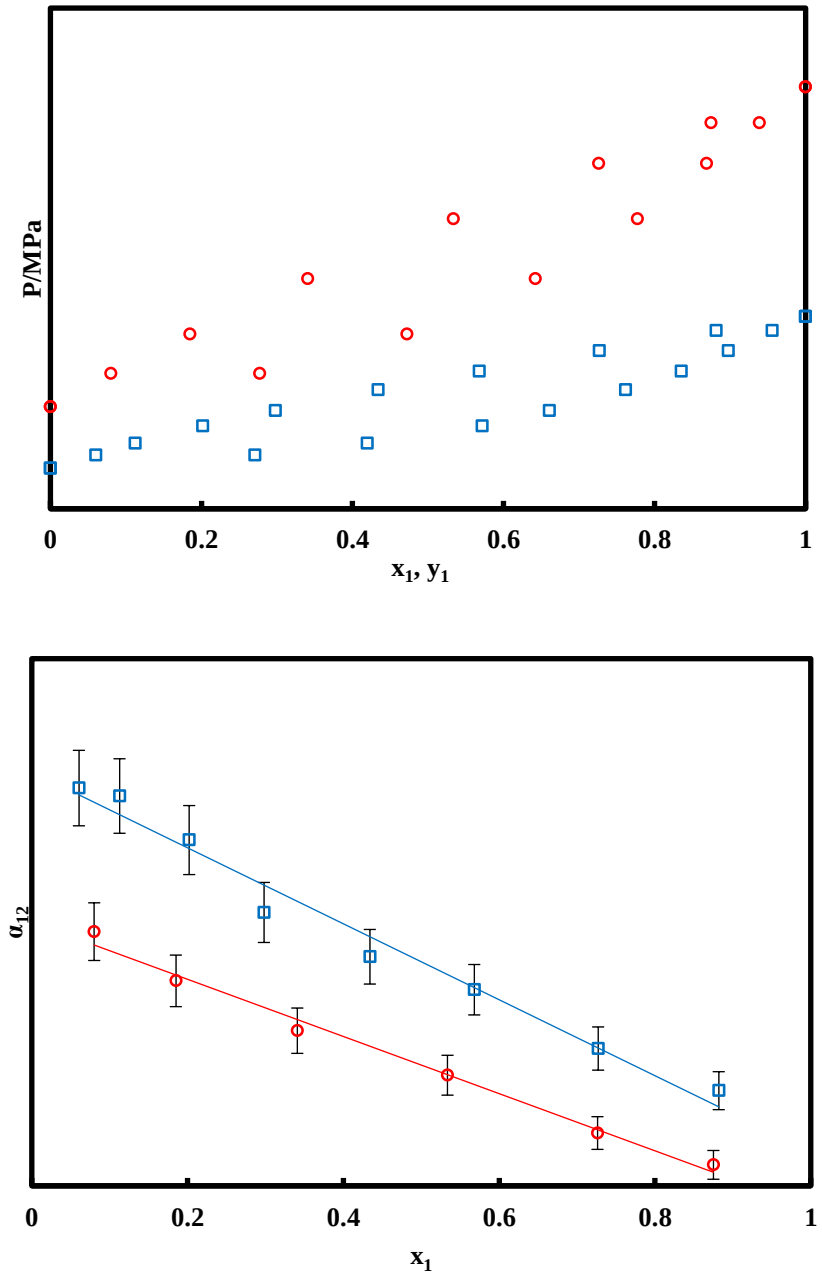

Figure 3.6 VLE results and relative volatility for R134a (1) + R1233zd(E) (2). (□) 303.07 K; (○) 333.23 K. U(T) = 0.06 K; U(P) = 0.0008 MPa; U(x_1) = 0.008; U(y_1) = 0.008. Error bars: ±6.2%.

3.1.2.1.2. Binary mixture (R152a + R1233zd(E))

The binary mixture (R152a + R1233zd(E)) was studied at two different isotherms T = 303.10 K and 333.23 K.

The critical temperatures of R152a and R1233zd(E) are respectively 386.41 K (Lemmon et al. 2010) and 438.75 K (Hulse et al. 2012).

The experimental results for this system are displayed in *Figure 3.7*, representing the pressure in function of the molar fraction, and the relative volatility as function of the liquid molar fraction.

As seen from the graphical representation, the relative volatility for this system has a linear trend in the limit of the experimental error.

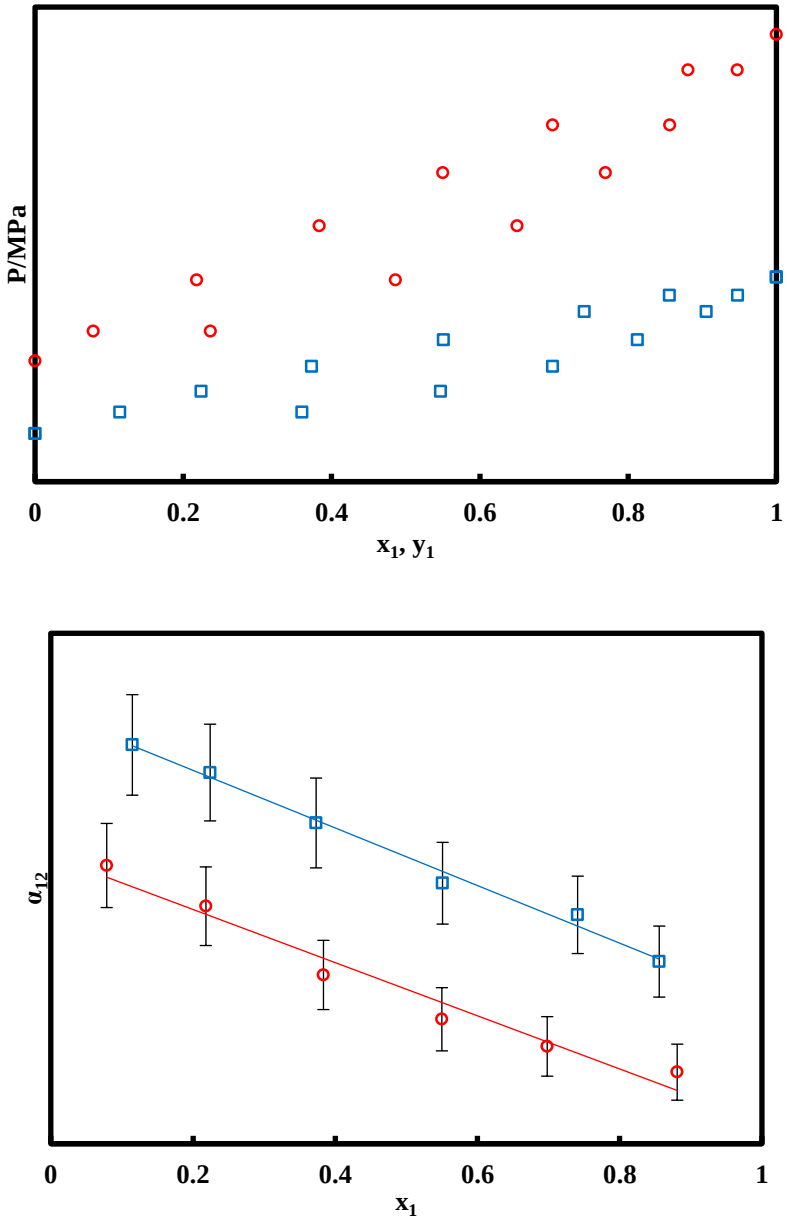

Figure 3.7 VLE results and relative volatility for R152a (1) + R1233zd(E) (2). (□) 303.10 K; (○) 333.23 K. U(T) = 0.06 K; U(P) = 0.0008 MPa; U(x_1) = 0.008; U(y_1) = 0.008. Error bars: ±6.8%.

3.1.2.1.3. Binary mixture (R134a + R1233xf)

The binary mixture (R134a + R1233xf) was studied at three different isotherms ranging from 298.30 K to 348.27 K.

The critical temperatures of R134a and R1233xf are respectively 374.21 K (Lemmon et al. 2010) and 439.98 K (Zhang et al. 2013).

The experimental results for this system are displayed in *Figure 3.8*, representing the pressure in function of the molar fraction, and the relative volatility as function of the liquid molar fraction.

The graphical representation shows an almost ideal phase behaviour for this system (that can be represented by Raoult's law). In addition, the relative volatility for this system follows a linear trend in the limit of the experimental error.

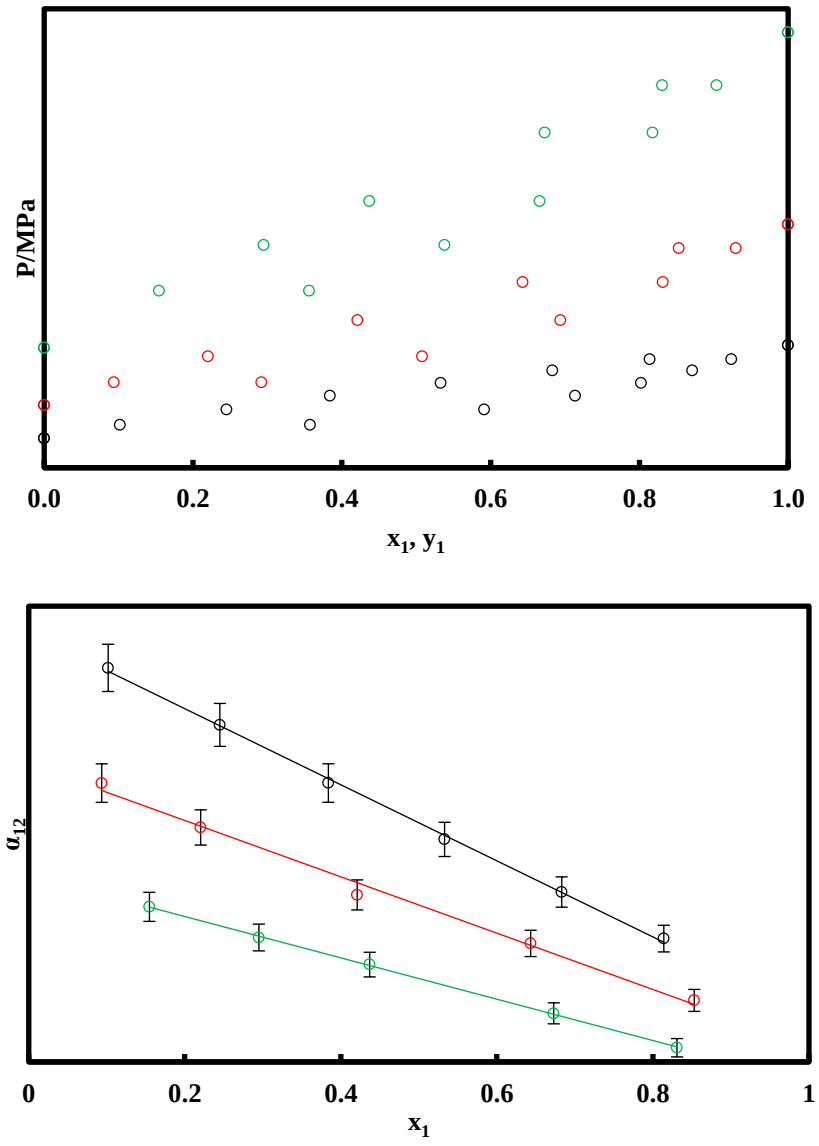

Figure 3.8 VLE results and relative volatility for R134a (1) + R1233xf (2). (○) 298.30 K; (○) 323.38 K; (○) 348.27 K. U(T) = 0.08 K; U(P) = 0.001 MPa; U(x_1) = 0.0086; U(y_1) = 0.0089. Error bars: ±3.8%.

3.1.2.1.4. Binary mixture (R1234yf + R1233xf)

The binary mixture (R1234yf + R1233xf) was studied at three different isotherms ranging from 298.31 K to 348.25 K.

The critical temperatures of the R1234yf and R1233xf are respectively 367.85 K (Lemmon et al. 2010) and 439.98 K (Zhang et al. 2013).

The experimental results for this system are displayed in *Figure 3.9*.

The graphical representation shows an almost ideal phase behaviour for this system (that can be represented by Raoult's law). In addition, the relative volatility for this system follows a linear trend in the limit of the experimental error.

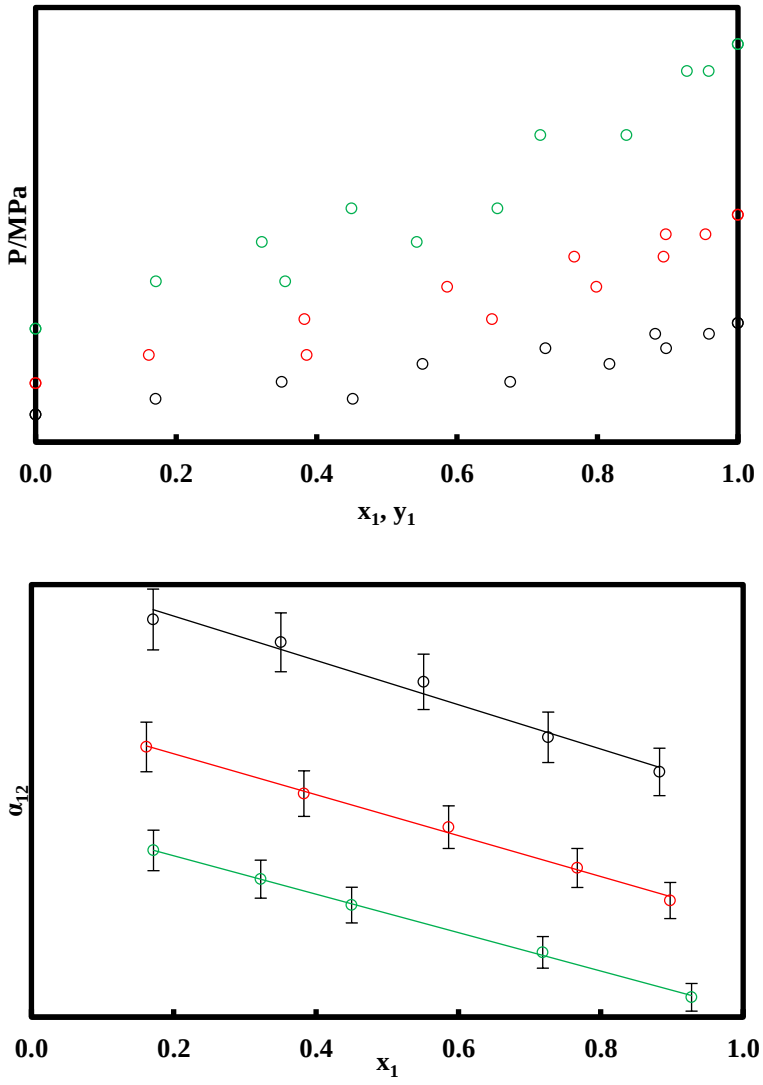

Figure 3.9 VLE results and relative volatility for R1234yf (1) + R1233xf (2). (○) 298.31 K; (○) 323.27 K; (○) 348.25 K. U(T) = 0.08 K; U(P) = 0.0005 MPa; U(x_1) = 0.0086; U(y_1) = 0.0087. Error bars: ±4.4%.

3.1.2.1.5. Binary mixture (R1234yf + R1233zd(E))

The binary mixture (R1234yf + R1233zd(E)) was studied at two different isotherms T = 303.22 K and 333.27 K.

The critical temperatures of the R1234yf and R1233zd(E) are respectively 367.85 K (Lemmon et al. 2010) and 438.75 K (Hulse et al. 2012).

The experimental results for this system are displayed in *Figure 3.10*, showing a quasi-ideal phase behaviour for this system (that can be represented by Raoult's law), and a relative volatility following a linear trend in the limit of the experimental error.

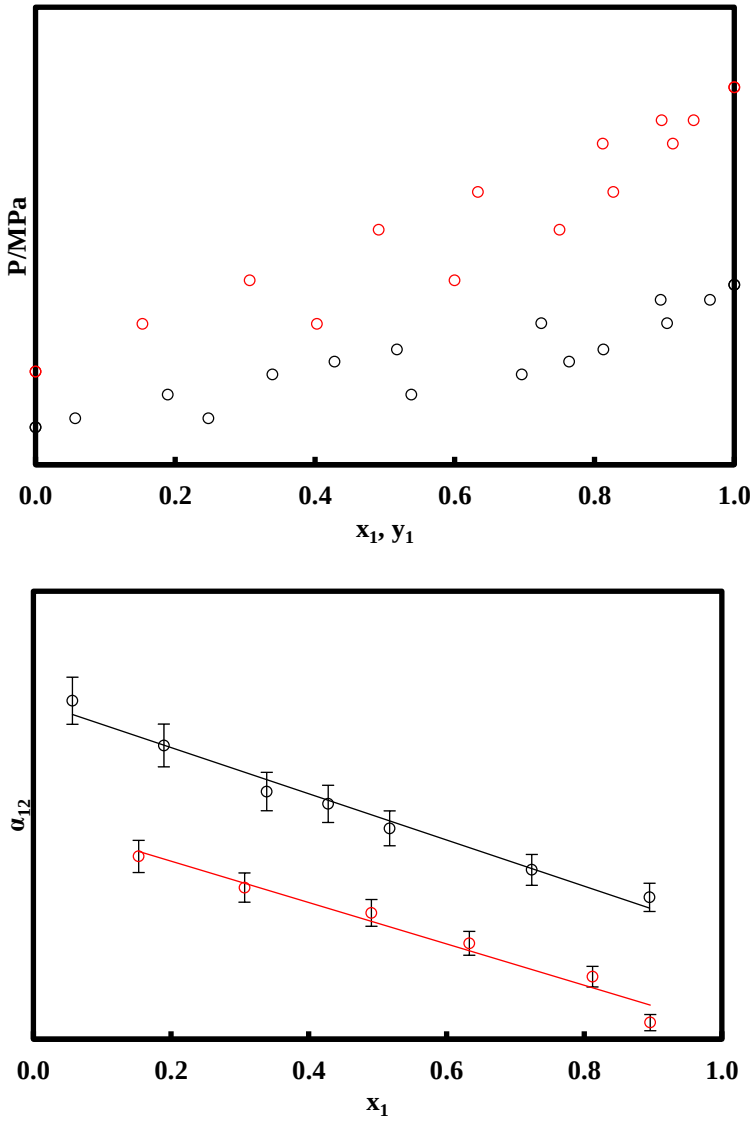

Figure 3.10 VLE results and relative volatility for R1234yf (1) + R1233zd(E) (2). (○) 303.22 K; (○) 333.27 K. U(T) = 0.08 K; U(P) = 0.0004 MPa; U(x_1) = 0.014; U(y_1) = 0.010. Error bars: ±4.8%.

3.1.2.2. Supercritical systems

In this section, we present the systems involving at least one supercritical component, leading to a supercritical behaviour in the phase diagram representation.

Two systems studied have this kind of behaviour. According to Van Konynenburg and Scott classification (Konynenburg & Scott 1980; Scott & van Konynenburg 1970), these systems are of type I.

3.1.2.2.1. Binary mixture (CO_2 + R1234yf)

The binary mixture (CO_2 + R1234yf) was studied at seven different isotherms ranging from 283.21 K to 353.25 K.

The critical temperatures of CO_2 and R1234yf are respectively 304.13 K and 367.85 K (Lemmon et al. 2010).

The experimental VLE results, as well as the relative volatility for this system are displayed in *Figure 3.11*. A critical behaviour is observed for this system for the four isotherms above the critical temperature of CO_2.

The relative volatility for this system follows a second order polynomial trend in the limit of the experimental error.

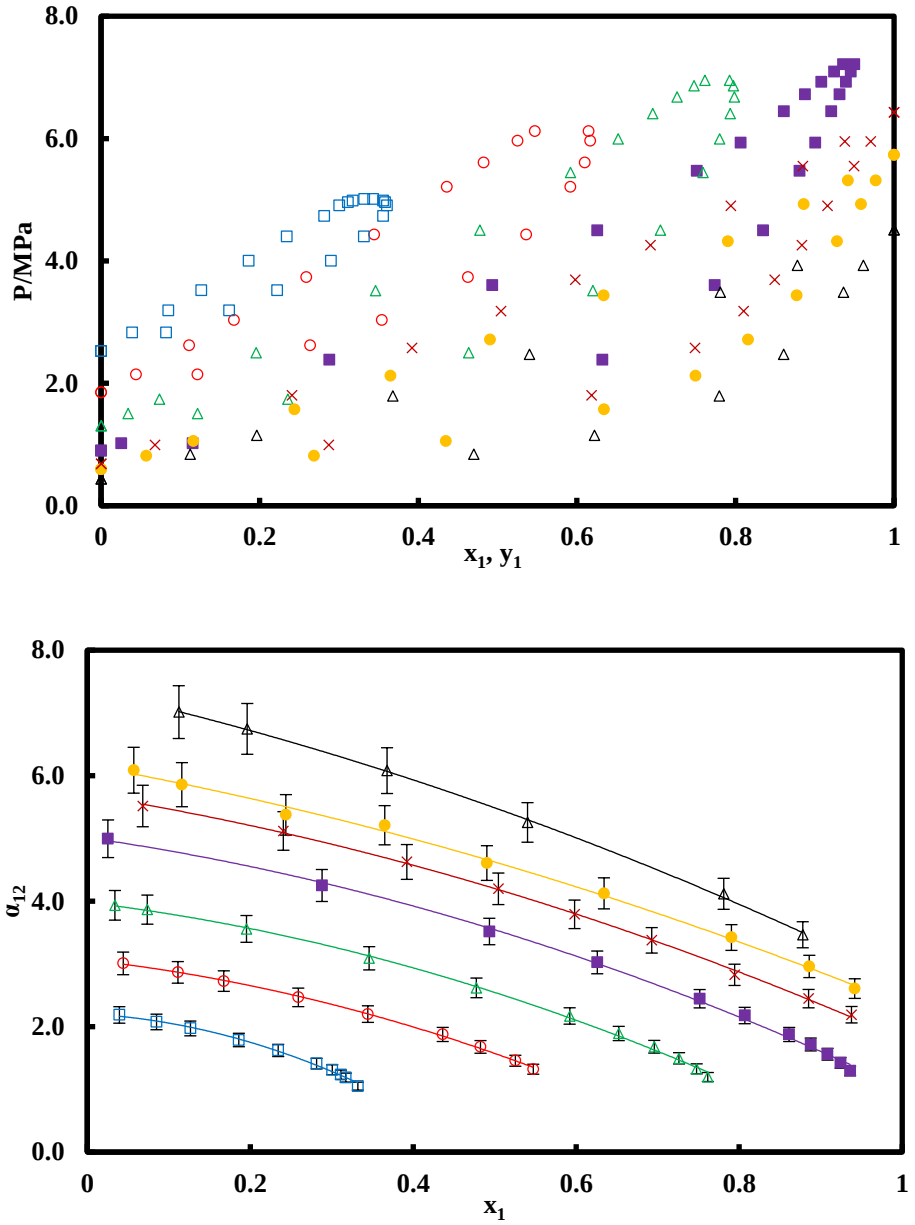

Figure 3.11 VLE results and relative volatility for CO_2 (1) + R1234yf (2). (Δ) 283.21 K; (●) 293.18 K; (×) 298.11 K; (■) 308.20 K; (Δ) 323.18 K; (○) 338.24 K; (□) 353.25 K. U(T) = 0.06 K; U(P) = 0.0008 MPa; U(x_1) = 0.008; U(y_1) = 0.008. Error bars: ±6%.

3.1.2.2.2. Binary mixture (CO_2 + R1233zd(E))

The binary mixture (CO_2 + R1233zd(E)) was studied at three different isotherms ranging from 278.28 K to 333.17 K.

The critical temperatures of CO_2 and R1233zd(E) are respectively 304.13 K (Lemmon et al. 2010) and 438.75 K (Hulse et al. 2012).

The experimental results for this system are displayed in *Figure 3.12*. A critical behaviour is observed for this system for the isotherm above the critical temperature of CO_2.

The relative volatility for this system follows a second order polynomial trend in the limit of the experimental error.

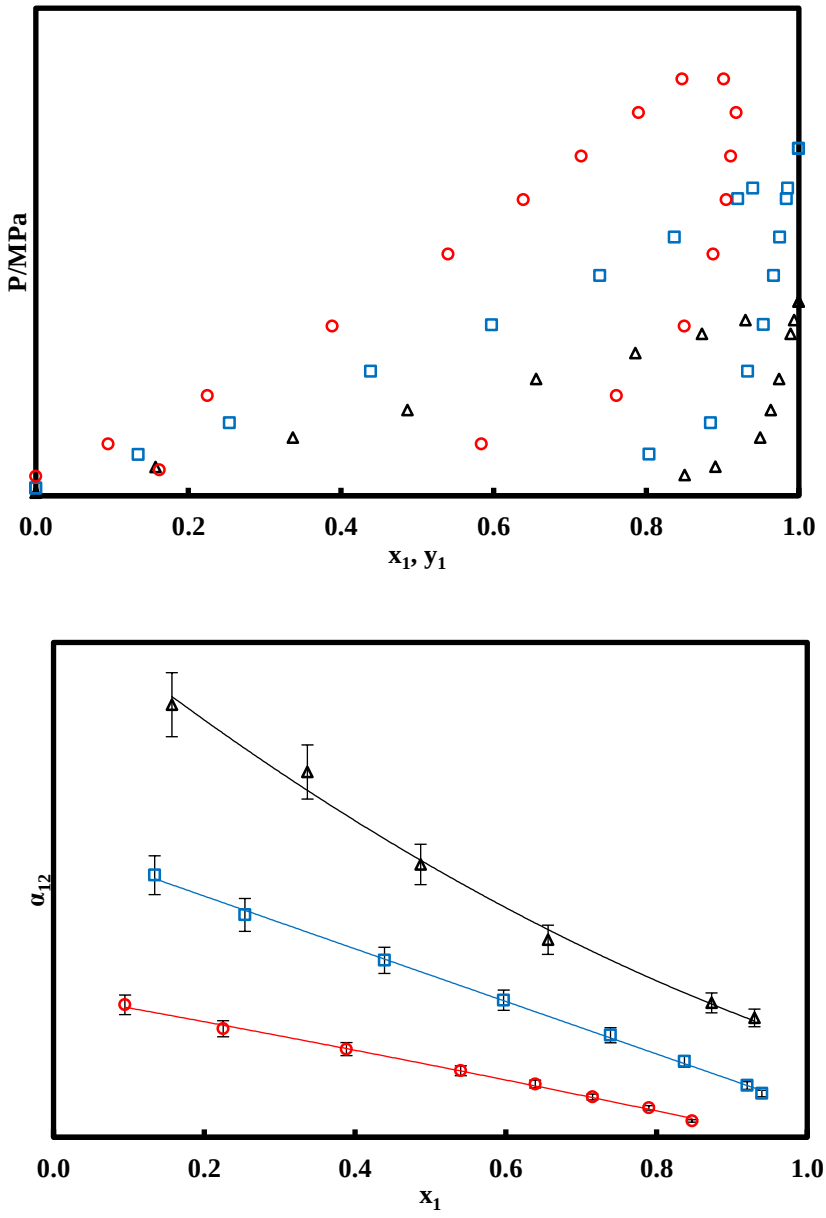

Figure 3.12 VLE results and relative volatility for CO_2 (1) + R1233zd(E) (2). (Δ) 278.28 K; (□) 302.59 K; (○) 333.17 K. U(T) = 0.06 K; U(P) = 0.0008 MPa; U(x1) = 0.008; U(y1) = 0.008. Error bars: ±7.4%

3.1.2.3. Azeotropic systems

In this section, we present the systems with an azeotropic behaviour. The azeotrope occurs generally in the systems with compounds having similar molecular properties, which is reflected on their thermodynamic properties, by having close values of the vapour pressures and the critical temperatures.

The azeotrope corresponds to an extremum of the pressure for a constant temperature, or an extremum of the temperature for a constant pressure. At the azeotrope, the compositions in the liquid phase and the vapour phase are identical, leading to a relative volatility $\alpha_{12} = 1$.

Four systems studied have this kind of behaviour. According to the classification of Van Konynenburg and Scott (Konynenburg & Scott 1980; Scott & van Konynenburg 1970), these systems are of type I.

3.1.2.3.1. Binary mixture (R1234yf + R134a)

The binary mixture (R1234yf + R134a) was studied at three different isotherms ranging from 278.17 K to 333.17 K.

The critical temperatures of the R1234yf and R134a are respectively 367.85 K and 374.21 K (Lemmon et al. 2010).

The experimental results for this system are displayed in *Figure 3.13*. This system presents an azeotropic behaviour, which can be expected due to the close values of the vapour pressures of the two refrigerants R1234yf and R134a. Also, we can notice that the phase envelope is very narrow for this system, due to the close mole fractions of the vapour and the liquid phases.

The relative volatility for this system follows a second order polynomial trend in the limit of the experimental error. We can also notice that the relative volatility is equal to 1 at the azeotrope composition (when $x_1 = y_1$).

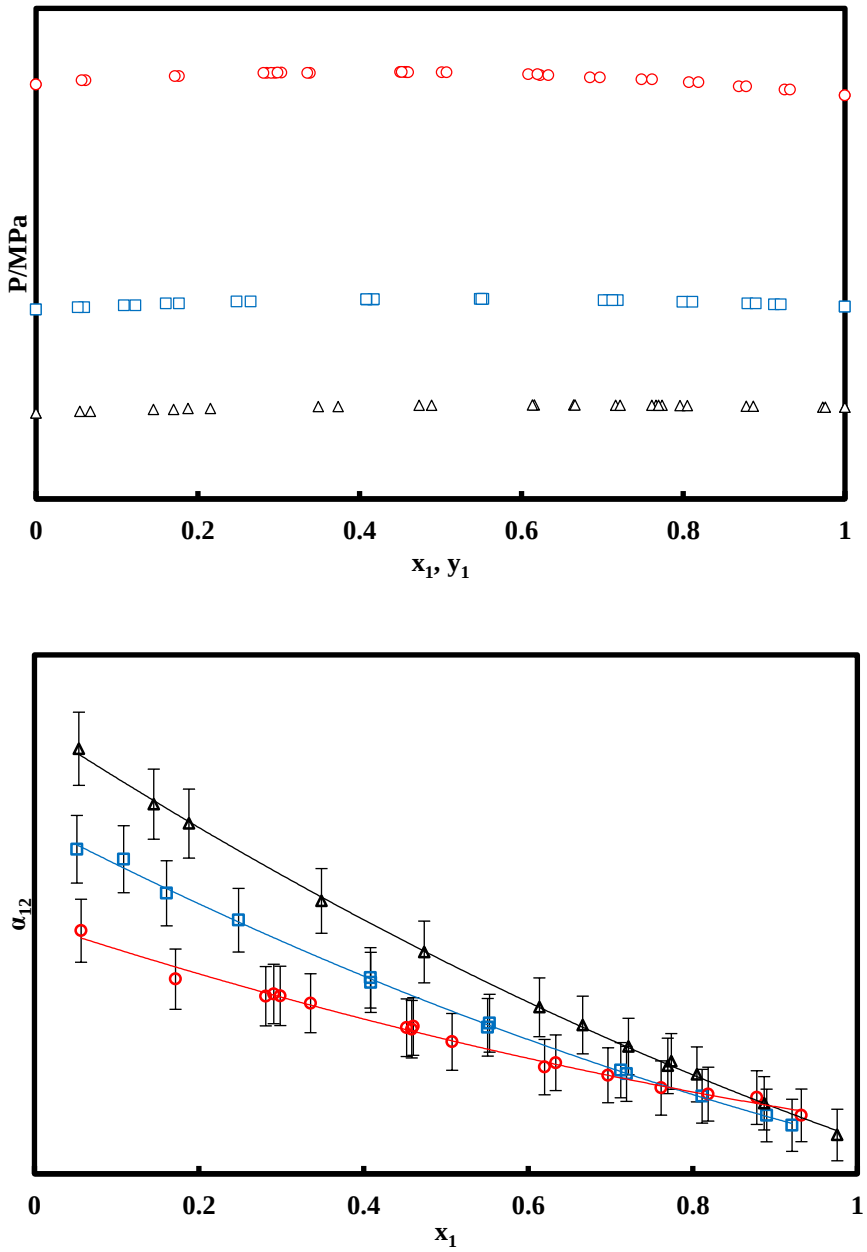

Figure 3.13 VLE results and relative volatility for R1234yf (1) + R134a (2). (Δ) 278.17 K; (□) 303.16 K; (○) 333.17 K. U(T) = 0.06 K; U(P) = 0.0008 MPa; U(x_1) = 0.008; U(y_1) = 0.008. Error bars: ±2.8%.

3.1.2.3.2. Binary mixture (R1234yf + R152a)

The binary mixture (R1234yf + R152a) was studied at three different isotherms ranging from 278.18 K to 333.29 K. The critical temperatures of R1234yf and R152a are respectively 367.85 K and 386.41 K (Lemmon et al. 2010).

The experimental results for this system are displayed in *Figure 3.14*, along with the relative volatility of this system.

As the previous system (R1234yf + R134a), this binary system has an azeotropic behaviour, which can be expected due to the close values of the vapour pressures of the two refrigerants R1234yf and R152a. Also, we can notice that the phase envelope is very narrow for this system, due to the close values of the mole fractions of the vapour and the liquid phases.

The relative volatility for this system follows a second order polynomial trend in the limit of the experimental error. We can also notice that the relative volatility is equal to 1 at the azeotrope composition (when $x_1 = y_1$).

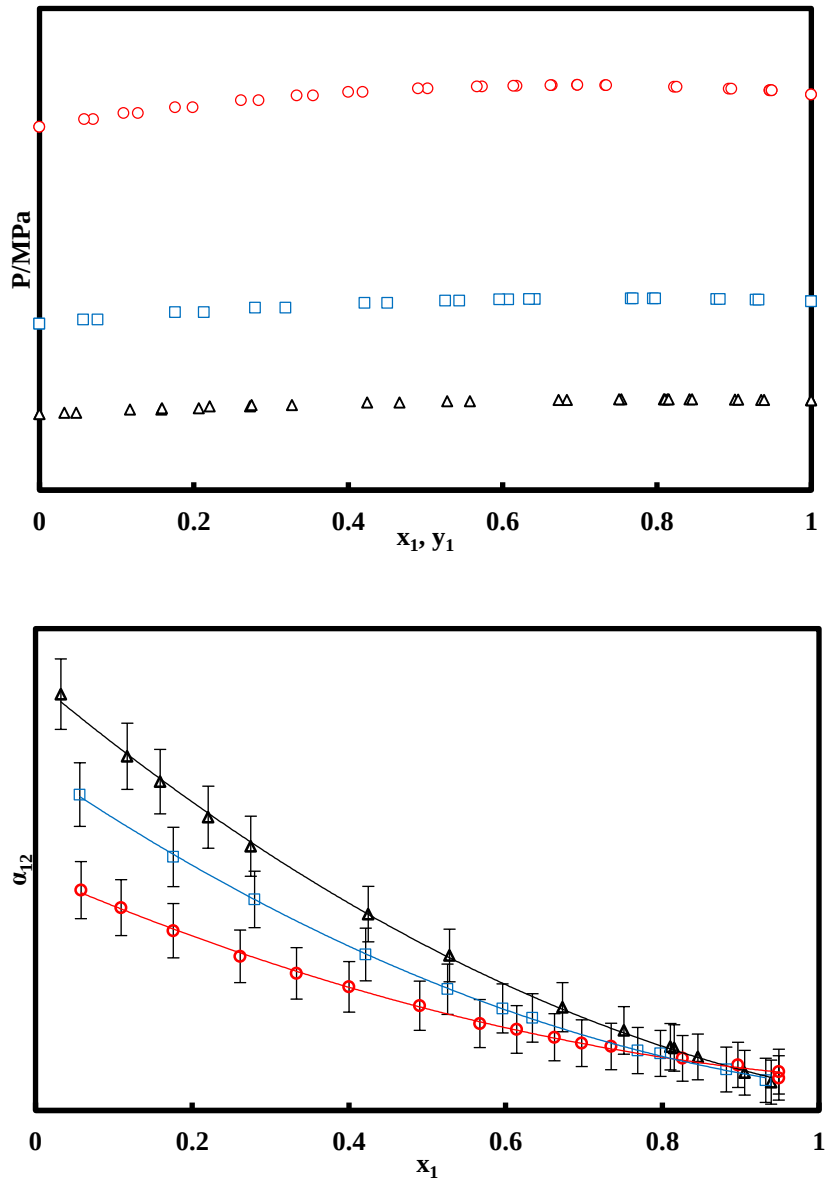

Figure 3.14 VLE results and relative volatility for R1234yf (1) + R152a (2). (Δ) 278.18 K; (□) 303.16 K; (○) 333.29 K. U(T) = 0.06 K; U(P) = 0.0008 MPa; U(x_1) = 0.008; U(y_1) = 0.008. Error bars: ±3.4%.

3.1.2.3.3. Binary mixture (R245fa + R1233xf)

The binary mixture (R245fa + R1233xf) was studied at two different isotherms ranging from 323.40 K to 353.27 K. The critical temperatures of R245fa and R1233xf are respectively 427.16 K (Lemmon et al. 2010) and 439.98 K (Zhang et al. 2013).

The experimental results for this system are displayed in *Figure 3.15*. This system has also an azeotropic behaviour, which is expected due to the close values of the vapour pressures of the two refrigerants R245fa and R1233xf. Also, we can notice that the phase envelope is very narrow for this system, due to the close values of the mole fraction of the vapour and the liquid phases.

The relative volatility for this system follows a second order polynomial trend in the limit of the experimental error. We can also notice that the relative volatility is equal to 1 at the azeotrope composition (when $x_1 = y_1$).

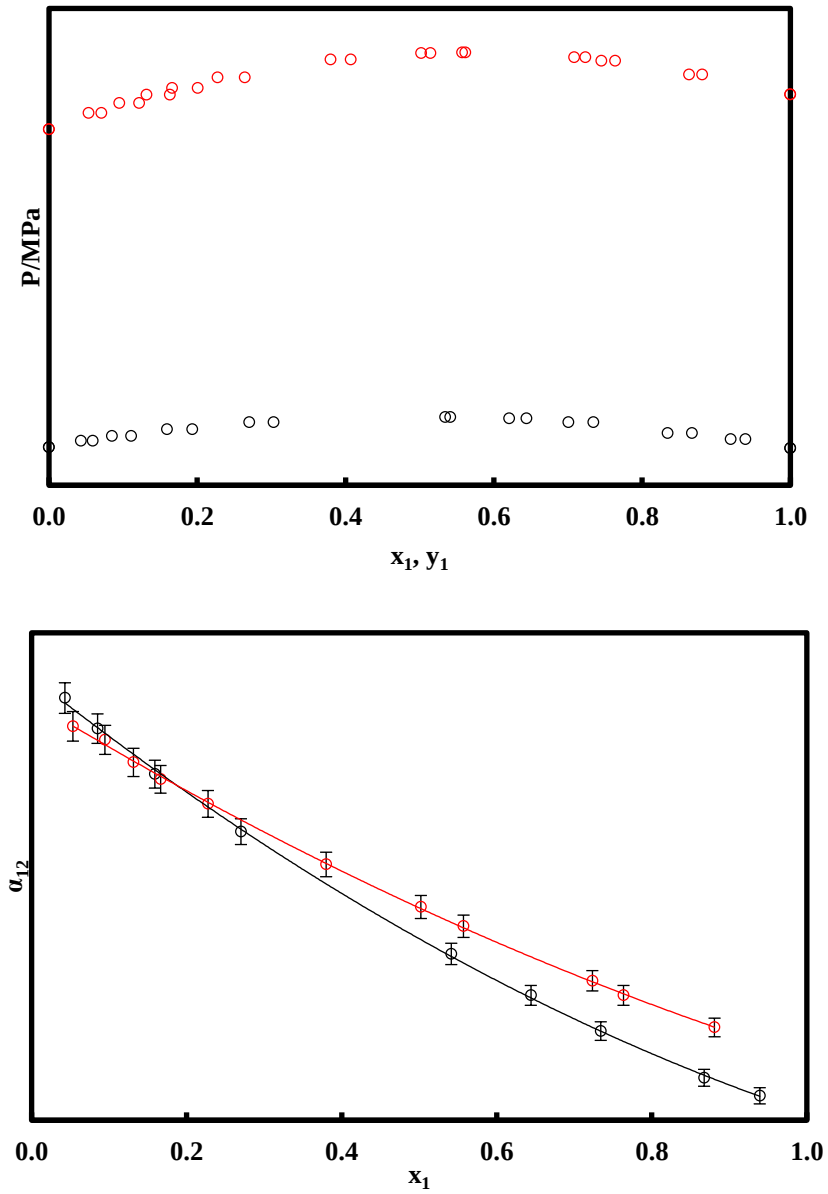

Figure 3.15 VLE results and relative volatility for R245fa (1) + R1233xf (2). (○) 323.40 K; (○) 353.27 K. U(T) = 0.08 K; U(P) = 0.0004 MPa; U(x_1) = 0.0086; U(y_1) = 0.0085. Error bars: ±1.8%.

3.1.2.3.4. Binary mixture (R245fa + R1233zd(E))

The binary mixture (R245fa + R1233zd(E)) was studied at two different isotherms T = 323.23 K and 353.27 K.

The critical temperatures of R245fa and R1233zd(E) are respectively 427.16 K (Lemmon et al. 2010) and 438.75 K (Hulse et al. 2012).

The experimental results for this system are displayed in *Figure 3.16*. This system presents also an azeotropic behaviour, which is expected due to the close values of the vapour pressures of the two refrigerants R245fa and R1233zd(E). We can also notice that the phase envelope is very narrow for this system, due to close mole fraction of the vapour and the liquid phases.

The relative volatility for this system follows a second order polynomial trend in the limit of the experimental error. We can also notice that the relative volatility is equal to 1 at the azeotrope composition (when $x_1 = y_1$).

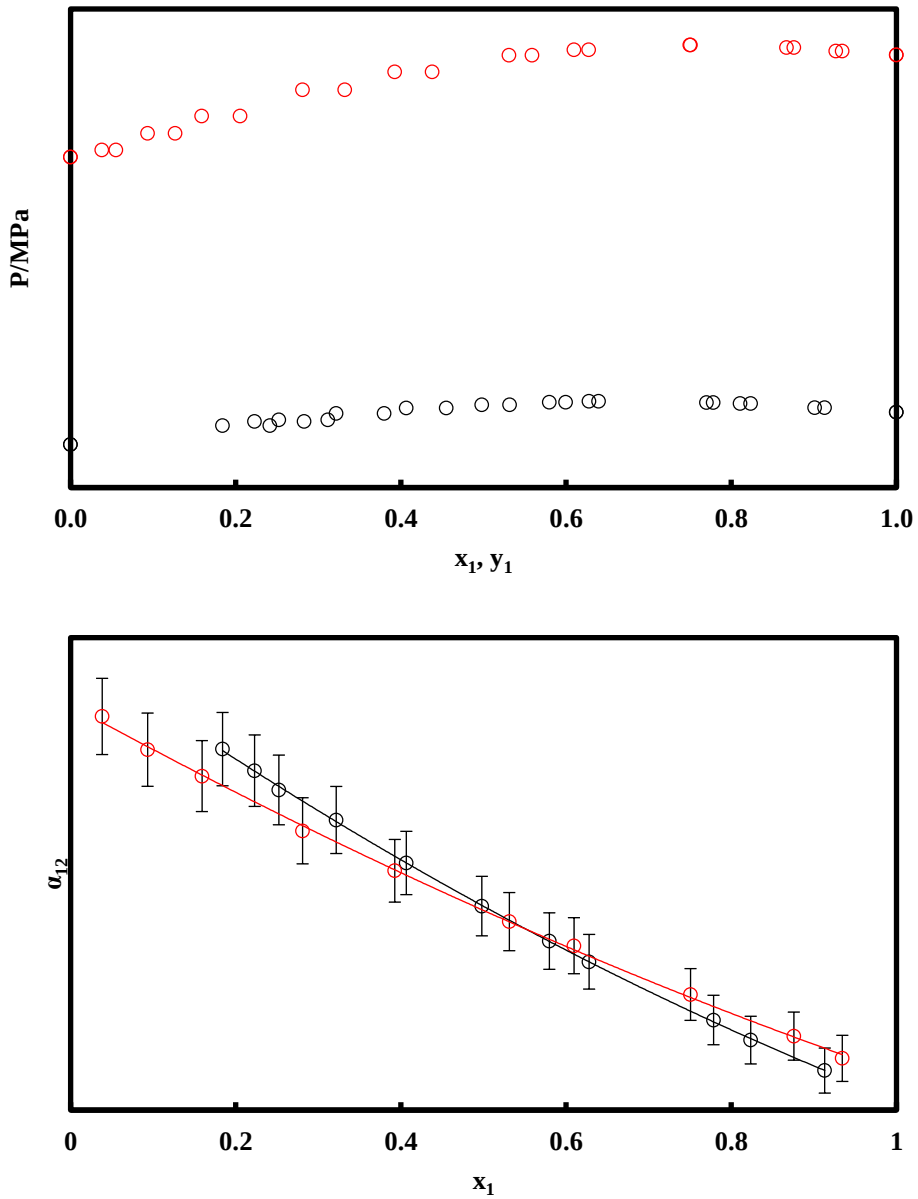

Figure 3.16 VLE results and relative volatility for R245fa (1) + R1233zd(E) (2). (○) 323.23 K; (○) 353.27 K. U(T) = 0.08 K; U(P) = 0.0004 MPa; U(x_1) = 0.0088; U(y_1) = 0.0088. Error bars: ±4.4%.

3.1.2.4. Azeotropic-supercritical systems

In this section, we present one system where two particular phase behaviours are observed. For this system, an azeotrope is detected for two isotherms studied, and a supercritical behaviour occurs for three other isotherms studied.

3.1.2.4.1. Binary mixture (R23 + Propane)

The binary mixture (R23 + Propane) was studied at five different isotherms ranging from 293.15 K to 353.15 K. The data for this system has already been published (Williams-Wynn et al. 2017), as part of a joint collaboration between the our research group and the *Thermodynamics Research Unit* from the *University of KwaZulu-Natal*.

The critical temperatures of the R23 and Propane are respectively 299.29 K and 369.89 K (Lemmon et al. 2010).

The experimental results for this system are displayed in *Figure 3.17*. A critical behaviour is observed for this system at the three isotherms above the critical temperature of the R23 (313.15 K, 323.15 K, 353.15 K), while an azeotropic behaviour is observed for the two isotherms below the critical temperature of the R23 (293.15 K, 298.15 K).

The relative volatility for this system follows a second order polynomial trend in the limit of the experimental error. We can also notice that the relative volatility is equal to 1 at the azeotrope composition (when $x_1 = y_1$), for the first two isotherms.

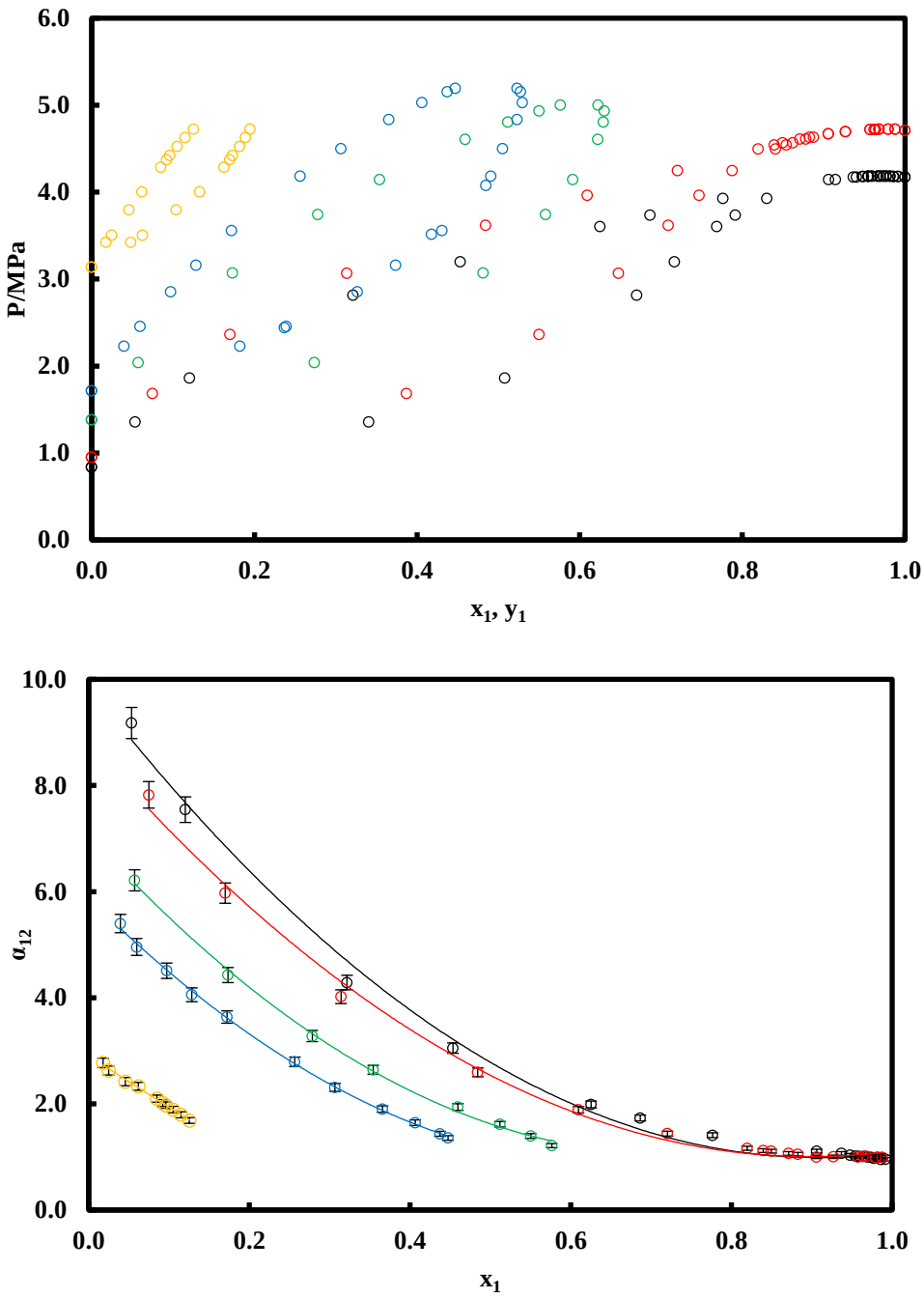

Figure 3.17 VLE results and relative volatility for R23 (1) + Propane (2). (○) 293.15 K; (○) 298.15 K; (○) 313.15 K; (○) 323.15 K; (○) 353.15 K. U(T) = 0.08 K; U(P) = 0.0008 MPa; U(x_1) = 0.009; U(y_1) = 0.009. Error bars: ±3.2%.

3.2. Density results

Five systems of refrigerants were studied using the vibrating-tube densimeter, in order to perform density measurements. The systems studied involve two pure compounds, two binary mixtures and one ternary mixture.

The details about the systems studied and the conditions of the measurements are reported in *Table 3.3*.

Table 3.3 Systems studied for density measurements.

Systems	*T/K*	*Molar composition (%)*	*Calibration fluid*
R1233xf	260.48, 273.43, 292.65, 312.44, 332.42	--	R134a
R1233zd(E)	278.15, 303.15, 323.15, 333.15, 343.15	--	R134a
R1234yf + R134a	278.15, 303.15, 333.15	1st: 46.36/53.64 2nd: 86.19/13.81 3rd: 8.74/91.26	R134a
R1234yf + R152a	278.15, 303.15, 333.15	1st: 45.53/54.47 2nd: 86.57/13.43 3rd: 9.26/90.74	R134a
R134a + R152a + R1234yf	278.15, 303.15, 333.15	1st: 29.53/19.92/50.56 2nd: 19.67/ 10.81/ 69.52 3rd: 33.85/ 31.41/ 34.74	R134a

3.2.1. Pure compounds density measurements

3.2.1.1. Pure compound R1233xf

The pure compound R1233xf was studied at five different temperatures ranging from 260.48 K to 332.49 K. The measurements for this system were carried out up to pressures of 8 MPa.

The experimental density results are displayed in *Figure 3.18*, with the reported expanded uncertainties on the temperature, pressure and densities.

We should note that the reported uncertainties on density include only the uncertainty from the calibration; since the measurements are performed in a dynamic way, and as a result, we have no repeatability on the measures. This applies to all the results given for the uncertainties on the density.

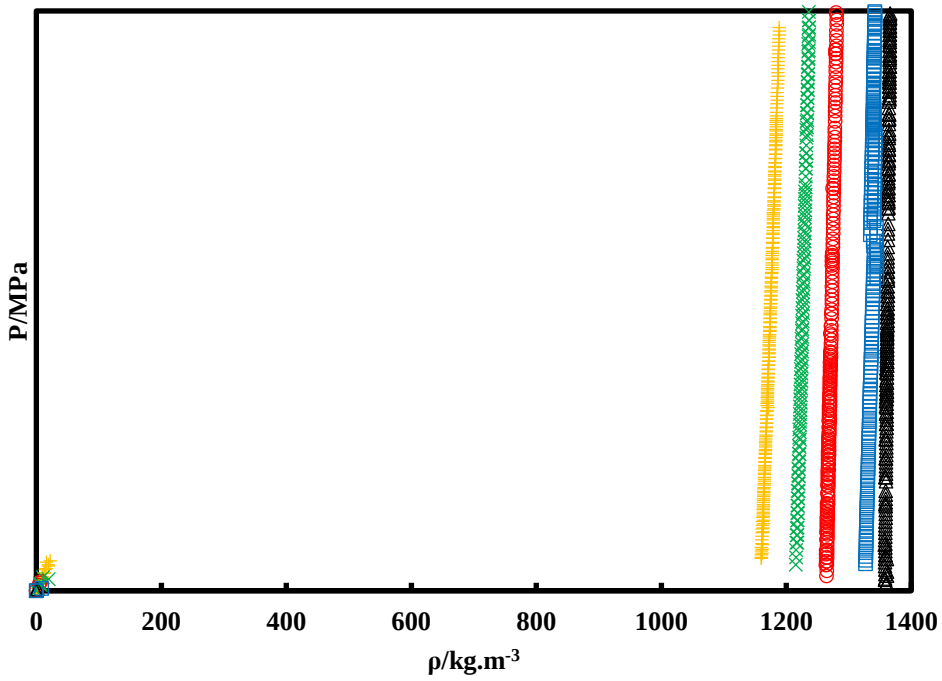

Figure 3.18 Experimental densities measurements for R1233xf. (Δ): 260.48 K; (□): 273.43 K; (○): 292.65 K; (×): 312.44 K; (+): 332.49 K. U(T) = 0.04 K; U(P) = 0.007 MPa; $U(\rho^V)/\rho^V$ = 2%; $U(\rho^L)/\rho^L$ = 0.2%.

3.2.1.2. Pure compound R1233zd(E)

The pure compound R1233zd(E) was studied at five different temperatures ranging from 278.15 K to 343.13 K. The measurements for this system were performed up to pressures of 10 MPa. The experimental density results are displayed in *Figure 3.19*, with the reported expanded uncertainties on the temperature, pressure and density (U(X), k = 2).

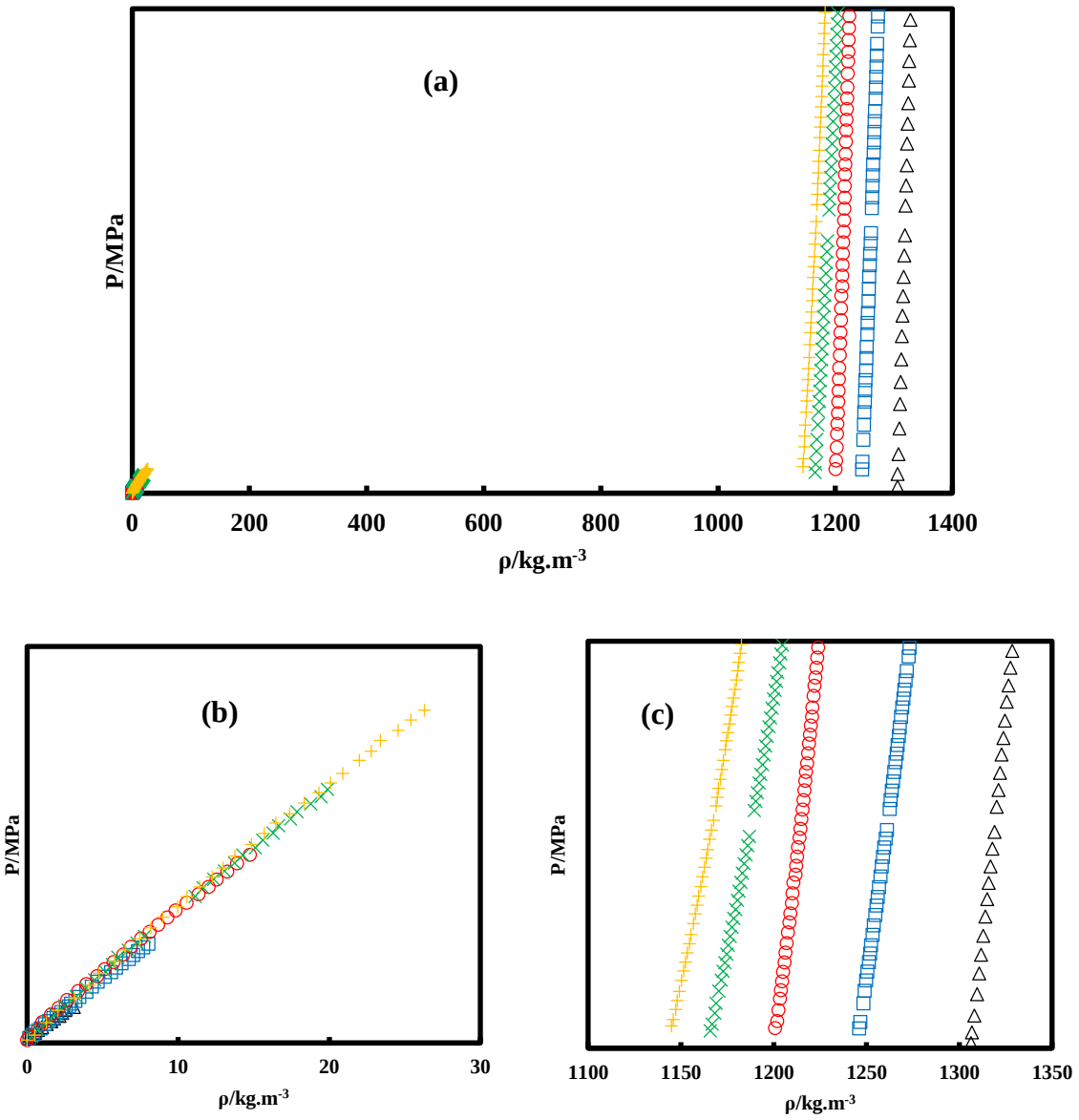

Figure 3.19 Experimental densities measurements for R1233zd(E). (a): Both phases; (b): Vapour phase; (c): Liquid phase. (Δ): 278.16 K; (□): 303.16 K; (○): 323.23 K; (×): 333.15 K; (+): 343.13 K. U(T) = 0.04 K; U(P) = 0.007 MPa; $U(\rho^V)/\rho^V$ = 2%; $U(\rho^L)/\rho^L$ = 0.2%.

Additional experimental measurements of the R1233zd(E) densities at high temperatures have been recently performed, using the same vibrating-tube densimeter. The temperatures covered are 354.08 K, 373.60 K, 392.84 K and 413.05 K, for pressures up to 12 MPa.
The results obtained are displayed in *Figure C.1* and *Figure C.2* of Appendix C.2.

From the densities measured out of saturation using the vibrating-tube densimeter, the densities at saturation for the temperatures studied have been determined using a graphical method. The full details about this graphical determination method can be found in (Bouchot & Richon 1998b).
In addition to that, the densities near the critical point have been measured using a "Critical point determination" apparatus, based on a static-synthetic method. The full details about this apparatus can be found in our recently published paper (Williams-Wynn et al. 2017).
The results obtained are displayed in *Figure C.3* of Appendix C.2.

3.2.2. Mixtures density measurements

3.2.2.1. Binary mixture (R1234yf + R134a)

The binary mixture (R1234yf + R134a) was studied at three different molar compositions, and at three different temperatures ranging from 278.34 K to 332.55 K. The measurements for this system were achieved up to pressures of 10 MPa.

The experimental density results are presented for the three compositions studied at each of the isotherms covered.

The expanded uncertainties on the temperature, pressure and densities are reported within the results of the measurements (U(X), k = 2).

The experimental results are displayed in *Figure 3.20* to *Figure 3.22*.

- ***1st composition: (46.36% R1234yf + 53.64% R134a)***

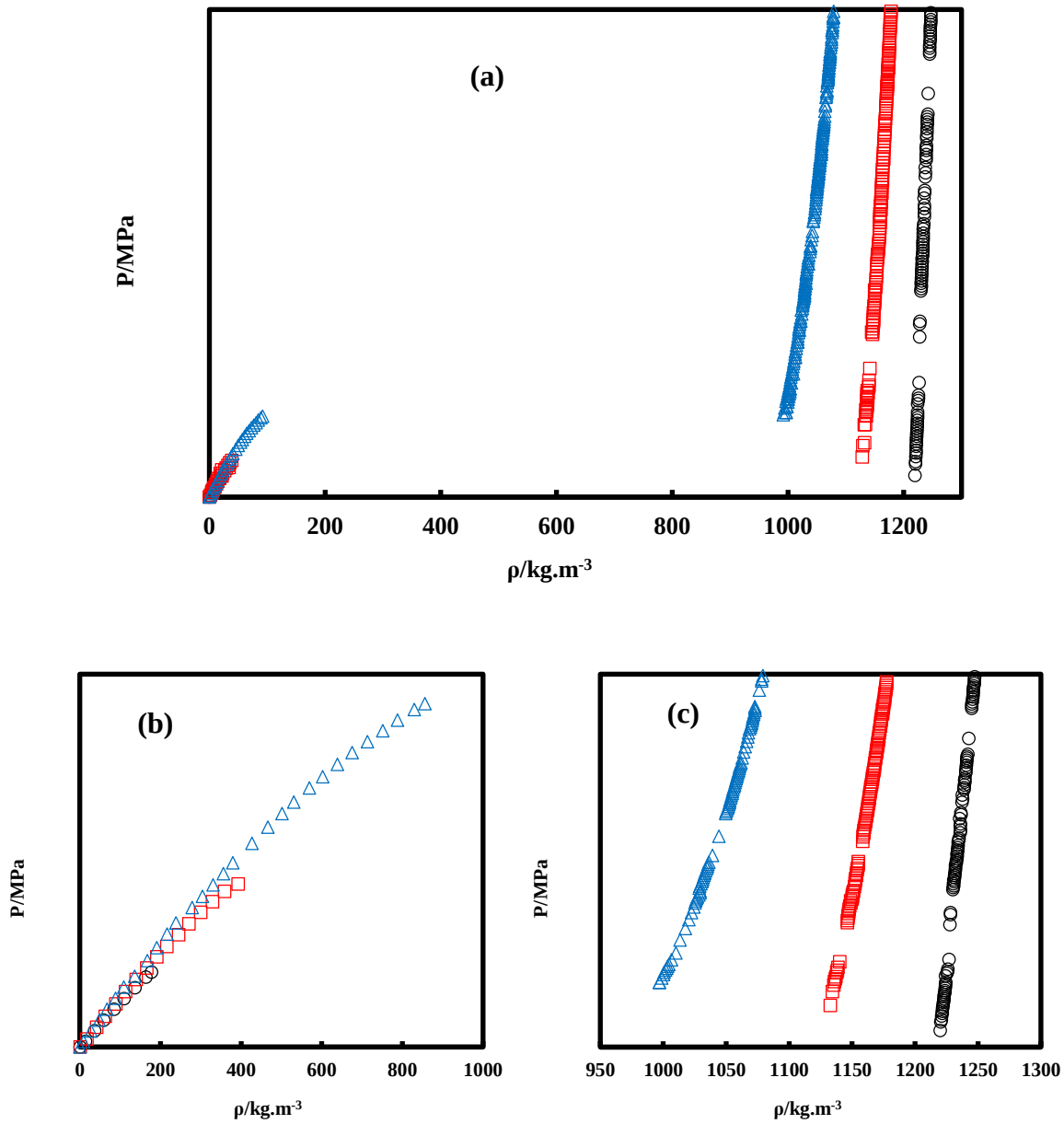

Figure 3.20 Experimental densities of R1234yf + R134a (1st composition). (a): Both phases; (b): Vapour phase; (c): Liquid phase. (○): 278.34 K; (□): 302.45 K; (Δ): 332.55 K. U(T) = 0.04 K; U(P) = 0.007 MPa; $U(\rho^V)/\rho^V$ = 2%; $U(\rho^L)/\rho^L$ = 0.2%.

● *2nd composition: (86.19% R1234yf + 13.81% R134a)*

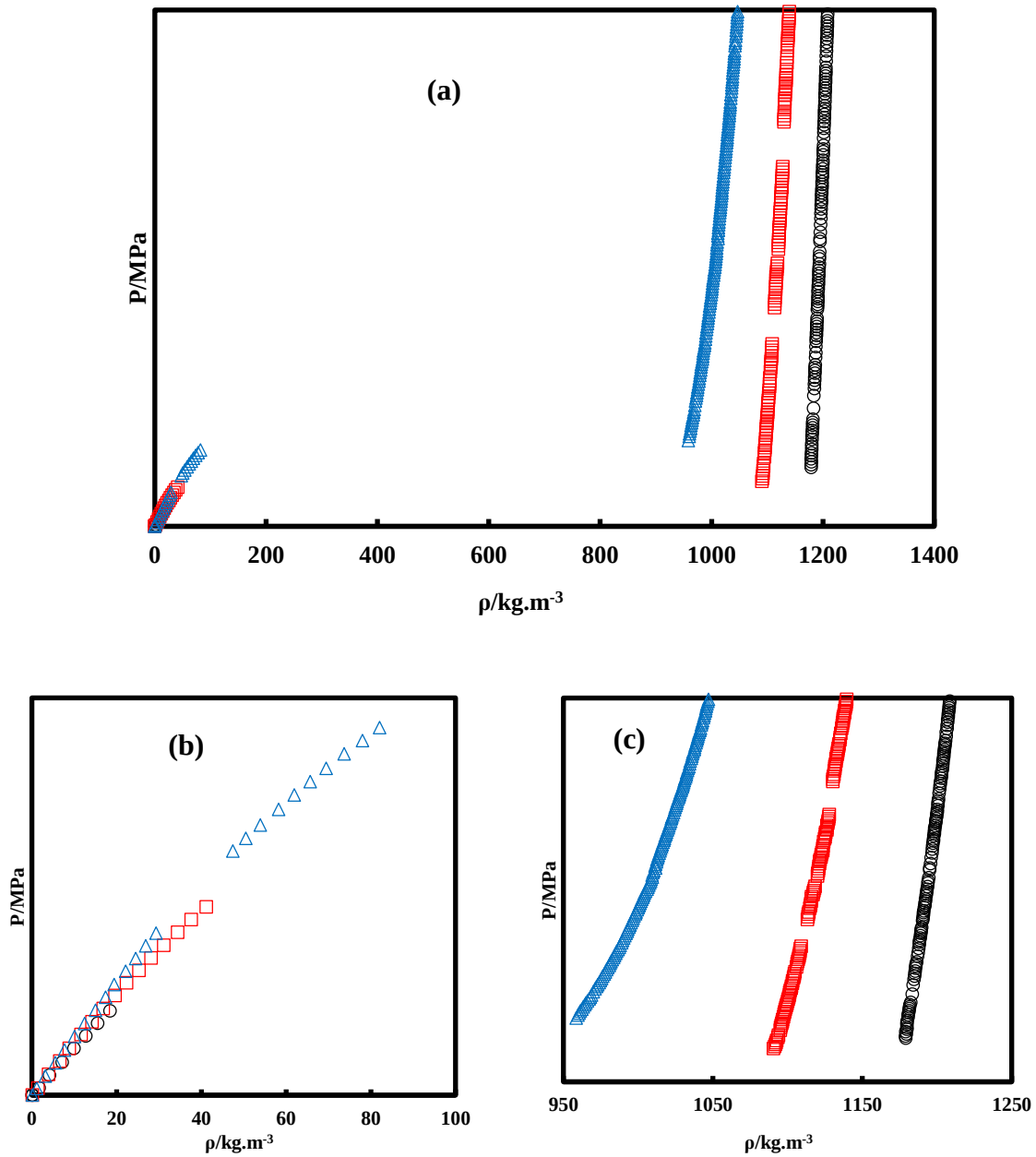

Figure 3.21 Experimental densities of R1234yf + R134a (2nd composition). (a): Both phases; (b): Vapour phase; (c): Liquid phase. (○): 278.36 K; (□): 302.74 K; (Δ): 332.54 K. U(T) = 0.04 K; U(P) = 0.007 MPa; $U(\rho^V)/\rho^V$ = 2%; $U(\rho^L)/\rho^L$ = 0.2%.

● ***3rd composition: (8.74% R1234yf + 91.26% R134a)***

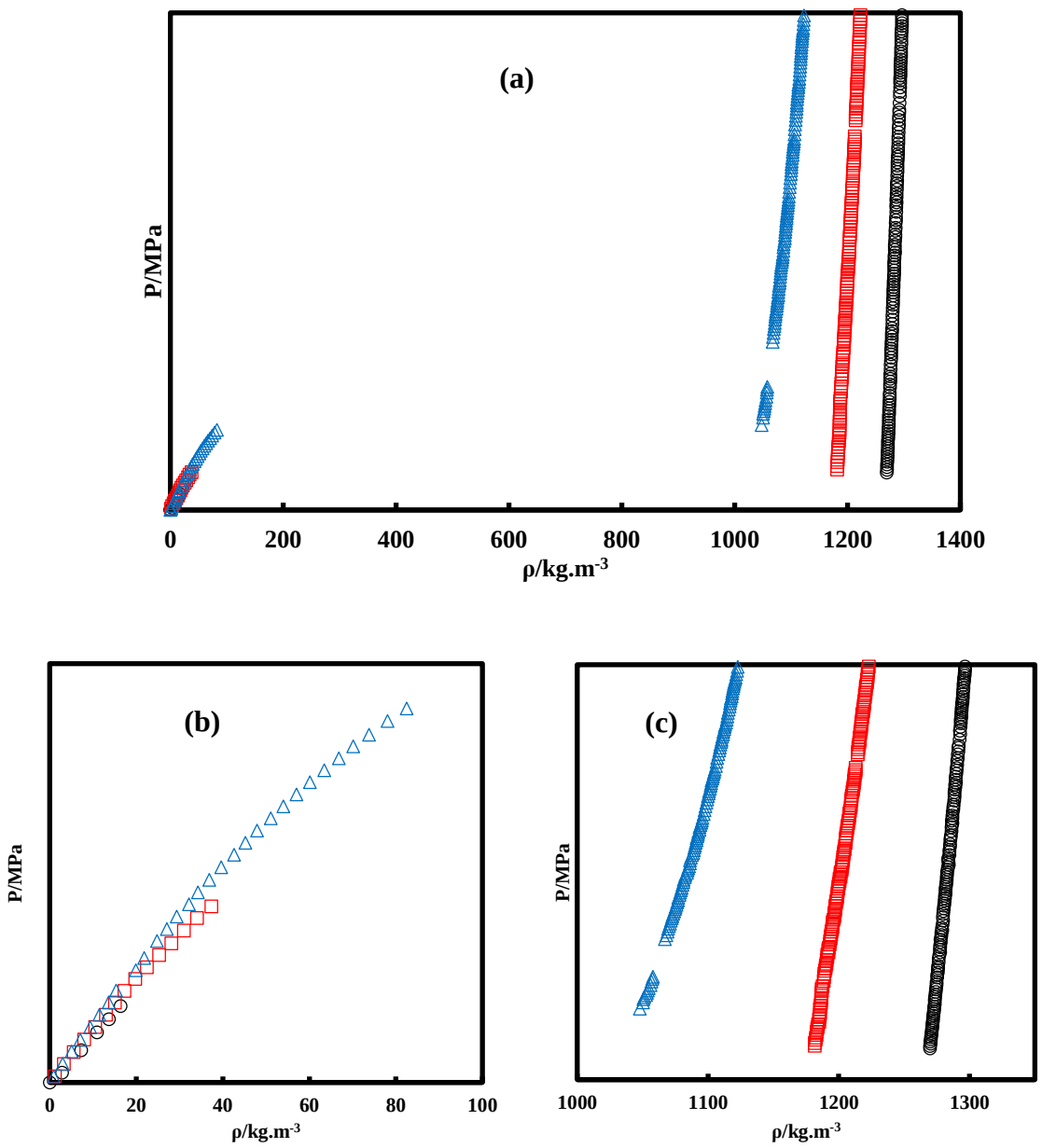

Figure 3.22 Experimental densities of R1234yf + R134a (3rd composition). (a): Both phases; (b): Vapour phase; (c): Liquid phase. (○): 278.40 K; (□): 302.93 K; (Δ): 332.53 K. U(T) = 0.04 K; U(P) = 0.007 MPa; $U(\rho^V)/\rho^V$ = 2%; $U(\rho^L)/\rho^L$ = 0.2%.

3.2.2.2. Binary mixture (R1234yf + R152a)

The binary mixture (R1234yf + R152a) was studied at three different molar compositions, and at three different temperatures ranging from 278.15 K to 333.15 K. The measurements for this system were carried out up to pressures of 16 MPa.

The experimental density results are presented for the three compositions studied at each of the isotherms covered.

The expanded uncertainties on the temperature, pressure and densities are reported along with the results of the measurements (U(X), k = 2).

The experimental results are displayed in *Figure 3.23* to *Figure 3.25*.

- ***1st composition: (45.53% R1234yf + 54.47% R152a)***

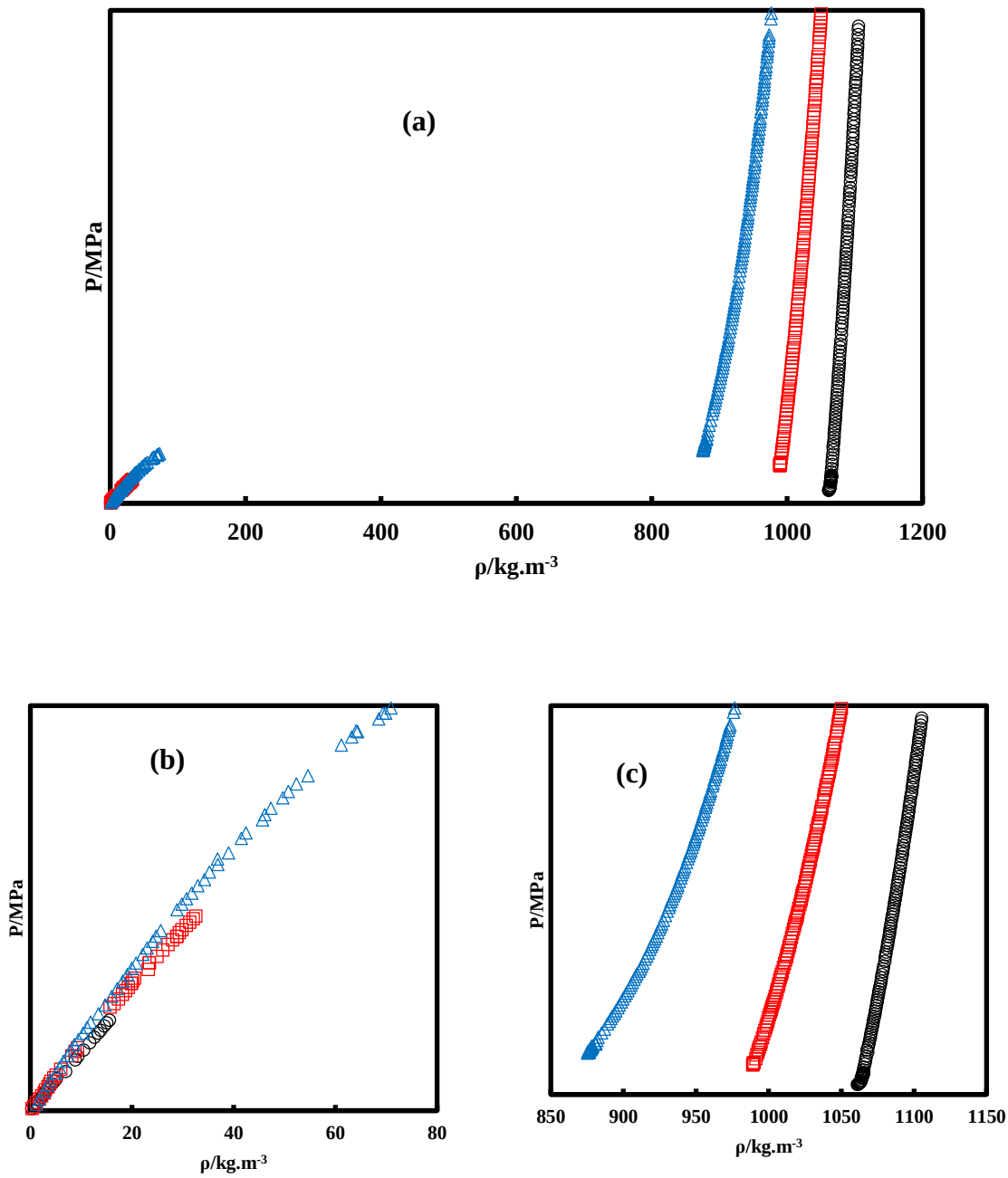

Figure 3.23 Experimental densities of R1234yf + R152a (1st composition). (a): Both phases; (b): Vapour phase; (c): Liquid phase. (○): 278.15 K; (□): 303.15 K; (Δ): 333.15 K. U(T) = 0.04 K; U(P) = 0.007 MPa; $U(\rho^V)/\rho^V$ = 2%; $U(\rho^L)/\rho^L$ = 0.2%.

● ***2nd composition: (86.57% R1234yf + 13.43 % R152a)***

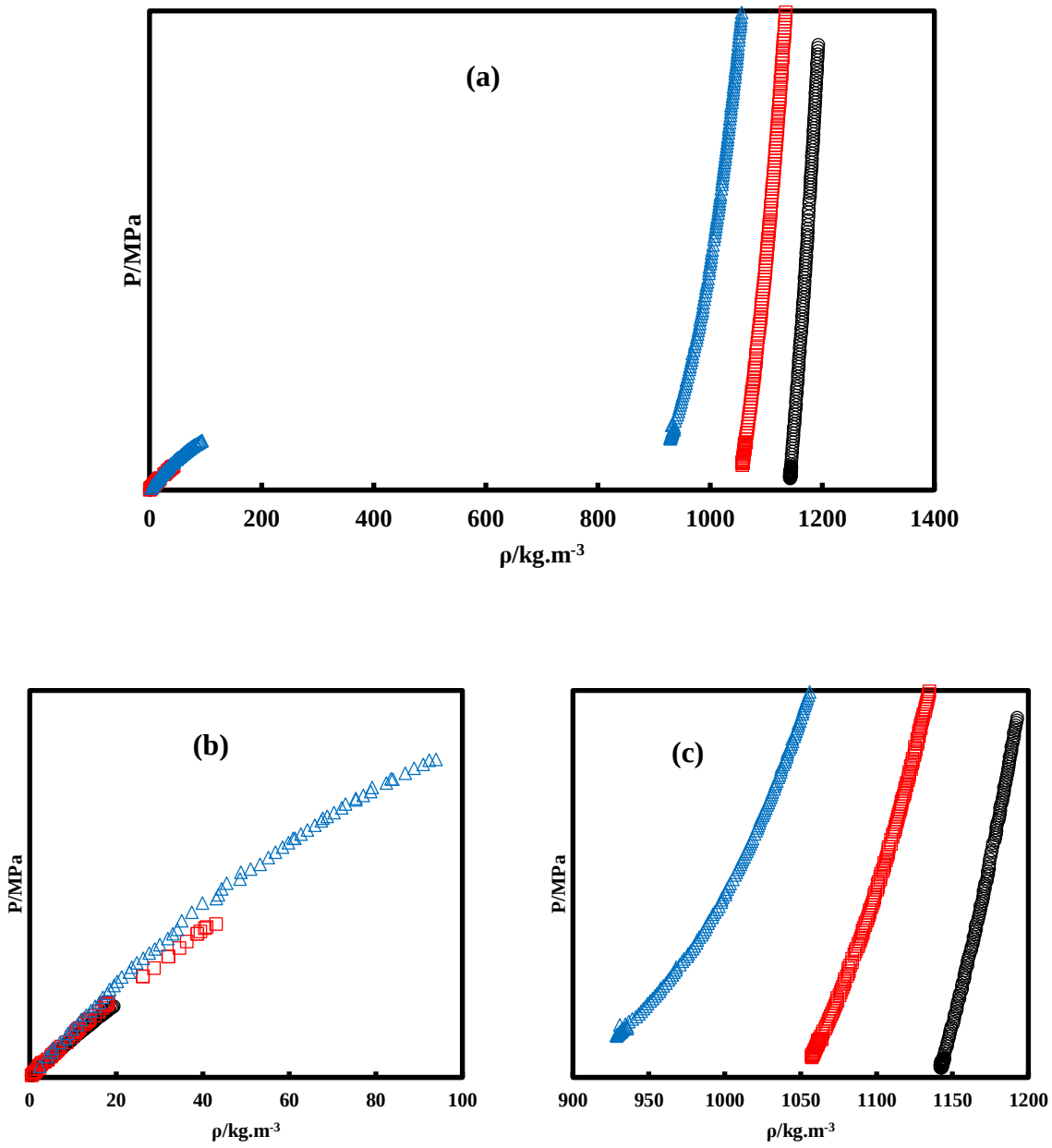

Figure 3.24 Experimental densities of R1234yf + R152a (2nd composition). (a): Both phases; (b): Vapour phase; (c): Liquid phase. (○): 278.15 K; (□): 303.15 K; (Δ): 333.15 K. U(T) = 0.04 K; U(P) = 0.007 MPa; $U(\rho^V)/\rho^V$ = 2%; $U(\rho^L)/\rho^L$ = 0.2%.

● *3rd composition: (9.26% R1234yf + 90.74% R152a)*

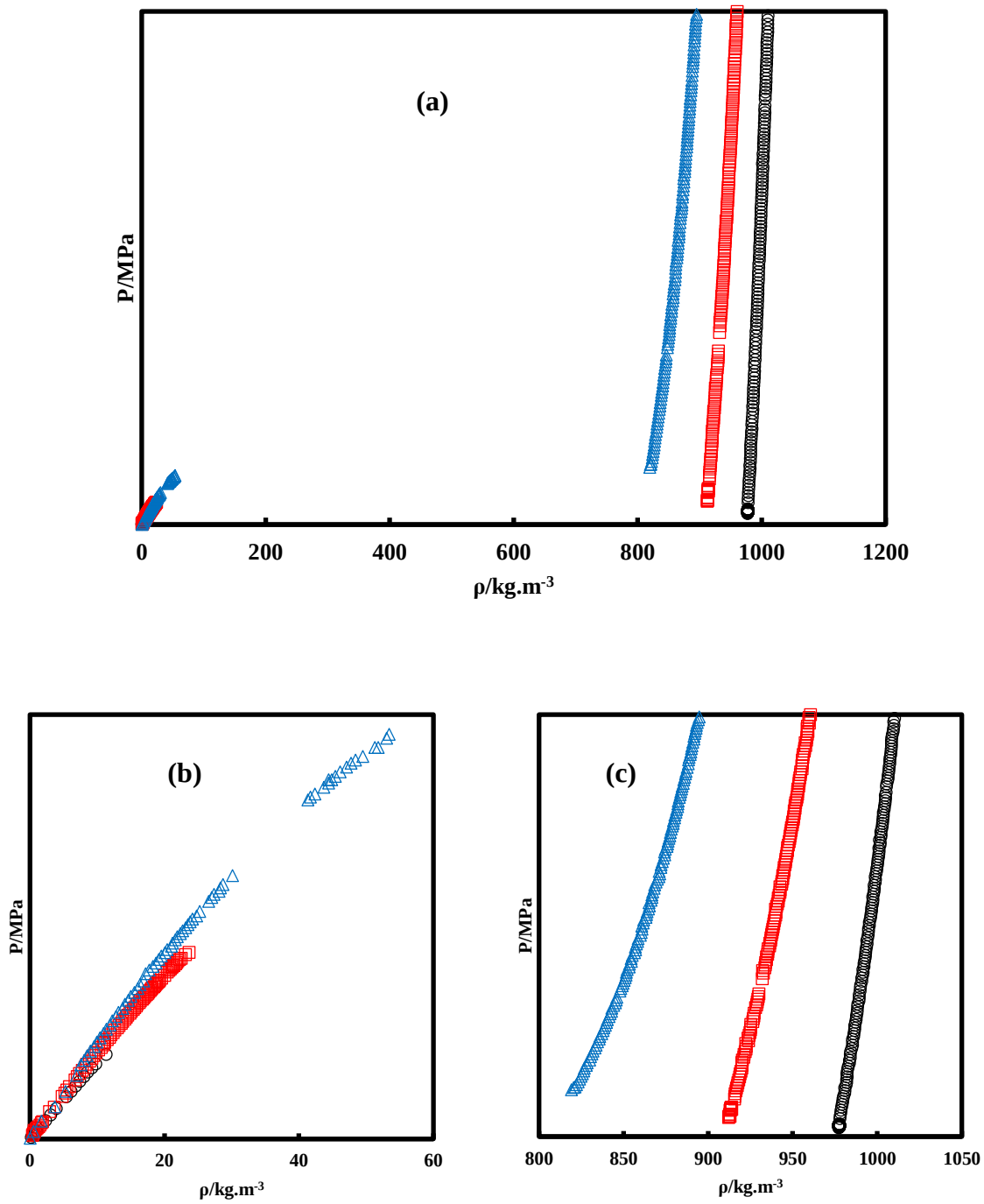

Figure 3.25 Experimental densities of R1234yf + R152a (3rd composition). (a): Both phases; (b): Vapour phase; (c): Liquid phase. (○): 278.15 K; (□): 303.15 K; (Δ): 333.15 K. U(T) = 0.04 K; U(P) = 0.007 MPa; $U(\rho^V)/\rho^V$ = 2%; $U(\rho^L)/\rho^L$ = 0.2%.

3.2.2.3. Ternary mixture (R134a + R152a + R1234yf)

The ternary mixture (R134a + R152a + R1234yf) was studied at three different molar compositions, and at three different temperatures ranging from 278.15 K to 333.15 K. The measurements for this system were carried out up to pressures of 20 MPa.

The experimental density results are presented for the three compositions studied at each of the isotherms covered.

The expanded uncertainties on the temperature, pressure and densities are reported within the results (U(X), k = 2).

The experimental results are displayed in *Figure 3.26* to *Figure 3.28*.

- ***1st composition: (29.53% R134a + 19.92% R152a + 50.56%R1234yf)***

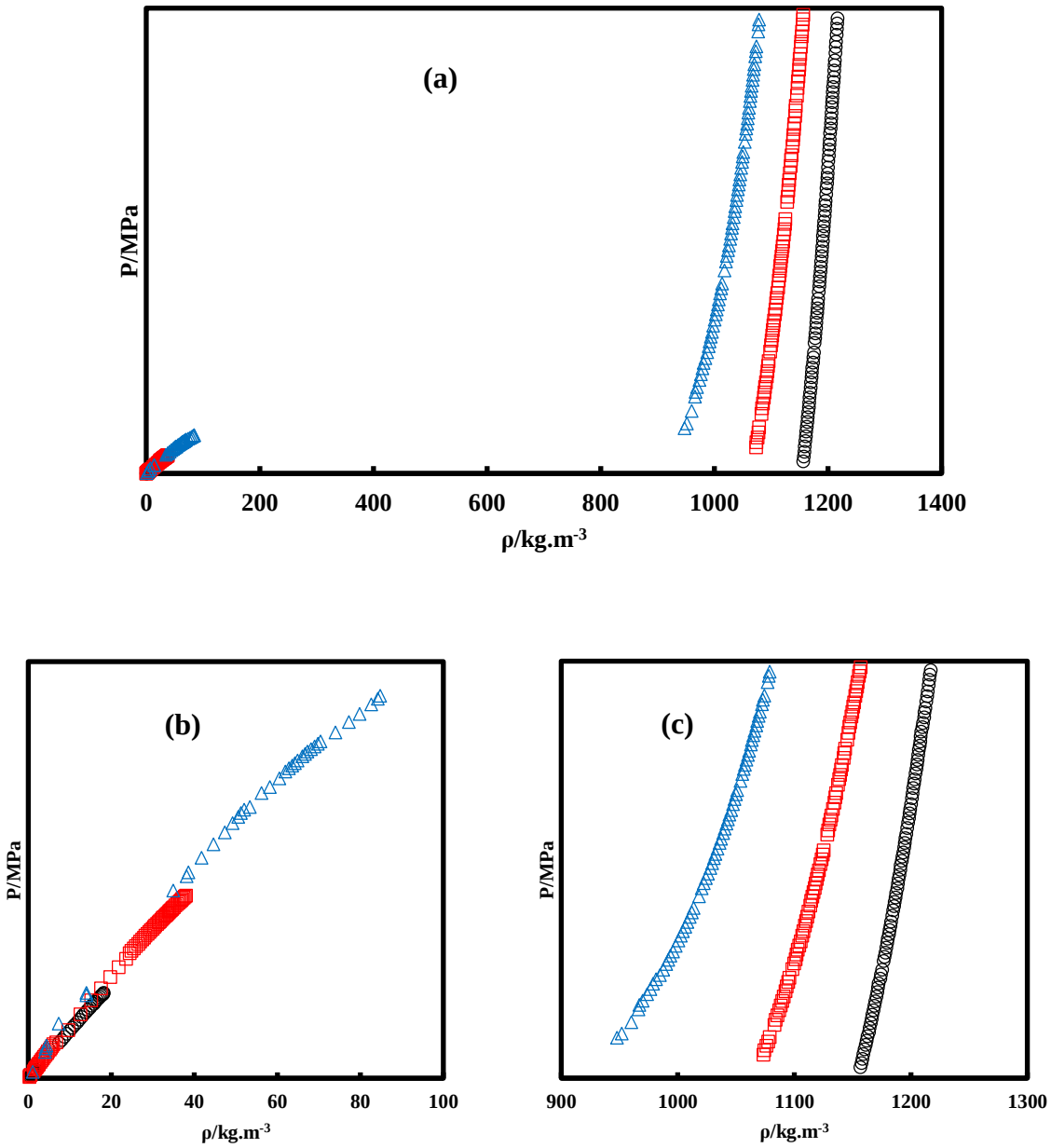

Figure 3.26 Experimental densities of (R134a + R152a + R1234yf) (1st composition). (a): Both phases; (b): Vapour phase; (c): Liquid phase. (○): 278.15 K; (□): 303.15 K; (Δ): 333.15 K. U(T) = 0.04 K; U(P) = 0.007 MPa; $U(\rho^V)/\rho^V$ = 2%; $U(\rho^L)/\rho^L$ = 0.2%.

- ***2nd composition: (19.67% R134a + 10.81% R152a + 69.52%R1234yf)***

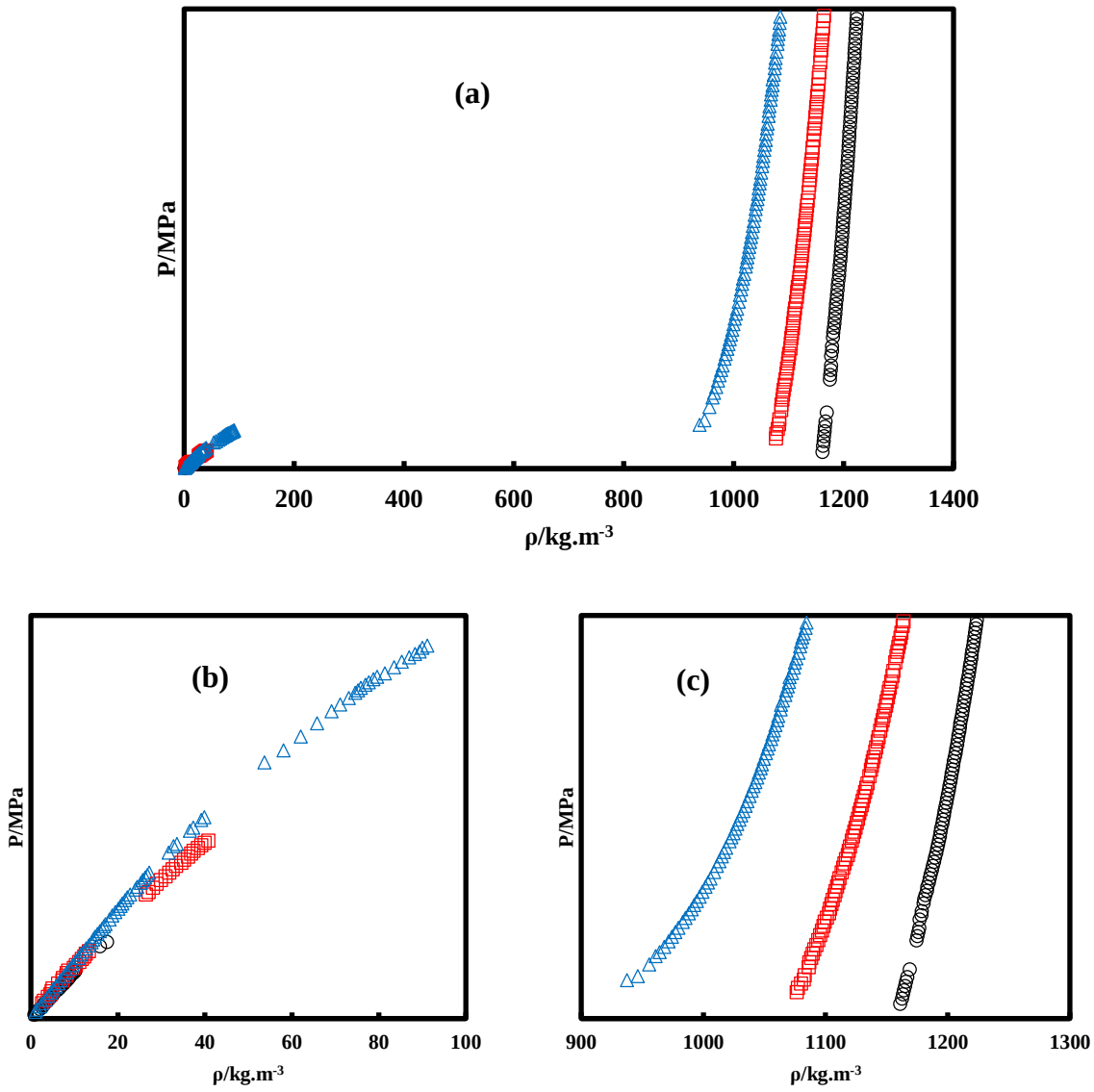

Figure 3.27 Experimental densities of (R134a + R152a + R1234yf) (2nd composition). (a): Both phases. (b): Vapour phase. (c): Liquid phase. (○): 278.15 K; (□): 303.15 K; (Δ): 333.15 K. U(T) = 0.04 K; U(P) = 0.007 MPa; $U(\rho^V)/\rho^V$ = 2%; $U(\rho^L)/\rho^L$ = 0.2%.

● ***3rd composition: (33.85% R134a + 31.41% R152a + 34.74%R1234yf)***

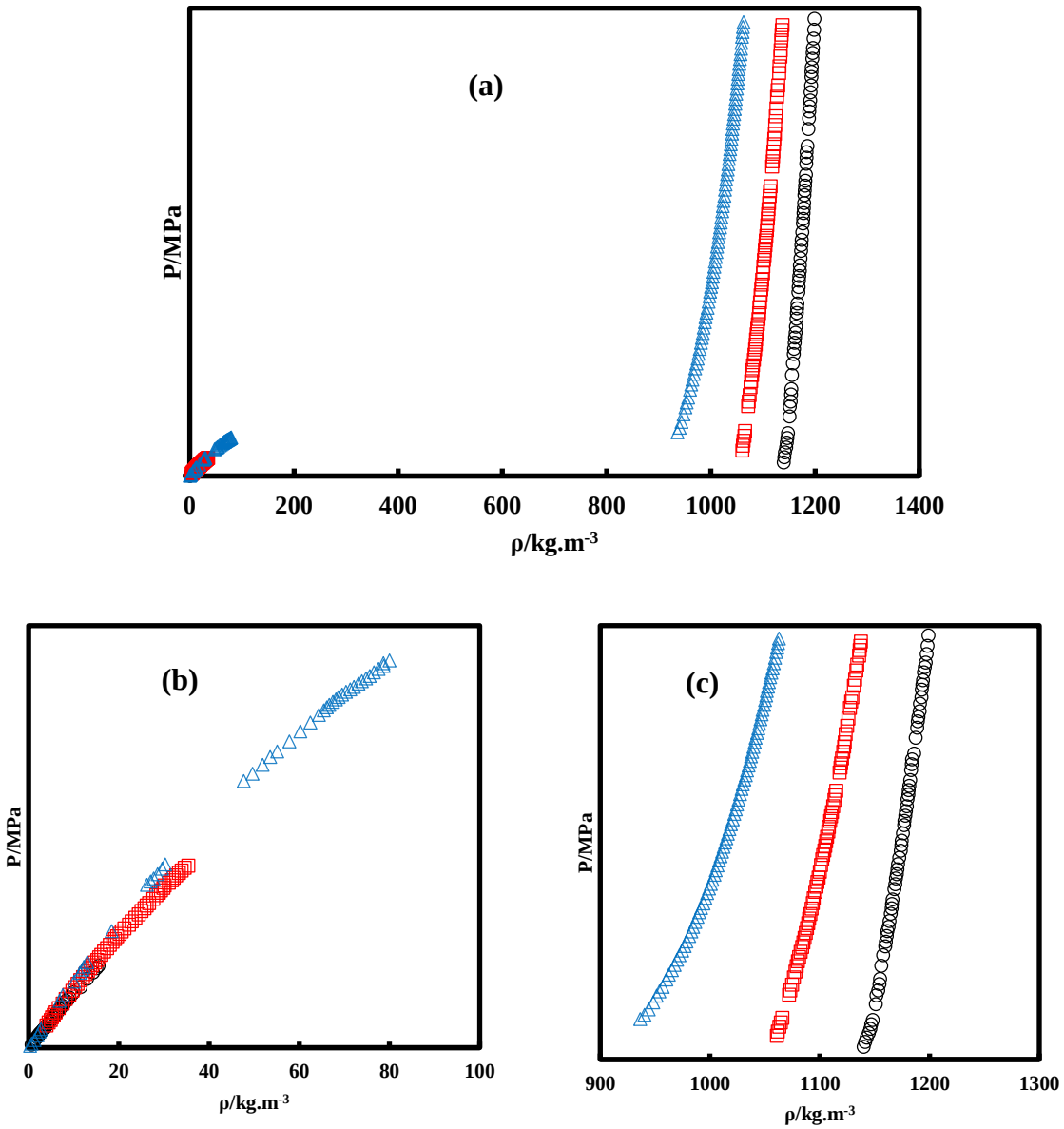

Figure 3.28 Experimental densities of (R134a + R152a + R1234yf) (3rd composition). (a): Both phases; (b): Vapour phase; (c): Liquid phase. (○): 278.15 K; (□): 303.15 K; (Δ): 333.15 K. U(T) = 0.04 K; U(P) = 0.007 MPa; $U(\rho^V)/\rho^V$ = 2%; $U(\rho^L)/\rho^L$ = 0.2%.

3.2.3. Compressibility factor Z

The vibrating tube densimeters are known to be well established tools for measuring fluid densities accurately at elevated temperatures and pressures (May et al. 2014). However at low pressures, the vibrating tube densimeters lose their precision (Dicko, Valtz, et al. 2011), and the results obtained should be used with care, especially for vapour densities.

In theory, the compressibility factor (Z) for should tend to 1 at low pressures. The expression of Z is given by Eq. (3.2) as follows:

$$Z = \frac{PV}{RT} \tag{3.2}$$

where P is the pressure, V the molar volume, R the ideal gas constant, and T the temperature.

In *Figure 3.29* is displayed the representation of the compressibility factor as a function of the pressure, for the binary mixture (R1234yf + R152a) at T = 333.15 K.

As we can see from this representation, in this example the compressibility factor Z is approaching the value of 1 at low pressures.

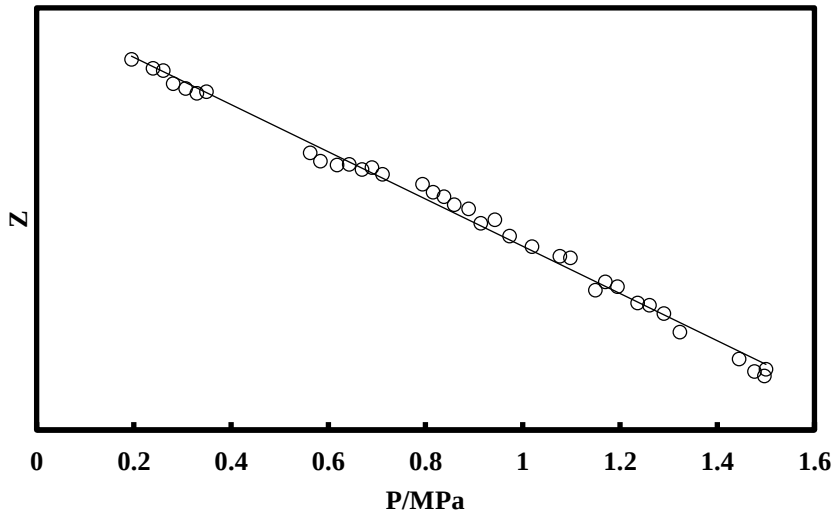

Figure 3.29 The compressibility factor representation for the binary mixture (R1234yf + R152a).

However, this result is not always obtained with the VTD, as we have cases where Z diverge from 1 at pressures approaching 0, as illustrated in *Figure 3.30*, with the example of the pure compound R1233zd(E), at T = 323.23 K.

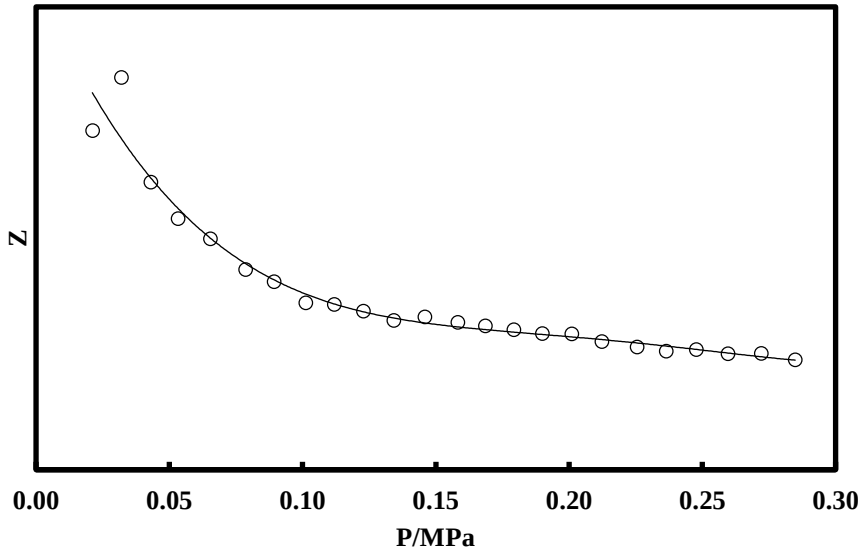

Figure 3.30 The compressibility factor representation for the pure compound R1233zd(E).

To overcome the problems encountered at low temperatures, we should ensure that we have a good value of the vacuum. With that, some modifications could be tested on the vibrating-tube densimeter (VTD) to ameliorate the results, such as reducing the length of the circuit line of the apparatus, or injecting the fluid directly in the VTD cell, without going through the circuit line. This could be combined with operating the VTD in a static mode in lieu of a dynamic way.

Concluding remarks

In this Chapter, we presented the experimental results obtained during our work for the VLE and density measurements of the refrigerants studied.

For the VLE measurements, the results were given for the vapour pressures of the pure compounds, then for the phase diagrams of the binary mixtures, along with the calculated relative volatility, for each of the systems studied.

For density measurements, the results were given for the pure compounds first, then for the binary and the ternary mixtures studied.

For the vapour densities obtained, we should note that the results should be used carefully, as the vibrating tube densimeter is known to be not very accurate at pressures below the atmospheric one.

The experimental results obtained in this Chapter will be used later for comparison with the results of the prediction calculated from our model. This will be the subject of Chapters 5 and 6.

We should note that the experimental data will not be provided in this manuscript due to the confidentiality restrictions. Also, the numerical values of the y-axes for the figures containing PREDIREF data were deleted. The data obtained will be published once we obtain the authorization from the project consortium. In this work, we will provide the complete data for only the systems not included in PREDIREF project, which can be found in Appendix C.

4. Model Presentation

Dans le but de calculer les propriétés thermodynamiques des fluides réfrigérants, il est important de disposer d'un modèle thermodynamique consistant permettant des calculs justes et précis. Dans cette optique, une nouvelle équation d'état (EdE) cubique à trois paramètres a été développée, basée sur la modification de l'équation d'état bien connue de Patel-Teja. Dans ce travail, cette nouvelle équation est associée à la fonction alpha de Mathias-Copeman, mais peut être associée à n'importe quelle autre fonction alpha parmi le vaste choix de fonctions disponibles dans la littérature.

Le choix de cette équation d'état est motivé par le fait d'avoir un modèle simple et facile à utiliser (puisque qu'il s'agit d'une équation cubique), et avoir un nombre réduit de paramètres à ajuster.

Une autre alternative était d'utiliser une équation d'état du type PC-SAFT par exemple, mais le problème rencontré avec ce type d'équations est leur limitation à présenter correctement la région critique. Aussi, comme nous ne travaillons pas avec des fluides associatifs, l'EdE PC-SAFT n'était pas un choix très convenable pour notre travail.

Une autre approche était de considérer une EdE cubique classique (Peng-Robinson par exemple), et lui appliquer une translation de volume. Le modèle de translation de volume peut être dépendant ou indépendant de la température. En appliquant un modèle de translation de volume indépendant de la température, la représentation des densités molaires liquides à saturation est nettement améliorée à des températures réduites inférieures à 0.8, mais ne réussit pas à représenter correctement les densités molaires à l'approche du point critique. En utilisant un modèle de translation de volume dépendant de la température, nous arrivons à résoudre ce problème, mais il est bien établi que ce modèle est thermodynamiquement inconsistant, et peut amener à un croisement d'isothermes dans un plan (pression, volume), et aussi à des capacités calorifiques isobariques négatives ($C_p < 0$).

Pour le choix de la fonction alpha de Mathias-Copeman, il était basé sur le fait d'avoir un compromis entre une fonction alpha qui représente bien les tensions de vapeur aussi bien dans la région subcritique que la région supercritique, et utiliser une fonction alpha bien connue, permettant de développer des corrélations généralisées en fonction de ses paramètres, dans une approche similaire à celle développée pour la fonction alpha de Soave, et ceci dans le but de pouvoir utiliser cette fonction alpha d'une manière prédictive. Nous allons voir dans ce chapitre qu'en se basant sur le principe des états correspondants, des corrélations ont été établies pour les paramètres de la fonction alpha, en fonction du facteur acentrique.

Introduction

To describe the thermodynamic properties of the refrigerant fluids, it is important to use a reliable thermodynamic model able to predict accurate results for both pure compounds and mixtures. In this Chapter, a new predictive three-parameter cubic equation of state is presented, based on the modification of the well-known Patel-Teja equation of state. The new equation of state is associated with the Mathias-Copeman alpha function.

By only knowing the acentric factor ω and the experimental critical compressibility factor Z_c of pure compounds, it is possible to predict the thermodynamic properties for both pure compounds and mixtures by means of the new cubic equation of state.

Based on the corresponding state principle, correlations have been developed to calculate the parameters of the Mathias-Copeman alpha function, along with the optimal critical compressibility factor of the equation of state.

We need to highlight that the contents of this Chapter have already been published and the description presented here closely follows the paper (Coquelet et al. 2016).

4.1. Generalities on equations of state

The detailed knowledge of the thermodynamic properties of refrigerants, and particularly of their vapour-liquid equilibrium (VLE) behaviour, is essential to design and optimize thermodynamic systems involving refrigerants, from the production and separation units to the refrigerant-based systems (such as air-conditioning systems, organic Rankine cycles, heat pumps etc.). In the field of refrigeration, there is a strong need for thermodynamic data of fluids, either to retrofit existing equipments with alternative refrigerants or to replace these equipments. In particular, when developing an alternative refrigerant, the list of possible mixtures is very large, and to obtain detailed experimental data for all the promising candidates can become rapidly time-consuming and expensive.

As a complement to experiment, equations of state (EOSs) are one of the most convenient tools to correlate, extrapolate and predict thermodynamic properties and phase behaviour for pure fluids and mixtures. For instance, they can be very useful to screen possible fluid candidates for their suitability in a particular application. Since van der Waals introduced his famous EoS in 1873 (Waals 1873), cubic EoSs (CEoSs) have been subject to active research and improvements, and were widely used in industrial process design and optimization, due to their

accuracy, generality, simplicity and speed of computation (Sengers et al. 2000), (Valderrama 2003).

The Soave-Redlich-Kwong (SRK) and Peng-Robinson (PR) equations are among the most popular cubic EoSs and are used for many applications, in which thermodynamic and VLE properties are required.

Concerning the vapour pressures, the capacity of prediction of the cubic EoSs is related to the model chosen for the temperature-dependent alpha function, while the prediction of volumetric properties depends on the volume function (Wei & Sadus 2000; Twu et al. 1992; Twu et al. 1991; Valderrama 2003). For instance, in the PR-EoS, the modification of the volume dependency of attractive term represents an improvement upon SRK-EoS, and allows one to obtain better results for liquid densities and better representation of VLE for many mixtures (Orbey & Sandler 1998; Valderrama 2003; Wei & Sadus 2000).

One of the drawbacks of the two-parameter cubic EoSs is that they involve a critical compressibility factor Z_c whose value is constant, regardless of the substance, providing saturated liquid densities and critical densities different from the experimental ones (Twu et al. 1992; Ji & Lempe 1998).

Also the Z_c obtained with the two-parameter cubic EoSs (Z_c[vdW] = 0.375; Z_c[SRK] = 0.333; Z_c[PR] = 0.3074) is larger than the experimental Z_c of most of the pure compounds (Ji & Lempe 1998), as shown in *Figure 4.1*.

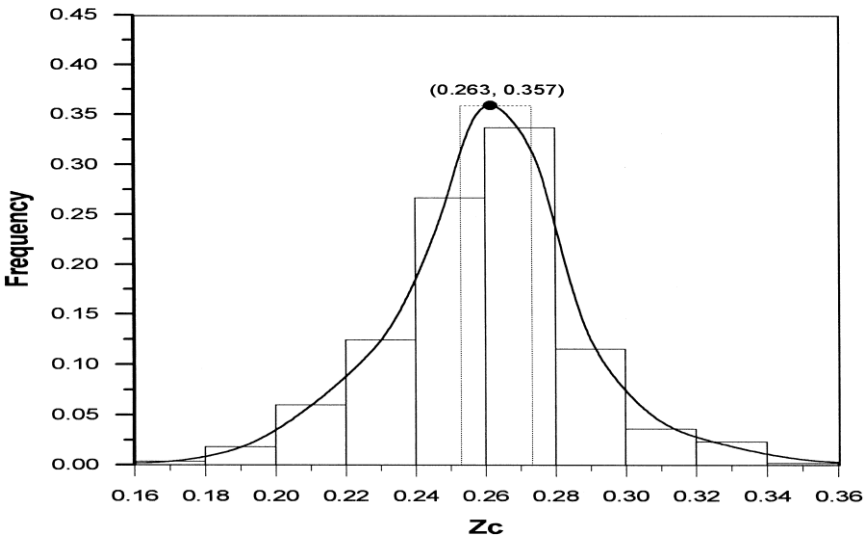

Figure 4.1 Distribution of the experimental critical compressibility factors Z_c for 555 substances (Ji & Lempe 1998).

The use of a substance-dependent critical parameter instead of a fixed value of Z_c has been proposed to overcome this deficiency (Abbott 1973). However, it has been shown that the optimal value of the critical compressibility factor is generally different from the experimental one (Schmidt & Wenzel 1980; Abbott 1973).

One of the well-known three-parameter equation of state is the Patel-Teja (PT) EoS and its generalized form (Patel & Teja 1982; Valderrama 1990), which has been successfully applied to correlate mixture VLE data (Danesh et al. 1991).

The three-parameter cubic EoS proposed in this work (denoted by NEoS), which is a modification of the PT-EoS, is based on the use of an optimized substance-dependent critical compressibility factor, yielding better representation of liquid densities. The NEoS is associated with the Mathias-Copeman alpha function.

The motivations behind the choice of a cubic EoS are mainly its simplicity and ease of computing, and also its reduced number of parameters to optimize. Another alternative would have been to use a PC-SAFT EoS for example, however the problem encountered with this type of equation is the misrepresentation near the critical region (Soo 2011; Madani et al. 2016). Also, since we are not working with associative fluids, PC-SAFT EoS was not a very convenient choice for our work.

Another alternative is to apply a volume translation to a classical cubic EoS (such as PR-EoS). The volume translation can be temperature-dependent or temperature-independent. However, when using a volume translation temperature independent, the representation of the saturated liquid density is significantly improved for reduced temperatures below 0.8, while it fails near the critical temperature (Jaubert et al. 2016). To overcome this problem near the critical temperature, a temperature-dependent volume translation can be used, however it is well established that this model is thermodynamically inconsistent, since it leads to the crossing of isotherms in a (pressure, volume) plane, and to negative isobaric heat capacities ($C_p < 0$) (Jaubert et al. 2016).

For the choice of the Mathias-Copeman alpha function, it was based on having a compromise between representing accurately the vapour pressures both below and above the critical temperature, and at the same time use a commonly known alpha function, that allow to develop generalized correlations with its parameters; in a similar way to the generalized Soave alpha function; in order to be used in a predictive way.

By applying the NEoS to pure compound refrigerants, we were able to develop correlations relating the alpha function parameters to the acentric factor, and the optimized critical

compressibility factor to the experimental one. As a result, the NEoS can be used for a wide range of refrigerants for which no experimental data are available. Furthermore, in this work, we show that by only calculating for pure compounds the alpha function parameters and the optimized critical compressibility factor, from the correlations developed, we can extend the prediction to mixtures.

4.2. Presentation of the new equation of state

In order to predict accurately the thermodynamic properties of refrigerants (both pure compounds and mixtures), a new three-parameter cubic EoS was developed, based on the modification of the well-known Patel-Teja equation of state (Patel & Teja 1982).
The NEoS is a three-parameter cubic EoS and is defined by the following relation:

$$P = \frac{RT}{v - b} - \frac{a(T)}{v^2 + ubv + wb^2} \tag{4.1}$$

where P is the pressure, T the temperature, v the volume, and R the universal constant for ideal gases. b is the volumetric parameter and a(T) the cohesive energy parameter.
u and w are two parameters defined in order to fulfil the condition: u + w = 0, which was shown to be the optimal combination for better liquid density calculations using cubic EoSs (Ji & Lempe 1998) - other authors such as Segura et al. (Segura et al. 2008) work on similar approaches, by the parameterization of u and w, without fixing a relation between them.
Here, u and w are defined as follows:

$$u = 1 + \frac{c}{b}$$
$$w = -u \tag{4.2}$$

While the PT-EoS (Patel & Teja 1982; Forero G. & Velásquez J. 2012; Ji & Lempe 1998) and the NEoS have the same definition for u, a different definition for w is chosen in the NEoS in order to fulfil the conditions defined by Ji and Lempe (Ji & Lempe 1998), i.e. u + w = 0 (note that in the case of the PT-EoS, u + w = 1).
The cohesive energy parameter a(T) depends on the temperature and is defined as follows:

$$a(T) = a_c \alpha(T) \tag{4.3}$$

α(T) is the alpha function that will be defined below, and which depends on both the temperature and the substance.

The parameters a_c, b and c of Eq. (4.1)-(4.3) can conventionally be obtained from the thermodynamic conditions at the critical point, defined as follows:

$$\left(\frac{\partial P}{\partial v}\right)_{T_c} = \left(\frac{\partial^2 P}{\partial^2 v}\right)_{T_c} = 0 \tag{4.4}$$

or from the mathematical constraint at the critical temperature:

$$(v - v_c)^3 = v^3 - 3v_c v^2 + 3{v_c}^2 v - {v_c}^3 = 0 \tag{4.5}$$

where v_c is the optimized critical volume.

After rewriting Eq. (4.1), we obtain:

$$v^3 - \left[\frac{RT}{P} - (u-1)b\right]v^2 + \left[\frac{RT}{P}ub - (w-u)b^2 - \frac{a}{P}\right]v - \frac{RT}{P}wb^2 + wb^3 + \frac{ab}{P} = 0 \tag{4.6}$$

The parameters a_c, b and c are calculated according to the following relations:

$$\begin{aligned} a_c &= \Omega_a \frac{R^2 {T_c}^2}{P_c} \\ b &= \Omega_b \frac{RT_c}{P_c} \\ c &= \Omega_c \frac{RT_c}{P_c} \end{aligned} \tag{4.7}$$

where Ω_a, Ω_b and Ω_c are factors depending on the substance (Forero G. & Velásquez J. 2012), T_c and P_c are respectively the experimental critical temperature and pressure.

We set $T = T_c$ and $P = P_c$ in Eq. (4.6), then the comparison with Eq. (4.5) results in:

$$\Omega_a = 1 - 3Z_{C,opt}\left(1 - Z_{c,opt}\right) + 3(1 - 2Z_{c,opt})\Omega_b + [2 - (u+w)]{\Omega_b}^2 \tag{4.8}$$

$$\Omega_b{}^3 + \left[\left(1 - 3Z_{c,opt}\right) + (u+w)\right]\Omega_b{}^2 + 3Z_{c,opt}^2\Omega_b - Z_{c,opt}^3 = 0$$

$$\Omega_c = 1 - 3Z_{c,opt}$$

$Z_{c,opt}$ is an apparent optimized critical compressibility factor. It is different from the experimental critical compressibility factor Z_c, and adjusted from the experimental VLE data (Ji et al. 2007; Ji & Lempe 1998), in order to improve the prediction of liquid densities.
Here, as u + w = 0, we can simplify Eq. (4.8) to obtain:

$$\begin{gathered}\Omega_a = 1 - 3Z_{C,opt}\left(1 - Z_{c,opt}\right) + 3(1 - 2\mathrm{Z_{c,opt}})\Omega_b + 2\Omega_b{}^2 \\ \Omega_b{}^3 + (1 - 3Z_{c,opt})\,\Omega_b{}^2 + 3Z_{c,opt}^2\Omega_b - Z_{c,opt}^3 = 0\end{gathered} \tag{4.9}$$

By including the critical compressibility factor in the calculations, better results can be obtained, even though the apparent critical compressibility factor $Z_{c,opt}$ is larger than the experimental one, Z_c.

4.3. Presentation of the Mathias-Copeman alpha function

The alpha function used in this work is the Mathias-Copeman (MC) alpha function (Mathias & Copeman 1983), defined as follows:

$$\begin{gathered}\alpha(T) = \left[1 + m_1\left(1 - \sqrt{\frac{T}{T_c}}\right) + m_2\left(1 - \sqrt{\frac{T}{T_c}}\right)^2 + m_3\left(1 - \sqrt{\frac{T}{T_c}}\right)^3\right]^2; \quad if\ T < T_c \\ \alpha(T) = \left[1 + \mathrm{m_1}\left(1 - \sqrt{\frac{T}{T_c}}\right)\right]^2; \quad if\ T > T_c\end{gathered} \tag{4.10}$$

where T and T_c are respectively the temperature and the critical temperature. m_1, m_2 and m_3 are three adjustable parameters fitted on the experimental data, and depending on the acentric factor ω[2]. The MC-alpha function is defined by two relations depending if we are above or below the critical temperature, as shown in Eq. (4.10).

[2] The acentric factor ω is a conceptual number introduced by Kenneth Pitzer in 1955, and it describes the non-sphericity (centricity) of molecules.

The MC-alpha function must satisfy the required conditions of an alpha function, as suggested by several authors (C. Coquelet et al. 2004; Forero G. & Velásquez J. 2012):

- It has to be real and positive at all temperatures;
- It has to be a decreasing function, approaching a positive value when the temperature tends to infinity;
- It has to be equal to one at the critical temperature;
- It has to be continuous as well as its first and second derivatives.

We can verify the conditions of the continuity of the MC-alpha function and its first derivative at the limit of the critical temperature (where the alpha function is defined from two relations). This latter condition is important in order to ensure the continuity of the thermodynamic properties (C. Coquelet et al. 2004):

$$\begin{aligned} &\alpha_{T<T_c}(T_c) = \alpha_{T>T_c}(T_c) = 1 \\ &\frac{\partial \alpha_{T<T_c}}{\partial T} = \frac{\partial \alpha_{T>T_c}}{\partial T} = -m_1 \end{aligned} \tag{4.11}$$

We can notice however that the second derivative of the MC-alpha function presents a discontinuity at the critical point.

In fact, a recent paper from (Le Guennec et al. 2016) defines the different conditions that an alpha function should satisfy (referred to as a consistency test): the alpha function must be positive, decreasing, convex with negative third derivative. According to this study no alpha function from the literature satisfies all the conditions of the consistency test.

The MC-alpha function can be associated to any cubic EoS. In this work it will be associated to the NEoS, PT-EoS, and Peng-Robinson EoS (denoted by PR-EoS).

4.4. Presentation of the mixing rules

For the mixtures, the classical van der Waals (vdW) mixing and combining rules (Kwak & Mansoori 1986) were used for the calculations. They are defined as follows:

$$a = \sum_{i=1}^{N}\sum_{j=1}^{N} x_i x_j a_{ij}$$

$$a_{ij} = \left(1 - k_{ij}\right)\sqrt{a_i a_j} \quad , \quad i = 1,2 \ldots . N \quad , \quad j = 1,2 \ldots . N \tag{4.12}$$

$$b = \sum_{i=1}^{N} x_i b_i$$

$$c = \sum_{i=1}^{N} x_i c_i$$

where x_i is the mole fraction of the component i, a_i is the energy parameter, and b_i and c_i are the covolume parameters of the component i, and k_{ij} is the binary interaction parameter. N is the number of components of the system.

The vdW mixing rules were chosen for their simplicity, and ease of computing and also to be able to use a predictive binary interaction parameter k_{ij}.

The k_{ij} if adjusted, is fitted on the VLE data of bubble pressure and vapour molar fraction according to the following objective function:

$$F_{obj} = \frac{100}{N}\left[\sum_{1}^{N}\left(\frac{P_{exp} - P_{cal}}{P_{exp}}\right)^2 + \sum_{1}^{N}\left(\frac{y_{exp} - y_{cal}}{y_{exp}}\right)^2\right] \tag{4.13}$$

where N is the number of data points, P_{exp} the experimental bubble pressure, P_{cal} the calculated bubble pressure, y_{exp} the experimental vapour molar fraction and y_{cal} the calculated vapour molar fraction.

4.5. Pure compounds parameters adjustment

In order to predict the thermodynamic properties for different fluids, the parameters of the alpha function, m_1, m_2, and m_3, and the optimized critical compressibility factor $Z_{c,opt}$ were adjusted from the data of 34 pure compounds collected from REFPROP 9.0 (Lemmon et al. 2010).

For the calculations, we used a modified simplex algorithm. The objective function (in the case of the NEoS and PT-EoS) is defined on the vapour pressures and the liquid densities and is expressed as follows:

$$F_{obj} = \frac{100}{N}\left[\sum_{1}^{N}\left(\frac{P_{exp} - P_{cal}}{P_{exp}}\right)^2 + \sum_{1}^{N}\left(\frac{\rho_{exp}^{L} - \rho_{cal}^{L}}{\rho_{exp}^{L}}\right)^2\right] \quad (4.14)$$

In the case of PR-EoS, the objective function is defined from the vapour pressures and is expressed as follows:

$$F_{obj} = \frac{100}{N}\left[\sum_{1}^{N}\left(\frac{P_{exp} - P_{cal}}{P_{exp}}\right)^2\right] \quad (4.15)$$

where N is the number of data points, P_{exp} the experimental vapour pressure, P_{cal} the calculated vapour pressure, ρ^{L}_{exp} the experimental saturated liquid density and ρ^{L}_{cal} the calculated saturated liquid density.

To fit the parameters, we need the values of the critical pressure P_c, the critical temperature T_c, the experimental critical compressibility factor Z_c (in the case of PR-EoS, Z_c is fixed to 0.3074), and the acentric factor ω. We need also the data of the vapour pressures P^{sat}, as well as the saturated liquid densities ρ^{L} for the range of temperatures considered (for PR-EoS, only the data of the vapour pressures are needed).

In this work, the range of temperatures considered is from the triple point temperature of the compound to its critical temperature (T_c), with a temperature step $\Delta T = 1$ K.

For the NEoS, PT-EoS, and PR-EoS, we optimized the alpha function parameter m_1, while the parameters m_2 and m_3 were set to constant values. For the NEoS and PT-EoS, the optimized critical compressibility factor $Z_{c,opt}$ is also adjusted, while the Z_c value is 0.3074 for the PR-EoS. In fact, several attempts were carried out before getting to this choice. At the beginning, the three parameters m_1, m_2 and m_3 along with $Z_{c,opt}$ were adjusted on the pure compounds data. We noticed that the parameters m_2 and m_3 are very dispersed in relation to the acentric factor ω, and no correlation could be deduced. We tried then to find an optimal set of values for the parameters m_2 and m_3 for all the compounds considered. Thus m_2 and m_3 were set to constant values, and m_1 and $Z_{c,opt}$ were adjusted.

For the three CEoSs, we carried out the parameters determination by associating each EoS with the MC alpha function, leading to three different sets of parameters.

Here, only the estimated parameters for the NEoS with the MC alpha function are presented (Cf. Table 4.1) and the parameters for both PT-EoS and PR-EoS are provided in Appendix D.

Table 4.1 Experimental and NEoS adjusted parameters for several refrigerant families (with $m_2 = 0.47$ and $m_3 = -0.08$). ω is the acentric factor, m_1 the alpha function parameter, and $Z_{c,opt}$ and Z_c the optimized and the experimental critical compressibility factors, respectively.

Families	*Compounds*	*ω*	m_1	$Z_{c,opt}$	Z_c
PFC	R-C318	0.35530	0.60916	0.29152	0.27751
	R-14	0.17850	0.39304	0.29695	0.27883
	R-116	0.25660	0.49092	0.29399	0.28151
	R-218	0.31720	0.53351	0.28765	0.27553
CFC	R-11	0.18875	0.36197	0.28744	0.27901
	R-12	0.17948	0.34391	0.28682	0.27643
	R-13	0.17230	0.34292	0.28839	0.27685
	R-113	0.25253	0.45677	0.28711	0.28019
	R-114	0.25230	0.47429	0.29044	0.27563
	R-115	0.25000	0.45928	0.29007	0.26779
HCFC	R-21	0.20610	0.38831	0.28473	0.27006
	R-22	0.22082	0.37537	0.27902	0.26825
	R-123	0.28192	0.46712	0.28022	0.26806
	R-124	0.28810	0.47540	0.28121	0.26865
	R-141b	0.21950	0.39624	0.28235	0.27057
	R-142b	0.23210	0.39073	0.27830	0.26786
HFC	R-125	0.30520	0.51102	0.28365	0.26844
	R-134a	0.32684	0.49929	0.27428	0.26004
	R-143a	0.26150	0.39374	0.26895	0.25502
	R-152a	0.27521	0.38981	0.26439	0.25233
	R-161	0.21700	0.33583	0.26915	0.25979
	R-227ea	0.35700	0.57089	0.28239	0.26849
	R-23	0.26300	0.39189	0.26924	0.25821
	R-236ea	0.37940	0.62687	0.28904	0.27578
	R-236fa	0.37721	0.59681	0.28170	0.26664
	R-245ca	0.35360	0.57228	0.28505	0.27003
	R-245fa	0.37760	0.59424	0.28041	0.26702
	R-32	0.27690	0.34346	0.25255	0.24291
	R-365mfc	0.38000	0.60464	0.28564	0.26686
	R-41	0.20040	0.25742	0.25587	0.24036
HFO	R-1234yf	0.27600	0.46360	0.28085	0.26519
	R-1234ze(E)	0.31300	0.50226	0.28049	0.26651
HCFO	R-1233zd(E)	0.34137	0.51623	0.28252	0.27884
Natural fluids	CO_2	0.22394	0.42919	0.28868	0.27458

4.6. Attempt of correlations

Based on these parameters adjusted, we deduced a correlation between the alpha function parameter m_1 and the acentric factor ω, as well as a correlation between the optimized critical compressibility factor $Z_{c,opt}$ and the experimental one Z_c.

In this way, we can calculate the alpha function parameter and the optimized critical compressibility factor for other compounds, whose thermodynamic properties are not known experimentally, allowing us to predict their thermodynamic properties.

The correlations obtained with the NEoS are shown in Figure 4.2 and given in Eq. (4.16).

From the graphical representations, we can see that there is a correlation between the alpha function parameter m_1 and the acentric factor ω, and between the optimized critical compressibility factor $Z_{c,opt}$ and the experimental one Z_c. Based on our calculations, the parameters m_2 and m_3 are taken as constants.

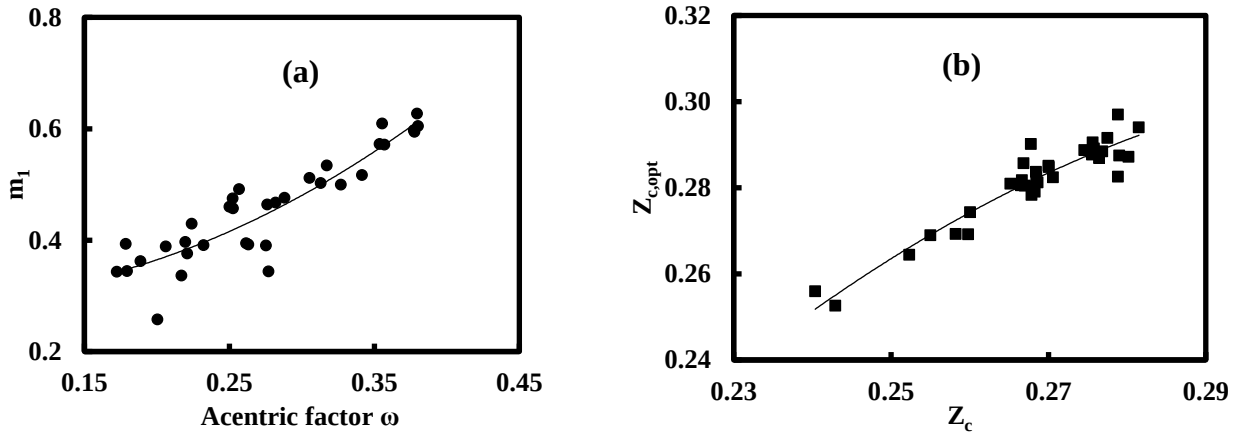

Figure 4.2 Correlations obtained with the NEoS. (a): The parameter m_1 as a function of the acentric factor ω (coefficient of determination $R^2 = 0.82$); (b): The optimized critical compressibility factor $Z_{c,opt}$ as a function of the experimental critical compressibility factor Z_c (coefficient of determination $R^2 = 0.89$).

$$
\begin{aligned}
m_1 &= 2.7868\omega^2 - 0.2376\omega + 0.3007 \\
m_2 &= 0.47 \\
m_3 &= -0.08 \\
\mathrm{Z_{c,opt}} &= -7.4737\mathrm{Z_c}^2 + 4.8824\mathrm{Z_c} - 0.4900
\end{aligned}
\tag{4.16}
$$

The same work has been carried out for the other EoSs considered (PT-EoS and PR-EoS). The parameters adjustment and the correlations development were performed for these EoSs, and the results are provided in Appendix D.

Concluding remarks

In this Chapter, the NEoS was presented in details, along with the MC-alpha function, and the classical mixing rules used. The adjustment procedure of the alpha function parameters (m_1, m_2 and m_3) and the optimized critical compressibility factor ($Z_{c,opt}$) was described. Then the correlations developed for the alpha function parameters and the $Z_{c,opt}$ were presented.

In order to improve the correlations obtained, and also to have a good correlation for the parameters m_2 and m_3 (other than taking them constant), it would be interesting to investigate additional approaches of adjusting the parameters, such as using the m_1 calculated from the correlations developed and the $Z_{c,opt}$ adjusted, or other alternatives to fit the parameters m_2 and m_3, and to see if that would improve the correlations obtained. Such approaches are currently studied and the results found will be presented in future works.

The MC-alpha function shows an undesirable discontinuity of its second derivative that may have an effect of representing accurately some second derivative thermodynamic properties, such as the heat capacities (C_v and C_p), at supercritical conditions.

This issue was approached by (Mahmoodi & Sedigh 2016) in a recent study, and proposed a slight modification in the expression of the MC-alpha function in order to tackle the discontinuity of its second derivative and meet all the requirements of the consistency test for the alpha functions (Le Guennec et al. 2016).

In this work, we use the classical MC-alpha function, and applied it for heat capacities calculations at supercritical conditions (see Appendix D). The modification proposed by (Mahmoodi & Sedigh 2016) could be a great way of improvement of the MC-alpha function and it would be interesting to investigate carefully the effects of such a modification on

representing the different thermodynamic properties, at both subcritical and supercritical conditions.

Following the introduction of the model used during this work, the results of the prediction of the VLE and density properties will be presented. This will be the subject of Chapter 5 (for the prediction of the pure compounds properties) and Chapter 6 (for the prediction of the mixtures properties).

5. Pure compounds modelling

Dans ce chapitre, nous nous intéressons aux résultats de la modélisation obtenus pour les réfrigérants composés purs. En utilisant les corrélations précédemment développées dans le chapitre 4, notre modèle thermodynamique a été testé, dans un premier temps, pour le calcul des densités de quatre réfrigérants : R1234yf, R1216, CO_2 et R134a. Les calculs ont été faits pour les densités à saturation et hors saturation. Les résultats ont été comparés aux résultats de REFPROP 9.0 et aux données de la littérature (quand elles sont disponibles), et aussi aux résultats de calculs obtenus à partir de deux autres équations d'état cubiques (EdE de Peng-Robinson et de Patel-Teja).

Ensuite, la NEoS a été utilisée pour la prédiction des propriétés thermodynamiques des réfrigérants étudiés expérimentalement dans ce travail. Les propriétés thermodynamiques couvertes par le calcul sont les pressions de vapeur et les densités vapeur et liquide hors saturation.

Les résultats obtenus montrent qu'en général la nouvelle équation (NEoS) permet une meilleure représentation des densités liquides à saturation et hors saturation. La NEoS permet aussi une meilleure représentation des densités au voisinage du point critique, et aussi pour les isothermes supercritiques. Les densités en phase vapeur et les pressions de vapeur quant à elles, restent bien représentées par la NEoS.

Quelques améliorations pourraient être ramenées, notamment pour la représentation des densités liquides à très basses températures.

Il est à noter que des parties de ce chapitre ont déjà fait l'objet d'une publication, et les résultats présentés ici suivent ceux de l'article (Coquelet et al. 2016).

Introduction

In this Chapter, the results of the prediction for the pure compounds refrigerants are presented. Based on the correlations developed in Chapter 4, and using the parameters calculated from it, we calculated the thermodynamic properties (density) of four pure compound refrigerants: R1234yf, R1216, CO_2 and R134a in order to test and validate our model. The P-ρ diagrams have been predicted at saturation and out of saturation.

The results of the prediction with the NEoS were compared to the results obtained from REFPROP 9.0, and to the literature data when available.

The results of the NEoS were also compared to the results obtained using the two other CEoS (PR-EoS and PT-EoS).

In a second part, the NEoS was used to predict the thermodynamic properties of the pure compound refrigerants studied experimentally in Chapter 3, first for the prediction of their vapour pressures, then for the calculation of their vapour and liquid density out of saturation. The parameters used for the pure compounds were obtained from the correlations developed in Chapter 4.

We need to highlight that some of the contents of this Chapter have already been published and the results presented here closely follows the paper (Coquelet et al. 2016).

5.1. Prediction for the pure compound R1234yf

5.1.1. Prediction at saturation

The prediction at saturation for the R1234yf was performed using the three EoSs, and were compared to the results from REFPROP 9.0, as well as to the literature data (Tanaka & Higashi 2010b). The results were calculated from the triple point temperature to the critical temperature. The parameters of the MC-alpha functions and the critical compressibility factors were calculated from the correlations given in Eq. (4.16) (for the PR-EoS, the value of Z_c is set to 0.30740). The values obtained for these parameters are reported in Table 5.1.

Table 5.1 Calculated parameters for R1234yf from the correlations (see Chapter 4; m_2 and m_3 are set to fixed values).

R1234yf				
CEoS	m_1	m_2	m_3	$Z_{c,opt}$
NEoS	0.44741	0.47	-0.08	0.27917
PT-EoS	0.73498	-0.01	0.4	0.30417
PR-EoS	0.74884	0	0.49	0.30740[a]

[a] For the PR-EoS, the value of Z_c is set to 0.30740.

The graphical representation of the P-ρ diagram for the R1234yf at saturation is shown in Figure 5.1.

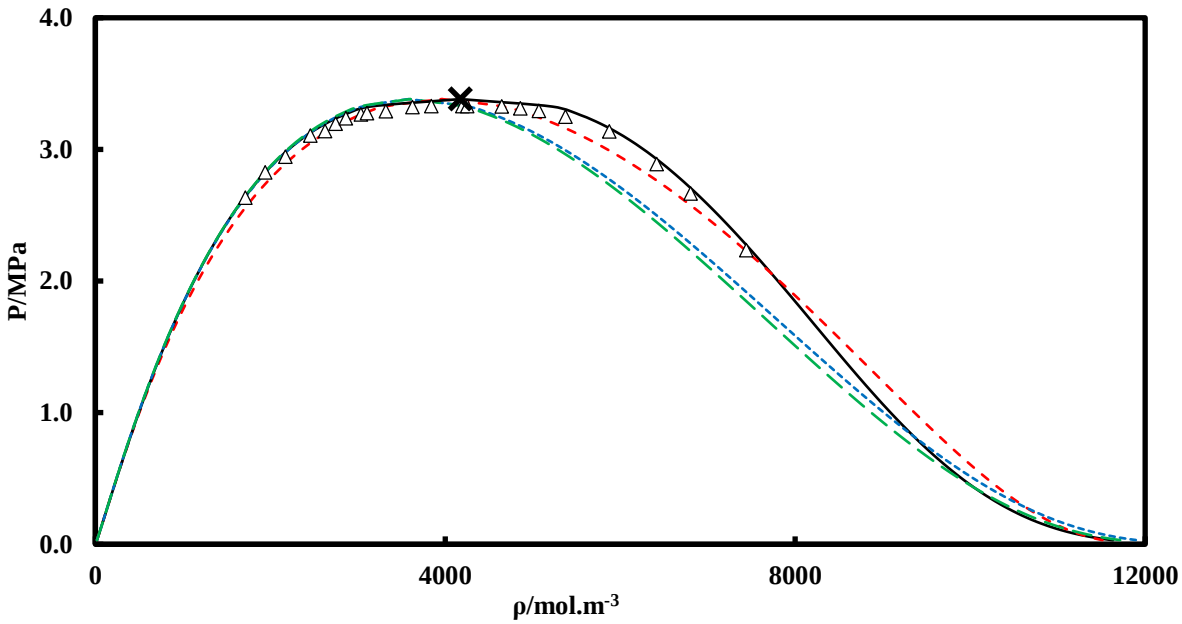

Figure 5.1 P-ρ diagram for R1234yf. (Δ) Experimental data (Tanaka & Higashi 2010b); (——) REFPROP; (×) Critical Point: REFPROP; (- - - -) NEoS; (……) PT-EoS; (— — —) PR-EoS.

Based on the results of the prediction, we calculated the average relative deviation (ARD), and the BIAS with each EoS used here. We calculated also the relative deviation (RD) using the NEoS. The calculations were compared to the results obtained from REFPROP 9.0.

The ARD, the BIAS and the RD are defined by Eq. (5.1):

$$ARD(X)\ \% = \left| \frac{100}{N} \sum_{1}^{N} \frac{X_{exp} - X_{cal}}{X_{exp}} \right|$$

$$BIAS\ (X)\ \% = \frac{100}{N} \sum_{1}^{N} \frac{X_{exp} - X_{cal}}{X_{exp}} \tag{5.1}$$

$$RD\ X\ (\%) = 100 * \frac{X_{exp} - X_{cal}}{X_{exp}}$$

The ARD and the BIAS calculated using the parameters of the correlations are reported in Table 5.2, while the ARD and the BIAS calculated using the adjusted parameters are shown in Table 5.3.

Table 5.2 ARD and BIAS for R1234yf using the calculated parameters for EoSs.

	ARD (%)			*BIAS (%)*		
CEoS	*P*	ρ^L	ρ^V	*P*	ρ^L	ρ^V
NEoS	1.4	2.2	2.9	-1.4	-0.6	-2.8
PT-EoS	2.2	3.9	2.0	-2.2	1.9	-1.8
PR-EoS	1.9	3.9	1.6	-1.9	3.4	-1.3

Table 5.3 ARD and BIAS for R1234yf using the adjusted parameters for EoSs.

	ARD (%)			*BIAS (%)*		
CEoS	P	ρ^L	ρ^V	P	ρ^L	ρ^V
NEoS	0.4	1.9	2.0	-0.2	0.2	-1.5
PT-EoS	0.5	4.3	0.9	-0.3	0.5	0.1
PR-EoS	0.9	3.9	0.8	-0.5	3.3	0.2

From the results of the prediction represented in Figure 5.1, we can see that the NEoS provides a better representation for the liquid density compared to PR-EoS and PT-EoS, especially at high temperature and in the vicinity of the critical point. We can also see that with the NEoS, it is possible to reproduce more accurately the location of the critical point, compared to the other two EoSs [ρ_c(NEoS) = 3961 mol/m^3; ρ_c(PT-EoS) = 3573 mol/m^3; ρ_c(PR-EoS) = 3597 mol/m^3; ρ_c(REFPROP) = 4170 mol/m^3].

The vapour pressure and the vapour density appear to be well represented by the three EoSs, with the better results obtained with the PR-EoS for vapour density.

From Table 5.3, we can notice that by using the adjusted parameters instead of the parameters calculated from the correlations, the results are improved for the ARD and the BIAS.

Based on the results obtained, we represented the RD as a function of the temperature, using the NEoS (Cf. Figure 5.2).

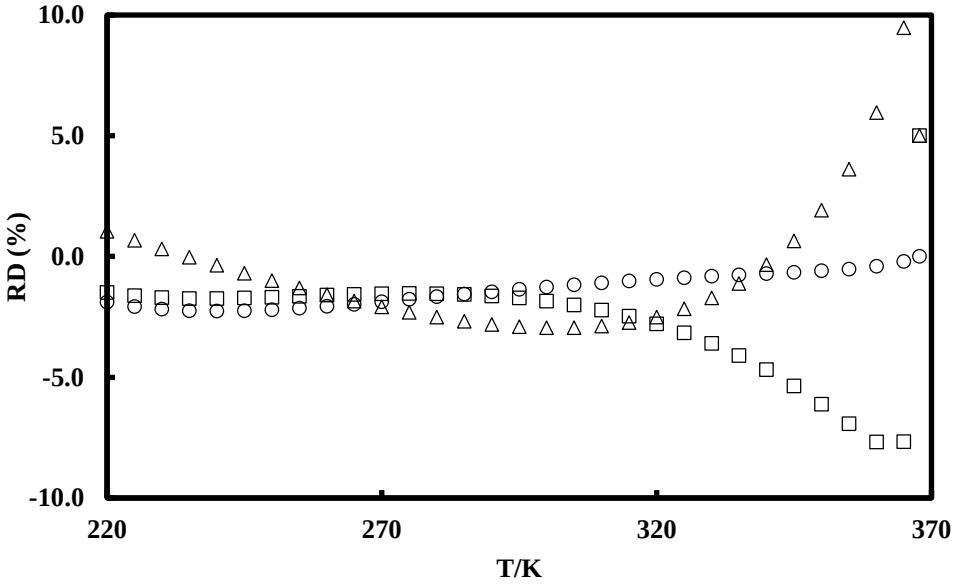

Figure 5.2 Relative deviation (RD) for R1234yf with NEoS using the calculated parameters. (○) RD of vapour pressure; (Δ) RD of saturated liquid density; (□) RD of saturated vapour density.

From the RD representation, we can see that the vapour pressure is slightly overestimated at low temperatures, and that the RD tends to zero with increasing temperatures.

The vapour density is overestimated at high temperatures and slightly overestimated at low and intermediate temperatures.

The liquid density is underestimated at high temperatures, and slightly underestimated at low temperatures, and slightly overestimated at intermediate temperatures.

5.1.2. Prediction out of saturation

For the prediction out of saturation, we used the same three EoSs as for the prediction at saturation. Four isotherms are considered here, for a reduced temperature T_r of 0.7, 0.9, 1, and 1.1 ($T_r = T/T_c$). We should note that the critical temperature of R1234yf is 367.85 K (Lemmon et al. 2010).

The graphical representation of the P-ρ diagram for the four isotherms out of saturation is shown in Figure 5.3.

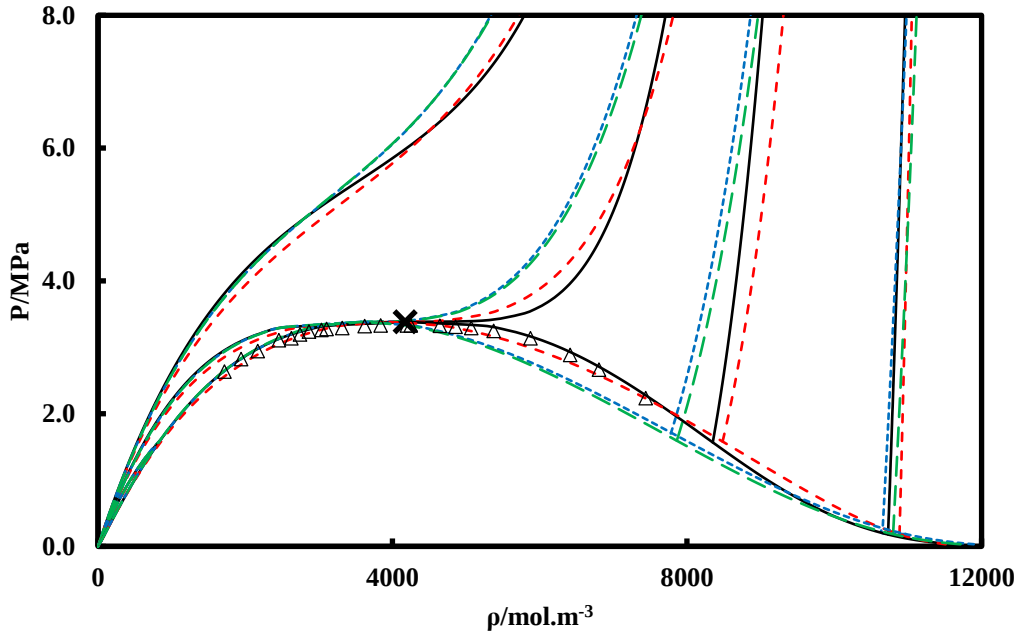

Figure 5.3 P-ρ diagram for R1234yf. (Δ) Experimental data (Tanaka & Higashi 2010b); (——) REFPROP; (×) Critical Point: REFPROP (T_c = 367.85K); (- - - -) NEoS; (……) PT-EoS; (— — —) PR-EoS. Out of saturation: T_r = 0.7, 0.9, 1.0, 1.1.

From Figure 5.3, we can see that the NEoS leads to better results for the liquid density than PT-EoS and PR-EoS. Furthermore, with the NEoS it is possible to represent rather accurately the density at supercritical conditions, while PT-EoS and PR-EoS show important deviations in this region, compared to REFPROP results. Concerning the vapour density, it appears to be well represented by the three EoSs considered.

5.2. Prediction for the pure compounds R1216, CO_2, and R134a

5.2.1. R1216, CO_2, and R134a: Prediction at saturation

The same study was carried out for the hexafluoropropylene (R1216), the carbone dioxide (CO_2), and the 1,1,1,2-tetrafluoroethane (R134a), using the three CEoSs. The results were predicted from the triple point temperature to the critical temperature (for R1216, the results are from $T_r = 0.6$ to $T_r = 1$).

The critical temperatures of R1216, CO_2, and R134a are respectively 358.9 K (Coquelet et al. 2010), 304.13 K (Lemmon et al. 2010), and 374.21 K (Lemmon et al. 2010).

The parameters of the MC alpha functions and the critical compressibility factor were calculated from the correlations established. The values of these parameters are reported in Table 5.4.

Table 5.4 Calculated parameters for pure compounds R1216, CO_2, and R134a (m_2 and m_3 are set to fixed values).

CEoS	*Compounds*	m_1	m_2	m_3	$Z_{c,opt}$
NEoS	R1216	0.56391	0.47	-0.08	0.28529
	CO_2	0.38725	0.47	-0.08	0.28714
	R134a	0.52074	0.47	-0.08	0.27424
PT-EoS	R1216	0.86744	-0.01	0.4	0.30979
	CO_2	0.66975	-0.01	0.4	0.31139
	R134a	0.81773	-0.01	0.4	0.29936
PR-EoS	R1216	0.85972	0	0.49	0.30740[a]
	CO_2	0.67314	0	0.49	0.30740
	R134a	0.82227	0	0.49	0.30740

[a] For the PR-EoS, the value of Z_c is set to 0.30740.

The graphical representations of the P-ρ diagram at saturation, using the three CEoSs associated to the MC alpha function, are shown in Figure 5.4 to *5-6*.

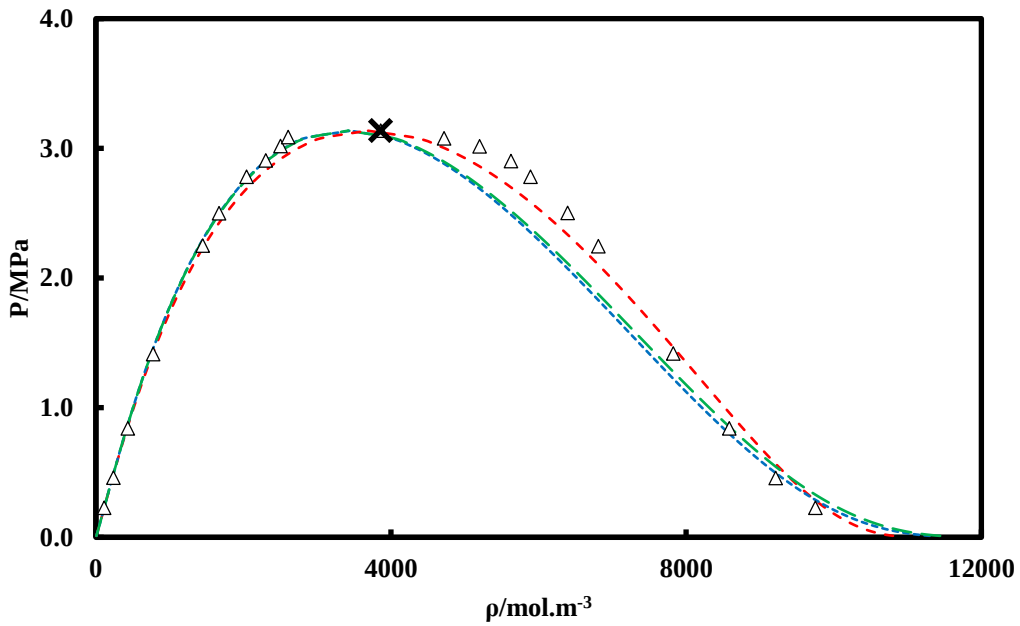

Figure 5.4 P-ρ diagram at saturation for R1216. (Δ) Experimental data (Coquelet et al. 2010); (×) Critical Point: Experimental (T_c=358.9 K) (Coquelet et al. 2010); (- - - -) NEoS; (……) PT-EoS; (— — —) PR-EoS.

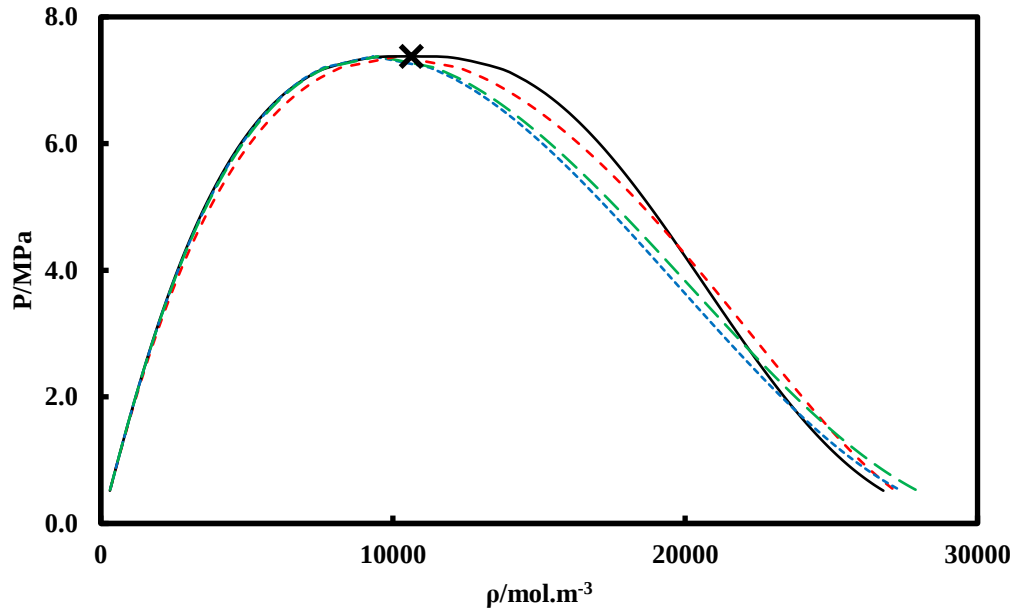

Figure 5.5 P-ρ diagram at saturation for CO_2. (——) REFPROP; (×) Critical Point: REFPROP (T_c=304.13 K); (- - - -) NEoS; (……) PT-EoS; (— — —) PR-EoS.

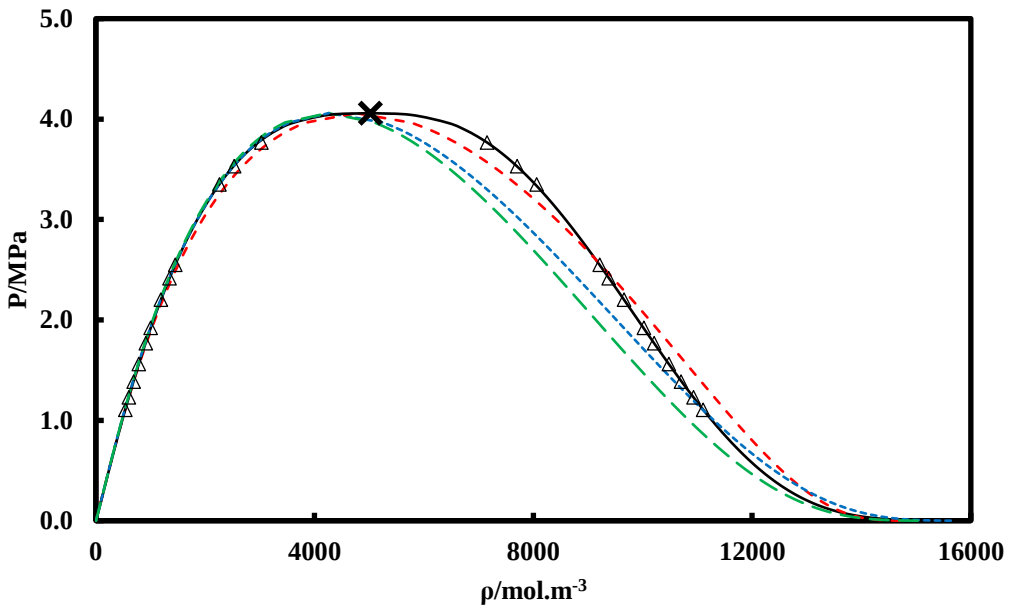

Figure 5.6 P-ρ diagram at saturation for R134a. (Δ) Experimental data (Niesen et al. 1994); (——) REFPROP; (×) Critical Point: REFPROP (T_c=374.21 K); (- - - -) NEoS; (……) PT-EoS; (— — —) PR-EoS.

The ARD and the BIAS were calculated for the results obtained with the EoSs, compared to the results of REFPROP 9.0 (experimental results in the case of R1216). The values obtained for the ARD and the BIAS are reported in Table 5.5.

Table 5.5 ARD and BIAS for pure compounds R1216, CO_2 and R134a.

		ARD (%)			*BIAS (%)*		
Compounds	*CEoS*	*P*	ρ^L	ρ^V	*P*	ρ^L	ρ^V
R1216	NEoS	0.5	5.2	6.2	-0.5	4.0	-4.9
	PT-EoS	0.9	9.9	3.2	-0.9	9.4	-0.8
	PR-EoS	0.6	9.5	3.5	-0.6	8.4	-0.8
CO_2	NEoS	2.7	2.3	5.9	-2.7	-0.2	-5.6
	PT-EoS	3.0	4.4	3.9	-3.0	3.7	-3.2
	PR-EoS	1.4	4.3	2.1	-1.3	1.5	-1.5
R134a	NEoS	4.4	2.8	5.5	4.4	-0.1	4.1
	PT-EoS	3.6	3.3	4.6	3.6	0.4	4.5
	PR-EoS	1.7	4.6	1.0	-1.0	4.6	0.0

From Figure 5.4 to Figure 5.6 and Table 5.5, the same conclusions as for R1234yf can be drawn in the case of R1216, CO_2, and R134a. For these three compounds, the NEoS provides a better representation of the saturated liquid density in general, and especially in the critical region. The PT-EoS and PR-EoS show deviations, relative to experiment and REFPROP, in representing the saturated liquid density, especially in the case of the R1216.

The saturated vapour density and the vapour pressure are well represented by all the three EoSs, with better results obtained when using PR-EoS.

5.2.2. Prediction out of saturation

As for R1234yf, the prediction out of saturation for R1216, CO_2, and R134a was performed for four isotherms, with T_r = 0.73, 0.9, 1, and 1.01 in the case of R1216, T_r = 0.8, 0.9, 1, and 1.1 in the case of CO_2, and T_r = 0.7, 0.9, 1, and 1.1 in the case of R134a.

The graphical representation of the P-ρ diagram for the four isotherms studied out of saturation is shown in *Figure 5.7* to *Figure 5.9*.

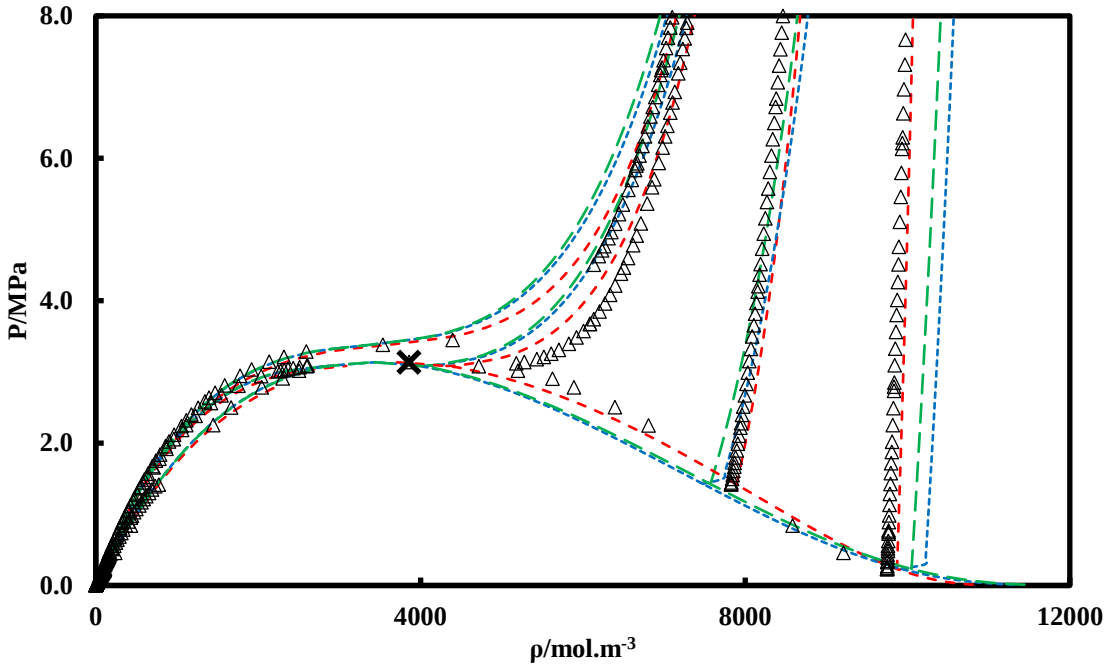

Figure 5.7 P-ρ diagram out of saturation for R1216. (Δ) Experimental data (Coquelet et al. 2010); (×) Critical Point: Experimental (T_c=358.9 K) (Coquelet et al. 2010); (- - - -) NEoS; (……) PT-EoS; (— — —) PR-EoS. Out of saturation: T_r = 0.73, 0.9, 1.0, and 1.01.

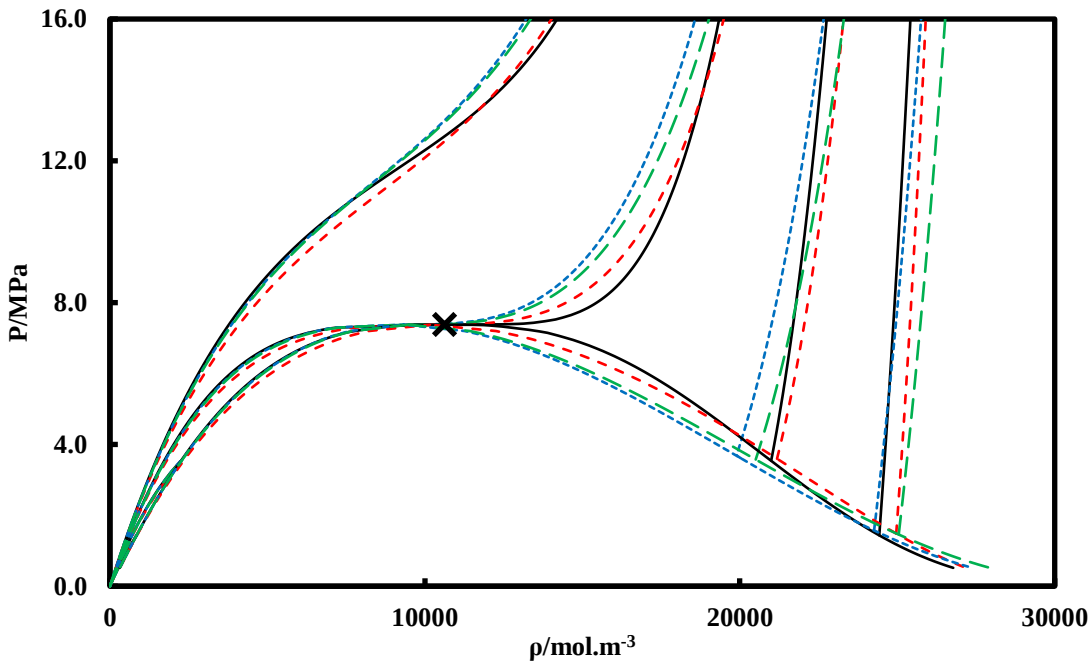

Figure 5.8 P-ρ diagram out of saturation for CO_2. (——) REFPROP; (×) Critical Point: REFPROP (T_c=304.13K); (- - - -) NEoS; (……) PT-EoS; (— — —) PR-EoS. Out of saturation: T_r = 0.8, 0.9, 1.0, and 1.1.

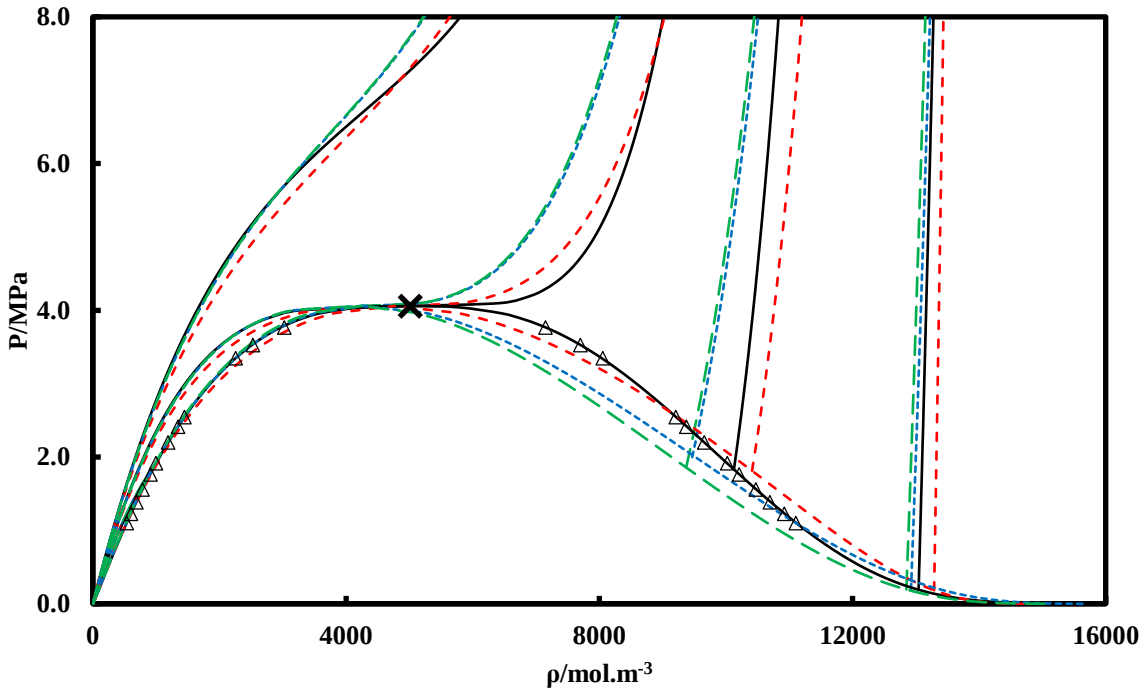

Figure 5.9 P-ρ diagram out of saturation for R134a. (Δ) Experimental data (Niesen et al. 1994); (——) REFPROP; (×) Critical Point: REFPROP (T_c=374.21K); (- - - -) NEoS; (……) PT-EoS; (— — —) PR-EoS. Out of saturation: T_r = 0.7, 0.9, 1.0, and 1.1.

From *Figure 5.7* to *Figure 5.9*, we can see that the NEoS provides a better representation of the liquid density than PT-EoS and PR-EoS. In addition, with the NEoS it is possible to represent accurately the density at supercritical conditions.

In the case of the R1216, we can see that PT-EoS and PR-EoS lead to important deviations in the prediction of the liquid density, relative to the experimental data, while the NEoS results are close to experiment.

For the CO_2 and R-134a, the representation of the liquid density at $T_r = 0.9$ obtained using the NEoS is not in very good agreement with REFPROP results, however, PT-EoS and PR-EoS fail also to reproduce these results.

The vapour phase is in overall well represented by the three EoSs for all the isotherms considered.

5.3. Application of the NEoS to the experimental results

After testing the NEoS on different pure compounds and comparing its results to the other EoSs (PR-EoS and PT-EoS), and the data from the literature and REFPROP 9.0, it was then applied in comparison to the results obtained from our experimental work. First it was used for calculating the vapour pressures of the pure compound refrigerants, then for calculating the density properties of these pure compound refrigerants.

5.3.1. Vapour pressures

5.3.1.1. Pure compound R152a

The first pure compound considered is R152a. The NEoS calculations are compared to the experimental vapour pressures measured during this work, and to the experimental vapour pressures from NIST database.

The graphical representation displayed in Figure 5.10, shows that the results of the prediction are in good agreement with the experimental results measured during this work, and also with the NIST data.

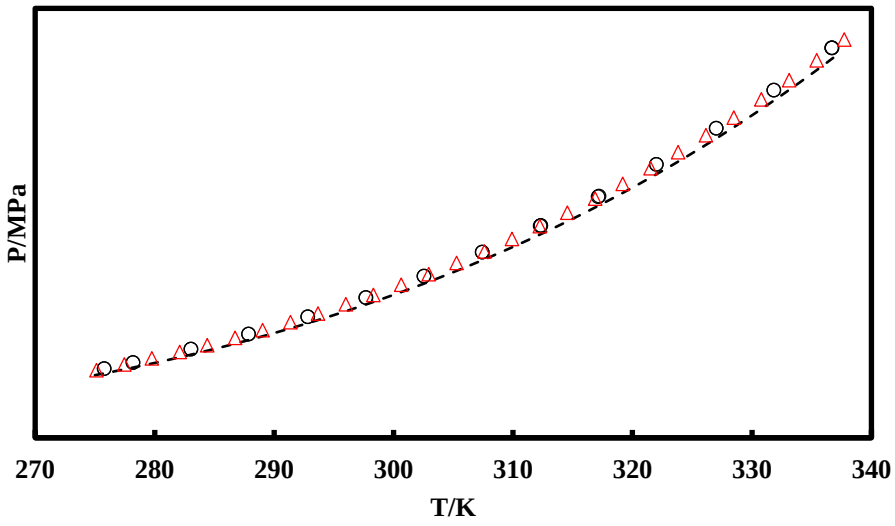

Figure 5.10 Vapour pressures of pure compound R152a. (○) Experimental data (This work); (Δ) Experimental data (NIST); (- - - -) NEoS.

In *Figure 5.11*, we represent the experimental pressure (P_{exp}) as a function of the predicted pressure (P_{cal}), as well as the deviation of the model from the experimental results; (P_{exp} - P_{cal}) as a function of P_{cal}.

We can see from this representation that the NEoS slightly underestimates the vapour pressures of the pure compound R152a, compared to the experimental results, with a maximal deviation of 0.05 MPa.

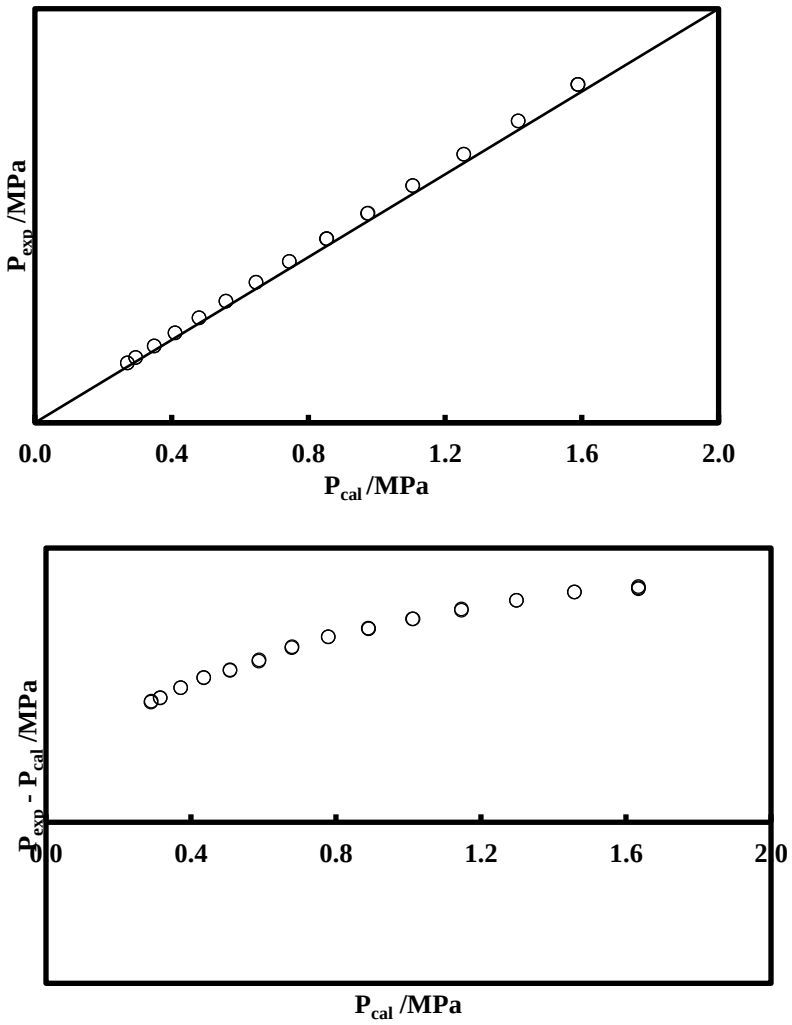

Figure 5.11 Experimental and calculated vapour pressures of the pure compound R152a.

5.3.1.2. Pure compound R1234yf

For the pure compound R1234yf, the prediction within the NEoS are compared to our experimental results, and also to the experimental data obatined from (Hu, L. X. Chen, et al. 2013) work. The calculations are in good agreement with the experimental data, as shown in Figure 5.12.

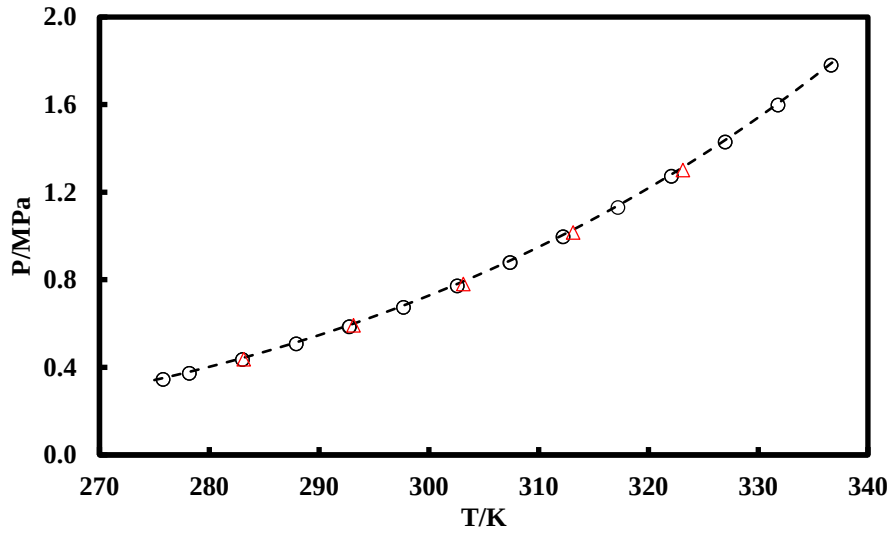

Figure 5.12 Vapour pressures of pure compound R1234yf. (○) Experimental data (This work); (Δ) Experimental data (Hu, L.-X. Chen, et al. 2013); (- - - -) NEoS.

In Figure 5.13, we represent the experimental pressure (P_{exp}) as a function of the predicted pressure (P_{cal}), as well as the deviation of the model from the experimental results, (P_{exp} - P_{cal}) in function of P_{cal}.

We can see from this representation that for the pure compound R1234yf, the NEoS slightly overestimates the vapour pressures, compared to the experimental results, with a maximal deviation of 0.01 MPa.

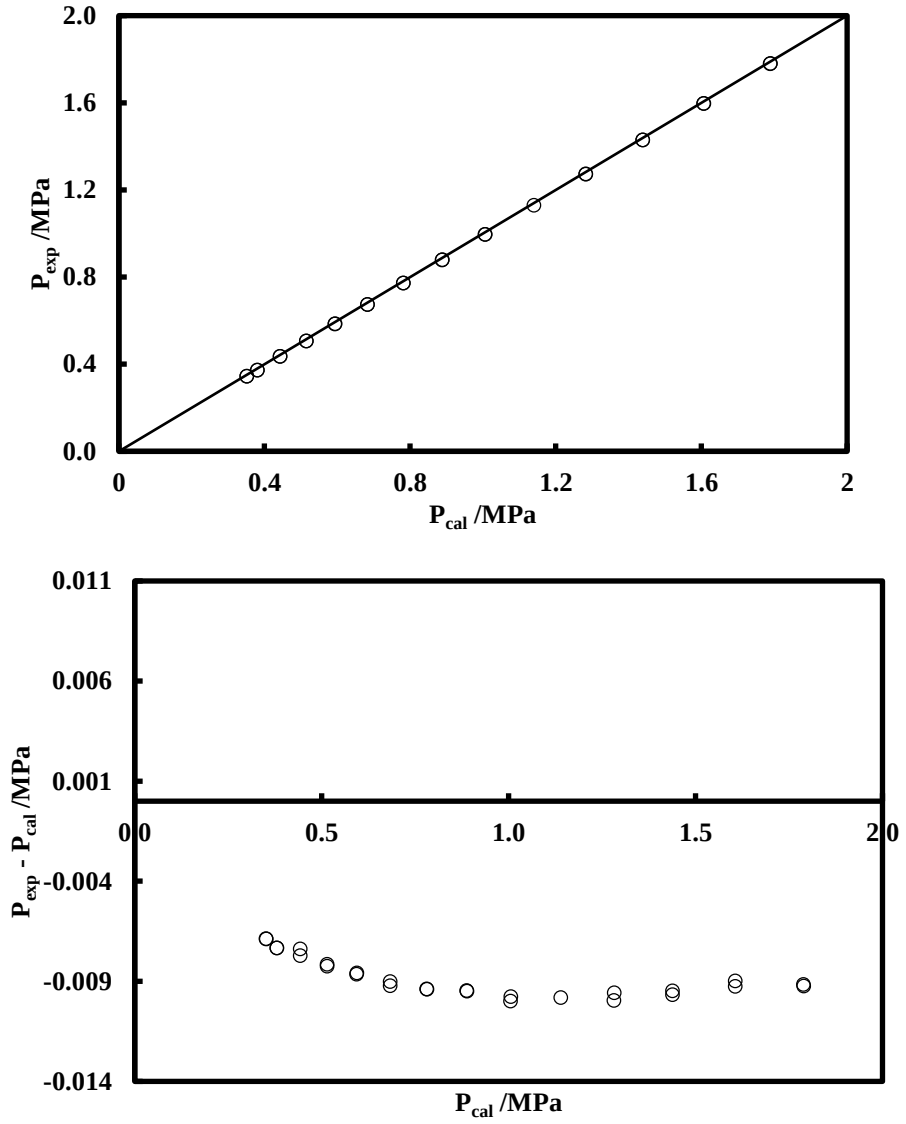

Figure 5.13 Experimental and calculated vapour pressures of the pure compound R1234yf.

5.3.1.3. Pure compound R1233zd(E)

For the pure compound R1233zd(E), the prediction within the NEoS are compared to our experimental results, and also to the experimental data from (Hulse et al. 2012) work. The calculations are in very good agreement with our experimental data, while a slight deviation is observed relative to (Hulse et al. 2012) data. The results of the prediction are dipslayed in Figure 5.14.

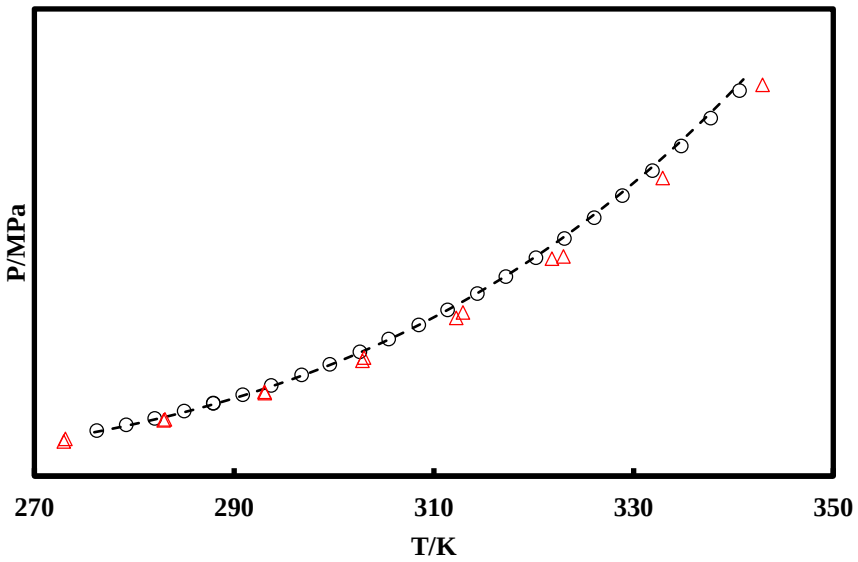

Figure 5.14 Vapour pressures of the pure compound R1233zd(E). (○) Experimental data (This work); (Δ) Experimental data (Hulse et al. 2012); (- - - -) NEoS.

In Figure 5.15, we represent the experimental pressure (P_{exp}) as a function of the predicted pressure (P_{cal}), as well as the deviation of the model from the experimental results, (P_{exp} - P_{cal}) as a function of P_{cal}.

We can see from this representation that the NEoS underestimates the vapour pressures of the R1233zd(E) for pressures up to 0.2 MPa, and overestimates its vapour pressures for higher pressures, with a maximal deviation of 0.01 MPa.

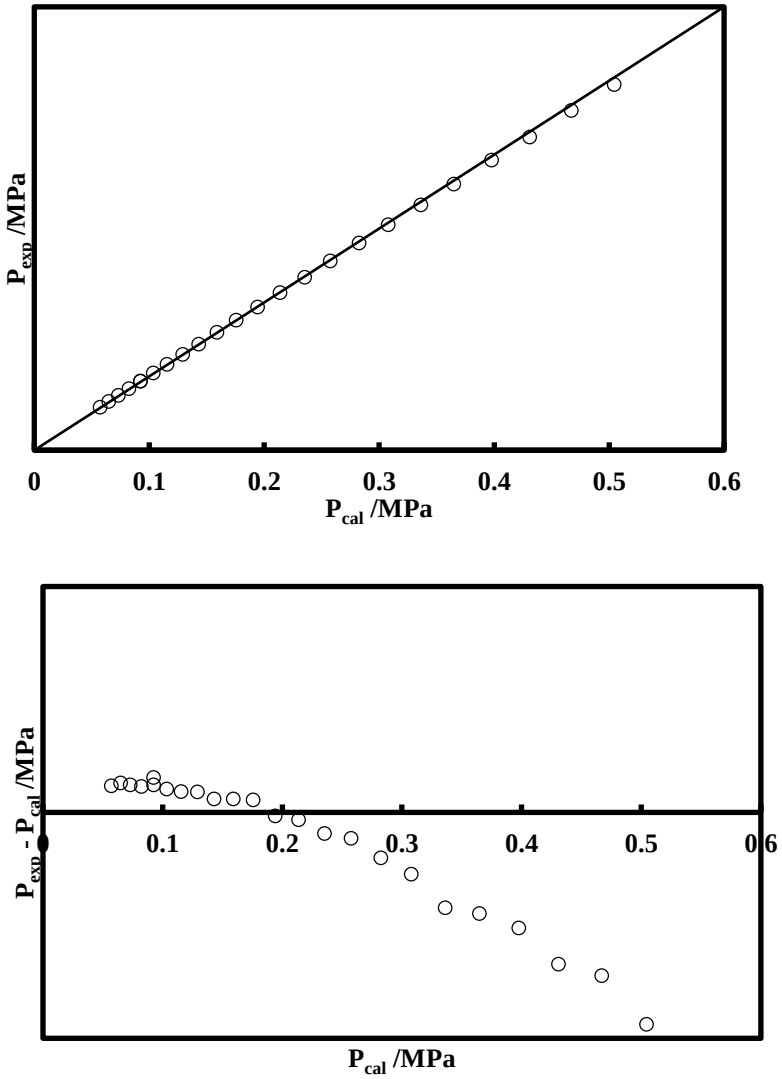

Figure 5.15 Experimental and calculated vapour pressures of the pure compound R1233zd(E).

5.3.1.4. Pure compound R1233xf

For the pure compound R1233xf, the prediction within the NEoS are compared to our experimental results, and also to the experimental data obtained from (Zhang et al. 2013) work. The results of the calculations are in good agreement with the experimental data at very low temperatures, but tends to deviate from the experimental vapour pressures with increasing temperatures. The graphical representation is displayed in Figure 5.16.

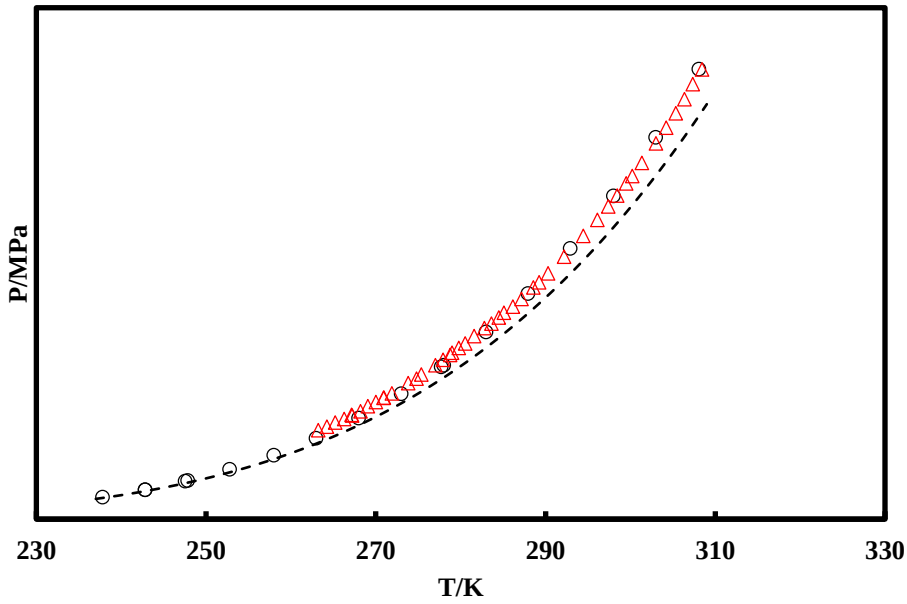

Figure 5.16 Vapour pressures of pure compound R1233xf. (○) Experimental data (This work); (Δ) Experimental data (Zhang et al. 2013); (- - - -) NEoS.

In *Figure 5.17*, we represent the experimental pressure (P_{exp}) as a function of the predicted pressure (P_{cal}), as well as the deviation of the model from the experimental results, (P_{exp} - P_{cal}) in function of P_{cal}.

We can see from this representation that the NEoS underestimates the vapour pressures of the pure compound R1233xf, with a maximal deviation of 0.025 MPa. We can also notice that the deviations increase with the temperature increasing (like if the product in not pure), which can be related to some impurities existing in the product.

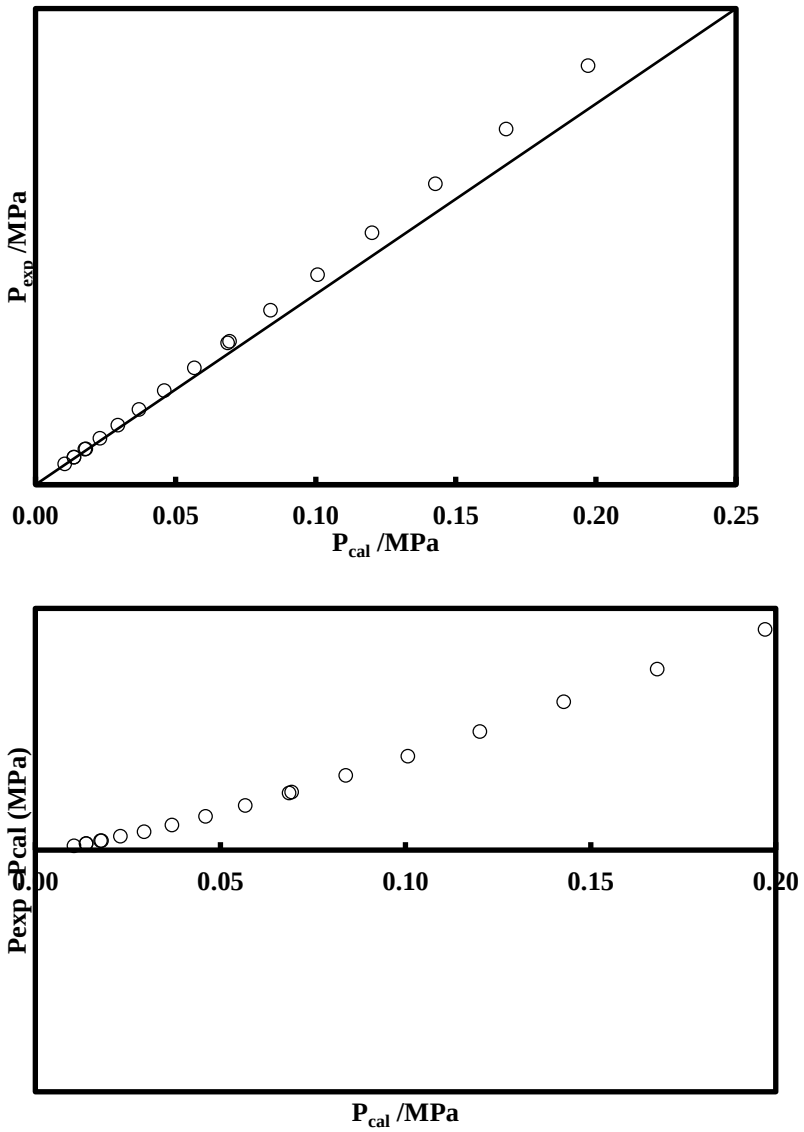

Figure 5.17 Experimental and calculated vapour pressures of the pure compound R1233xf.

5.3.1.5. Pure compound R245fa

For the pure compound R245fa, the NEoS calculations are compared to the experimental results obtained during this work, and to the experimental data from NIST database.

The graphical representation displayed in Figure 5.18 shows that the results of the prediction are in good agreement with the experimental results measured during this work, as well as with the NIST data.

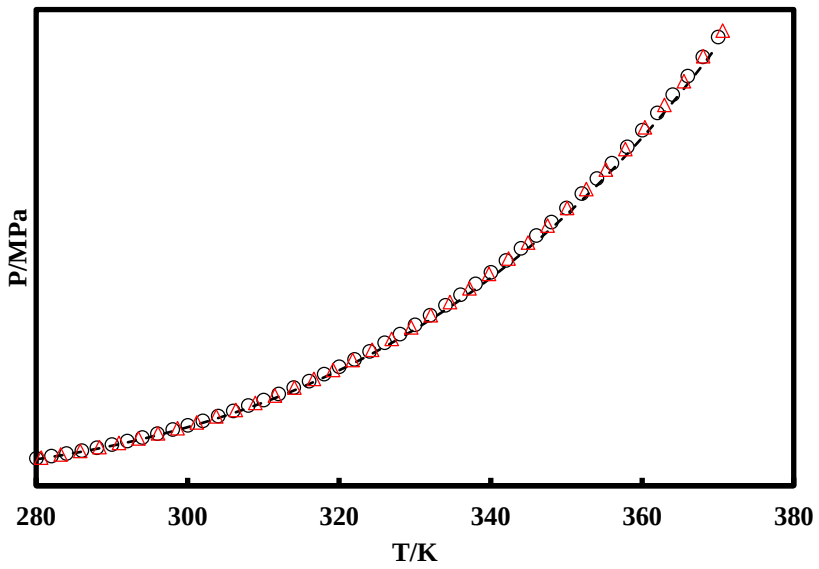

Figure 5.18 Vapour pressures of pure compound R245fa. (○) Experimental data (This work); (Δ) Experimental data (NIST); (- - - -) NEoS.

In *Figure 5.19*, we represent the experimental pressure (P_{exp}) as a function of the predicted pressure (P_{cal}), as well as the deviation of the model from the experimental results, (P_{exp} - P_{cal}) as a function of P_{cal}.

We can see from this representation that the NEoS underestimates the vapour pressures of the pure compound R245fa, with a maximal deviation around 0.02 MPa.

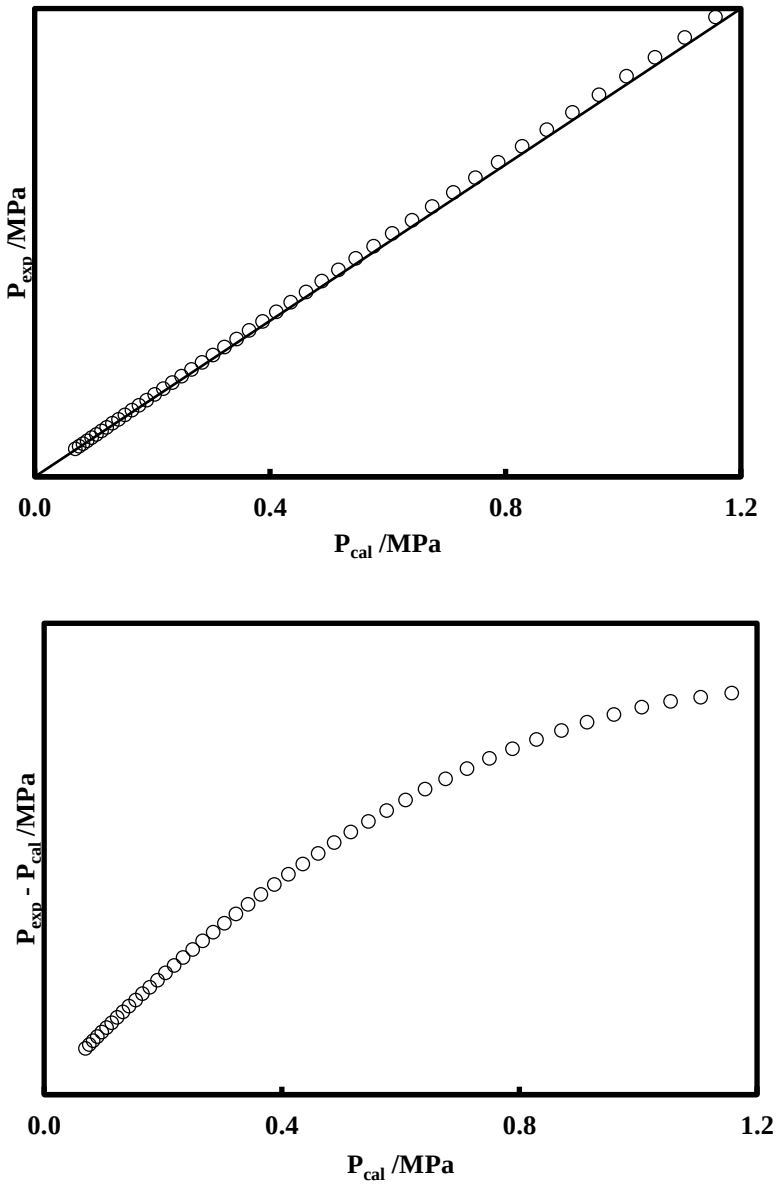

Figure 5.19 Experimental and calculated vapour pressures of the pure compound R245fa.

5.3.2. Density prediction

5.3.2.1. Pure compound R1233xf

The experimental density results of the pure compound R1233xf obtained during this work are compared to the results obtained using the NEoS.

Here an attention is given to the results of the liquid density, which are displayed in *Figure 5.20*.

We can notice that the representation with the NEoS is not in good accordance with the experimental liquid density, especially at the lower temperature (260.48 K) as well as for the higher temperature (332.49 K). Taking into account the experimental uncertainty of 0.2% on the liquid density, the deviation is slightly high for some isotherms and a maximal deviation of 3.9% can be reported.

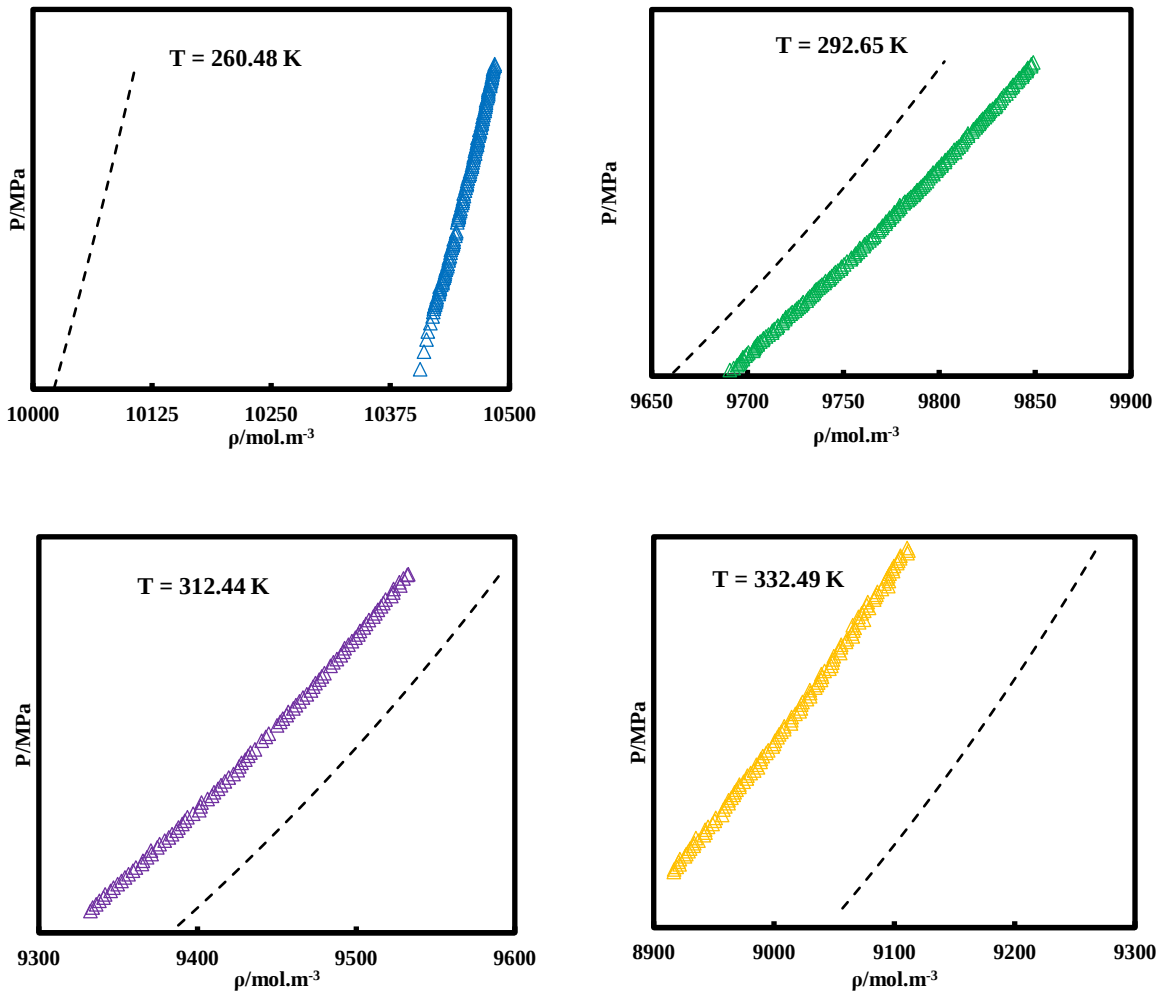

Figure 5.20 Liquid density prediction for pure compound R1233xf. (Δ) Experimental data; (- - - -) NEoS.

5.3.2.2. Pure compound R1233zd(E)

The experimental density results of pure compound R1233zd(E) are compared to the results obtained using the NEoS.

The results of vapour density for the R1233zd(E) are displayed in Figure 5.21. We can notice that we obtain a very good representation with the NEoS for all the temperatures studied.

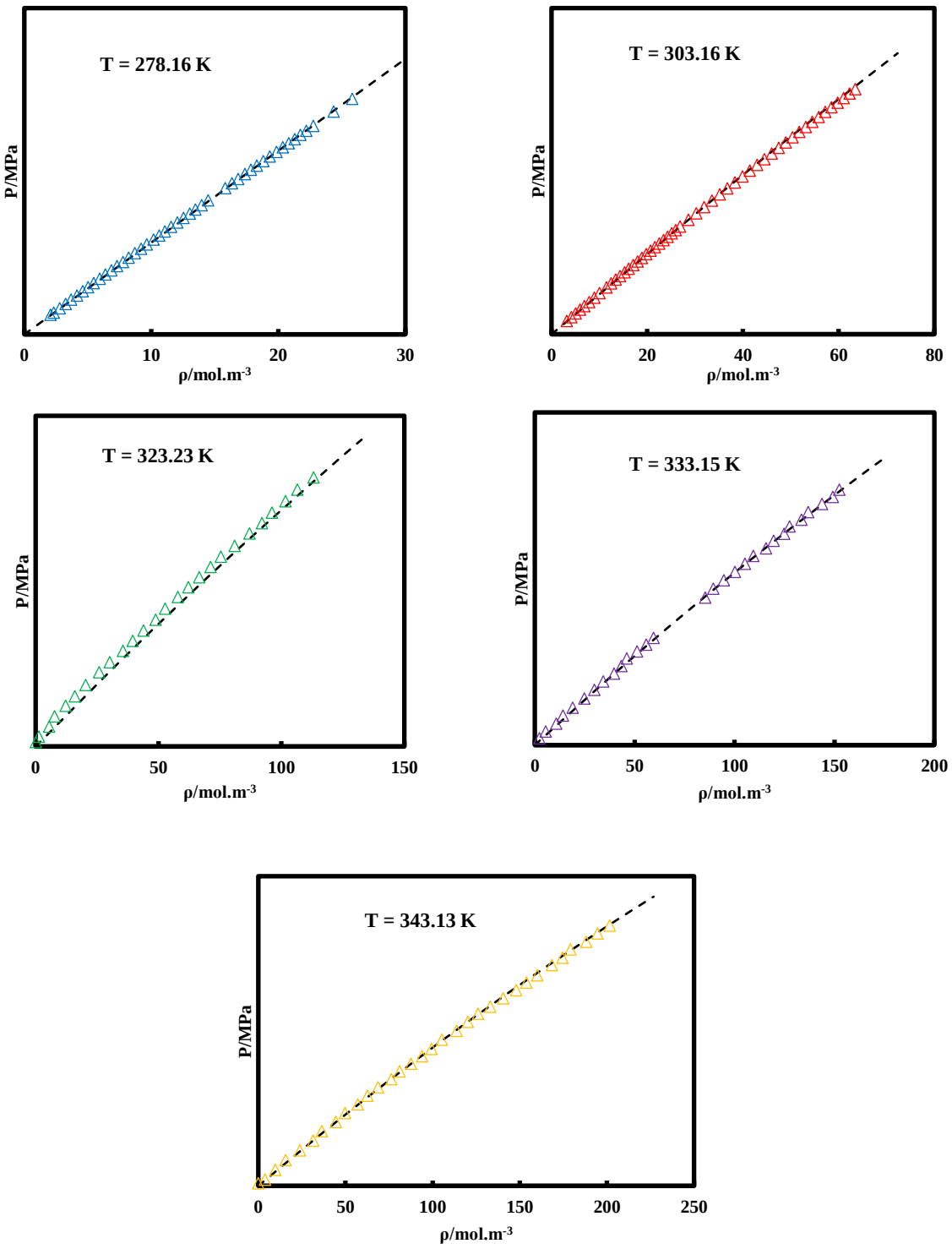

Figure 5.21 Vapour density prediction of pure compound R1233zd(E). (Δ) Experimental data; (- - - -) NEoS.

The results for the liquid density of the pure compound R1233zd(E) are displayed in *Figure 5.22*.

We can notice that the representation with the NEoS is not very good for the liquid density, especially at the lower temperatures (278.16 K, 303.16 K), where we have large deviations from the experimental results. The prediction is more accurate for higher temperatures (at T = 333.15 K and T = 343.13 K).

Taking into account the experimental uncertainty of 0.2% on the liquid density, the deviation is slightly high for some isotherms and a maximal deviation of 3.4% can be reported.

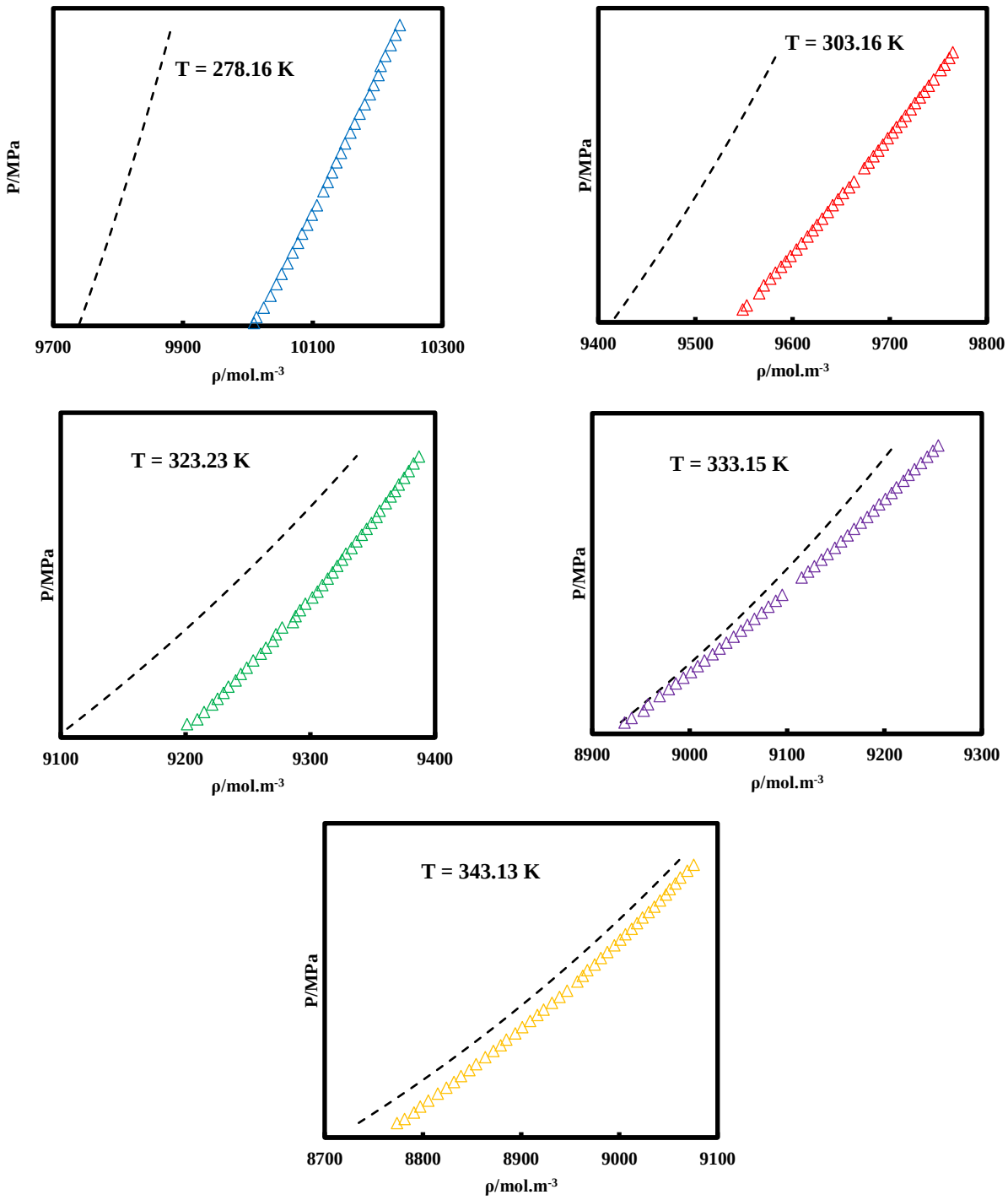

Figure 5.22 Liquid density prediction for pure compound R1233zd(E). (Δ) Experimental data; (- - - -) NEoS.

Concluding remarks

In this Chapter, the results of the prediction using the NEoS was presented for the pure compounds refrigerants.

In a first part, the NEoS was used to predict the density of the pure compounds R1234yf, R134a, R1216 and CO_2 at saturation and out of saturation. The results of the prediction were compared to the data from REFPROP 9.0, and the literature data when available, in addition to a comparison with other cubic EoS (PT-EoS and PR-EoS).

The results obtained show that the NEoS allow better representation for the liquid density at saturation and out of saturation. Also, the representation using the NEoS is better in the vicinity of the critical region, as well as for supercritical isotherms.

In a second part, the NEoS was used to calculate the thermodynamic properties of the pure compounds refrigerants studied experimentally, mainly to predict their vapour pressures, and then to predict their vapour and liquid density out of saturation.

The results of the prediction are very good for the vapour pressures and for the vapour densities. For the liquid densities, the results are in good agreement with experiment at some temperatures (average temperatures), but still not good at low temperatures. Overall, the results obtained are satisfactory, but still some improvements can be made in order to have better prediction for the densities of the single liquid phase.

6. Mixtures modelling

Dans ce chapitre, la nouvelle équation d'état (NEoS) est utilisée pour le calcul des propriétés thermodynamiques des mélanges de réfrigérants. Les propriétés thermodynamiques calculées sont les ELV et les densités.

Dans un premier temps, la NEoS a été utilisée pour le calcul des ELV de six mélanges binaires, en comparaison avec des données expérimentales issues de la littérature. Dans la plupart des cas, le calcul a été fait avec un paramètre d'interaction binaire $k_{ij} = 0$; et les résultats étaient cohérent avec les données expérimentales; sauf pour les systèmes plus complexes (systèmes supercritiques et azéotropiques), où il fallait ajuster le k_{ij} pour avoir une bonne représentation des ELV.

Ensuite la NEoS a été utilisée pour le calcul des densités de trois mélanges (deux binaires et un ternaire), en comparaison avec les résultats de REFPROP 9.0, ainsi qu'avec les résultats obtenus en utilisant les équations d'état de Peng-Robinson et de Patel-Teja. Les trois équations d'état ont été utilisées en mode prédictif, et les résultats obtenus montrent que la NEoS permet une meilleure représentation des densités liquides à saturation et hors saturation. Elle permet aussi de mieux représenter les densités dans la région critique et pour des isothermes supercritiques.

La NEoS a été ensuite utilisée pour représenter les ELV et les densités des systèmes de réfrigérants étudiés expérimentalement durant ce travail. Les mêmes remarques citées précédemment s'appliquent pour les ELV de ces systèmes, avec une bonne représentation même en mode prédictif pour les systèmes relativement simples, et la nécessité d'utiliser un k_{ij} (ajusté sur les données expérimentales) pour bien représenter les systèmes plus complexes (systèmes supercritiques et azéotropiques).

Pour les densités des mélanges de réfrigérants étudiés, la NEoS arrive à bien représenter les densités vapeurs hors saturation. La représentation des densités liquide hors saturation reste dans l'ensemble correcte.

Dans le but d'améliorer les performances de la NEoS, certaines voies s'avèrent intéressantes à explorer plus profondément, notamment par l'utilisation de règles de mélanges plus complexes telles que les règle de mélanges g^E (à noter que les règles de mélanges utilisées dans ce travail sont celles de van-der-Waals), ou bien par l'addition d'un terme polaire pour tenir en compte la polarité des réfrigérants.

Une autre voie d'amélioration serait d'utiliser la NEoS avec une méthode de contribution de groupes, pour calculer un k_{ij} prédictif, de façon similaire à ce qui a été utilisée pour la PPR78 (Jaubert & Mutelet 2004; Jaubert et al. 2005; Privat et al. 2008; Xu, Jaubert, et al. 2015; Xu, Privat, et al. 2015).

Introduction

In this Chapter, the NEoS is applied to the mixtures of refrigerants, to predict the VLE and density properties. In a first part, it was used for VLE prediction of six binary mixtures and compared to the literature data.

Then, it was used to predict the densities properties of three mixtures, in comparison to REFPROP 9.0 results, and also was compared to the results of the calculations obtained using PR-EoS and PT-EoS. For densities prediction, the work was carried out with a binary interaction parameter $k_{ij} = 0$.

In the second part of this Chapter, the NEoS was used to predict the VLE and density properties for the systems studied experimentally during this thesis.

In all this Chapter; if not specified; the alpha function parameters and the critical compressibility factor used for pure compounds are calculated from the correlations developed in Chapter 4.

We need to highlight that some of the contents of this Chapter have already been published and the results presented here closely follows the paper (Coquelet et al. 2016).

6.1. VLE prediction

The VLE prediction was performed for six binary mixtures of refrigerants using the NEoS, and the obtained results were compared to the experimental data. The experimental data used were collected from publically available papers.

For some systems, the binary interaction parameter k_{ij} was set to 0, and we obtained accurate results compared to the experimental ones. For the systems more delicate to model, like the azeotropic ones, we noticed that with k_{ij} set to 0, it is not possible to represent the azeotropic behaviour. An adjusted k_{ij} parameter is thus needed in this case. We can also note that for supercritical temperatures, an adjusted k_{ij} parameter leads to more accurate results than a k_{ij} set to zero.

6.1.1. Quasi ideal systems

For the two systems studied below, we use a $k_{ij} = 0$, since these systems have an almost ideal behaviour, and the intermolecular interactions could be neglected.

We can see from Figure 6.1 and Figure 6.2 that the results of the prediction are in good accordance with the experimental data.

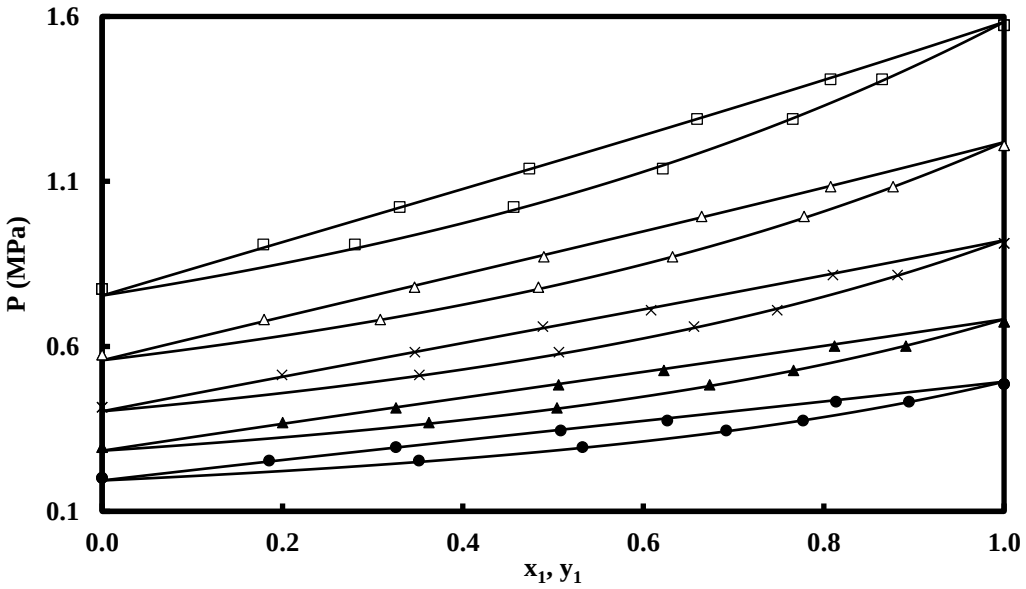

Figure 6.1 VLE prediction for R125 (1) + R134a (2). Experimental data (Kim & Park 1999): (●) 263.15 K; (▲) 273.15 K; (×) 283.15 K; (Δ) 293.15 K; (□) 303.15 K. NEoS: (—) k_{ij} = 0.

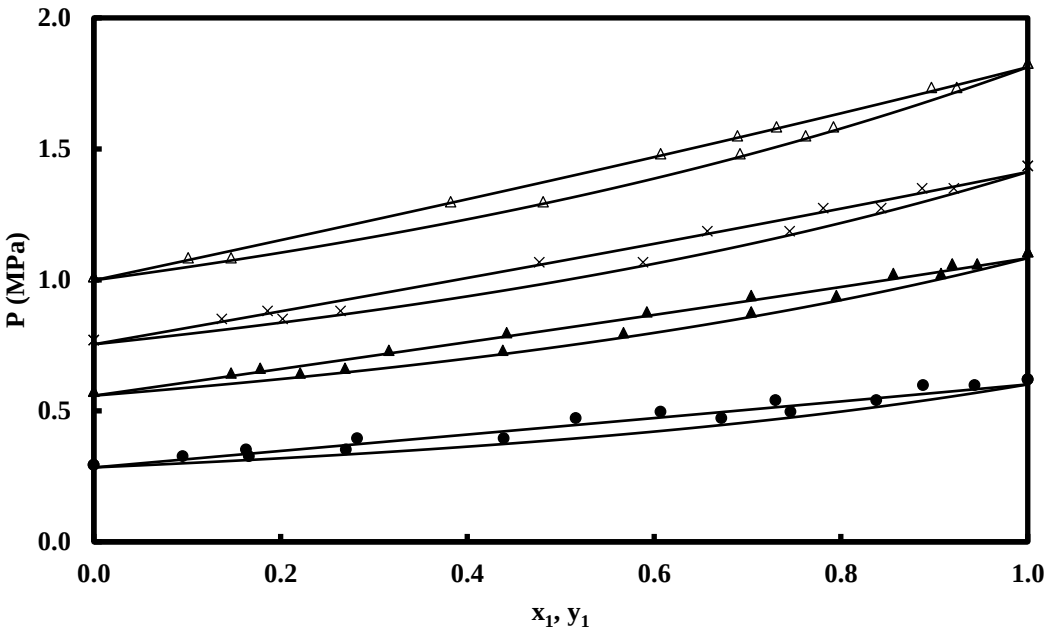

Figure 6.2 VLE prediction for R143a (1) + R134a (2). Experimental data (Lim, J.-Y. Park, et al. 2002): (●) 273.15K; (▲) 293.15K; (×) 303.15 K; (Δ) 313.15 K. NEoS: (—) k_{ij} = 0.

6.1.2. Supercritical Systems

For these systems, we tested the NEoS, with a $k_{ij} = 0$, and with an adjusted k_{ij}, and compared the results obtained.

We can see from Figure 6.3 and Figure 6.4 that the results are very similar with and without a k_{ij} for subcritical temperatures and no high improvement can be noticed.

For the supercritical isotherms, the results are improved when using an adjusted k_{ij}, the representation accurately agrees with the experimental data, and we obtain a good representation of the critical composition for the systeme (R32 + SO_2). For the system (CO_2 + R32), the critical region is not very well represented. We can notice that by replacing SO_2 by CO_2, the representation is less good, which could be due to the inversion of the critical temperatures, as the critical temperature of R32 (351.26 K (Lemmon et al. 2010)) is lower than the critical temperature of SO_2 (430.64 K (Lemmon et al. 2010)) but higher than the critical temperature of CO_2 (304.13 K (Lemmon et al. 2010)).

The values of the k_{ij} used for the NEoS, in comparison to the values obtained if we use PR-EoS are reported in Table 6.1.

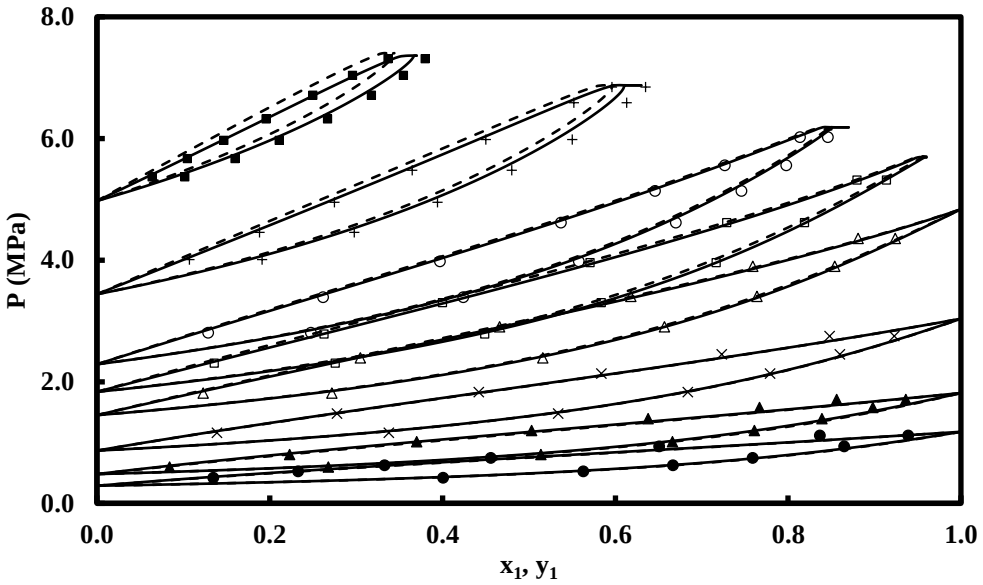

Figure 6.3 VLE prediction for R32 (1) + SO_2 (2). Experimental data (Valtz et al. 2004): (●) 288.07 K; (▲) 303.16 K; (×) 323.15 K; (Δ) 343.15 K; (□) 353.15 K; (○) 363.15 K; (+) 383.18 K; (■) 403.16 K. NEoS: (- - - -) $k_{ij} = 0$; (——) k_{ij} adjusted.

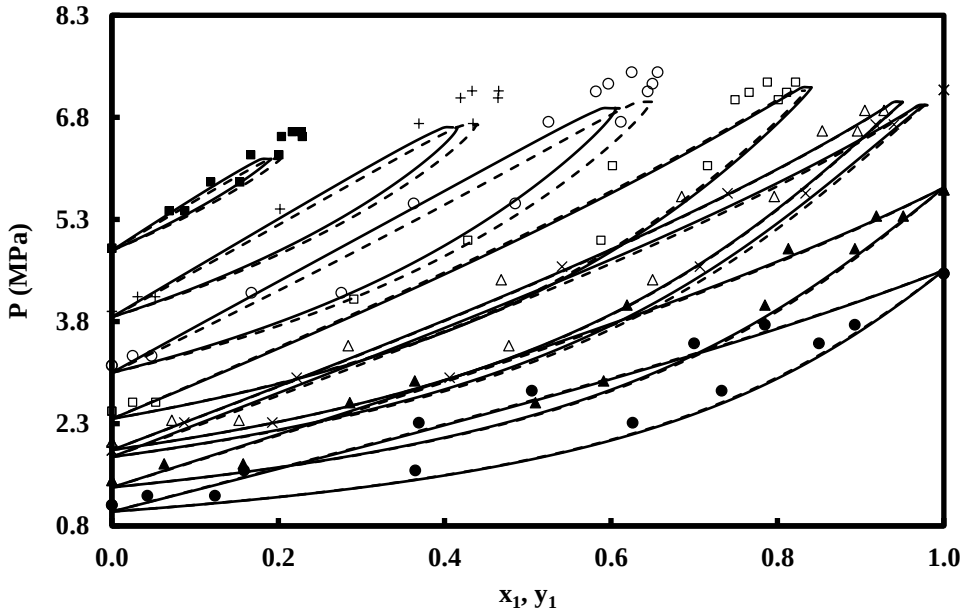

Figure 6.4 VLE prediction for CO_2 (1) + R32 (2). Experimental data (Rivollet et al. 2004): (●) 283.12 K; (▲) 293.11 K; (×) 303.13 K; (Δ) 305.15 K; (□) 313.30 K; (○) 323.34 K; (+) 333.33 K; (■) 343.23 K. NEoS: (- - - -) $k_{ij} = 0$; (——) k_{ij} adjusted.

6.1.3. Azeotropic Systems

For these systems, we tested the NEoS, with a $k_{ij} = 0$, and with an adjusted k_{ij}, and compared the results obtained.

We can see from *Figure 6.5* and *Figure 6.6*, that an adjusted k_{ij} is required in order to have an accurate representation of the phase diagram of these binary systems.

The values of the k_{ij} used for the NEoS, in comparison to the values obtained if we use PR-EoS are reported in *Table 6.1*.

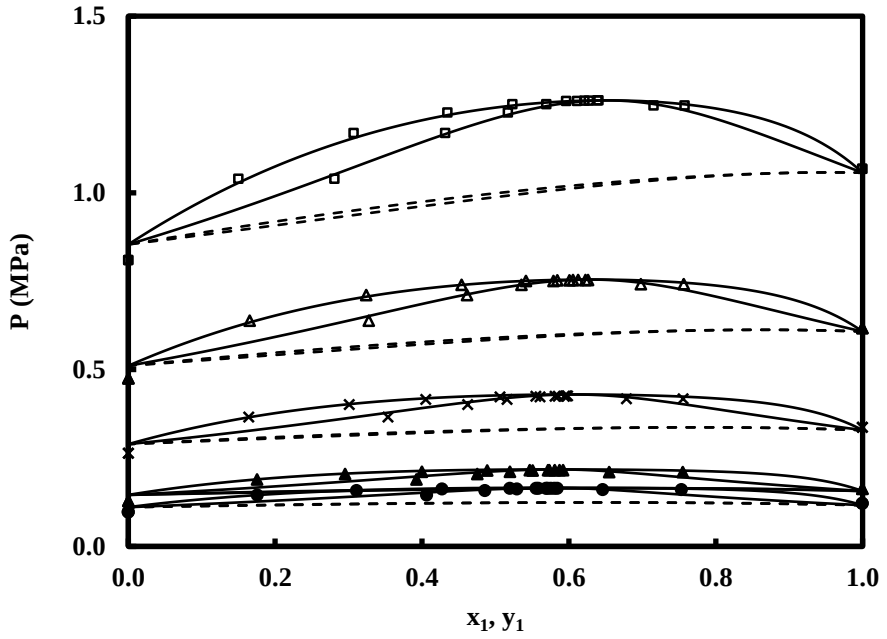

Figure 6.5 VLE prediction for R23 (1) + R116 (2). Experimental data (Zhang et al. 2008): (●) 194.33 K; (▲) 199.71 K; (×) 214.19 K; (Δ) 229.63 K; (□) 244.94 K. NEoS: (- - - -) $k_{ij} = 0$; (——) k_{ij} adjusted.

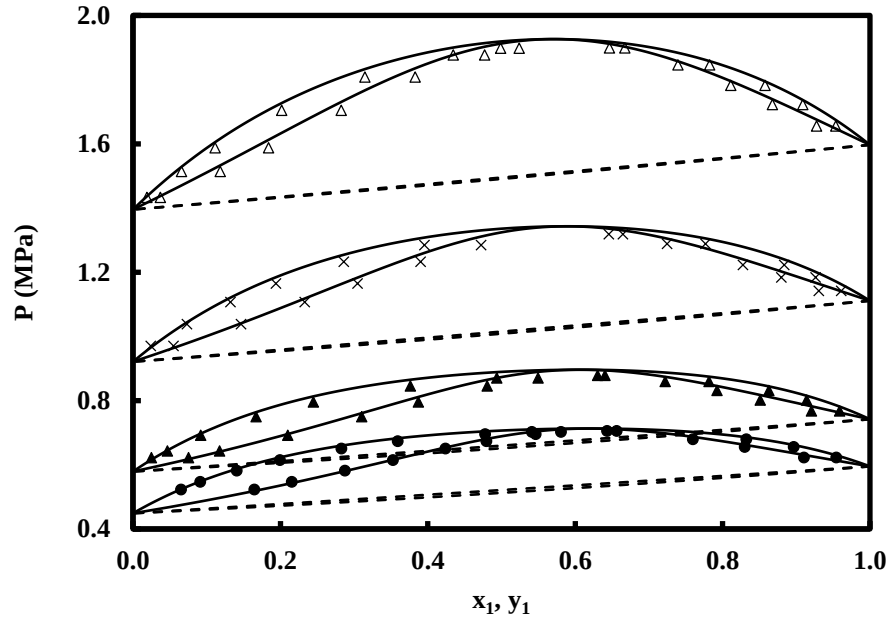

Figure 6.6 VLE prediction for Isopentane (1) + R365mfc (2). Experimental data (ElAhmar et al. 2012): (●) 363.12 K;(▲) 373.20 K; (×) 393.22 K; (Δ) 413.09 K. NEoS: (- - - -) $k_{ij} = 0$; (——) k_{ij} adjusted.

Table 6.1 k_{ij} values used with the NEoS and PR-EoS, for supercritical and azeotropic systems.

		Binary interaction parameter k_{ij}	
Systems	*T/K*	*NEoS*	*PR-EoS*
SO_2 + R32	288.07	0.0030	-0.0189
	303.16	0.0044	-0.0152
	323.15	0.0008	-0.0183
	343.15	-0.0035	-0.0191
	353.15	-0.0067	-0.0205
	363.15	-0.0031	-0.0188
	383.18	-0.0082	-0.0036
	403.16	-0.0165	-0.0133
CO_2 + R32	283.12	-0.0023	0.0196
	293.11	0.0030	0.0212
	303.13	0.0068	0.0373
	305.15	0.0008	0.0167
	313.30	-0.0028	0.0174
	323.34	0.0189	0.0276
	333.33	0.0119	0.0363
	343.23	0.0129	0.0600
R23 + R116	194.33	0.0890	0.1025
	199.71	0.0901	0.1033
	214.90	0.0907	0.1043
	229.63	-	0.1068
	244.94	-	-
Isopentane + R365mfc	363.12	0.1168	0.1233
	393.22	0.1161	0.1250
	373.20	0.1189	0.1261
	413.09	0.1111	0.1218

From *Table 6.1*, we can note that lower k_{ij} values are generally obtained when using the NEoS compared to PR-EoS. These k_{ij} values are represented as a function of temperature in *Figure 6.7* to *Figure 6.10*, for the four systems for which an adjusted k_{ij} value was used.

From these figures, we can note a correlation between k_{ij} and the temperature, with the NEoS and PR-EoS, for the different binary systems considered here.

For the systems whose one component has its critical temperature in the range considered (*Figure 6.7* and *Figure 6.8*), we can see a discontinuity of the $k_{ij}(T)$ function: two correlations have thus been employed for these latter systems, depending on if we are below or above the critical temperature. For the CO_2 + R32 system (Figure 6.7), we can note that the correlation between k_{ij} and the temperature is not very good above the critical temperature of CO_2 with the NEoS, while it is better with PR-EoS (coefficients of determination respectively equal to 0.58 and 0.99).

For the (SO_2 + R32) system (Figure 6.8), in the case of the NEoS, there is a strong correlation between k_{ij} and the temperature, both below and above the critical temperature of CO_2 (both coefficients of determination around 0.96), while with the PR-EoS, the correlation is weaker (coefficients of determination equal to 0.51 and 0.78, respectively below and above the critical temperature).

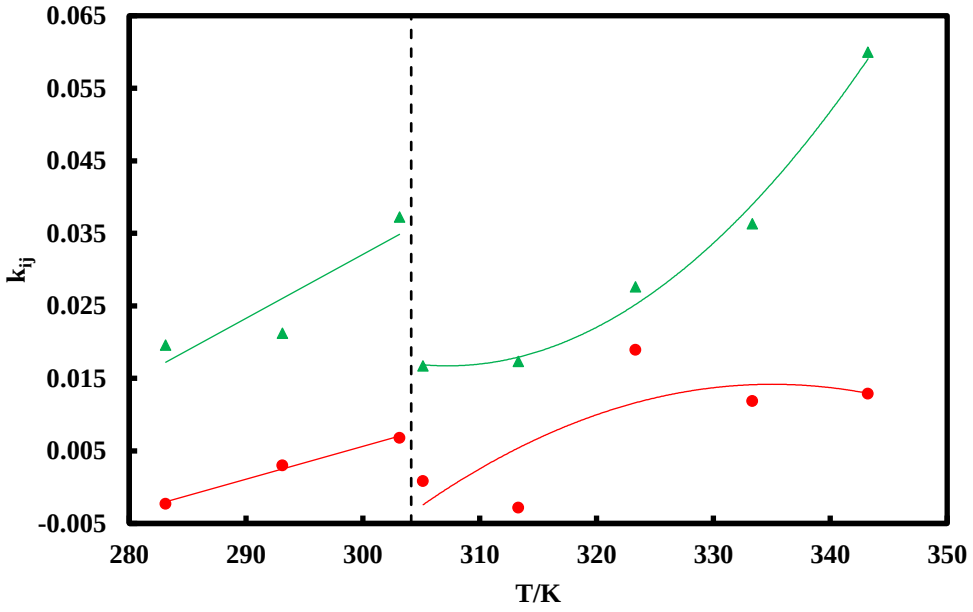

Figure 6.7 k_{ij} as a function of temperature: (CO_2 + R32). (●) NEoS; (▲) PR-EoS; (- - - -) CO_2 critical temperature (T_c = 304.13 K).

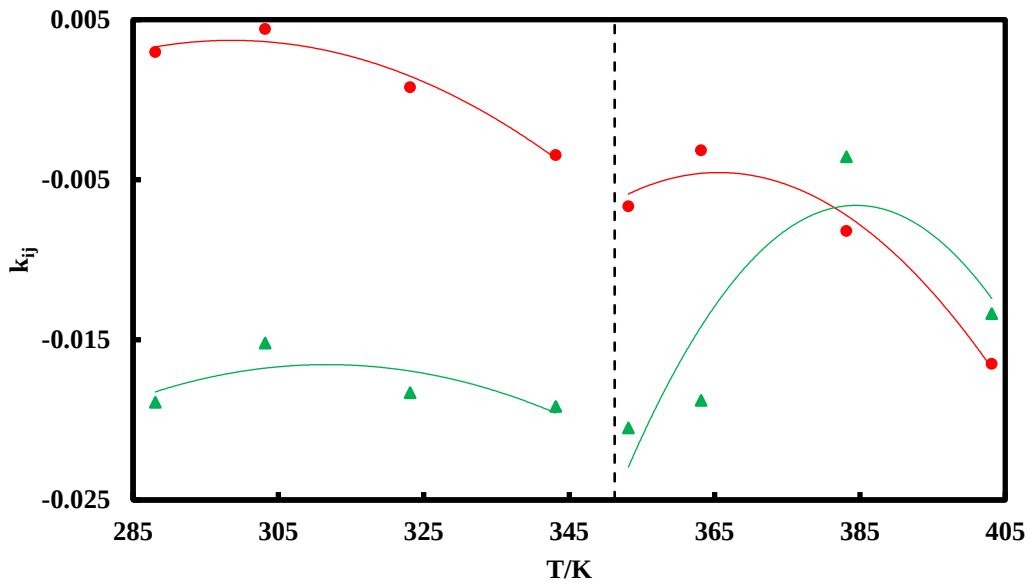

Figure 6.8 k_{ij} as a function of temperature: (R32 + SO_2). (●) NEoS; (▲) PR-EoS; (- - - -) R32 critical temperature (T_c = 351.26 K).

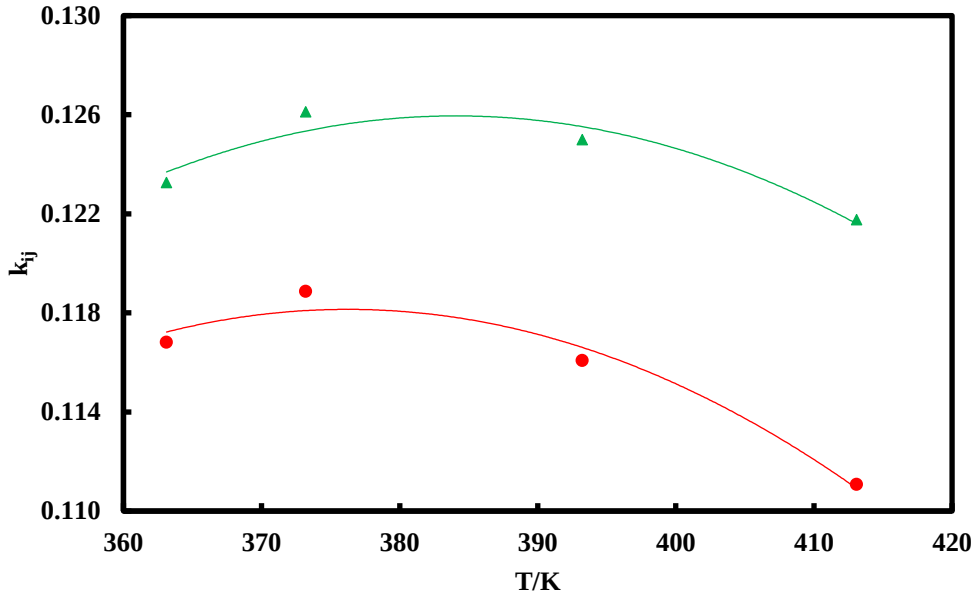

Figure 6.9 k_{ij} as a function of temperature: (Isopentane + R365mfc). (●) NEoS; (▲) PR-EoS.

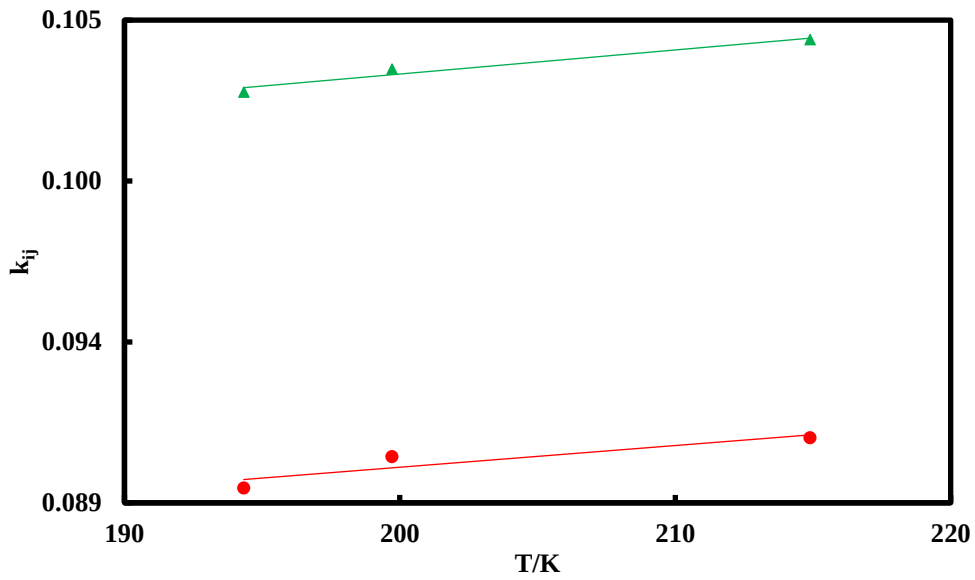

Figure 6.10 k_{ij} as a function of temperature: (R23 + R116). (●) NEoS; (▲) PR-EoS.

Based on these results, we can deduce that considering an adjusted binary interaction parameter k_{ij} is necessary to model accurately the VLE behaviour of some systems (azeotropic and supercritical systems), due to the intermolecular interactions occurring in these systems.

6.2. Density prediction

The density prediction was performed for two binary mixtures and one ternary mixture of refrigerants using the NEoS, and the obtained results were compared to the results from REFPROP 9.0, along the results obtained using PR-EoS and PT-EoS. For the three EoSs considered, we used a $k_{ij} = 0$.

In this section, we present the results of the prediction obtained.

6.2.1. Binary mixtures: R421A and R508A

Based on the correlations and the parameters calculated for the pure compounds, we studied the two binary systems:

- R421A, which is a mixture at fixed composition of R125 (58 wt%) and R134a (42 wt%).
- R508A which is a mixture at fixed composition of R23 (39 wt%) and R116 (61 wt%).

The prediction was performed using the three above-mentioned EoSs, associated with the MC alpha function. The MC-alpha function parameters and the critical compressibility factor were calculated from the correlations established in Chapter 4 and their values are reported in

Table 6.2.

Table 6.2 Calculated parameters for R125, R134a, R23, and R116 (m_2 and m_3 are set to fixed values).

CEoS	*Compound*	m_1	m_2	m_3	$Z_{c,opt}$
NEoS	R125	0.48777	0.47	-0.08	0.28208
	R134a	0.52074	0.47	-0.08	0.27424
	R23	0.43097	0.47	-0.08	0.27239
	R116	0.42322	0.47	-0.08	0.29217
PT-EoS	R125	0.78021	-0.01	0.4	0.30689
	R134a	0.81773	-0.01	0.4	0.29936
	R23	0.71684	-0.01	0.4	0.29750
	R116	0.70837	-0.01	0.4	0.31543
PR-EoS	R125	0.79107	0	0.49	0.30740[a]
	R134a	0.82227	0	0.49	0.30740
	R23	0.72999	0	0.49	0.30740
	R116	0.72069	0	0.49	0.30740

[a] For PR-EoS, the value of Z_c is set to 0.30740.

The predicted pressure-density diagrams are shown in Figure 6.11 and Figure 6.12, together with the results obtained from REFPROP 9.0. The prediction out of saturation was performed for four isotherms: T_r = 0.7, 0.9, 1.0, 1.1. The critical temperatures are 355.93 K for R421A and 283.34 K for R508A (Lemmon et al. 2010).

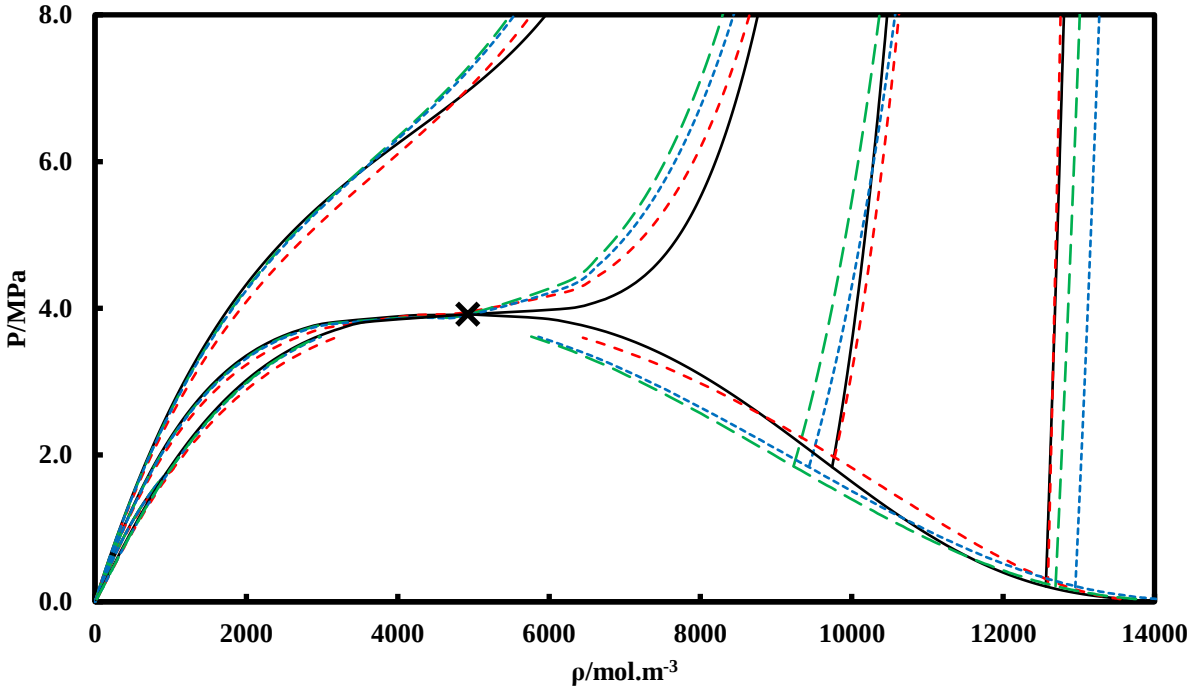

Figure 6.11 P-ρ diagram for R421A. (——) REFPROP; (×) Critical Point: REFPROP (T_c = 355.93 K); (- - - -) NEoS; (……) PT-EoS; (— — —) PR-EoS. Out of saturation: T_r = 0.7, 0.9, 1.0, 1.1.

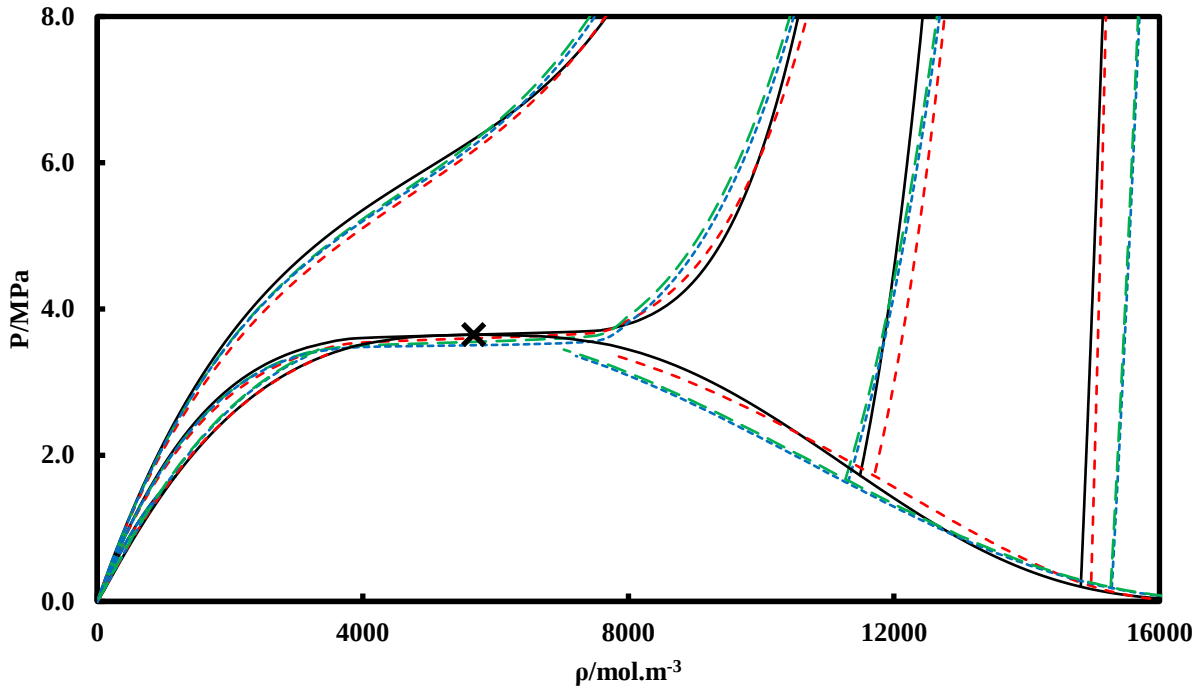

Figure 6.12 P-ρ diagram for R508A. (——) REFPROP; (×) Critical Point: REFPROP (T_c = 283.34K); (- - - -) NEoS; (……) PT-EoS; (— — —) PR-EoS. Out of saturation: T_r = 0.7, 0.9, 1.0, 1.1.

From Figure 6.11 and Figure 6.12, we can see that the NEoS provides a better representation for the liquid density, both at saturation and out of saturation, especially at low (T_r = 0.7) and critical temperatures, for the two systems R421A and R508A. Note that PR-EoS and PT-EoS fail to represent accurately the liquid densities of the two systems considered here at saturation, and at T_r = 0.7 and T_r = 1.0, while the vapour densities out of saturation appear to be well represented by the three EoSs.

However, for the vapour density at saturation, we can see from Table 6.3 that the deviations to REFPROP 9.0 results are quite large for the R421A. For the R508A, the deviations are smaller, and we obtain the best results with the NEoS, compared to PR-EoS and PT-EoS.

For the R421A, for T_r = 1.0, the results predicted by the three EoSs don't match very well the REFPROP 9.0 results when increasing pressure, however, the best agreement is obtained with the NEoS, relative to PR-EoS and PT-EoS. For the R508A, for T_r = 0.9, PR-EoS and PT-EoS provide results in slightly better agreement with REFPROP 9.0 results, compared to the NEoS.

Table 6.3 ARD and BIAS for the binary mixtures R421A and R508A.

		ARD (%)			*BIAS (%)*		
Compounds	*CEoS*	*P*	ρ^L	ρ^V	*P*	ρ^L	ρ^V
R421A	NEoS	1.1	2.4	23.2	-0.4	-1.8	-23.2
	PT-EoS	1.5	3.6	22.7	-1.4	0.5	-22.7
	PR-EoS	1.4	3.3	22.2	-1.3	2.5	-22.2
R508A	NEoS	1.0	1.7	1.7	-0.4	-1.1	1.0
	PT-EoS	1.9	2.7	5.3	1.0	0.4	4.9
	PR-EoS	2.9	2.8	8.6	2.9	-0.4	8.6

6.2.2. Ternary mixture: R404A

In this section, we study the ternary system R404A, which is a mixture of R125 (44 wt%), R134a (4 wt%), and R143a (52 wt%). The same work as described in section 6.2.1 for the binary mixtures was carried out for the R404A system.

The prediction was performed using the three EoSs presented above, associated with the MC alpha function. The MC alpha function parameters and the critical compressibility factor were calculated with the correlations established (Cf. Table 6.4).

Table 6.4 Calculated parameters for the R125, R134a and R143a (m_2 and m_3 are set to fixed values).

CEoS	*Compound*	m_1	m_2	m_3	$Z_{c,opt}$
NEoS	R125	0.48777	0.47	-0.08	0.28208
	R134a	0.52074	0.47	-0.08	0.27424
	R143a	0.42914	0.47	-0.08	0.26906
PT-EoS	R125	0.78021	-0.01	0.4	0.30689
	R134a	0.81773	-0.01	0.4	0.29936
	R143a	0.71483	-0.01	0.4	0.29409
PR-EoS	R125	0.79107	0	0.49	0.30740[a]
	R134a	0.82227	0	0.49	0.30740
	R143a	0.72781	0	0.49	0.30740

[a] For the PR-EoS, the value of Z_c is set to 0.30740.

The results of the prediction for the pressure-density diagram were compared to the results obtained from REFPROP 9.0. (Cf. Figure 6.13). The prediction out of saturation was performed for four isotherms: T_r = 0.7, 0.9, 1.0, 1.1. The critical temperature of the R-404A is estimated to be T_c = 345.2 K (Lemmon et al. 2010).

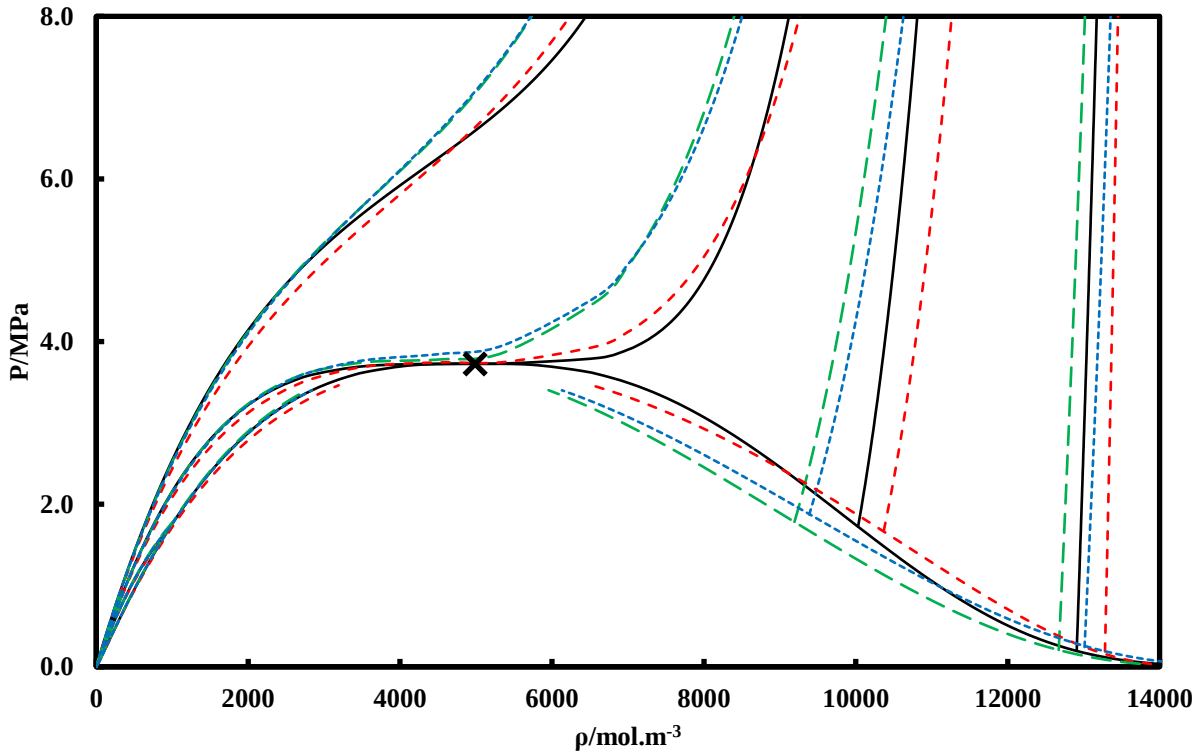

Figure 6.13 P-ρ diagram for R404A. (——) REFPROP; (×) Critical Point: REFPROP (T_c=345.2 K); (- - - -) NEoS; (……) PT-EoS; (— — —) PR-EoS. Out of saturation: T_r = 0.7, 0.9, 1.0, 1.1.

For the ternary mixture R404A, and as we can see from Figure 6.13, the NEoS gives a good representation of the density at the critical and supercritical temperatures, compared to PT-EoS and PR-EoS, but the NEoS results are less satisfactory at subcritical temperatures for liquid density. However, the saturation liquid density is well represented by using the NEoS, relative to the other two EoSs.

For T_r = 0.7, the PT-EoS provides results in better agreement with REFPROP results, compared to PR-EoS and the NEoS.

For T_r = 0.9, the three EoSs fail to represent accurately the liquid density. The vapour density appears to be well represented by the three EoSs for all the isotherms considered.

However, for the vapour density at saturation, and as we can see from

Table 6.5, the deviations to REFPROP are quite large with the three EoSs.

Table 6.5 ARD and BIAS for the ternary mixture R404A.

		ARD (%)			*BIAS (%)*		
Compounds	*CEoS*	*P*	ρ^L	ρ^V	*P*	ρ^L	ρ^V
R404A	NEoS	1.6	2.3	5.8	-1.6	-1.1	-5.8
	PT-EoS	2.6	3.7	5.3	-2.6	1.3	-5.3
	PR-EoS	4.7	5.4	6.6	-4.7	5.4	-6.6

6.3. Application to experimental results

6.3.1. VLE prediction

In this section, we use the NEoS to represent the phase diagrams for the different systems studied experimentally during this work, in order to compare its accuracy with our experimental data.

When we use the term "predictive" for the alpha function parameters, we refer to the parameters calculated from the correlations developed in Chapter 4. Also, when we use the term "predictive" for the binary interaction parameter k_{ij}, it means that $k_{ij} = 0$.

6.3.1.1. Binary mixture (R134a + R1233zd(E))

For the binary mixture (R134a + R1233zd(E)), the prediction was performed with a $k_{ij} = 0$ and compared with the results obtained using an adjusted k_{ij}, fitted on the experimental data for each of the two isotherms considered. The results of the prediction are displayed in *Figure 6.14*.

From the results obtained with a $k_{ij} = 0$, we can notice deviations from the experimental results, the curves are slightly shifted, and the shape of the curves is slightly different.

When using an adjusted k_{ij}, the results are much accurate, and correspond well to the experimental data.

We can see however that the vapour pressure of the R134a, is a little underestimated in both cases, which can be related to the use of predictive alpha function parameters.

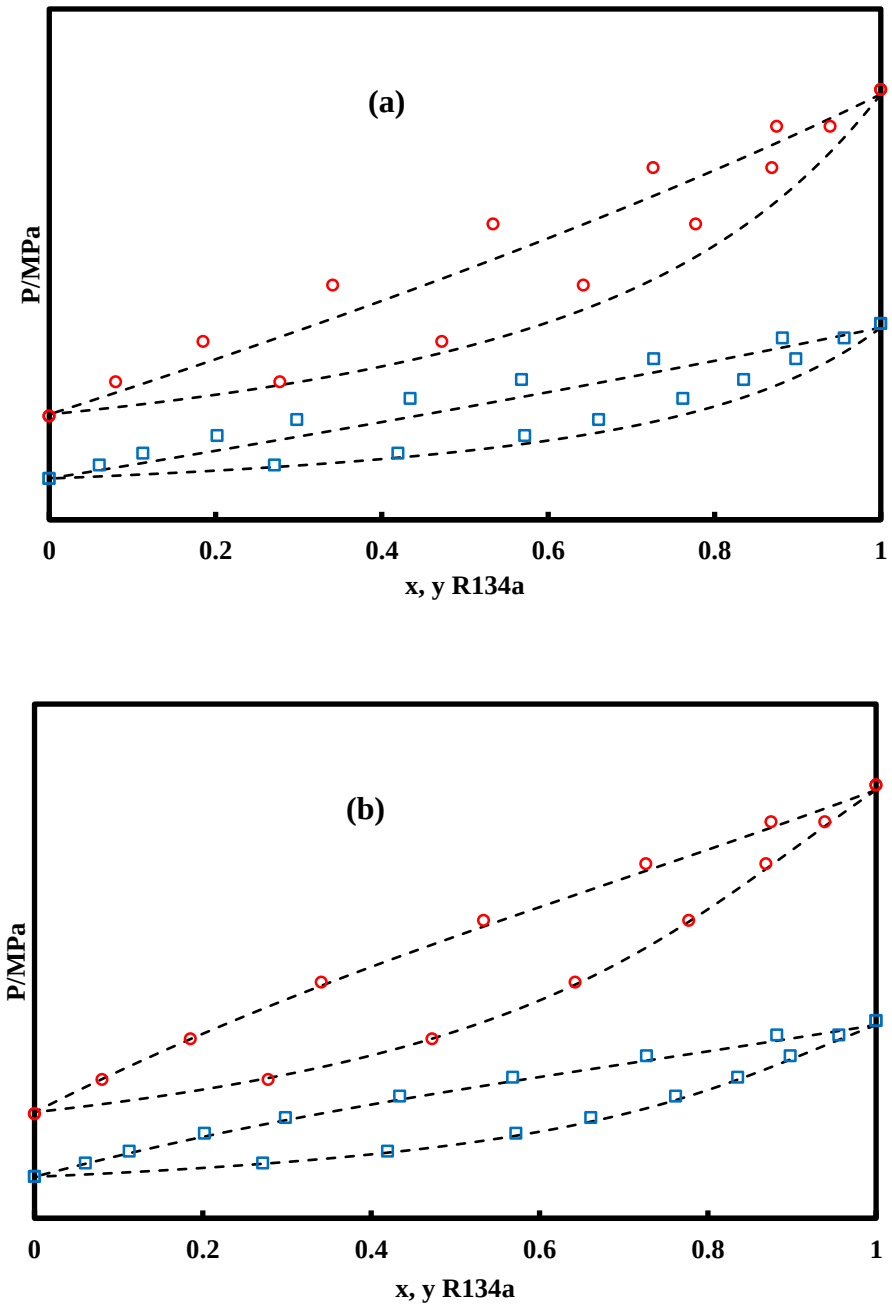

Figure 6.14 VLE prediction for binary mixture (R134a + R1233zd(E)). (a): With k_{ij} = 0. (b): With k_{ij} adjusted. (□) 303.07 K; (○) 333.23 K.; (- - - -) NEoS.

This finding can be supported by calculating the deviations on the bubble pressure and the vapour molar composition.

The results reported in

Table 6.6 show clearly that the results are better when using an adjusted k_{ij}, with smaller deviations from the experimental results.

Table 6.6 ARD and BIAS for the binary mixture (R134a + R1233zd(E)).

T/K	k_{ij}	*ARD P (%)*	*ARD yR134a (%)*	*BIAS P (%)*	*BIAS yR134a (%)*
303.07	0	11.3	7.7	11.3	7.1
333.23		8.6	6.9	8.2	6.0
303.07	0.0411	2.5	0.7	2.5	0.3
333.23	0.0447	1.3	0.8	0.8	0.8

6.3.1.2. Binary mixture (R152a + R1233zd(E))

The binary mixture (R152a + R1233zd(E)) is quite similar to the previous system (R134a + R1233zd(E)), and the same observations can be drawn for this system. The same comparison was performed, by using a $k_{ij} = 0$ and an adjusted k_{ij}.

The results of the prediction are displayed in Figure 6.15. From the graphical representation, we can see that we have better results when using a fitted k_{ij}, with less deviations from the experimental results.

We can see however that the vapour pressure of the R152a is a little underestimated in both cases, which can be related to the use of predictive alpha function parameters. Indeed, when the vapour pressures are not precisely represented, this influences the well representation of the VLE curve.

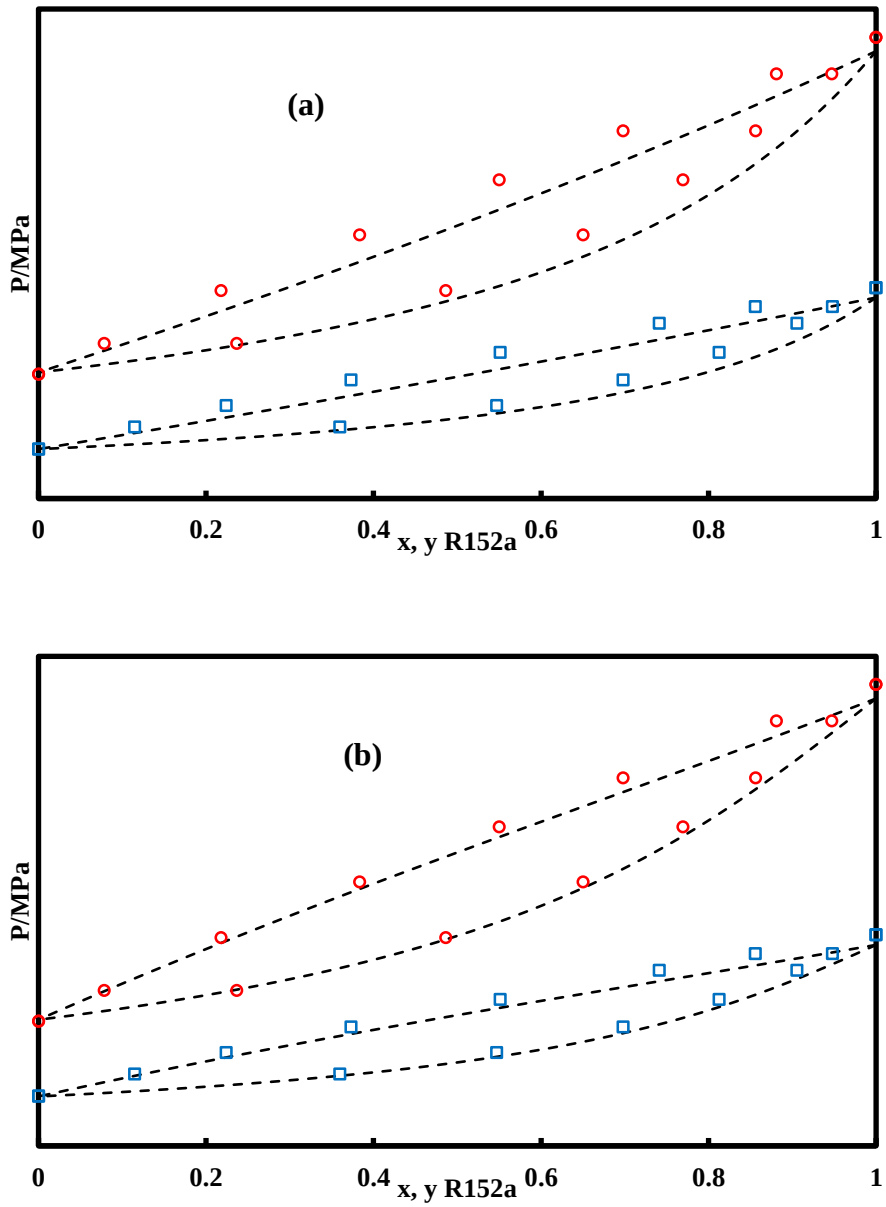

Figure 6.15 VLE prediction for binary mixture (R152a+ R1233zd(E)). (a): With k_{ij} = 0. (b): With k_{ij} adjusted. (□) 303.10 K; (○) 333.23 K.; (- - - -) NEoS.

This finding can be confirmed from calculating the deviations on the bubble pressure and the vapour molar composition, as reported in *Table 6.7*, from which we can see that the deviations from the experimental results are lower when using an adjusted k_{ij}.

Table 6.7 ARD and BIAS for the binary mixture (R152a + R1233zd(E)).

T/K	k_{ij}	*ARD P (%)*	*ARD yR152a (%)*	*BIAS P (%)*	*BIAS yR152a (%)*
303.10	0	5.7	2.4	5.5	1.7
333.23		4.9	3.7	4.7	3.1
303.10	0.0233	1.5	0.9	1.2	-0.8
333.23	0.0274	0.8	0.7	0.6	0.5

6.3.1.3. Binary mixture (R134a + R1233xf)

For the binary mixture (R134a + R1233xf), the prediction was performed by using predictive parameters (calculated alpha function parameters and $k_{ij} = 0$), in comparison with adjusted parameters (adjusted alpha function parameters and k_{ij}). The alpha function parameters were adjusted in order to evaluate their effect on representing the vapour pressure of the pure compounds.

We can see from Figure 6.16, that the results obtained when using adjusted parameters are in very good agreement with the experimental results, and better than the results obtained with predictive parameters.

We can also notice that the vapour pressures of the pure compounds are well represented, due to the use of adjusted alpha function parameters.

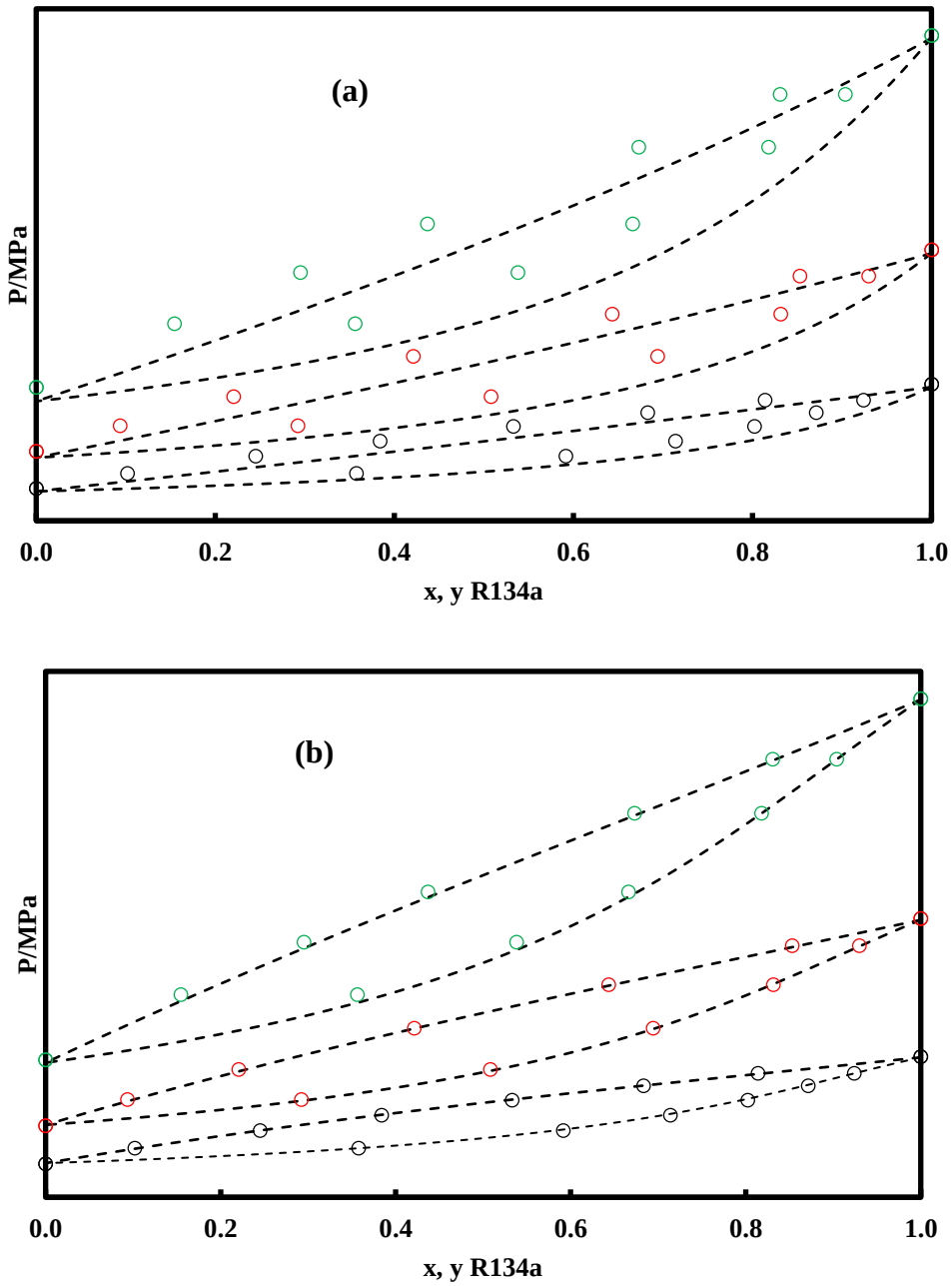

Figure 6.16 VLE prediction for binary mixture (R134a + R1233xf). (a): With predictive parameters. (b): With adjusted parameters. (○) 298.30 K; (○) 323.38 K; (○) 348.27 K; (- - - -) NEoS.

This finding can be confirmed from calculating the ARD and the BIAS on the bubble pressure and the vapour molar composition, as reported in Table 6.8. From these results, we can see that the deviations from the experimental data are very low when using adjusted parameters, while the deviations are much important when using predictive parameters (especially for the pressure).

Table 6.8 ARD and BIAS for the binary mixture (R134a + R1233xf).

T/K	k_{ij}	*ARD P (%)*	*ARD yR134a (%)*	*BIAS P (%)*	*BIAS yR134a (%)*
298.30		11.1	3.3	11.1	1.7
323.38	0	10.2	3.1	10.2	1.4
348.27		9.8	1.4	9.8	-0.5
298.30	0.0343	0.7	0.9	-0.3	0.9
323.38	0.0349	0.9	0.5	0.5	0.5
348.27	0.0353	1.5	0.6	1.5	-0.3

6.3.1.4. Binary mixture (R1234yf + R1233xf)

For the binary mixture (R1234yf + R1233xf), the prediction was performed in a similar way to the previous system (R134a + R1233xf), by using predictive parameters (calculated alpha function parameters and $k_{ij} = 0$), in comparison with adjusted parameters (adjusted alpha function parameters and k_{ij}). The alpha function parameters were adjusted in order to see their effect on representing the vapour pressure of the pure compounds.

We can see from *Figure 6.17*, that the results obtained when using adjusted parameters are in very good agreement with the experimental results and better than the results obtained with predictive parameters.

We can also notice that the vapour pressures of the pure compounds are well represented, due to the use of adjusted alpha function parameters.

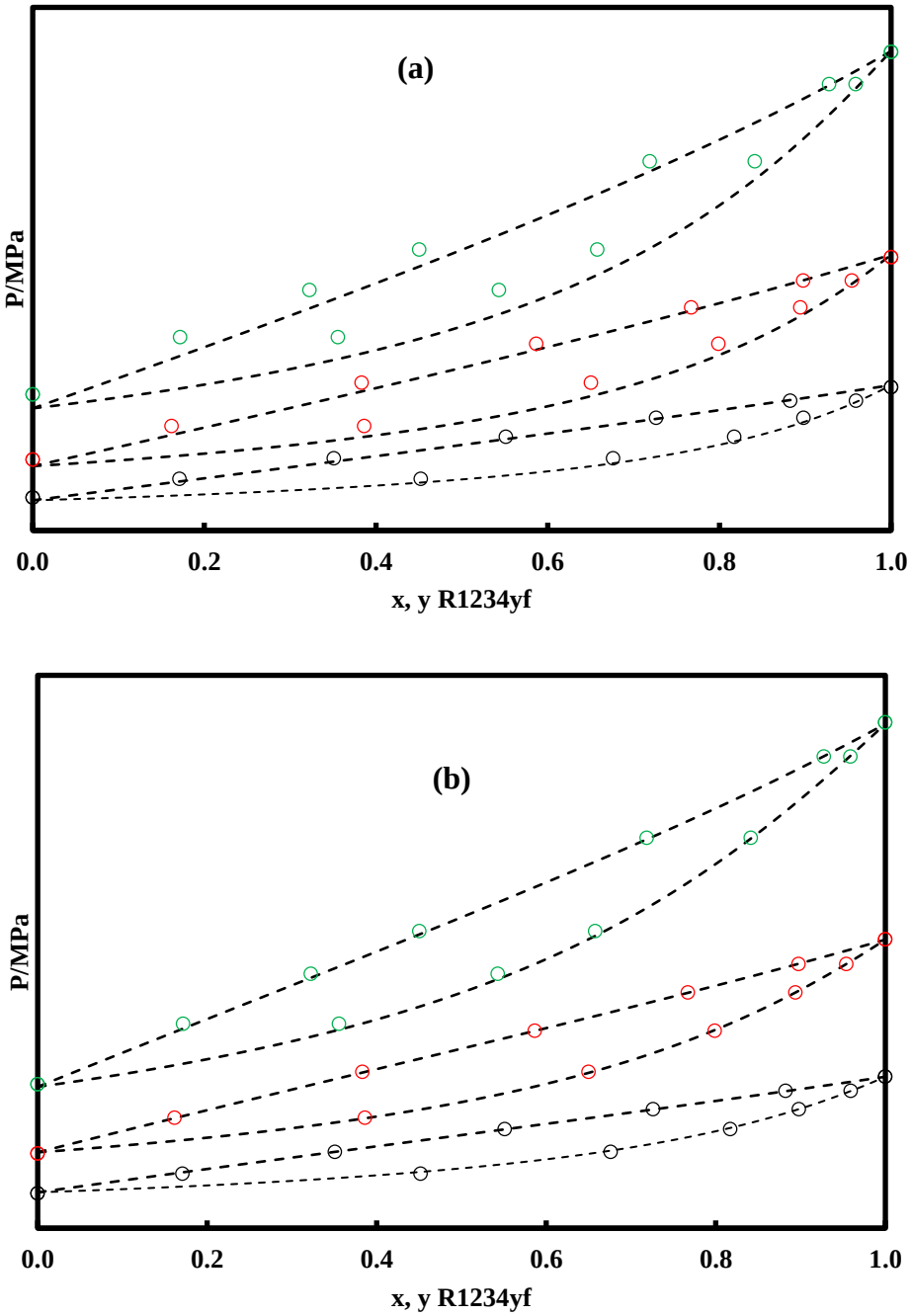

Figure 6.17 VLE prediction for binary mixture (R1234yf + R1233xf). (a): With predictive parameters. (b): With adjusted parameters. (○) 298.31 K; (○) 323.27 K; (○) 348.25 K; (- - - -) NEoS.

This finding can be supported from calculating the deviations on the bubble pressure and the vapour molar composition, as reported in Table 6.9, from which we can see that the deviations from the experimental results are very small when using adjusted parameters, while the deviations are much important when using predictive parameters (especially for the pressure).

Table 6.9 ARD and BIAS for the binary mixture (R1234yf + R1233xf).

T/K	k_{ij}	*ARD P (%)*	*ARD yR1234yf (%)*	*BIAS P (%)*	*BIAS yR1234yf (%)*
298.31		3.6	1.5	3.2	-1.5
323.27	0	4.2	1.9	4.1	-1.9
348.25		5.4	2.1	5.3	-2.1
298.31	0.0053	0.8	0.7	-0.4	0.7
323.27	0.0091	0.4	0.1	0.1	-0.0
348.25	0.0101	1.1	0.5	1.1	-0.4

6.3.1.5. Binary mixture (R1234yf + R1233zd(E))

For the binary mixture (R1234yf + R1233zd(E)), the prediction was performed in a similar way to the previous system (R1234yf + R1233xf), by using predictive parameters (calculated alpha function parameters and $k_{ij} = 0$), in comparison with adjusted parameters (adjusted alpha function parameters and k_{ij}). The alpha function parameters were adjusted in order to see their effect on representing the vapour pressure of the pure compounds.

We can see from Figure 6.18, that the results obtained when using adjusted parameters are in very good agreement with the experimental results, with slight improvement compared to the results obtained when using predictive parameters.

We can also notice that the vapour pressures of the two pure compounds are well represented, in both cases.

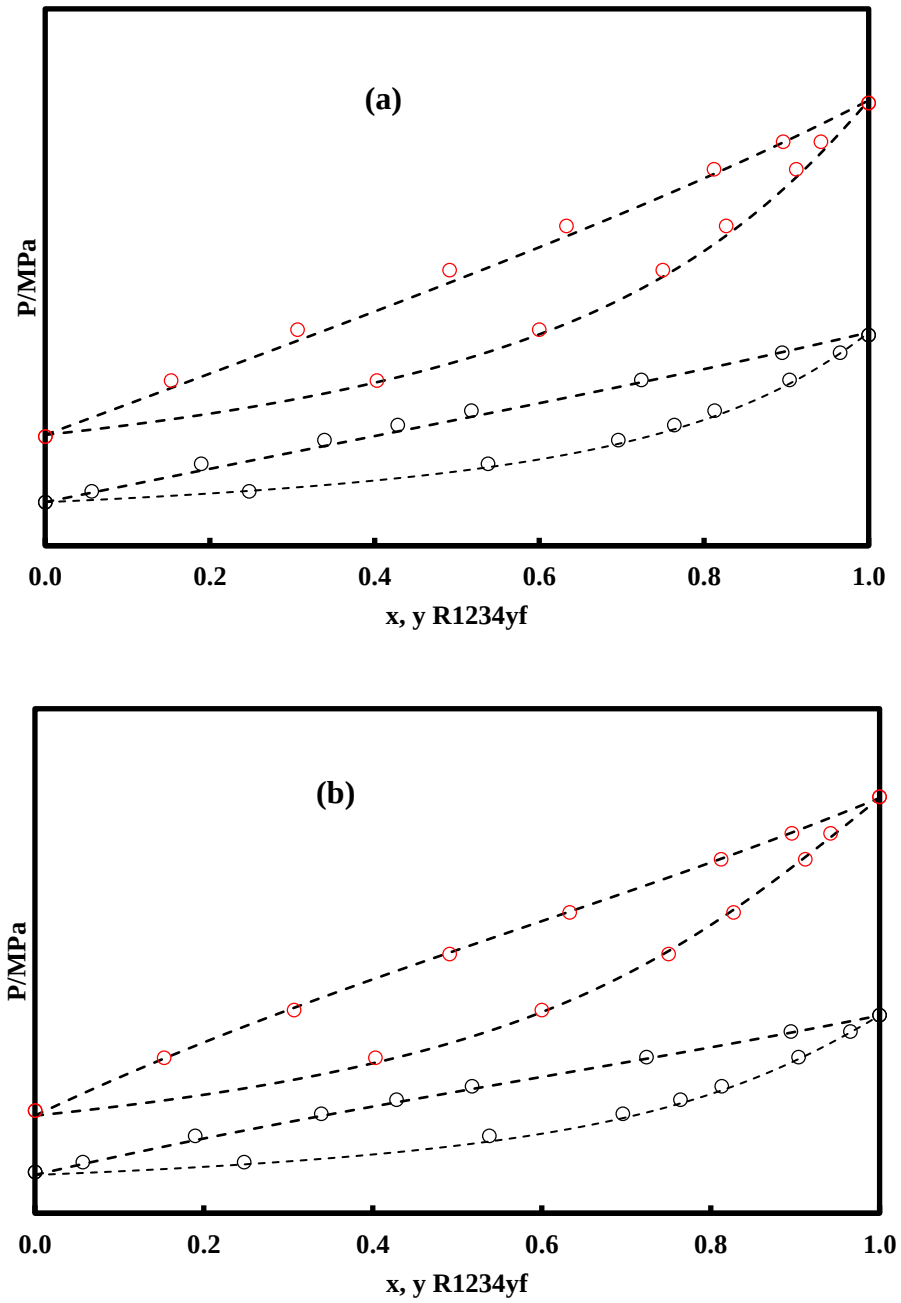

Figure 6.18 VLE prediction for binary mixture (R1234yf + R1233zd(E)). (a): With predictive parameters. (b): With adjusted parameters. (○) 303.22 K; (○) 333.27 K; (- - - -) NEoS.

This finding can be supported from calculating the ARD and the BIAS on the bubble pressure and the vapour molar composition, as reported in Table 6.10. From these results, we can see that the deviations from the experimental results are slightly lower when using adjusted parameters.

Table 6.10 ARD and BIAS for the binary mixture (R1234yf + R1233zd(E)).

T/K	k_{ij}	*ARD P (%)*	*ARD yR1234yf (%)*	*BIAS P (%)*	*BIAS yR1234yf (%)*
303.22	0	3.3	2.8	3.0	2.6
333.27		2.7	2.1	2.2	1.6
303.22	0.0167	2.7	0.9	2.7	-0.9
333.27	0.0284	1.0	1.3	0.4	-1.0

6.3.1.6. Binary mixture (CO_2 + R1234yf)

The experimental VLE measurements of the system (CO_2 + R1234yf) are compared to the results of the prediction obtained using the NEoS, for the seven isotherms studied.

The results of the prediction displayed in Figure 6.19 are obtained while using predictive parameters (calculated alpha function parameters and $k_{ij} = 0$), in comparison with the prediction using calculated alpha function parameters and an adjusted k_{ij}.

We can see from the graphical representation that the prediction is in good agreement with the experimental results for the three isotherms below the critical temperature of CO_2 (with both $k_{ij} = 0$ and adjusted k_{ij}).

For the supercritical isotherms, we obtain slightly better results when using an adjusted k_{ij}, especially when approaching the critical composition.

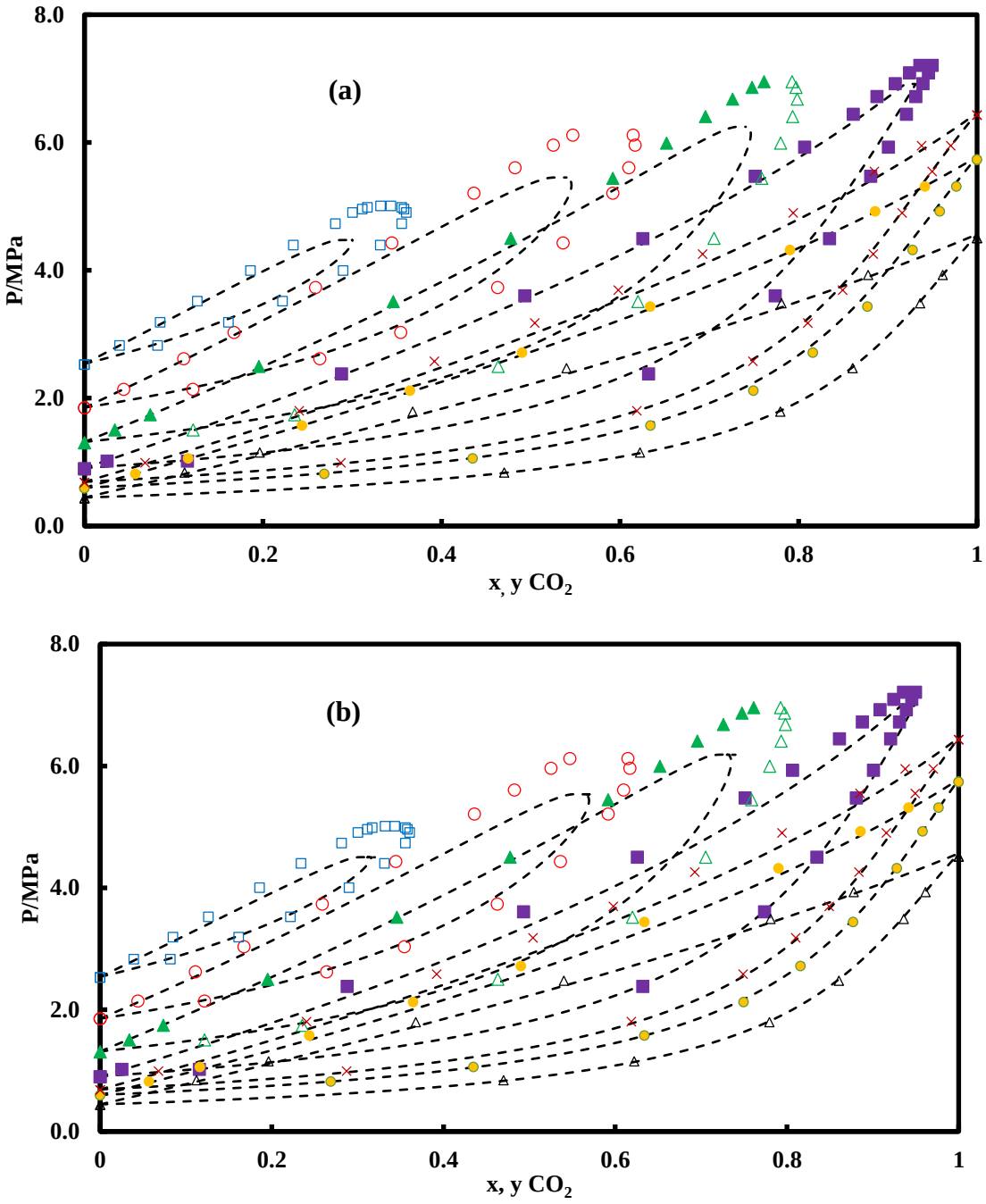

Figure 6.19 VLE prediction for the binary mixture (CO_2 + R1234yf). (a): With k_{ij} = 0. (b): With an adjusted k_{ij}. (Δ) 283.21 K; (●) 293.18 K; (×) 298.11 K; (■) 308.20 K; (Δ) 323.18 K; (○) 338.24 K; (□) 353.25 K; (- - - -) NEoS.

This finding can be confirmed from calculating the deviations on the bubble pressure and the molar composition, as reported in *Table 6.11*.

From the reported results, we can see important deviations from the experimental results, at the isotherms above the critical temperature of CO_2, the deviations decrease slightly when using an adjusted k_{ij}, but are still quite important. We can notice however that we have better results with

k_{ij} = 0 at the isotherms T = 293.18 K and 298.15 K, where we obtain deviations lower than the deviations obtained if we use an adjusted k_{ij}.

Table 6.11 ARD and BIAS for the binary mixture (CO_2 + R1234yf).

T/K	k_{ij}	*ARD P (%)*	*ARD yCO_2 (%)*	*BIAS P (%)*	*BIAS yCO_2 (%)*
283.21		2.6	1.2	1.9	1.2
293.18		0.7	1.4	0.2	1.4
298.11		3.7	1.4	3.5	1.4
308.20	0	19.3	5.3	19.0	5.3
323.18		16.3	9.0	16.1	9.0
338.24		17.0	15.6	17.0	15.6
353.25		17.0	16.0	16.9	16.0
283.21	0.0020	2.3	1.1	1.6	1.1
293.18	-0.0166	2.8	2.3	2.4	2.3
298.11	-0.0120	5.3	1.8	5.0	1.8
308.20	-0.0280	10.1	3.9	9.9	3.9
323.18	0.0086	15.5	8.6	15.1	8.6
338.24	-0.0200	12.9	13.4	12.9	13.4
353.25	-0.0200	16.3	14.5	16.2	14.5

The representation could be improved for instance by considering different mixing rules (more complex mixing rules than vdW ones), such as Wong-Sandler mixing rules with NRTL model. These mixing rules have been used with PR-EoS to represent the system (R23 + R1234yf), and give good results for representing the critical region of this system (Madani et al. 2016). Also, the modification of the mathematical expression of the MC alpha function in order to respect all the conditions of the consistency test could lead to a good improvement of the representation in the critical region (Le Guennec et al. 2016).

6.3.1.7. Binary mixture (CO_2 + R1233zd(E))

For the binary mixture (CO_2 + R1233zd(E)), the prediction was performed using the NEoS with a k_{ij} = 0, and compared to the prediction with an adjusted k_{ij}, fitted on the experimental VLE results at T = 278.28 K. This k_{ij} was used for all the isotherms, since the k_{ij} obtained at T = 302.59 K and 333.17 K were not physically correct, and give erroneous results.

The results of the prediction are displayed in *Figure 6.20*. The results are in overall in good agreement with the experimental results when using a k_{ij} = 0. A slight improvement is observed when using the adjusted k_{ij}, especially for representing the liquid phase.

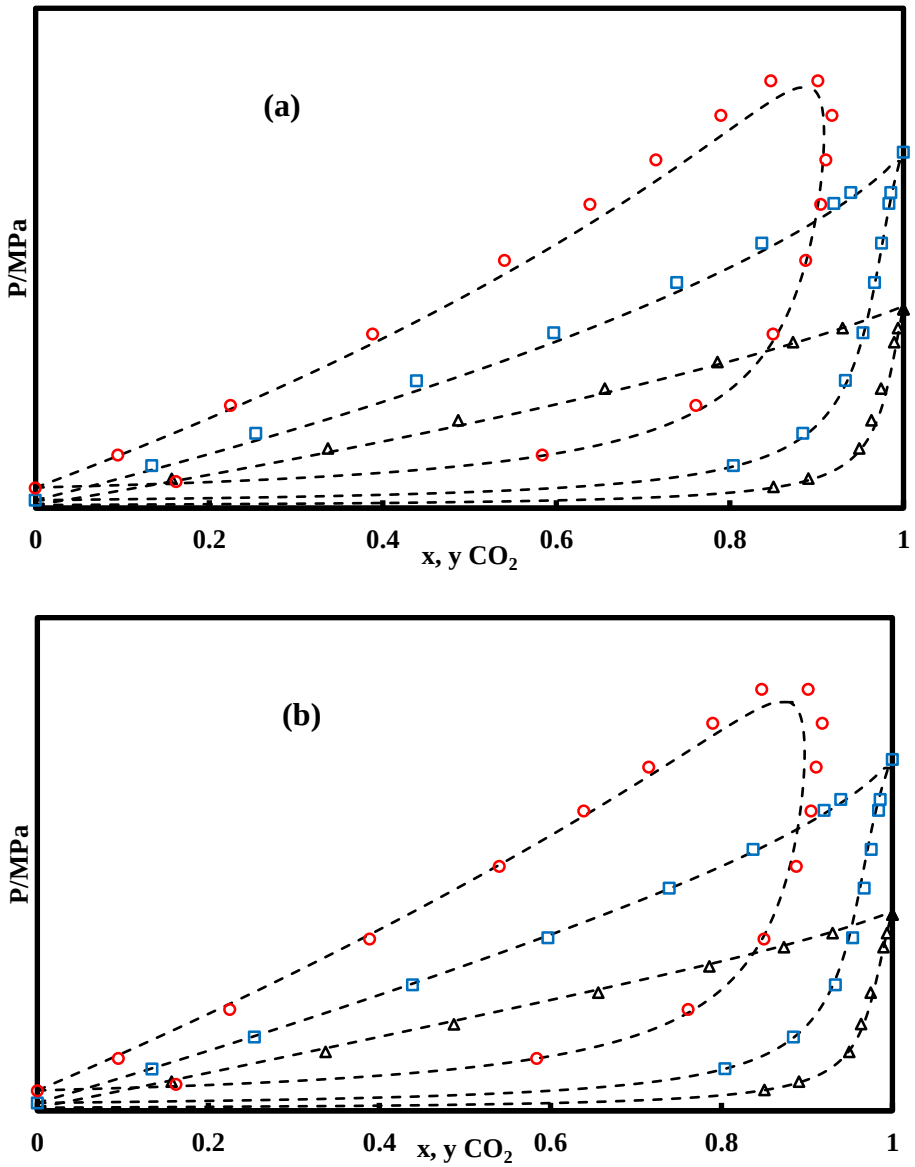

Figure 6.20 VLE prediction for binary mixture (CO_2 + R1233zd(E)). (a): With k_{ij} = 0. (b): With k_{ij} = 0.0285. (Δ) 278.18 K; (□) 303.16 K; (○) 333.29 K; (- - - -) NEoS.

This finding can be supported by calculating the deviations on the bubble pressure and the vapour molar composition. The results reported in *Table 6.12*, show that we obtain lower deviations from the experimental results when using an adjusted k_{ij} (especially on the pressure).

Table 6.12 ARD and BIAS for the binary mixture (CO_2 + R1233zd(E)).

T/K	k_{ij}	*ARD P (%)*	*ARD yCO_2 (%)*	*BIAS P (%)*	*BIAS yCO_2 (%)*
278.28	0	4.2	0.3	4.2	-0.1
302.59		4.9	0.5	4.8	0.5
333.17		4.7	0.5	4.7	0.3
278.28	0.0285	2.8	0.3	-2.8	-0.3
302.59		1.0	0.4	-0.2	0.2
333.17		3.4	1.8	-0.5	0.2

6.3.1.8. Binary mixture (R1234yf + R134a)

For this binary mixture, and since it is a system with an azeotropic behaviour, adjustments have been performed in order to have an accurate representation.

The k_{ij} was fitted on the experimental VLE data in order to take into account the molecular interactions occurring, and the alpha function parameter m_1 was fitted on the pure compounds data, in order to accurately represent the vapour pressures.

The results of the prediction are displayed in Figure 6.21. We can notice from the graphical representation that the prediction for this system is not ideal (especially at T = 333.17 K). The representation at T = 278.15 K is in good agreement with the experimental data.

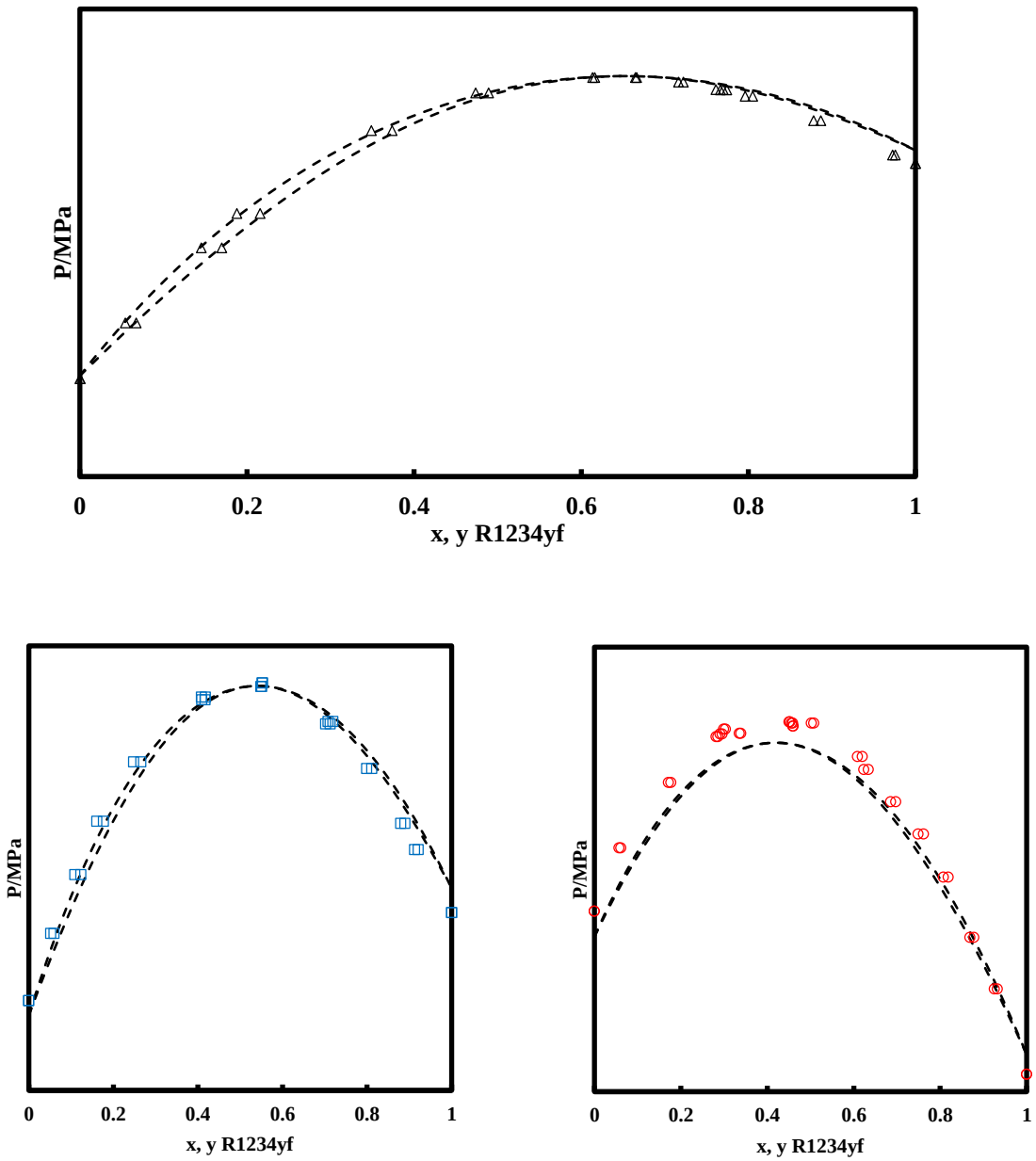

Figure 6.21 VLE prediction for binary mixture (R1234yf + R134a). (Δ) 278.17 K; (□) 303.16 K; (○) 333.17 K; (- - - -) NEoS.

From calculating the ARD and the BIAS on the bubble pressure and the vapour molar composition reported in Table 6.13, we can notice that the deviations are not very high.

Table 6.13 ARD and BIAS for the binary mixture (R1234yf + R134a).

T/K	k_{ij}	*ARD P (%)*	*ARD yR1234yf (%)*	*BIAS P (%)*	*BIAS yR1234yf (%)*
278.17	0.0136	1.3	1.7	0.5	-1.7
303.16	0.0143	1.1	1.2	0.6	-1.2
333.17	0.0143	0.7	0.7	0.6	-0.7

6.3.1.9. Binary mixture (R1234yf + R152a)

Here again we have an azeotropic system, so adjustments have been done in order to have an accurate representation for this mixture.

The k_{ij} was fitted on the experimental VLE data, and the alpha function parameter were fitted on the pure compounds data.

The results of the prediction are displayed in *Figure 6.22*.

From this graphical representation, we can notice that the prediction for this system is in overall in good agreement with the experimental results. Slight deviations from the experimental results can however be noticed at T = 333.29 K, in the region where the azeotrope is occurring.

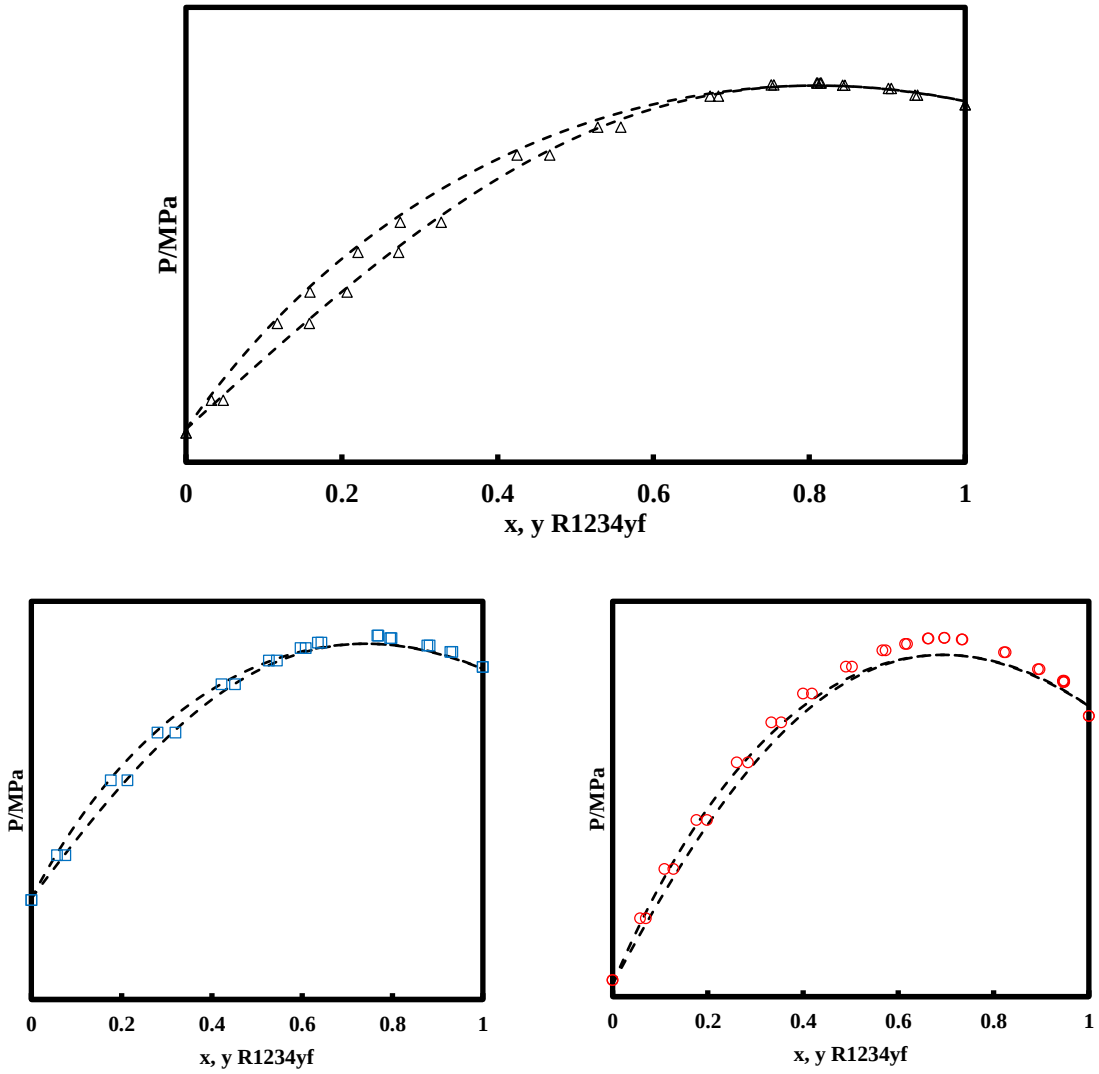

Figure 6.22 VLE prediction for binary mixture (R1234yf + R152a). (Δ) 278.18 K; (□) 303.16 K; (○) 333.29 K; (- - - -) NEoS.

This finding can be supported from calculating the ARD and the BIAS on the bubble pressure and the vapour molar composition reported in Table 6.14, from which we can see that the deviations are not very high in comparison to the experimental results.

Table 6.14 ARD and BIAS for the binary mixture (R1234yf + R152a).

T/K	k_{ij}	*ARD P (%)*	*ARD yR1234yf (%)*	*BIAS P (%)*	*BIAS yR1234yf (%)*
278.18	0.0137	0.2	0.3	-0.1	-0.3
303.16	0.0148	0.3	0.2	0.3	0.0
333.29	0.0142	0.4	0.1	0.4	-0.1

6.3.1.10. Binary mixture (R245fa + R1233xf)

For the binary mixture (R245fa + R1233xf)**,** we used adjusted pure compounds alpha function parameters and an adjusted binary interaction parameter k_{ij}.

From the results of the prediction displayed in Figure 6.23, we can see that the representation at T = 323.40 K is relatively good, while the representation at T = 353.27 K is quite far from the experimental results.

We can also notice that the vapour pressure of R1233xf is misrepresented (especially at T = 353.27 K). This could be related to some impurities contained in the product used during the experiment. We recall that we noticed the same thing for the vapour pressures of R1233xf in Chapter 5; the deviations from the model increase with increasing temperature; and this confirm the hypothesis of impurities contained in this product.

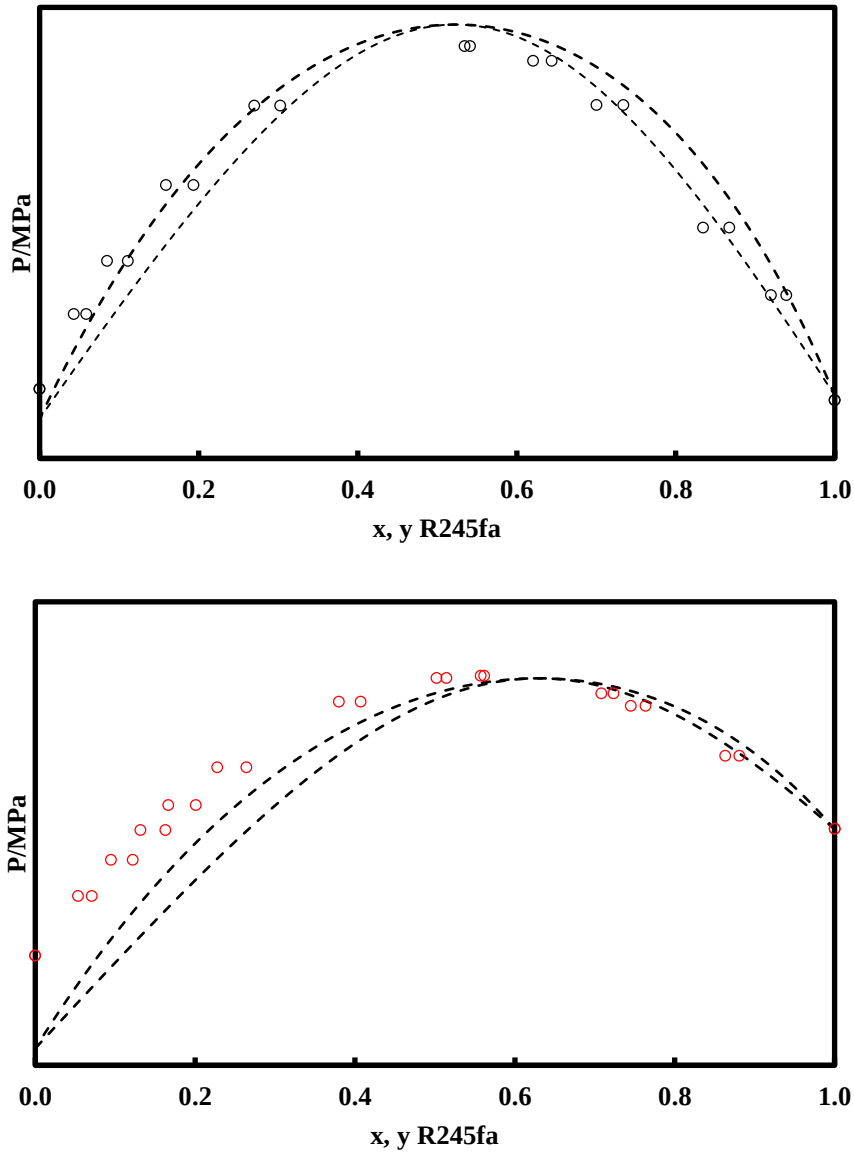

Figure 6.23 VLE prediction for binary mixture (R245fa+ R1233xf). (○) 323.40 K; (○) 353.27 K; (- - - -) NEoS.

This finding can be supported from calculating the ARD and the BIAS on the bubble pressure and the vapour molar composition. As reported in Table 6.15, we can see that the deviations are more important at T = 353.27 K compared to the deviations at T = 323.40 K.

Table 6.15 ARD and BIAS for the binary mixture (R245fa + R1233xf).

T/K	k_{ij}	*ARD P (%)*	*ARD yR245fa (%)*	*BIAS P (%)*	*BIAS yR245fa (%)*
323.40	0.0377	0.6	1.4	0.1	-1.0
353.27	0.0397	2.0	2.4	1.9	-2.3

6.3.1.11. Binary mixture (R245fa + R1233zd(E))

For the binary mixture (R245fa + R1233zd(E))**,** we used adjusted pure compounds alpha function parameters and an adjusted binary interaction parameter k_{ij}.

From the results of the prediction displayed in Figure 6.24, we can see that the representation is in good agreement with the experimental results, with a good representation of the vapour pressure of both pure compounds R1233zd(E) and R245fa.

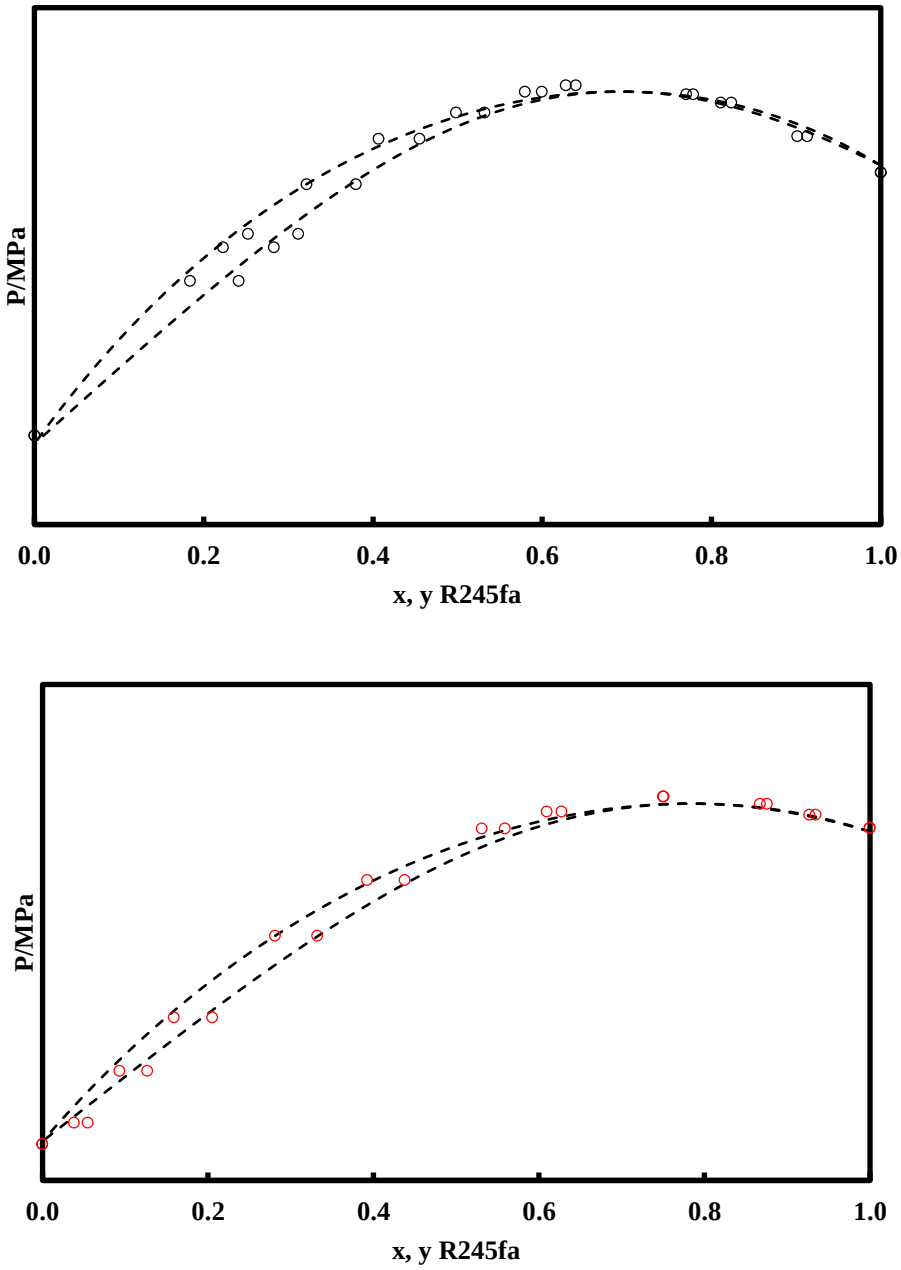

Figure 6.24 VLE prediction for binary mixture (R245fa + R1233zd(E)). (○) 323.23 K; (○) 353.27 K; (- - - -) NEoS.

This finding can be supported from calculating the ARD and the BIAS on the bubble pressure and the vapour molar composition. As reported in Table 6.16, we can see that the deviations on the vapour composition at T = 323.23 K are slightly higher compared to the deviations at T = 353.27 K.

Table 6.16 ARD and BIAS for the binary mixture (R245fa + R1233zd(E)).

T/K	k_{ij}	*ARD P (%)*	*ARD yR245fa (%)*	*BIAS P (%)*	*BIAS yR245fa (%)*
323.23	0.0300	0.4	0.7	0.0	0.7
353.27	0.0299	0.3	0.3	-0.1	-0.2

6.3.1.12. Binary mixture (R23 + Propane)

For the binary mixture (R23 + Propane)**,** we used adjusted pure compounds alpha function parameters as well as an adjusted binary interaction parameter k_{ij}.

We can observe from the graphical representation displayed in Figure 6.25 that the results of the calculations are in overall in good agreement with the experimental results for the subcritical isotherms. Slight deviations can be observed for the supercritical isotherms.

We can see slight deviations in representing the critical composition at T = 313.15 K and 323.15 K.

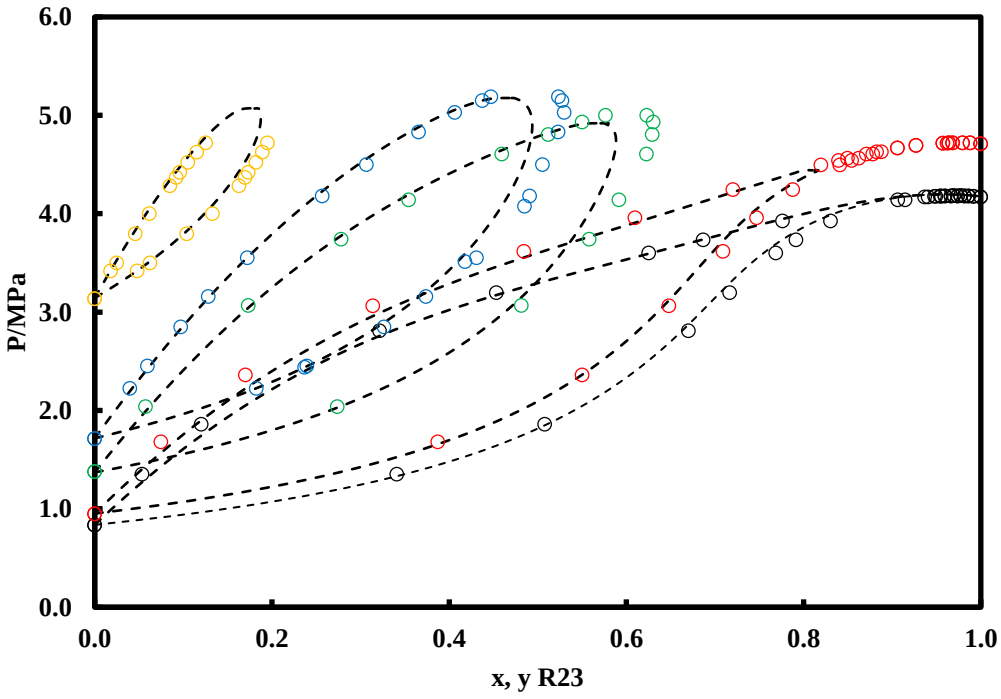

Figure 6.25 VLE prediction for binary mixture (R23 + Propane). (○) 293.15 K; (○) 298.15 K; (○) 313.15 K; (○) 323.15 K; (○) 353.15 K; (- - - -) NEoS.

From calculating the ARD and the BIAS on the bubble pressure and the vapour molar composition, reported in *Table 6.17*, we can see that we have important deviations on the pressure at T = 298.15 K and 323.15 K.

We can also report high deviations on the vapour molar fraction at the supercritical isotherms (especially at T = 323.15 K and 353.15 K).

Table 6.17 ARD and BIAS for the binary mixture (R23 + Propane).

T/K	k_{ij}	*ARD P (%)*	*ARD yR23 (%)*	*BIAS P (%)*	*BIAS yR23 (%)*
293.18	0.1760	4.0	1.3	4.0	1.1
298.15	0.1733	12.1	1.9	12.1	1.9
313.15	0.1928	1.1	5.2	0.3	5.2
323.15	0.1971	25.0	17.2	25.0	17.2
353.15	0.2346	3.6	16.7	-2.2	16.1

The representation could be improved for example by considering different mixing rules (more complex than vdW mixing rules), such as Wong-Sandler mixing rules with NRTL model. These mixing rules have been used with PR-EoS to represent the system (R23 + R1234yf), and give good results for representing the critical region of this system (Madani et al. 2016). Also, the modification of the mathematical expression of the MC alpha function in order to respect all the conditions of the consistency test could lead to a good improvement of the representation in the critical region (Le Guennec et al. 2016).

6.3.2. Density prediction

In this section, we use the NEoS to predict the density properties for the systems studied experimentally during this work.

In all this section, the NEoS is used in a predictive way, meaning that the alpha function parameters as well as the critical compressibility factor of the pure compounds are calculated from the correlations developed in Chapter 4. In addition, the binary interaction parameter used is $k_{ij} = 0$.

6.3.2.1. Binary mixture (R1234yf + R134a)

The experimental density results of the binary mixture (R1234yf + R134a) obtained during this work are compared to the results obtained using the NEoS. The results of the prediction are presented for the three compositions studied, as displayed in Figure 6.26 to Figure 6.28.

The results presented show a very good prediction for the density of the vapour phase, for the three compositions, at all the isotherms.

For the density at the liquid phase, we can see for the three compositions some deviations from the experimental results, with a maximal deviation around 3.8%. We can notice that the deviations relatively increase with increasing temperatures.

- ***1st composition: (46.36% R1234yf + 53.64% R134a)***

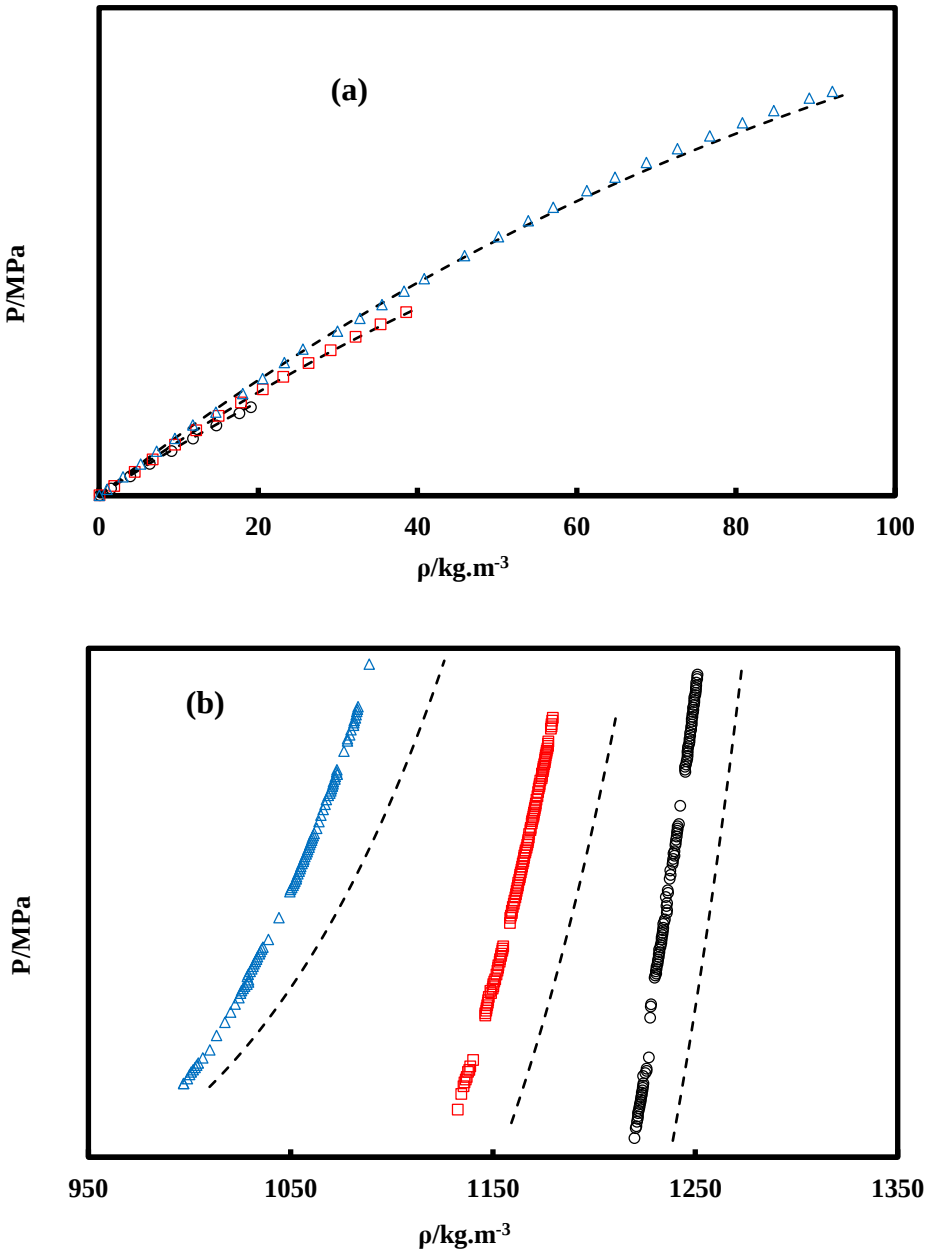

Figure 6.26 Density prediction for (R1234yf + R134a), 1st composition. (a): Vapour phase. (b): Liquid phase. (○): 278.34 K; (□): 302.45 K; (Δ): 332.55 K; (- - - -) NEoS.

- ***2nd composition: (86.19% R1234yf + 13.81% R134a)***

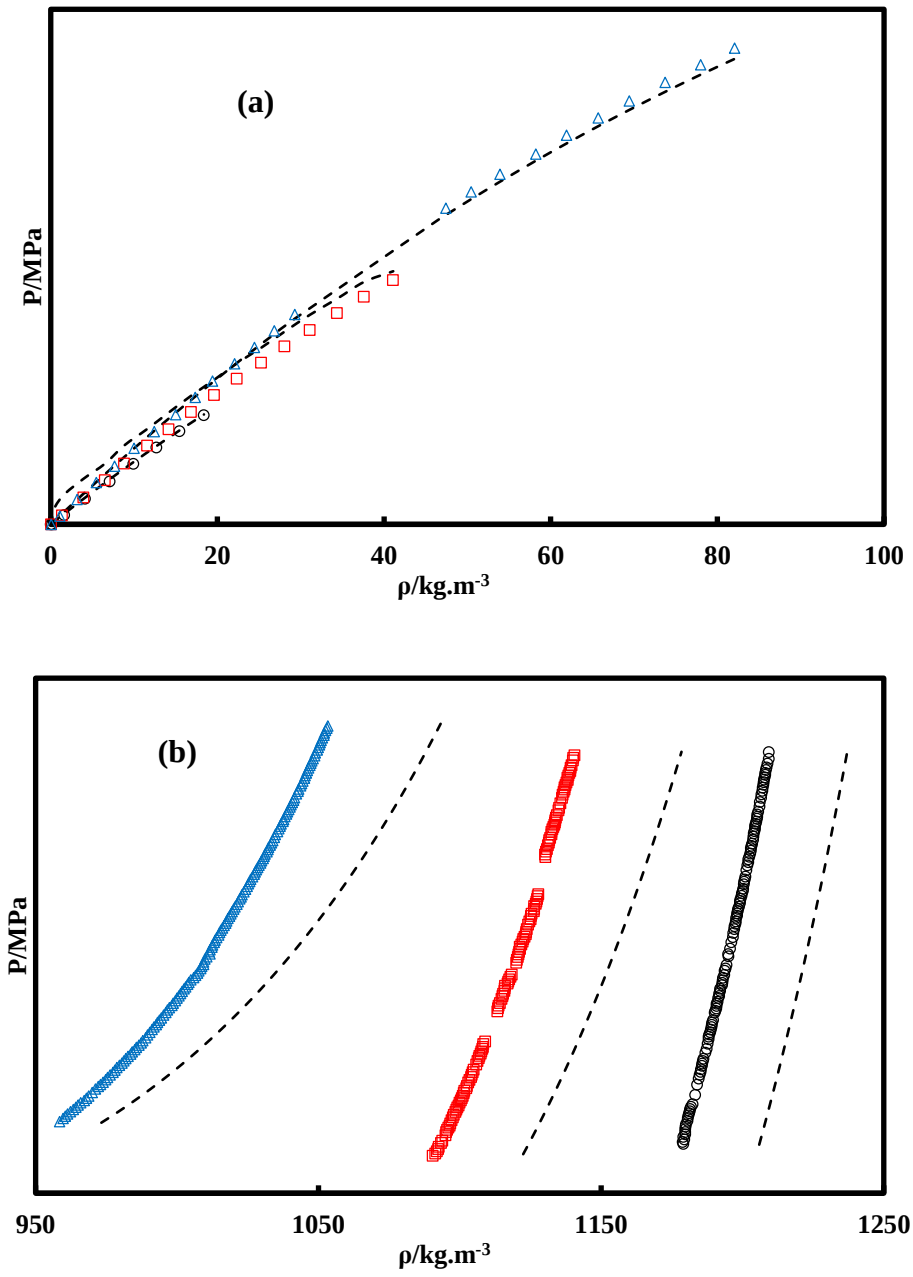

Figure 6.27 Density prediction for (R1234yf + R134a), 2nd composition. (a): Vapour phase. (b): Liquid phase. (○): 278.36 K; (□): 302.74 K; (Δ): 332.54 K; (- - - -) NEoS.

- ***3rd composition: (8.74% R1234yf + 91.26% R134a)***

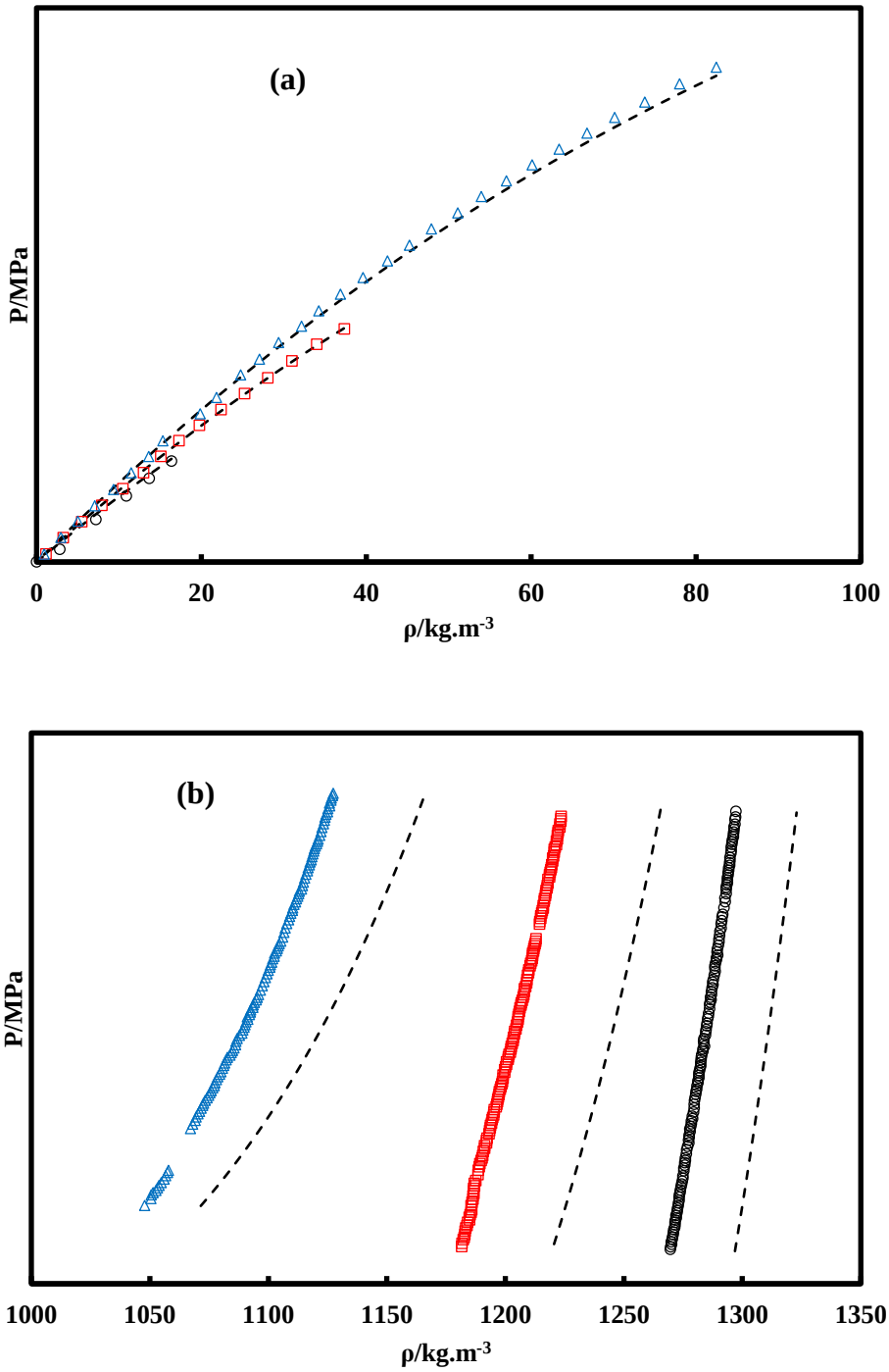

Figure 6.28 Density prediction for R1234yf + R134a, 3rd composition. (a): Vapour phase. (b): Liquid phase. (○): 278.40 K; (□): 302.93 K; (Δ): 332.53 K; (- - - -) NEoS.

6.3.2.2. Binary mixture (R1234yf + R152a)

The experimental density results of the binary mixture (R1234yf + R152a) obtained during this work are compared to the results obtained using the NEoS. The results of the prediction are presented for the three compositions studied, and displayed in *Figure 6.29* to *Figure 6.31*.

The results presented show a very good prediction for the density of the vapour phase, for the three compositions, at all the isotherms.

For the density of the liquid phase, we can see for the three compositions that we have some deviations from the experimental results comparing to the NEoS prediction, with a maximal deviation around 3%. We can notice that the deviations relatively increase with increasing temperatures.

- ***1st composition: (45.53% R1234yf + 54.47% R152a)***

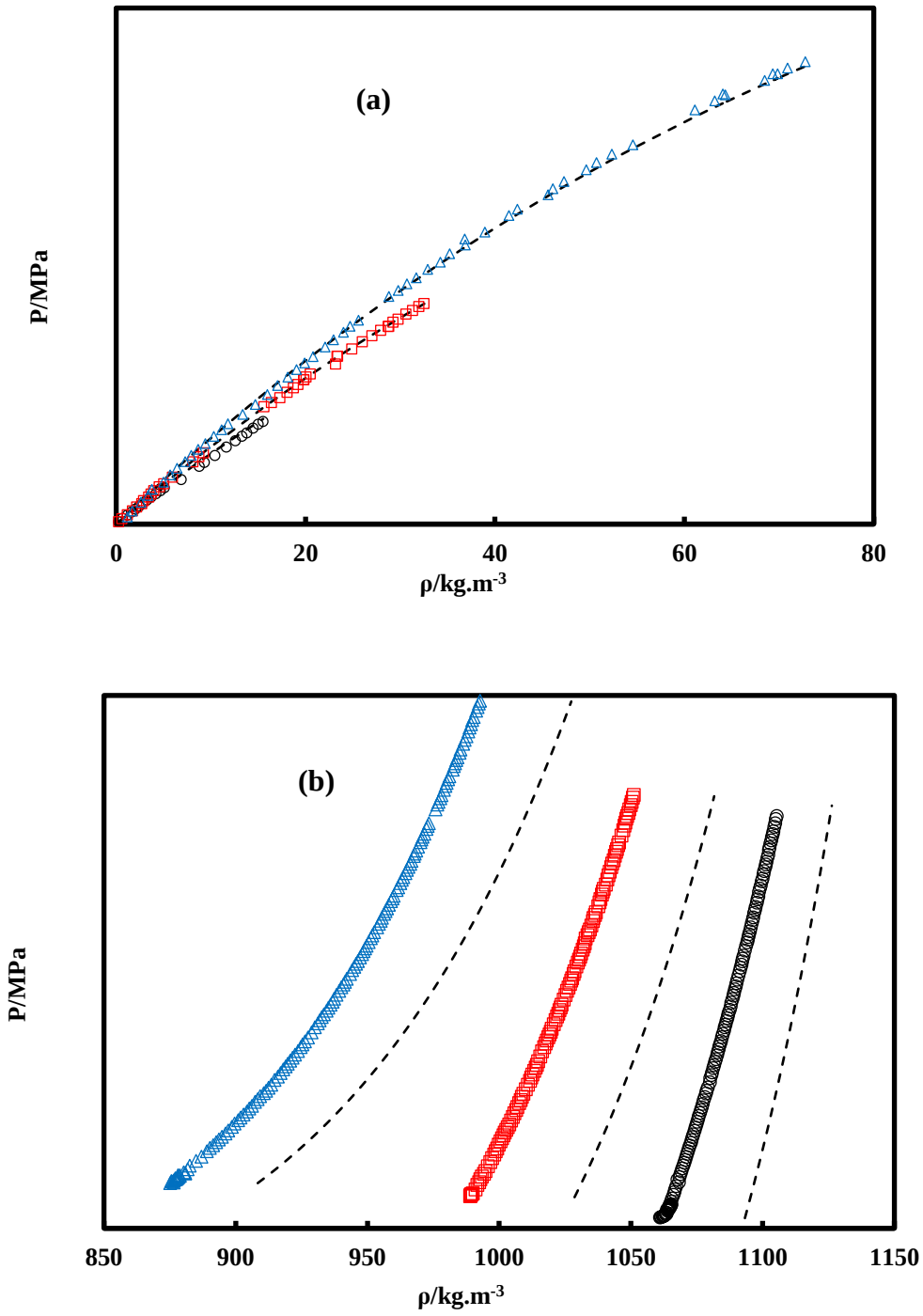

Figure 6.29 Density prediction for (R1234yf + R152a), 1st composition. (a): Vapour phase. (b): Liquid phase. (○): 278.15 K; (□): 303.15 K; (Δ): 333.15 K; (- - - -) NEoS.

- ***2nd composition: (86.57% R1234yf + 13.43 % R152a)***

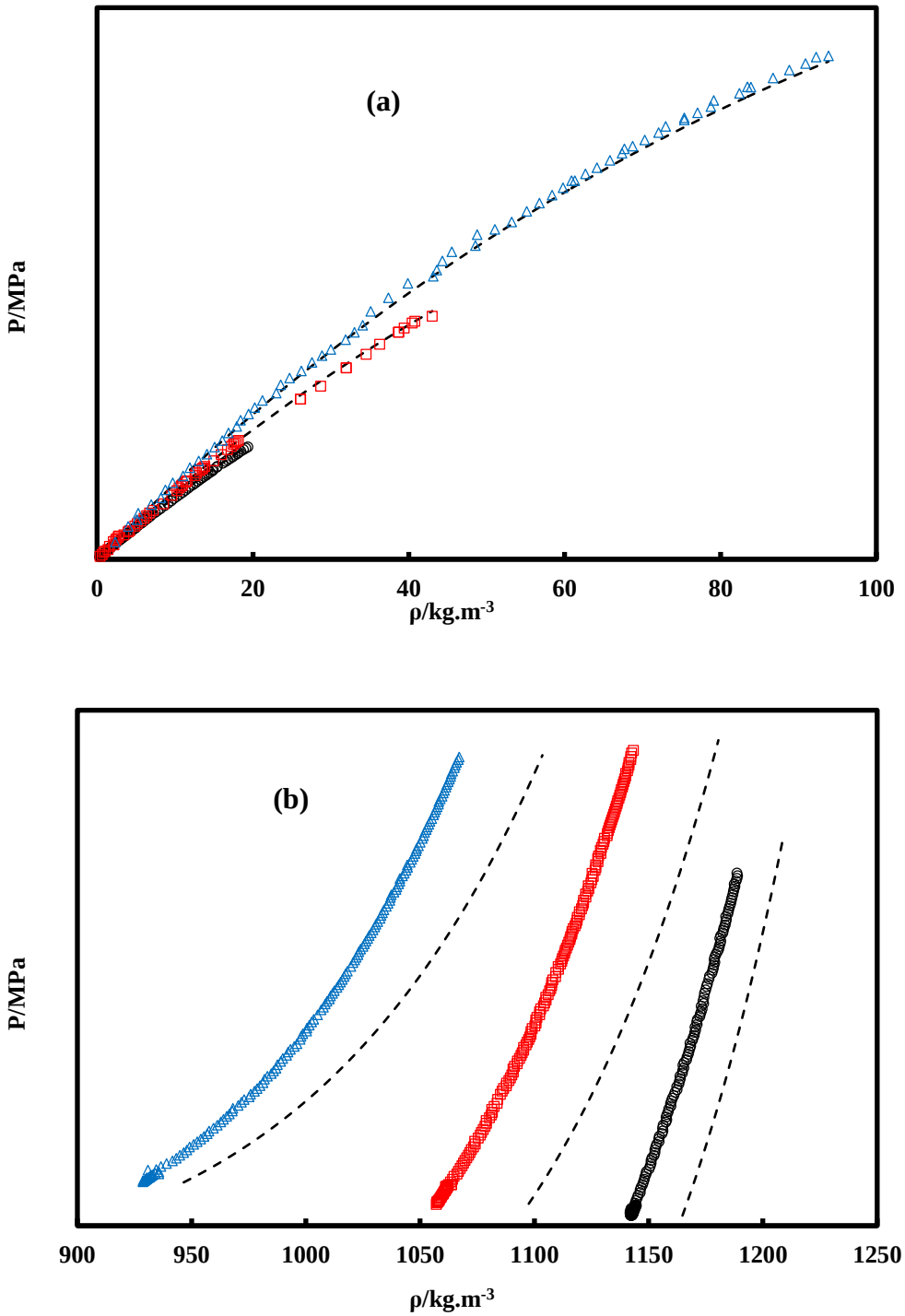

Figure 6.30 Density prediction for (R1234yf + R152a), 2nd composition. (a): Vapour phase. (b): Liquid phase. (○): 278.15 K; (□): 303.15 K; (Δ): 333.15 K; (- - - -) NEoS.

- ***3rd composition: (9.26% R1234yf + 90.74% R152a)***

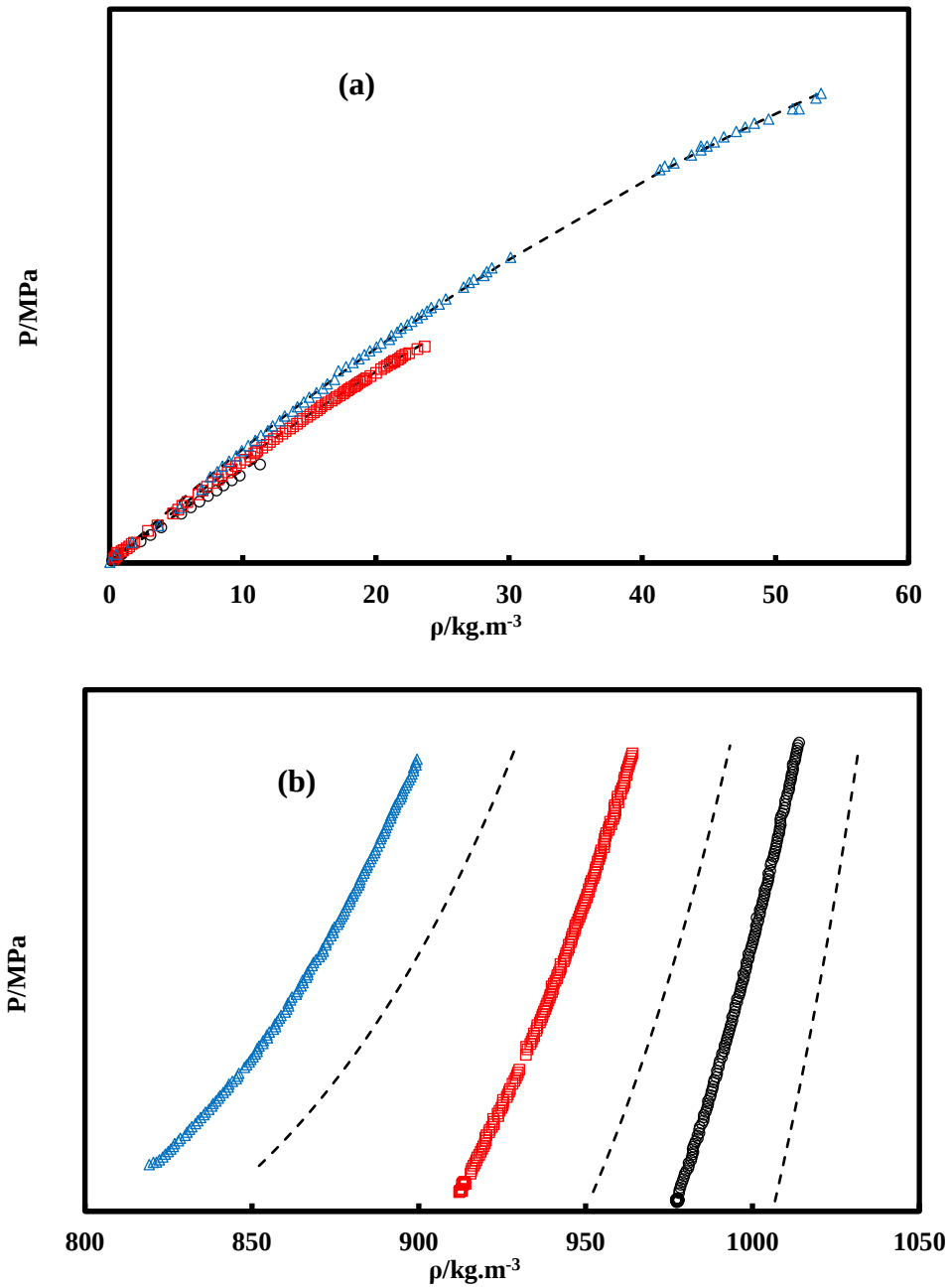

Figure 6.31 Density prediction for (R1234yf + R152a), 3rd composition. (a): Vapour phase. (b): Liquid phase. (○): 278.15 K; (□): 303.15 K; (Δ): 333.15 K; (- - - -) NEoS.

6.3.2.3. Ternary mixture (R134a + R152a + R1234yf)

The experimental density results of the ternary mixture (R134a + R152a + R1234yf) obtained during this work are compared to the results obtained using the NEoS. The results of the prediction are presented for the three compositions studied, and displayed in Figure 6.32 to Figure 6.34.

Similar to the two previous binary systems, the results presented show a very good prediction for the density of the vapour phase, for the three compositions, for all the isotherms.

For the density of the liquid phase, we can see for the three compositions that we have some deviations from the experimental results comparing to the NEoS prediction, with a maximal deviation around 4.2%. We can notice that the deviations relatively increase with increasing temperatures.

- ***1st composition: (29.53% R134a + 19.92% R152a + 50.56%R1234yf)***

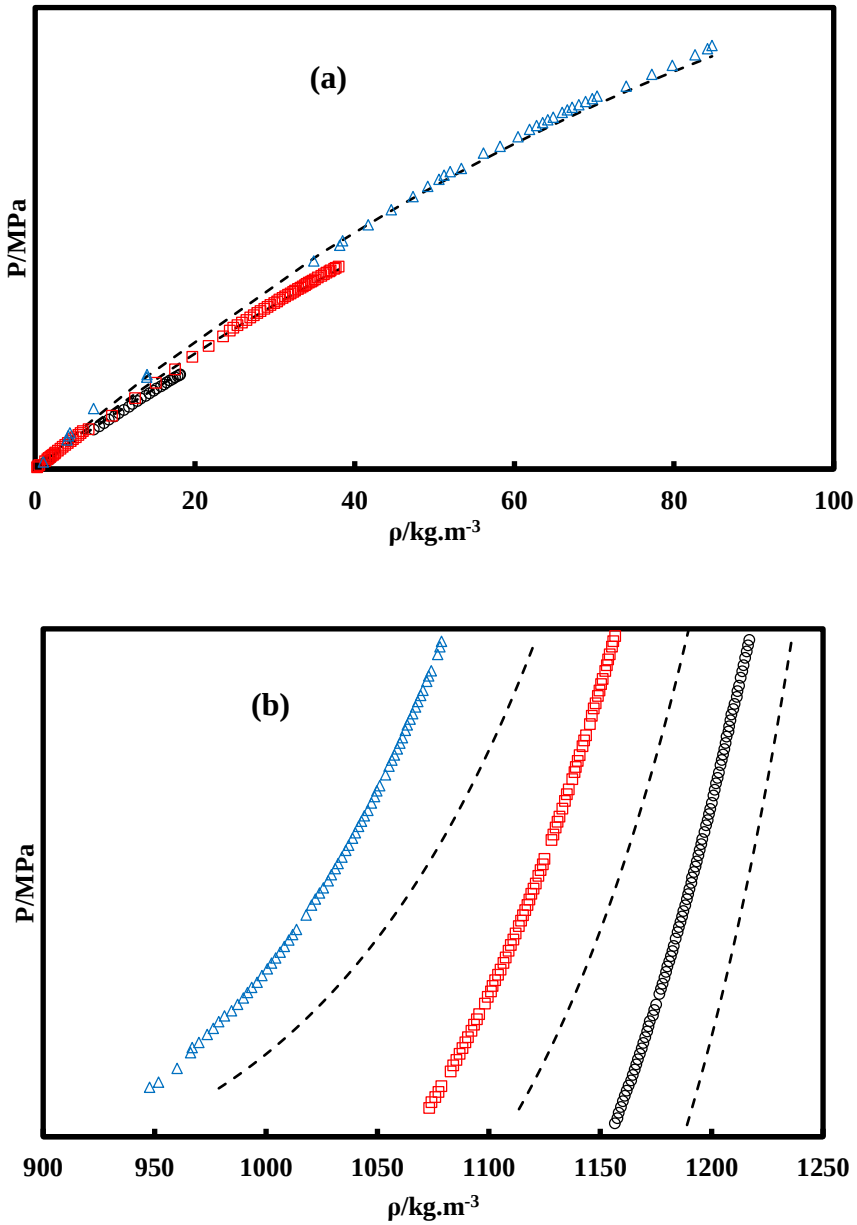

Figure 6.32 Density prediction for (R134a + R152a + R1234yf), 1st composition. (a): Vapour phase; (b): Liquid phase. (○): 278.15 K; (□): 303.15 K; (Δ): 333.15 K; (- - - -) NEoS.

- ***2nd composition: (19.67% R134a + 10.81% R152a + 69.52%R1234yf)***

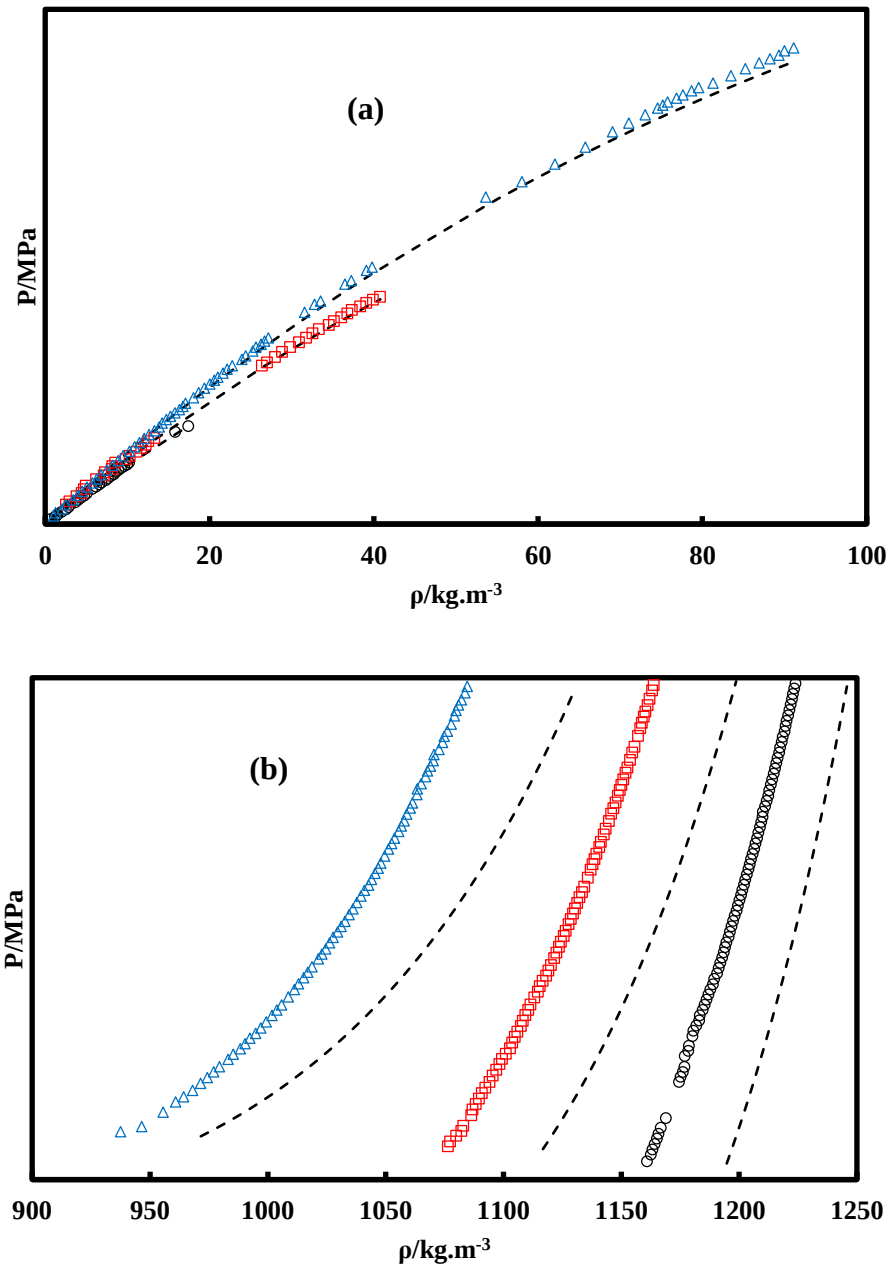

Figure 6.33 Density prediction for (R134a + R152a + R1234yf), 2nd composition. (a): Vapour phase; (b): Liquid phase. (○): 278.15 K; (□): 303.15 K; (Δ): 333.15 K; (- - - -) NEoS.

- ***3rd composition: (33.85% R134a + 31.41% R152a + 34.74%R1234yf)***

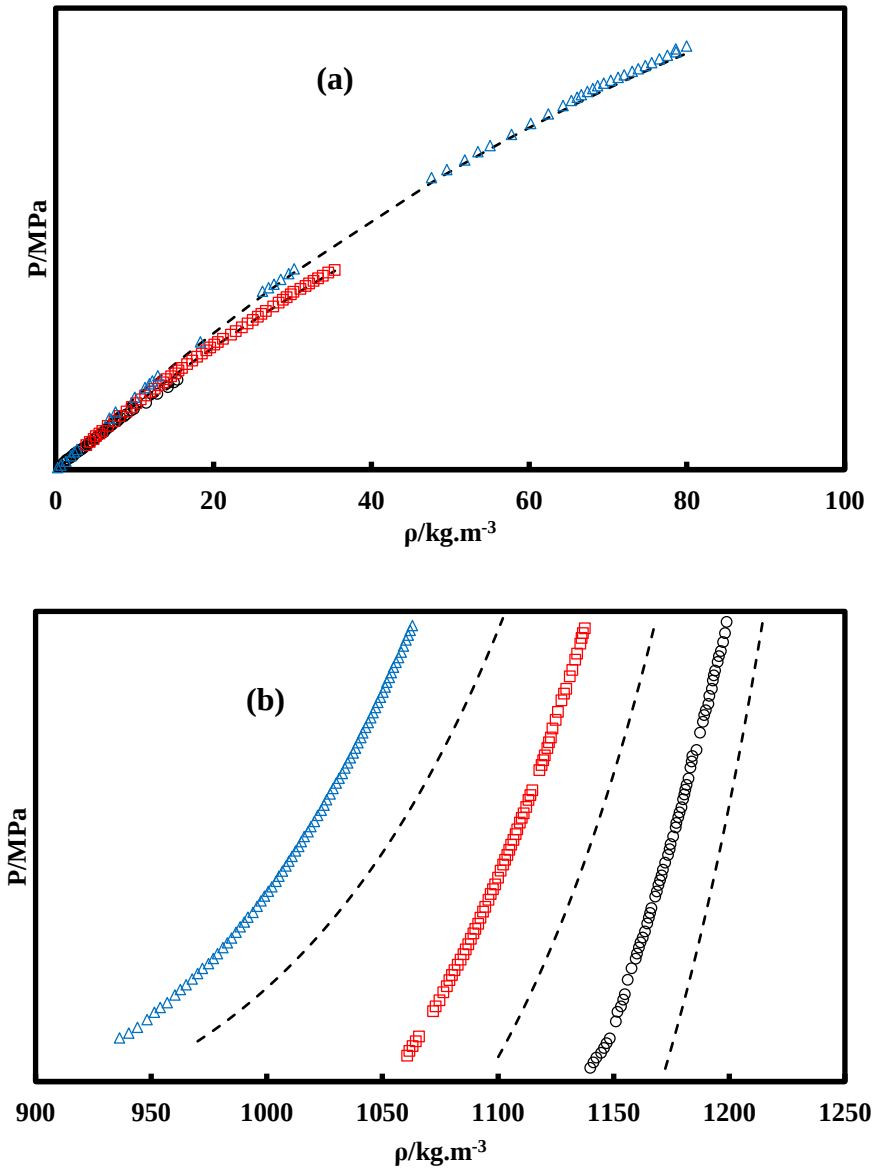

Figure 6.34 Density prediction for (R134a + R152a + R1234yf), 3rd composition. (a): Vapour phase. (b): Liquid phase. (○): 278.15 K; (□): 303.15 K; (Δ): 333.15 K; (- - - -) NEoS.

Concluding remarks

In this Chapter, the results of the prediction using the NEoS were presented for the mixtures of refrigerants.

In a first part, the NEoS was used to predict the VLE diagrams for six binary systems from the literature, including two quasi-ideal systems, two azeotropic systems, and two supercritical systems. Then, the NEoS was used to predict the density of the binary mixtures R421A and R508A, and the ternary mixture R404A at saturation and out of saturation. The results of the prediction were compared to the data from REFPROP 9.0, in addition to a comparison with other cubic EoSs (PT-EoS and PR-EoS).

In a second part, the NEoS was used to calculate the thermodynamic properties of the mixtures of refrigerants studied experimentally during this thesis, mainly to predict their phase diagrams, and then to predict their vapour and liquid density out of saturation.

From all the results obtained for VLE prediction, we can deduce that considering an adjusted binary interaction parameter k_{ij} is necessary to model accurately the VLE behaviour of some systems (azeotropic and supercritical systems). Indeed, a k_{ij} parameter is needed for systems including asymmetric components (in terms of molecular size, and nature and strength of intermolecular interactions, such as the quadrupolar ones, for instance).

It would be interesting to assess the effect of using mixing rules more complex than the van der Waals ones, such as g^E –mixing rules, and of adding a polar term to the NEoS, to take into account the polarity of refrigerants.

Inspired from the work of Jaubert and co-workers (Jaubert & Mutelet 2004; Jaubert et al. 2005; Privat et al. 2008; Xu, Jaubert, et al. 2015; Xu, Privat, et al. 2015), an additional path that could be interesting to investigate is to apply a group contribution method to the NEoS, allowing the use of the van der Waals mixing rules, and to calculate a predictive k_{ij}, in the same way that has been applied to PPR78.

For the density prediction, we evaluated the capacity of the NEoS of predicting density, while using predictive pure compounds parameters and $k_{ij} = 0$. The results obtained at saturation, show clearly that the NEoS give better results compared to PT-EoS and PR-EoS, for predicting the liquid density, and in the vicinity of the critical region. The results obtained out of saturation also show better representation for the liquid density compared to PT-EoS and PR-EoS, especially at supercritical temperatures. However, the deviations can still be higher for the liquid single phase in some cases, reaching values of 4%, which leave room to further improvements, in particular by adding a polar term to the expression of the NEoS.

7. Correlations for density and surface tension

Dans ce chapitre, notre intérêt se porte sur le calcul des densités et des tensions superficielles des réfrigérants corps purs à partir de corrélations développées lors de ce travail de thèse.

Les corrélations développées pour les densités sont basées sur les lois d'échelle, reliant ainsi les densités liquide et vapeur à saturation aux températures et densités critiques, par le biais de deux paramètres ajustables A et B.

Ces corrélations ont été utilisées d'une manière prédictive, en développant des relations entre les paramètres A et B de ces corrélations et les densités critiques des réfrigérants. Ainsi ces corrélations peuvent être utilisées pour n'importe quel réfrigérant en disposant seulement de sa densité critique.

Les résultats obtenus à partir de ces corrélations ont été comparés à des données expérimentales pour cinq réfrigérants (R134a, R1234yf, R1234ze(Z), R1243zf et R1233zd(E)), et montrent une bonne capacité de ces corrélations à bien représenter les densités de ces fluides, particulièrement au voisinage du point critique, où la plupart des équations d'état rencontrent le plus de problèmes.

Les corrélations développées pour les tensions superficielles sont inspirées des travaux sur la théorie du gradient (Miqueu et al. 2000; Miqueu et al. 2003), et consistent en une loi de puissance reliant la tension de surface à la différence entre la densité liquide et vapeur à saturation, au biais de deux paramètres ajustables C et D.

D'une manière similaire que pour les corrélations sur les densités, ces corrélations ont été utilisées d'une manière prédictive, en développant des relations entre les paramètres C et D de et les densités critiques des réfrigérants.

Les résultats obtenus à partir de ces corrélations ont été comparés à des données expérimentales pour les mêmes réfrigérants (R134a, R1234yf, R1234ze(Z), R1243zf et R1233zd(E)), et montrent une capacité en général bonne de ces corrélations à bien représenter les tensions superficielles de ces fluides.

Les corrélations développées lors de cette thèse peuvent être très utiles pour la génération des données pour les densités et les tensions de surface pour les fluides dont on ne dispose pas d'assez de données expérimentales (comme le cas des réfrigérants de nouvelle génération). Les données générées peuvent être utiles pour la validation des modèles thermodynamiques prédictifs et l'ajustement de leurs paramètres.

Introduction

The conception and design of organic Rankine cycle (ORC), refrigeration machines or heat pumps require accurate thermophysical properties. Densities and surface tensions are examples of the properties needed.

As a complement to experiment, predictive models, as well as molecular simulation are of a great interest. In addition, suitable correlations can be used to generate thermophysical data, that can be used when experimental data are not available, and also to test and validate the thermodynamic models used for the prediction. Our interest in this Chapter is oriented to the density and surface tension properties.

Surface tension is a basic but often overlooked physical property that plays an important role in chemical engineering applications. For instance, the surface tension influences the heat transfer, the flow, and the phase-change characteristic of the working fluid. The control of surface tension is essential for condenser and evaporator design in a refrigerator (Zhao et al. 2010). Surface tension is also important to analyse the heat transfer through a heat-exchanging surface with bubbles or fluid drops on it (Lin & Duan 2003).

Several attempts have been made to determine the surface tension of simple fluids and mixtures ranging from simple empirical correlations to those based on statistical thermodynamics. The parachor method (Macleod 1923; Sugden 1924b; Sugden 1924a; Weinaug & Katz 1943) and its derivatives, the corresponding states principle (Guggenheim 1945; Zuo & Stenby 1997; Kim et al. 2009), Monte Carlo simulation (Attard & Moule 1993; Gloor et al. 2005), molecular dynamic simulation (Vega & de Miguel 2007), perturbation theory (Toxvaerd 1972; Haile et al. 1976), density functional theory (Evans 1979; Winkelmann et al. 1994; Winkelmann 1994) and gradient theory (Cahn & Hilliard 1958; Rowlinson 1979; Miqueu et al. 2003) are all examples of methods that can be applied to compute surface tension.

In this Chapter, correlations have been developed for pure compounds refrigerants, in order to calculate the liquid and vapour densities at saturation, as well as the interfacial tensions.

The only property needed to determine the parameters of these correlations is the critical density.

Based on the correlations developed for densities, other correlations were obtained for the surface tensions, from the difference between the liquid and vapour densities at saturation.

The correlations developed for densities are based on the scaling laws relations, allowing one to describe the density all along the saturation curve. The results obtained with these correlations are in good agreement with the experimental data. The results are particularly

interesting around the critical region, where most equations of state fail to reproduce correctly densities in this region.

The correlations developed for surface tension are deduced directly from the densities calculated at saturation through a power law relating the surface tension to the difference between liquid and vapour densities at saturation.

The results obtained with these correlations are in good agreement with the experimental data.

7.1. Density calculations

The determination of the critical temperature T_c and the critical density ρ_c, can be obtained usually from the densities at saturation, by using two laws. The first is a scaling law directly related to the difference between the liquid and vapour densities at saturation, and the second is the law of rectilinear diameters. The two laws can be expressed by Eq. (7.1) as follows:

$$\begin{aligned} \rho^L - \rho^V &= A(T - T_c)^\beta \\ \frac{\rho^L + \rho^V}{2} &= B(T - T_c) + \rho_c \end{aligned} \tag{7.1}$$

where A and B are adjusted parameters, and β is a universal exponent constant (β = 0.325). ρ^L and ρ^V are respectively the liquid and vapour densities at saturation, and T is the temperature. These equations have been previously considered to estimate the critical properties of the R1216 from density measurements (Coquelet et al. 2010).

In this work, our aim was to develop correlations allowing the calculations of the parameters A and B for a given component, from only knowing its experimental critical density ρ_c.

In order to establish these correlations, an adjustment of the parameters A and B was performed, using the data of 33 pure compounds obtained from REFPROP 9.0 (Lemmon et al. 2010). The data needed are the liquid and vapour densities at saturation, as well as the critical temperature and the critical density.

The temperature range used for the parameters fitting is from T_r = 0.6 to 1 (T_r is the reduced temperature; $T_r = T/T_c$).

The parameters A and B are determined by minimizing the difference between the calculated densities and the densities obtained from REFPROP 9.0, according to the following objective function:

$$F_{obj} = \left[\sum_{1}^{N} \left(\rho_{exp}^{L} - \rho_{cal}^{L} \right)^2 + \sum_{1}^{N} \left(\rho_{exp}^{V} - \rho_{cal}^{V} \right)^2 \right] \tag{7.2}$$

The values of the adjusted parameters A and B are reported in Table 7.1.

Table 7.1 Adjusted parameters A and B for several refrigerants families.

Families	*Compounds*	ρ_c/mol m^{-3}	*A*	*B*
PFC	RC318	3099.40	1689.64	8.14
	R14	7109.40	4319.78	25.19
	R116	4444.00	2608.23	14.63
	R218	3340.00	1854.75	9.22
CFC	R11	4033.00	2007.09	7.96
	R12	4672.80	2449.62	10.73
	R13	5580.00	3143.02	15.90
	R113	2988.70	1527.13	6.48
	R114	3393.20	1773.97	7.72
	R115	3980.00	2102.44	9.15
HCFC	R21	5110.80	2573.42	10.43
	R22	6058.20	3289.14	15.66
	R123	3596.40	1842.42	7.79
	R124	4103.30	2190.19	10.06
	R141b	3921.00	1955.16	7.80
	R142b	4438.00	2346.50	10.61
HFC	R125	4779.00	2698.76	13.97
	R134a	5017.15	2791.92	14.09
	R143a	5128.50	2926.46	15.60
	R152a	5571.50	3094.75	15.62
	R161	6280.00	3494.62	17.72
	R227ea	3495.00	1917.89	9.35
	R23	7520.00	4507.85	26.63
	R236ea	3703.00	1990.00	9.32
	R236fa	3626.00	1963.39	9.33
	R245ca	3906.00	2021.01	8.72
	R245fa	3850.00	2046.80	9.37
	R32	8150.10	4803.26	27.75
	R365mfc	3200.00	1625.56	6.72
	R41	9300.00	5418.75	30.16
HFO	R1234yf	4170.03	2304.64	11.45
	R1234ze	4290.00	2338.12	11.25
NATURAL FLUIDS	CO_2	10624.86	6179.78	33.15

Once the parameters A and B adjusted, two correlations were determined, one relating the parameter A to the experimental critical density ρ_c, and the other one relating the parameter B to the parameter A, through a linear relation.

The correlations obtained are expressed by Eq. (7.3) as follows:

$$A = 0.6232\rho_c - 347.2671$$
$$B = 0.0062A - 3.3452 \quad (7.3)$$

The graphical representations of the correlations obtained are displayed in Figure 7.1 and Figure 7.2, from which we can see that we have excellent trends between the parameter A and the critical density ρ_c from one hand (with a coefficient of determination $R^2 = 0.99$), and between the parameter B and the parameter A from the other hand (with a coefficient of determination $R^2 = 0.98$).

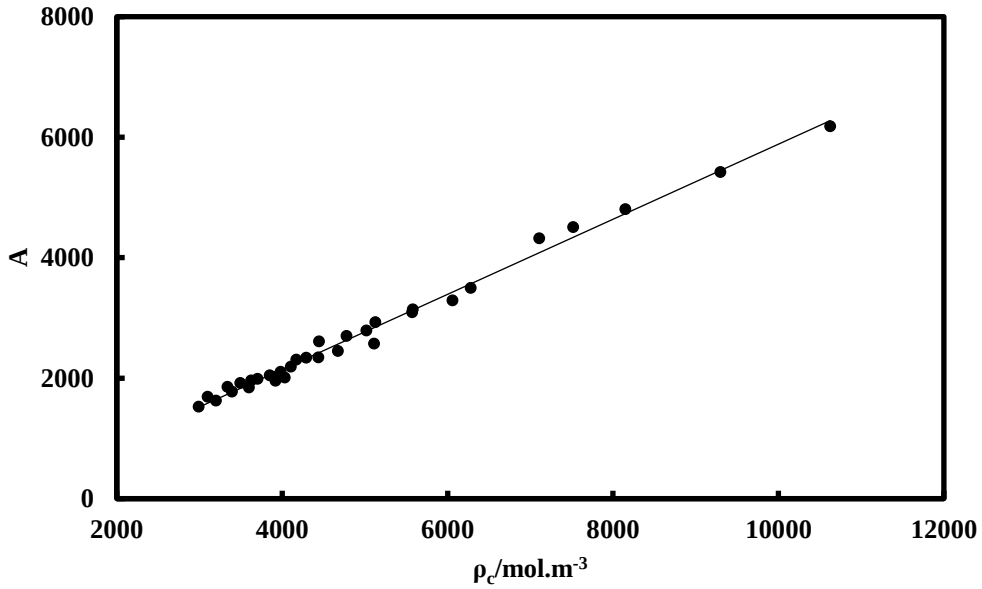

Figure 7.1 The parameter A as a function of the experimental critical density ρ_c. (Coefficient of determination $R^2 = 0.99$).

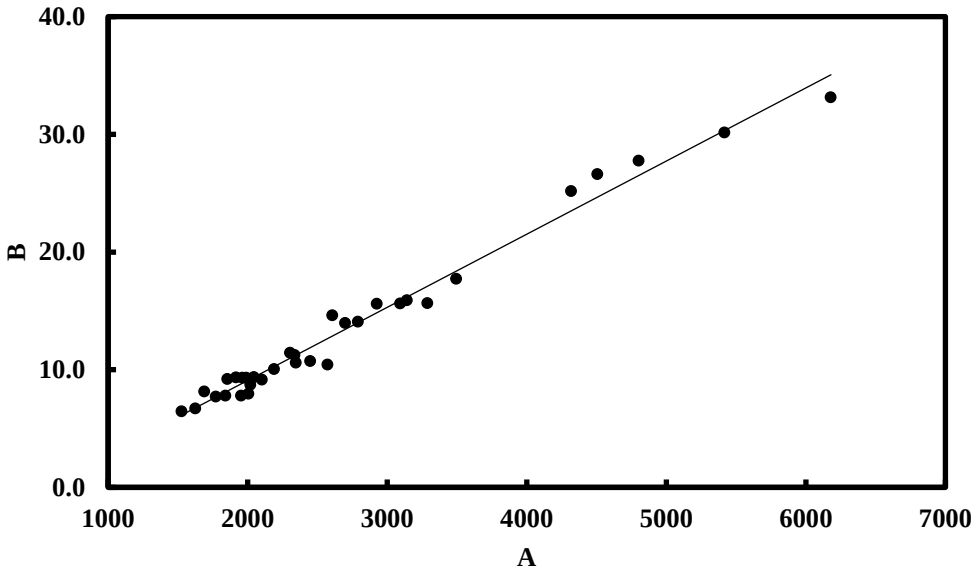

Figure 7.2 The parameter B as a function of the parameter A. (Coefficient of determination R^2 = 0.98).

These correlations are then used to recalculate the parameters A and B (different from the adjusted parameters A and B). These parameters are used to generate the density curve at saturation for selected refrigerant fluids, including the HFC: R134a; the HFOs: R1234yf, R1234ze(Z), and R1243zf; and the HCFO: R1233zd(E).

The results of the calculations are displayed in Figure 7.3 to Figure 7.7.

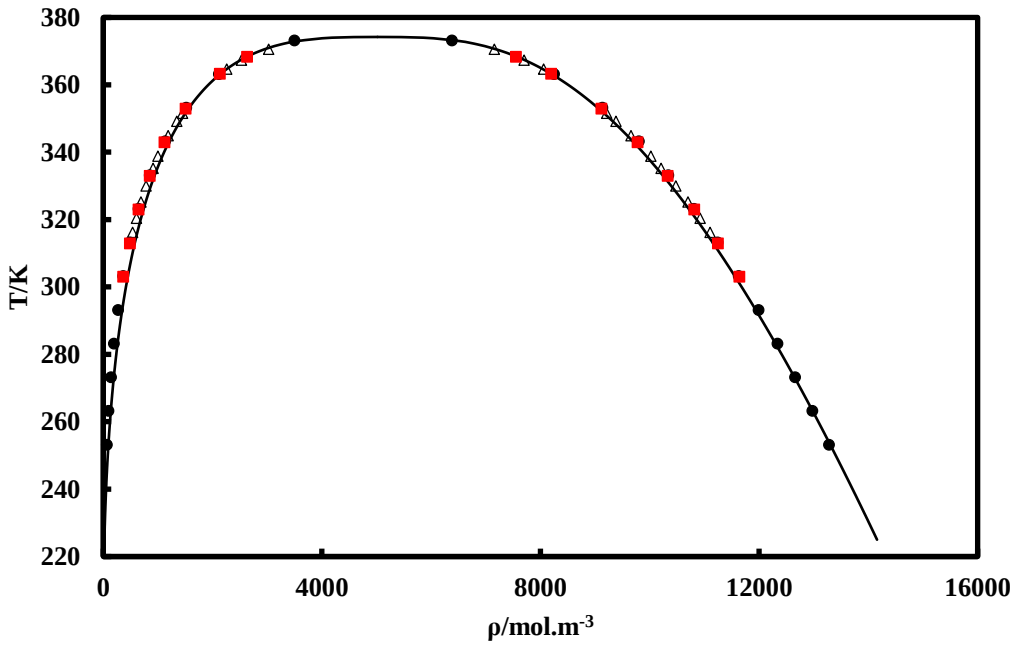

Figure 7.3 T-ρ diagram for R-134a. (Δ) (Niesen et al. 1994); (●) (Chae et al. 1990); (■) (Zhao et al. 2014); (——) Correlation.

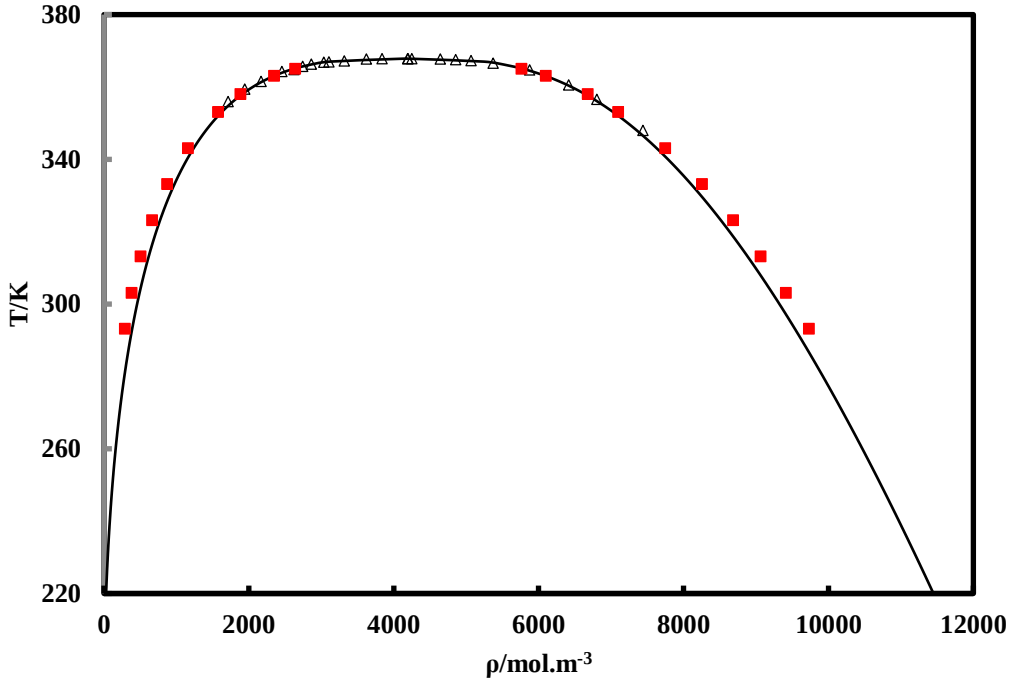

Figure 7.4 T-ρ diagram for R-1234yf. (Δ) (Tanaka & Higashi 2010b); (■) (Zhao et al. 2014); (──) Correlation.

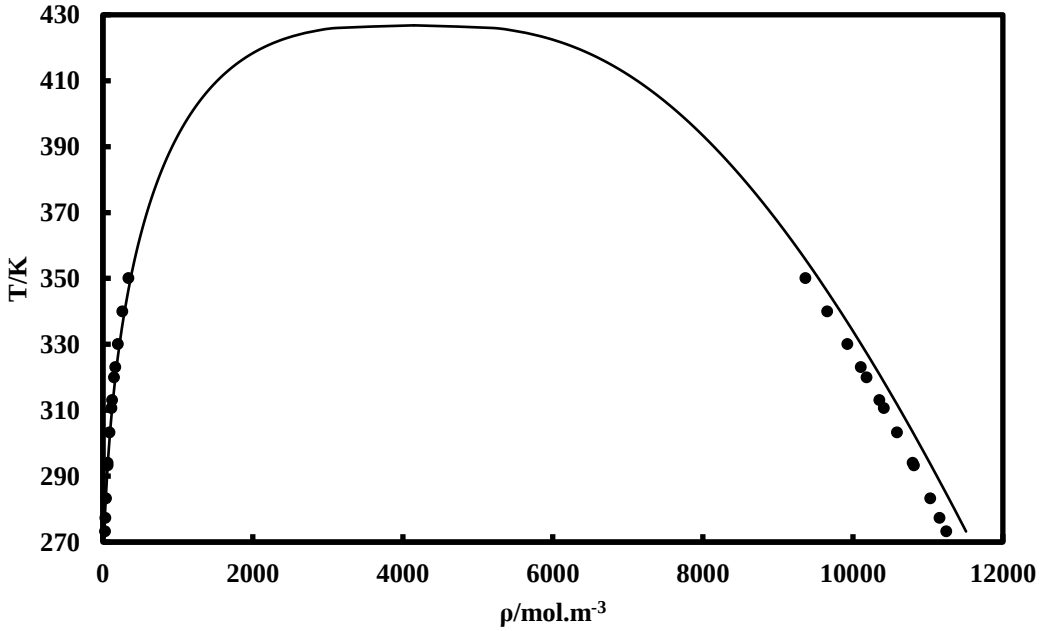

Figure 7.5 T-ρ diagram for R-1234ze(Z). (●) (Kondou et al. 2015); (──) Correlation.

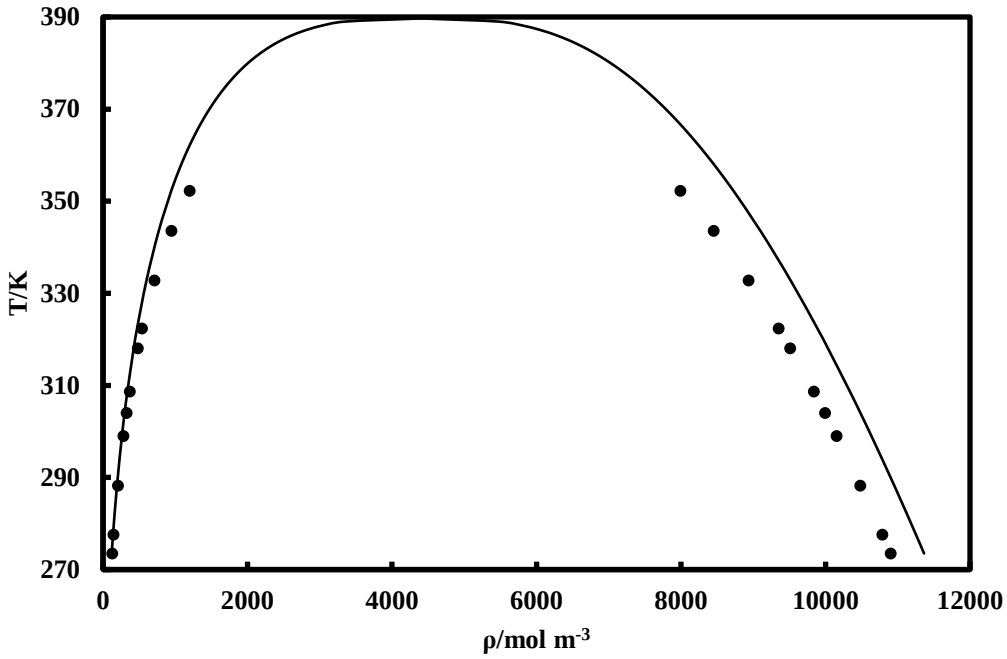

Figure 7.6 T-ρ diagram for R-1243zf. (●) (Kondou et al. 2015); (—) Correlation.

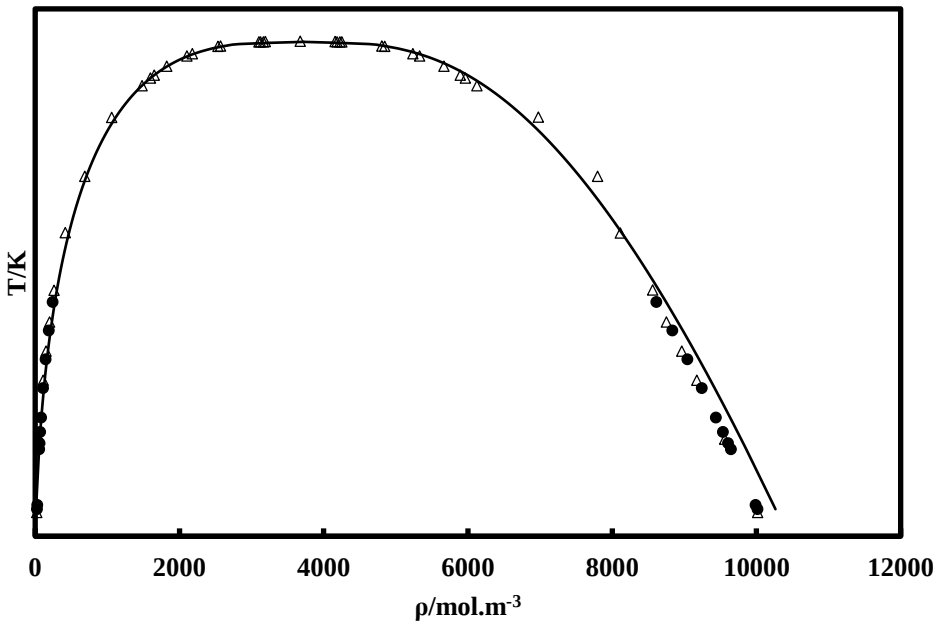

Figure 7.7 T-ρ diagram for R-1233zd(E). (Δ) This work; (●) (Kondou et al. 2015); (—) Correlation.

Based on the results of the calculations, the average relative deviation (ARD) and the BIAS of the correlations to the experimental data were calculated. The ARD and the BIAS are calculated according to Eq. (5.1) (defined in Chapter 5).

The ARD and BIAS calculated for the different fluids studied are reported in *Table 7.2***.**

Table 7.2 ARD and BIAS of saturated liquid and vapour densities.

Compounds	*Data reference*	*ARD (%)*		*BIAS (%)*	
		ρ^L	ρ^V	ρ^L	ρ^V
R134a	(Chae et al. 1990)	0.6	19.1	0.4	-19.1
	(Niesen et al. 1994)	0.6	7.2	0.5	-6.6
	(Zhao et al. 2014)	0.6	9.1	0.5	-9.0
R1234yf	(Tanaka & Higashi 2010b)	1.1	2.1	-0.2	-1.4
	(Zhao et al. 2014)	1.3	12.5	1.3	-12.4
R1234ze(Z)	(Kondou et al. 2015)	2.0	12.1	-2.0	1.5
R1243zf	(Kondou et al. 2015)	5.6	12.2	-5.6	12.2
R1233zd(E)	(Kondou et al. 2015)	2.0	16.4	-2.0	7.2
	(This work)	2.1	21.9	-2.1	0.6

From the graphical representation, we can see that the correlations provide good results for the refrigerants selected, with very good accuracy for some compounds (R134a for instance), but less good accuracy for others (R1243zf, especially for liquid densities).

From analysing the deviations from the experimental results, we can see that the liquid phase is in overall well represented, with a maximal deviation of 5.6%, while we notice some important deviation for the vapour phase (33.2% for R1234yf, for example). The deviation is more important at low temperature for the vapour phase, where the density is low.

7.2. Surface tensions calculations

For the calculations of the surface tensions σ, we use the calculated densities at saturation, obtained using the correlations developed previously.

Inspired from the parachor method (Wright 1961), and from correlations relating the surface tension to the temperature (Miqueu et al. 2000; Miqueu et al. 2003), correlations have been developed relating the interfacial tension to the densities, in a similar way to the general relation of the density-gradient theory:

$$\sigma = \sqrt{2c} \int_{\rho_V}^{\rho_L} \sqrt{f_0(\rho) - \sum_i \rho_i \mu_i - P_{equil}} d\rho \tag{7.4}$$

where σ is the surface tension, f_0 the Helmholtz free energy density, μ the chemical potential, P_{equil} the equilibrium pressure and c a real constant. This relation basically defines the interfacial tension from an integral over the density.

From the densities calculated using the correlations developed before, we establish a relation between the difference of saturated liquid and vapour densities Δρ ($\Delta\rho = \rho^L - \rho^V$) and the surface tension σ, according to the following power law relation:

$$\sigma = C \Delta\rho^D \tag{7.5}$$

Where C and D are two adjustable parameters, obtained using the data of 33 pure compounds obtained from REFPROP 9.0. The data needed are the surface tensions. The temperature range used for the parameters fitting is T_r = 0.6 to 1.

The parameters adjustment is achieved by minimizing the difference between the calculated surface tension and the surface tension given by REFPROP 9.0, according to the following objective function:

$$F_{obj} = \sum_1^N \left(\sigma_{exp} - \sigma_{cal}\right)^2 \tag{7.6}$$

The adjusted parameters C and D are reported in *Table 7.3*.

Table 7.3 Adjusted parameters C and D for several refrigerants families.

Families	*Compounds*	ρ_c/*mol* m^{-3}	$C\times10^{18}$	*D*
PFC	RC318	3099.40	9.65	3.89
	R14	7109.40	2.43	3.71
	R116	4444.00	7.23	3.77
	R218	3340.00	9.21	3.86
CFC	R11	4033.00	7.97	3.78
	R12	4672.80	6.81	3.74
	R13	5580.00	5.18	3.71
	R113	2988.70	9.85	3.89
	R114	3393.20	9.12	3.84
	R115	3980.00	8.06	3.79
HCFC	R21	5110.80	6.02	3.72
	R22	6058.20	4.32	3.69
	R123	3596.40	8.75	3.82
	R124	4103.30	7.84	3.78
	R141b	3921.00	8.17	3.79
	R142b	4438.00	7.24	3.75
HFC	R125	4779.00	6.62	3.74
	R134a	5017.15	5.00	3.75
	R143a	5128.50	5.99	3.72
	R152a	5571.50	5.20	3.70
	R161	6280.00	2.46	3.73
	R227ea	3495.00	8.93	3.84
	R23	7520.00	1.03	3.77
	R236ea	3703.00	8.56	3.82
	R236fa	3626.00	8.70	3.83
	R245ca	3906.00	8.19	3.80
	R245fa	3850.00	9.52	3.79
	R32	8150.10	0.33	3.85
	R365mfc	3200.00	9.47	3.86
HFO	R1234ze	4290.00	7.59	3.77

Once the parameters C and D adjusted, two correlations were determined, one relating the parameter C to the experimental critical density ρ_c through a linear relation, and the other one relating the parameter D to the same experimental critical density ρ_c, through a second order polynomial relation.

The correlations obtained are expressed by Eq. (7.7) as follows:

$$C = -0.0019\rho_c + 15.7422$$
$$D = 2\times10^{-8}\rho_c{}^2 - 0.0003\rho_c + 4.5056 \quad (7.7)$$

The graphical representations of the correlations obtained are displayed in Figure 7.8 and Figure 7.9, where we can see that we have very good trends between the parameter C and the critical density (ρ_c) from one hand (with a coefficient of determination $R^2 = 0.98$), and between the parameter D and the critical density (ρ_c) from the other hand (with a coefficient of determination $R^2 = 0.96$).

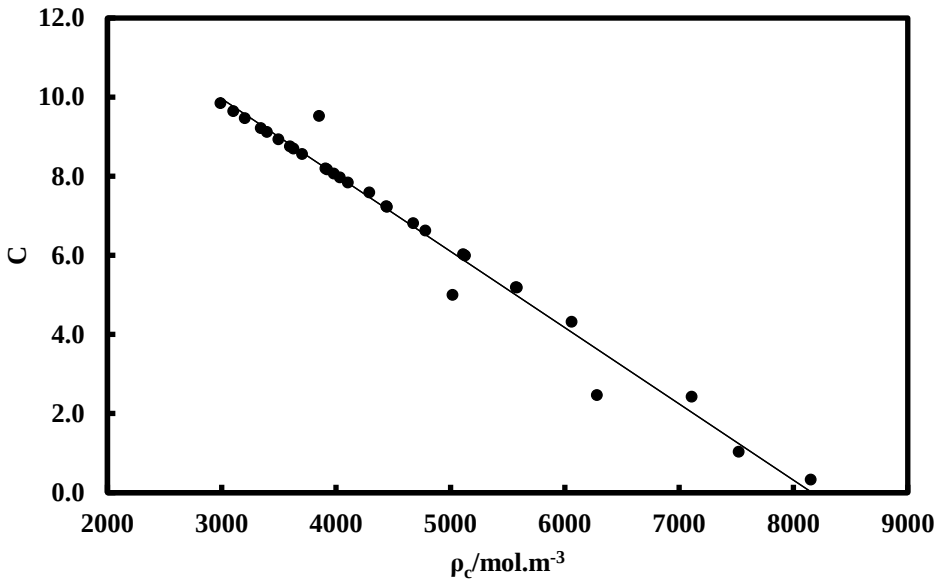

Figure 7.8 The parameter C as a function of the experimental critical density ρ_c. (Coefficient of determination $R^2 = 0.98$).

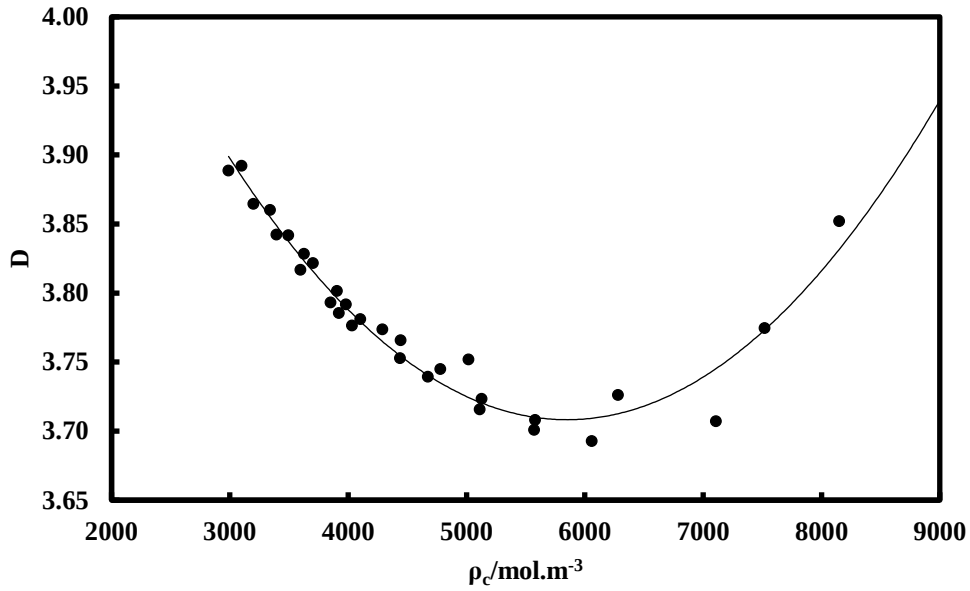

Figure 7.9 The parameter D as a function of the experimental critical density ρ_c. (Coefficient of determination $R^2 = 0.96$).

Once the correlations established, they are used to recalculate the parameters C and D. We use these parameters to calculate the surface tension, for the same refrigerant fluids studied before, including the HFC: R134a; the HFOs: R1234yf, R1234ze(Z), and R1243zf; and the HCFO: R1233zd(E). The results obtained are displayed in Figure 7.10 to Figure 7.14.

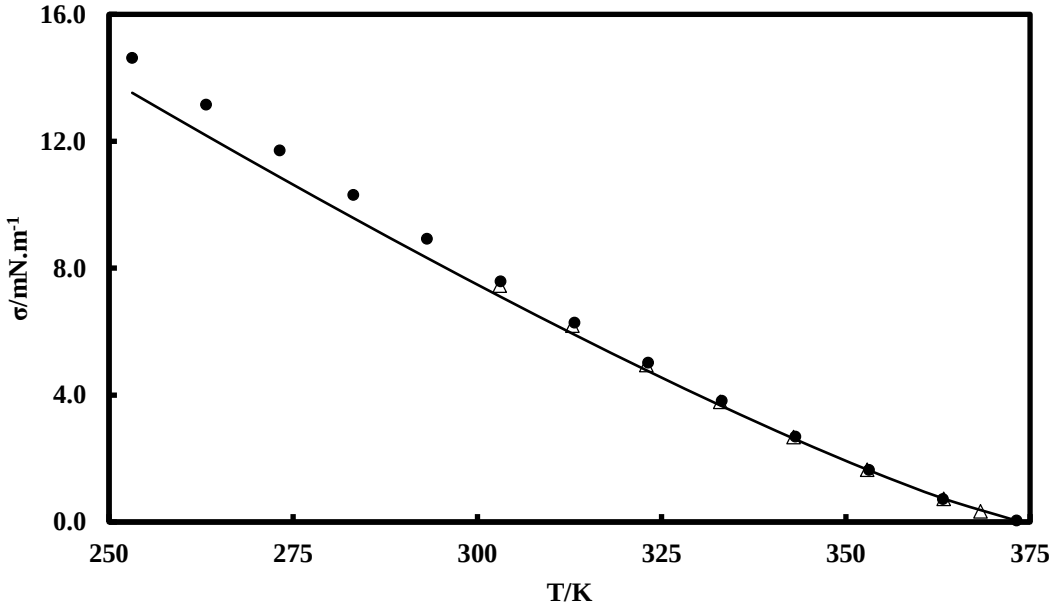

Figure 7.10 σ-T diagram for R134a. (●) (Chae et al. 1990); (Δ) (Zhao et al. 2014); (—) Correlation.

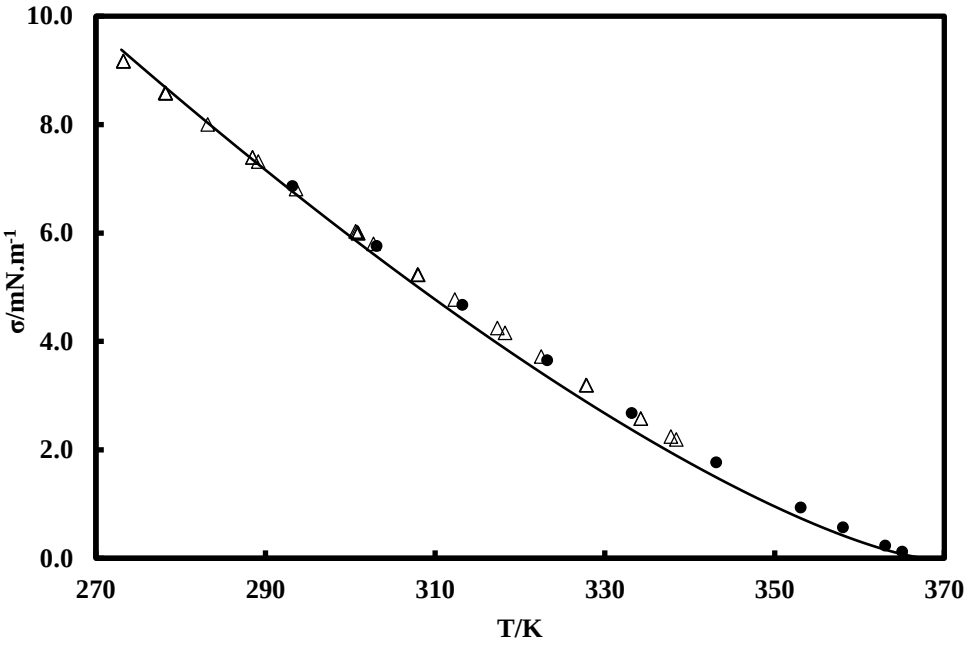

Figure 7.11 σ-T diagram for R1234yf. (●) (Zhao et al. 2014); (Δ) (Tanaka & Higashi 2010b); (—) Correlation.

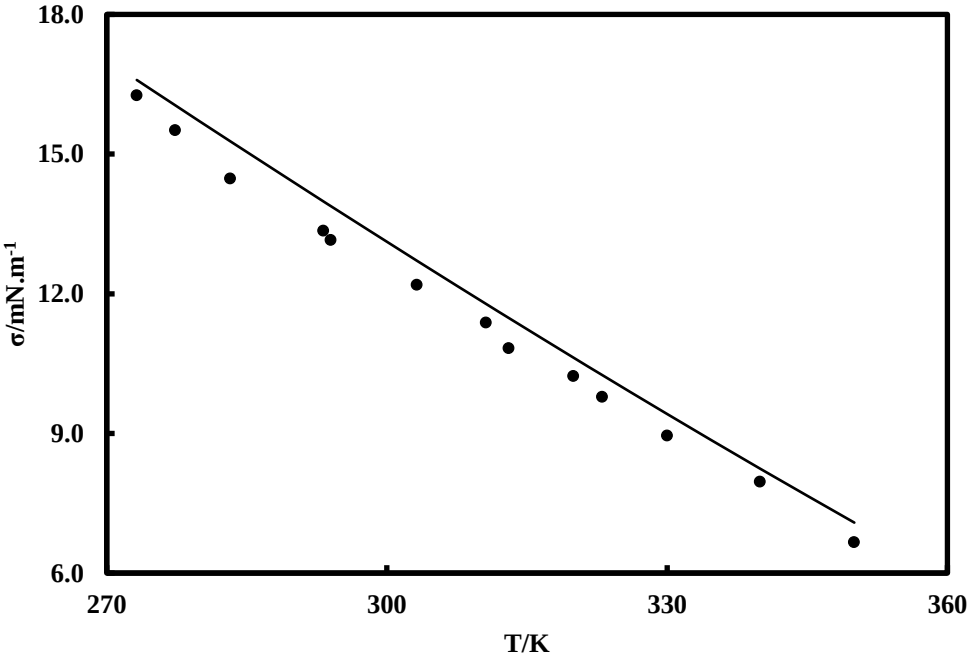

Figure 7.12 σ-T diagram for R1234ze(Z). (●) (Kondou et al. 2015); (—) Correlation.

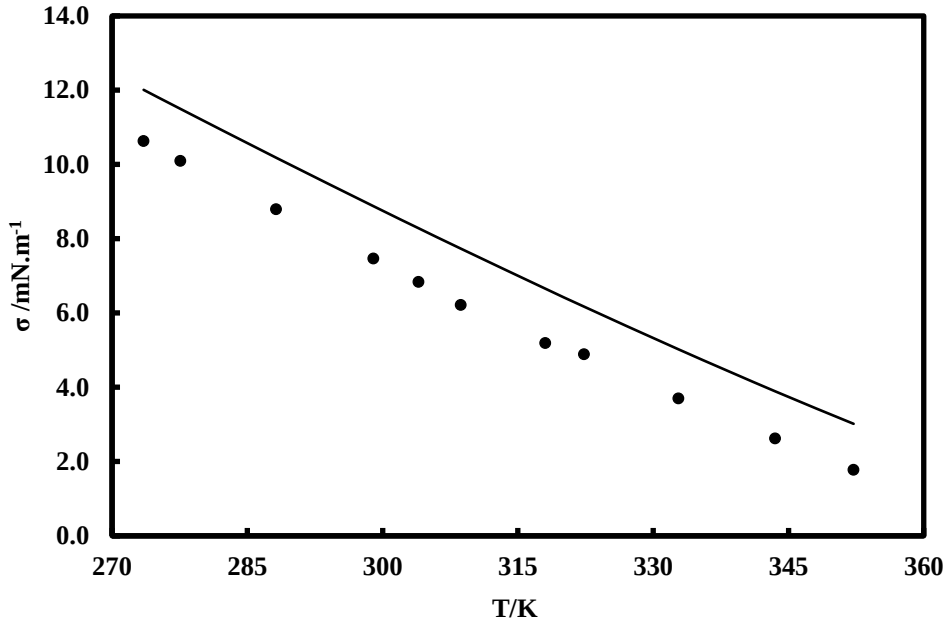

Figure 7.13 σ-T diagram for R1243zf. (●) (Kondou et al. 2015); (──) Correlation.

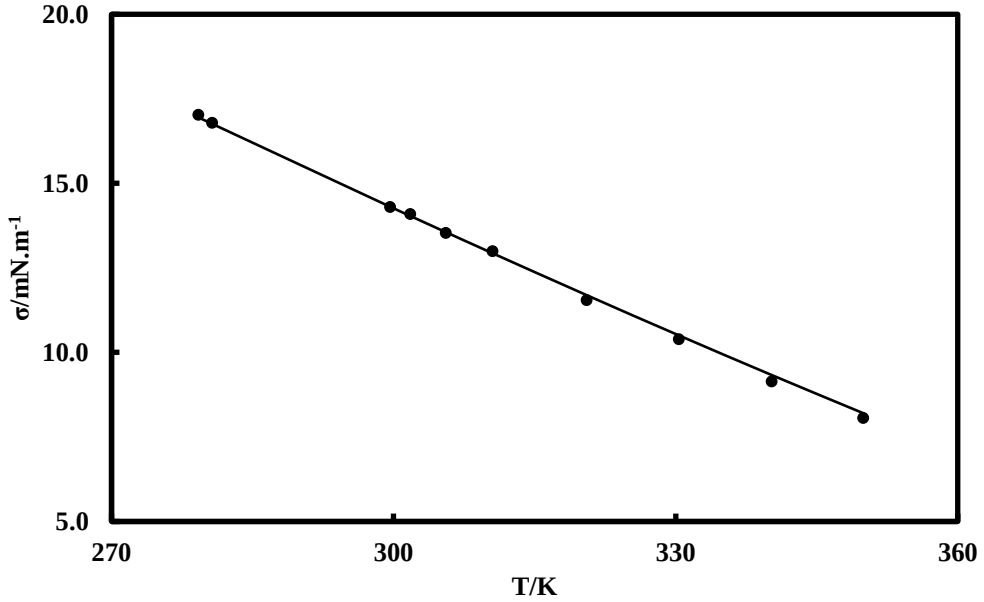

Figure 7.14 σ-T diagram for R1233zd(E). (●) (Kondou et al. 2015); (──) Correlation.

Based on the results of the calculations, the ARD and the BIAS of the correlation to the experimental data were calculated, as reported in Table 7.4.

Table 7.4 ARD and BIAS of surface tension for different compounds.

Compounds	*Data reference*	σ	
		ARD (%)	*BIAS (%)*
R134a	(Chae et al. 1990)	5.7	3.7
	(Zhao et al. 2014)	2.7	1.5
R1234yf	(Zhao et al. 2014)	26.1	-26.1
	(Tanaka & Higashi 2010b)	5.5	-4.8
R1234ze(Z)	(Kondou et al. 2015)	4.5	-4.5
R1243zf	(Kondou et al. 2015)	28.6	-28.6
R1233zd(E)	(Kondou et al. 2015)	0.8	-0.5

From the graphical representation, we can see that the calculations obtained using the correlations are in good agreement with the experimental results. The results are very accurate for some compounds (R1233zd(E) for instance), but less accurate for other compounds (such as R1243zf).

From analysing the deviations to experimental results, one can see that the surface tension is in overall well represented, with a maximal deviation of 28.6% (in the case of R1243zf), and 26.1% (in the case of R1234yf). These deviations are more important at high temperatures where the surface tensions are low.

Concluding remarks

In this Chapter, we introduced two correlations for densities and surface tension calculations. The correlations for densities are based on the scaling laws relations, while the correlations for surface tension are deduced directly from the calculated densities through a power law relation. The correlations developed give results in good agreement with the experimental data, in representing the vapour and liquid densities at saturation. In particular, the densities are very well represented in the vicinity of the critical region.

The results obtained for interfacial tensions are also satisfactory, with very good agreement to the experimental data for some refrigerants (R1233zd(E)).

The correlations are among the simplest and fastest tools, and easy to use. The correlations developed in this work can be very useful to generate data of densities and interfacial tensions for the pure compounds with no data available in the literature (as it is the case for many new generation refrigerants, HFOs and HCFOs). The data generated can also be used to test and validate the predictive thermodynamic models developed.

An additional path that would be interesting to investigate is to use the NEoS for surface tensions calculations in order to test and compare the results obtained with the correlations.

8. Viscosity measurements

Ce chapitre a pour objet de présenter les mesures de viscosités faites lors de ma période de visite à l'Imperial College London. Ce séjour a eu lieu au Thermophysics Laboratory, au sein du groupe de recherche du Professeur J.P. Martin Trusler, pour une période de cinq mois.

Les mesures établies lors de ce séjour concernent les viscosités des deux réfrigérants R134a et R1234yf. L'appareil utilisé pour les mesures de viscosités est un viscomètre-densimètre à fil vibrant (VWVD), qui permet une mesure simultanée de la densité et la viscosité du fluide étudié. Le VWVD peut opérer à très hautes températures (jusqu'à 473 K) et à très hautes pressions (jusqu'à 200 MPa), et il est basé sur une méthode statique-synthétique à température fixe.

Les mesures des viscosités-densités des deux réfrigérants étudiés ont été faites pour des températures allant de 303 K à 393 K dans le cas du R134a et de 303 K à 423 K dans le cas du R1234yf.

Dans ce chapitre, nous présentons le principe du fil vibrant et la théorie bien établie derrière. Ensuite nous nous intéressons à présenter et à décrire l'équipement expérimental utilisé et ses différentes composantes, pour enchaîner après par la présentation de la procédure expérimentale suivie et la procédure d'étalonnage afin d'avoir de des mesures correctes et précises.

Les résultats des mesures expérimentales de viscosités et densités obtenus sont présentés et comparés aux résultats de REFPROP 9.0, ainsi qu'à des données issues de la littérature. Les mesures de densités du R134a obtenues à partir du VWVD sont comparées aux mesures obtenues en utilisant le densimètre à tube vibrant (mesures établies au CTP). Cette comparaison montre que les deux appareils de mesures donnent les mêmes résultats.

Dans le but d'avoir un outil de calcul des viscosités, un modèle basé sur la théorie de la friction a été développé. Ce modèle nécessite d'utiliser une équation d'état avec; dans notre cas nous avons utilisé la NEoS; et trois paramètres de friction ajustables. Les paramètres de friction de ce modèle ont été ajustés sur les données expérimentales mesurées lors de ce travail.

Les viscosités calculées à partir de ce modèle sont comparées aux mesures expérimentales, montrant une bonne capacité de ce modèle à bien représenter les viscosités dans un large domaine de températures et de pressions.

Il serait toutefois intéressant de tester les capacités de ce modèle en mode prédictif (sans ajustement des paramètres de friction sur des données expérimentales). Comme point de départ, nous avons essayé de voir la dépendance de ces paramètres de la température. Ceci pourrait être une piste à étudier pour voir la possibilité de développer par exemple des corrélations liant ces paramètres à la température.

Introduction

This chapter is dedicated to present the work carried out during my visiting period to Imperial College London. This short stay took place at the Chemical Engineering Department, within the research group of Prof. J.P. Martin Trusler, and aimed to perform experimental measurements of the viscosities of the refrigerants.

To achieve that, a vibrating-wire viscometer-densimeter (VWVD) was used, providing simultaneous measurements of densities and viscosities.

The viscosity is an important transport property for many industrial applications, and arouses interest in different industries, from petroleum to refrigeration industry. In particular for the refrigeration industry, the knowledge of the viscosities (along with the densities) is important for the optimal design of refrigeration cycles and equipment and the characterization of systems of (refrigerant + lubricant) (Ciotta 2010).

The aim of this work is to complete the data obtained for density and VLE measurements, with viscosity measurements, and also compare the data of the densities obtained from the two equipments used (the vibrating-tube densimeter and the vibrating-wire viscometer-densimeter).

In this chapter, we first present the principle of the vibrating wire, then we give the description of the equipment used, along with the experimental procedure followed. Then, the results obtained are presented and compared to other experimental data from the literature in addition to REFPROP 9.0 data. Finally, we present a model based on the friction theory to correlate the experimental viscosities measured.

8.1. Principle of the vibrating wire

Vibrating wire sensors have been widely used to determine viscosity and density of fluids under high temperature and pressure conditions, due to their versatility (Caudwell et al. 2004; Ciotta et al. 2009; Dix et al. 1991; Ciotta & Trusler 2010; Caudwell 2004).

The theory of the vibrating wire systems relies to the basic idea that a fluid surrounding a vibrating solid body will affect its natural mode of oscillation observed *in vacuo.*

The theory of these devices is well-established and relies upon working equations in which all the parameters have a physical meaning (Retsina et al. 1986; Retsina et al. 1987; Ciotta & Trusler 2010).

In the apparatus employed in this work, the vibrating wire is suspended vertically in the fluid, between the poles of a permanent magnet, and tensioned by a suspended sinker. An alternating current is passed through the wire, setting it into transverse oscillation, and the voltage developed across the wire is measured by means of a lock-in amplifier (Ciotta & Trusler 2010; Caudwell et al. 2009; Caudwell et al. 2004; Ciotta 2010).

The steady-state frequency response of the oscillating wire is measured in the vicinity of the fundamental transverse resonance mode (Ciotta & Trusler 2010; Caudwell et al. 2009; Caudwell et al. 2004).

The resonance frequency of this mode is sensitive to the density of the surrounding fluid, mainly as a consequence of the buoyancy effect exerted on the weight and the resulting changes in the tension of the wire, while the width of the resonance curve is sensitive to the viscosity of the fluid (Ciotta & Trusler 2010; Caudwell et al. 2009; Caudwell et al. 2004).

The measured voltage V comprises mainly two terms: $V_1(f)$ and $V_2(f)$. The first term $V_1(f)$ comes from the electrical impedance of the stationary wire, while the second term $V_2(f)$ is related to the motion of the wire. The measured voltage V is expressed as the sum of the two terms:

$$V = V_1(f) + V_2(f) \tag{8.1}$$

with $V_1(f)$ and $V_2(f)$ expressed as follows:

$$\begin{aligned} V_1(f) &= a_0 + ia_1 + ia_2 f \\ V_2(f) &= \frac{\Lambda f i}{{f_0}^2 - f^2(1+\beta) + f^2(\beta' + 2\Delta_0)i} \end{aligned} \tag{8.2}$$

where a_0, a_1, and a_2 are real constants, f_0 the "buoyancy-corrected" fundamental transverse resonance frequency of the wire in vacuum, Λ the amplitude, Δ_0 the logarithmic decrement of the wire in vacuum and the terms β and β' arise respectively from the added mass and the viscous damping of the fluids.

f_0 is related to the true vacuum resonance frequency $f_{0,vac}$ as follows:

$${f_0}^2 = {f_{0,vac}}^2 - \frac{gV\rho}{4\pi\rho_s R^2 L^2} \tag{8.3}$$

where V is the volume of the sinker, ρ the density of the fluid, g the gravitational acceleration, ρ_s the density of the wire, R the radius of the wire and L the length of the wire.

The true vacuum frequency is approximated by that of an end-pinned rod tensioned by the sinker (Retsina et al. 1986; Ciotta & Trusler 2010), with an additional parameter κ accounting for the non-ideal end condition of the wire, which is a situation in which the end conditions do not conform to either ideal pinned-pinned conditions or ideal clamped-clamped conditions (Retsina et al. 1986; Retsina et al. 1987; Ciotta & Trusler 2010).

$$f_{0,vac} = \kappa\left(\frac{\pi^2 R^2 E}{16\rho_s L^4}\kappa^2 + \frac{mg}{4\pi R^2 \rho_s L^2}\right)^{1/2} \tag{8.4}$$

where m is the mass of the tensioning sinker, E the Young's modulus of the wire material, and κ an empirical parameter that is adjusted to fit the true vacuum resonance frequency (Caudwell et al. 2004; Caudwell 2004).

Accurate results can be obtained with this form, allowing one to measure the viscosity and density of fluids with experimental uncertainties of 2% and 0.2%, respectively (Caudwell et al. 2004; Caudwell 2004; Ciotta et al. 2009; Ciotta & Trusler 2010).

However, Eq. (8.4) is not exact, as the empirical parameter κ does not have a full theoretical justification. To address this problem, another equation was developed by (Ciotta 2010; Ciotta & Trusler 2010) to express the working equation for the resonance frequency, given by:

$$f = \frac{n}{2L}\left[a\sqrt{\frac{(m-\rho V)g}{\rho_s \pi R^2}} + \sqrt{\frac{ER^2}{\rho_s L^2}} + \left(4 + \frac{n^2\pi^2}{2}\right)\sqrt{\frac{E^2\pi R^6}{16(m-\rho V)g\rho_s L^4}}\right] \tag{8.5}$$

It is important to highlight that Eq (8.5) in this form represents the resonance frequency for the hypothetical situation of the wire in vacuum with the sinker immersed in the fluid (Ciotta 2010; Ciotta & Trusler 2010).

The full details about the development of this equation can be found in (Ciotta 2010; Ciotta & Trusler 2010).

8.2. Equipment description

The vibrating-wire viscometer-densimeter (VWVD) used in this work is composed of three main blocks: the vibrating wire cell, the fluid handling system and the accumulator. These three modules are linked together to form a closed loop.

The overall layout of the apparatus is displayed in *Figure 8.1*.

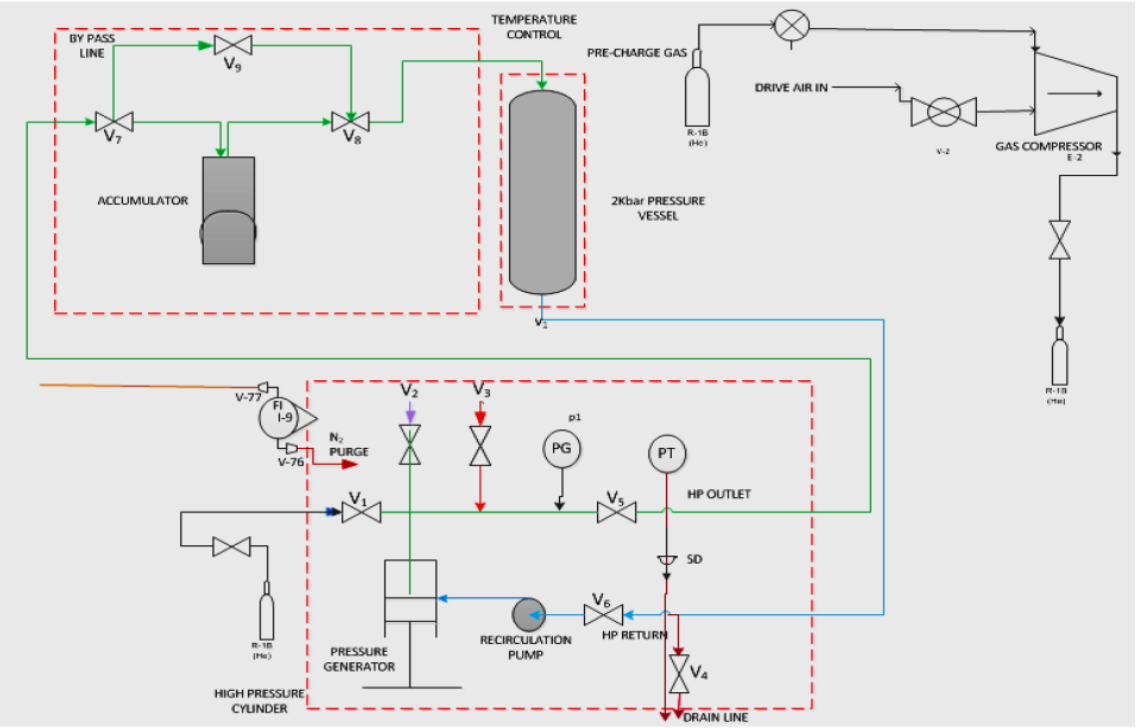

Figure 8.1 Overall layout of the VWVD (Malami & Trusler 2014).

8.2.1. Vibrating wire cell

The vibrating wire cell consists of a tungsten vibrating wire attached to a rigid stainless steel clamp on the top, and tensioned by a sinker attached to the bottom. The wire is placed in the centre of a magnetic field generated by two samarium-cobalt (Sm-Co) permanent magnets, (50×10×4) mm. The magnets are held in a gold-plated iron yoke which is free to rotate around the wire. The rotational movement of the yoke is necessary to orientate the magnetic field generated by the magnets and for the tuning-out of orthogonal vibration modes of the wire. The magnets are plated with nickel to prevent ingress of fluid at high pressures (Ciotta 2010).

Sinkers of different materials and volumes can be adapted to the cell according to the needs. In this work, the sinker used is made of Aluminium (Al).

The cell is placed inside a high-strength stainless steel vessel operating up to pressures of 200 MPa. The barrel was designed to an outer diameter of 79 mm and an inner diameter of 31.75 mm (Ciotta 2010).

The end closure of the barrel is achieved by means of a plug supported by a screw cap. The cap of the vessel also contains two holes where temperature sensors can be immersed.

The schematic of the vibrating wire cell is displayed in *Figure 8.2*.

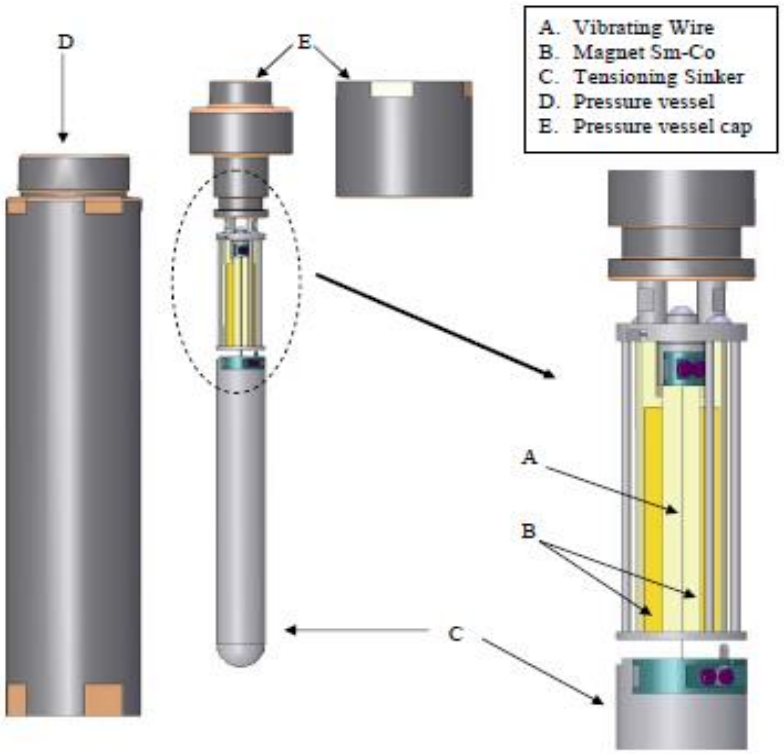

Figure 8.2 Schematic of the vibrating wire cell (Ciotta 2010; Schmidt et al. 2015).

The sealing ring used is a T-shape NBR (Nitrile butadiene rubber). This sealing ring was chosen due its compatibility with fluorinated compounds, and replaced the existing sealing ring FKM-936 (which was not suitable for measurements with fluorinated compounds).

The sealing ring is fitted in the cap of the vessel and supported by two anti-extrusion rings made of PEEK.

The cell is held in place using an aluminium frame to which the vessel is attached. The frame serves also as a support for an automatic lift designed to manoeuvre the vessel during the assembling.

The temperature of the pressure vessel is controlled using an aluminium jacket, weighing approximately 11 kg, in which ten 110 W heater cartridges are inserted to heat the system up to 473 K (Ciotta 2010).

The temperature is controlled by means of a three-channel PID controller regulating the temperature in three distinct zones: top zone, middle zone and bottom zone. The top and bottom zones contain two heaters each, while the middle zone contains six heaters.

Each zone is controlled by a temperature controller (Eurotherm 2216e), while platinum resistance thermometers (PRTs) - positioned on the aluminium block in the middle of each zone - are used to sense the temperature (Ciotta 2010).

An additional thermometer is inserted in the cap of the vessel which in case of excessively high temperature actuated a thermal cut-out relay. The aluminium jacket has an internal loop of 8 mm diameter where a refrigerant fluid can be pumped to cool down the system, when working at temperatures below the ambient temperature.

To ensure a good insulation of the cell in temperatures between 253 K and 473 K, the jacket is placed inside a thick thermal ceramic box (20 mm) (Ciotta 2010; Ciotta & Trusler 2010; Caudwell et al. 2004). The schematic of the assembly is given in *Figure 8.3*.

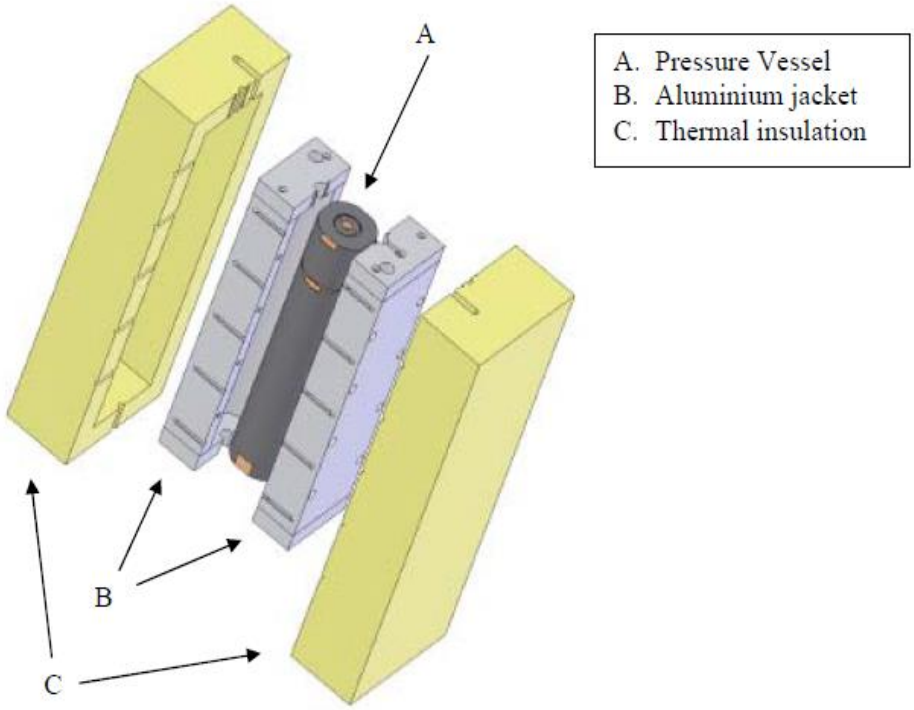

Figure 8.3 Schematic of the assembly (Ciotta 2010; Schmidt et al. 2015).

The electrical connections to the vibrating wire are made at the top and bottom wire clamps using a silver-plated copper lead wire (7-strand 28 AWG) with PTFE insulation. The electrical joints are made of high temperature soft solder (5 % tin, 93.5 % lead, 1.5 % silver alloy, melting point 573 K) (Ciotta 2010).

To connect the sinker with the lead wires fixed to the magnet cage, bare copper wires with a diameter of 50 μm are used. Such a thin wire is chosen in order to minimise the possible variation in the tensioning force due to the plastic deformation of the wires.

To prevent any part of the vessel from making electrical contact with the vibrating-wire circuit PEEK insulators were used where necessary. The lead wires are passed into the system by means of a four-wire feed-through appositely made. The feed-through consisted of four 0.25 mm copper wires, insulated with polyurethane, passed within 1/4" stainless steel nipple with an internal bore of 1.6 mm, and sealed using an epoxy resin (Stycast 2850 FT–Catalyst 9) (Ciotta 2010).

A special six port connection piece was designed to accommodate four commercial single wire feed-throughs rated for operation up to 400 MPa to improve the sealing capability of the resin.

A four wire measuring technique is used to set the vibrating wire into motion and detect the induced voltage, as illustrated in *Figure 8.4*.

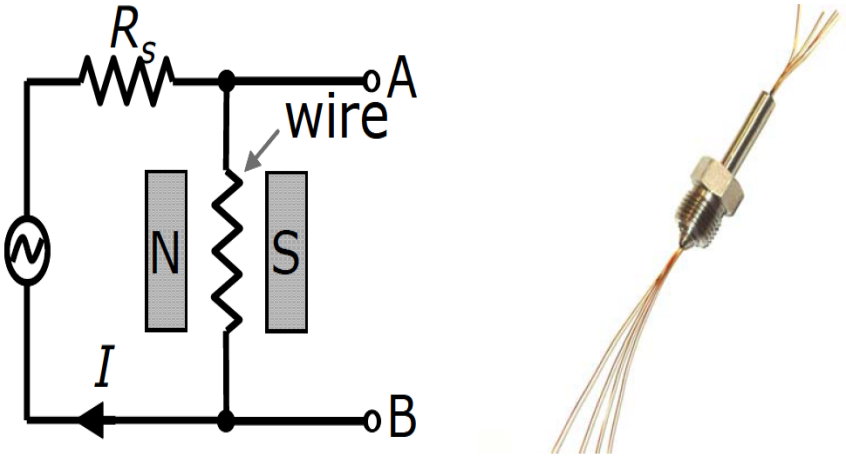

Figure 8.4 Electrical circuit and four pin electrical feed-throughs (Ciotta 2010).

According to Faraday's law, the motion of the vibrating wire in a magnetic field induces a voltage. A lock-in amplifier (Stanford Research Systems SR830 DSP) is used to detect this voltage.

Internally, the inputs are amplified and mixed with the reference frequency, demodulated and filtered to give a DC (direct current) voltage. This technique gives a very narrow bandwidth; hence high amplification of the small signal is possible while ignoring the signals at other frequencies.

The lock-in amplifier used is also able to provide a constant voltage amplitude sinusoidal drive source. By means of a 1.4 kΩ fixed resistor (R_s) in series with the vibrating wire (VW), the constant voltage is converted into a constant current. The fixed resistor has an impedance of less than 1 Ω at the measurement frequency (Ciotta 2010; Caudwell 2004).

The schematic of the lock-in amplifier is displayed in *Figure 8.5*.

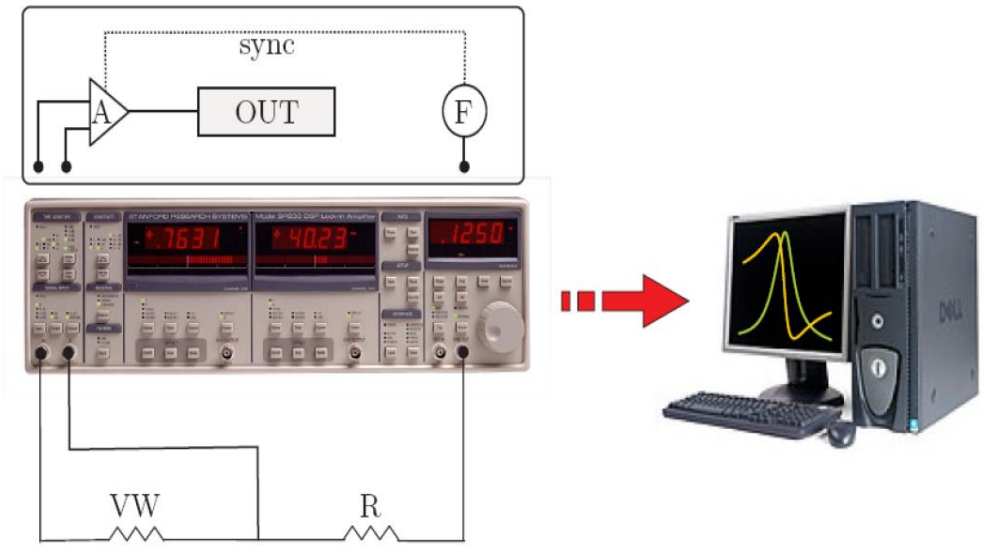

Figure 8.5 Schematic of the lock-in amplifier (Ciotta 2010; Caudwell 2004).

The signal passing across the wire is amplified (A) then output (OUT) to a display unit read across a GPIB interface by a computer. In order to minimise the electrical interference from other sources, all the connections from the lock-in amplifier are shielded.

8.2.2. Fluid handling system

The second block of the VWVD is the fluid handling system. The purpose of this block is to:

- Fill and drain the system
- Homogenise the components of the mixture
- Pressurize the viscometer to reach a maximum pressure of 200 MPa

The fluid handling system contains a screw injector (Sitec – 200 MPa), a pressure gauge (PG), a pressure transducer (PT) (Digiquartz - model 40K-110) and a magnetic circulating pump, in addition to the necessary valves and pipes (Ciotta 2010).

The entire system is placed in a thermally insulated box, regulated at 323 K (which is the maximum working temperature of the pressure transducer) by means of a PID controller, a thermocouple sensor and two 150 W finned-strip heaters (Ciotta 2010).

For safety measures, a thermal cut-out switch set at 323 K, and placed near the pressure transducer, is used to prevent over temperature exposures of the pressure transducer. Also, a burst disc (SD) set at 240 MPa is used to ensure that the maximum working pressure of the transducer is not exceeded (Ciotta 2010; Caudwell 2004).

The valves V_1, V_2, V_3 and V_4 (cf. *Figure 8.1*), are the inlet, the vacuum, the gas and the drain valves respectively. The circulating pump is inserted to circulate the fluid through the system and facilitate the mixing when necessary.

8.2.3. Accumulator

The last block of the VWVD is the accumulator. This module serves as an external vessel, made of stainless steel with an internal variable volume.

Its internal volume is divided in two compartments and it is connected on one side to the system by a two-way port and on the other side to a gas line (Nitrogen) in order to regulate the pressure. The pressure is transmitted to the system using an elastomeric bladder (made of Nitrile), separating the two compartments, and that could move freely inside the vessel. The total internal volume of the vessel is 100 ml, and the maximum working temperature and pressure are 263 K 28 MPa, respectively (Ciotta 2010).

The system is placed in a thermally insulated box and its temperature is controlled using a PID controller (Eurotherm 2216e), which regulates the power of a 150 W finned strip heater.

As the working pressure of the accumulator is lower than the rest of the system, it is placed in a low-pressure part of the circuit. The thermal box is equipped with a burst disc set at 33 MPa to prevent the accumulator from being exposed to over-pressure and a thermal switch unit set at 323 K to prevent the accumulator from being exposed to over-temperature (Ciotta 2010; Caudwell 2004).

A high-pressure bypass line is inserted in order to separate the accumulator from the system, and enable one if necessary to circulate the fluid at the maximum rated pressure of the system (200 MPa).

The valves V_7 and V_8 are three-way valves used to isolate the accumulator from the main system, and valve V_9, when shut, is used to force the fluid to pass through the accumulator when the pump is operated (see *Figure 8.1*).

The accumulator mainly serves as a temperature and pressure controlled storage volume, especially in situations when we are using liquid mixtures with dissolved gases.

8.3. Experimental procedure

8.3.1. Operating setting

As described earlier in this chapter, the wire is set into motion by passing an alternating current through the wire, thus setting it into transverse oscillations. The voltage developed across the wire is measured by means of a lock-in amplifier. The steady-state frequency response of the oscillating wire is measured in the vicinity of the fundamental transverse resonance mode. To achieve this, the lock-in amplifier is programmed to measure the induced voltage at incremental frequency steps which become closer in the vicinity of the resonance peak. The sampling is in accordance with the following expressions:

$$f_1 = f_r - n\frac{f_b}{2}$$
$$f_{i+1} = f_i + \frac{f_b}{4}\left[1.01 - exp\left(-\frac{|f_i - f_r|}{f_b}\right)\right] \tag{8.6}$$

where f_r is the resonance frequency, f_b the bandwidth and n the number of bandwidths to scan. The value of 1.01 is used to prevent the step size tending to zero when f_i tends to f_r, and to maintain a minimum step size near resonance. Following the work of (Ciotta 2010; Caudwell 2004), the frequency range expressed in terms of the bandwidth of the signal is fixed at four.

To allow the lock-in amplifier and the vibrating wire to reach a steady state following each step in frequency, a wait time between points is necessary. The wait time used is usually set to fifteen times the filter time constant on the lock-in amplifier, which is usually set to 100 ms for fluids or 1 s for vacuum measurements (Caudwell 2004; Ciotta 2010).

To help ensure the accuracy of the voltage sampled, measurements are made in both directions (increasing and decreasing frequency), thereby averaging out the effect of slow drifts in

temperature or pressure. This results in a measurement taking about three minutes in liquid and ten minute in gas (Caudwell 2004; Ciotta 2010).

To compute the density and the viscosity, the working equations need to be fitted to the sampled voltage across the wire. Six parameters need to be determined in an iterative fitting procedure: the viscosity η, the density ρ, the amplitude of the signal Λ, and the three parameters describing the voltage background a, b and c. The problem is highly non-linear, thus necessitating accurate starting values to converge to the correct solution.

The fitting was implemented using a χ^2 minimization technique using the Marquardt method to speed up convergence. This fitting technique is used due to its robustness and easiness to implement. Further details can be found in (Caudwell 2004; Ciotta 2010).

Typical results of the fitting procedure are shown in *Figure 8.6*.

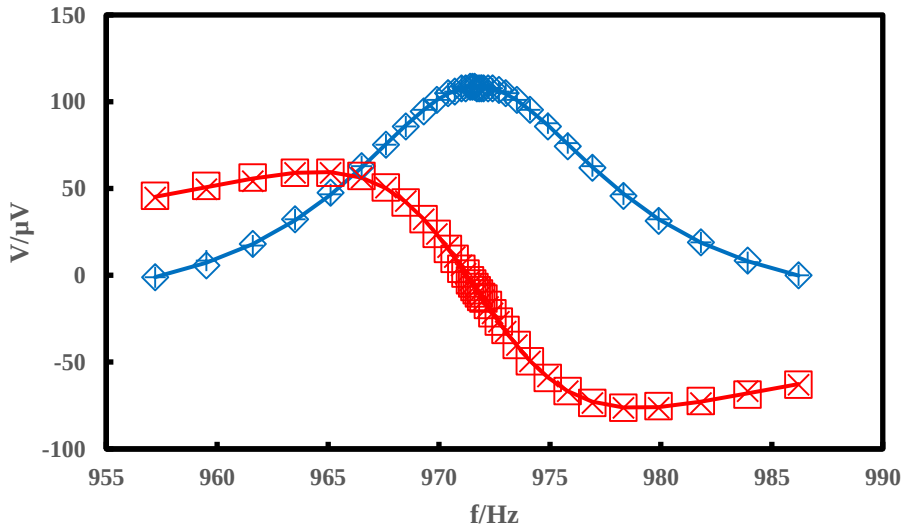

Figure 8.6 Typical response of the viscometer cell. (□) In-phase voltage (up); (×) In-phase voltage (down); (◊) Quadrature voltage (up); (+) Quadrature voltage (down), (▬) Fitted in-phase voltage; (▬) Fitted quadrature voltage.

8.3.2. Calibration

The calibration of the VWVD is performed in two stages: the calibration with air or nitrogen, and the calibration using a fluid with known properties (n-octane for example).

The calibration at atmospheric conditions aims to determine the logarithmic decrement of the wire in vacuum Δ_0. However, Δ_0 is usually calculated from measurements made in air or nitrogen, due to the difficulty of obtaining a good vacuum in the system. Δ_0 is calculated as follows:

$$\Delta_0 = \Delta_0' - \frac{1}{2}\beta' \tag{8.7}$$

where Δ_0' is the logarithmic decrement of the wire in air, and β' is for the viscous damping of the air.

The calibration using a fluid with known properties (such as n-octane in our measurements), aims to fit the radius of the wire R.

In addition to that, the mass of the tensioning sinker m is determined by weighing using an electronic balance.

The volume of the tensioning sinker V is deduced accordingly from its mass (previously weighed) and its density (density of the sinker's material).

The pressure transducer has been previously calibrated against a dead-weight pressure balance using the technique outlined by (Ball 2003). Further details about the calibration procedure can be found in (Caudwell 2004; Ball 2003).

The temperature sensor has been previously calibrated against a standard platinum resistance thermometer that had itself been calibrated on ITS-90 at the UK National Physical Laboratory, following the method described by (Caudwell 2004; Len 2003).

8.4. Experimental results

The viscosities and densities of the two pure compounds refrigerants R134a and R1234yf have been measured using the vibrating-wire viscometer-densimeter. The results obtained are presented hereinafter.

8.4.1. Pure compound R134a

The experimental measurements carried out for the R134a cover the range of temperatures between 303.15 K and 393.15 K, for pressures up to 50 MPa. The results obtained along with the expanded uncertainties (k = 2) are displayed in *Figure 8.7*. The numerical data can be found in *Table C.4* of Appendix C. We should note that the uncertainties of densities and viscosities reported are for the liquid phase. The uncertainties might be higher in the supercritical region.

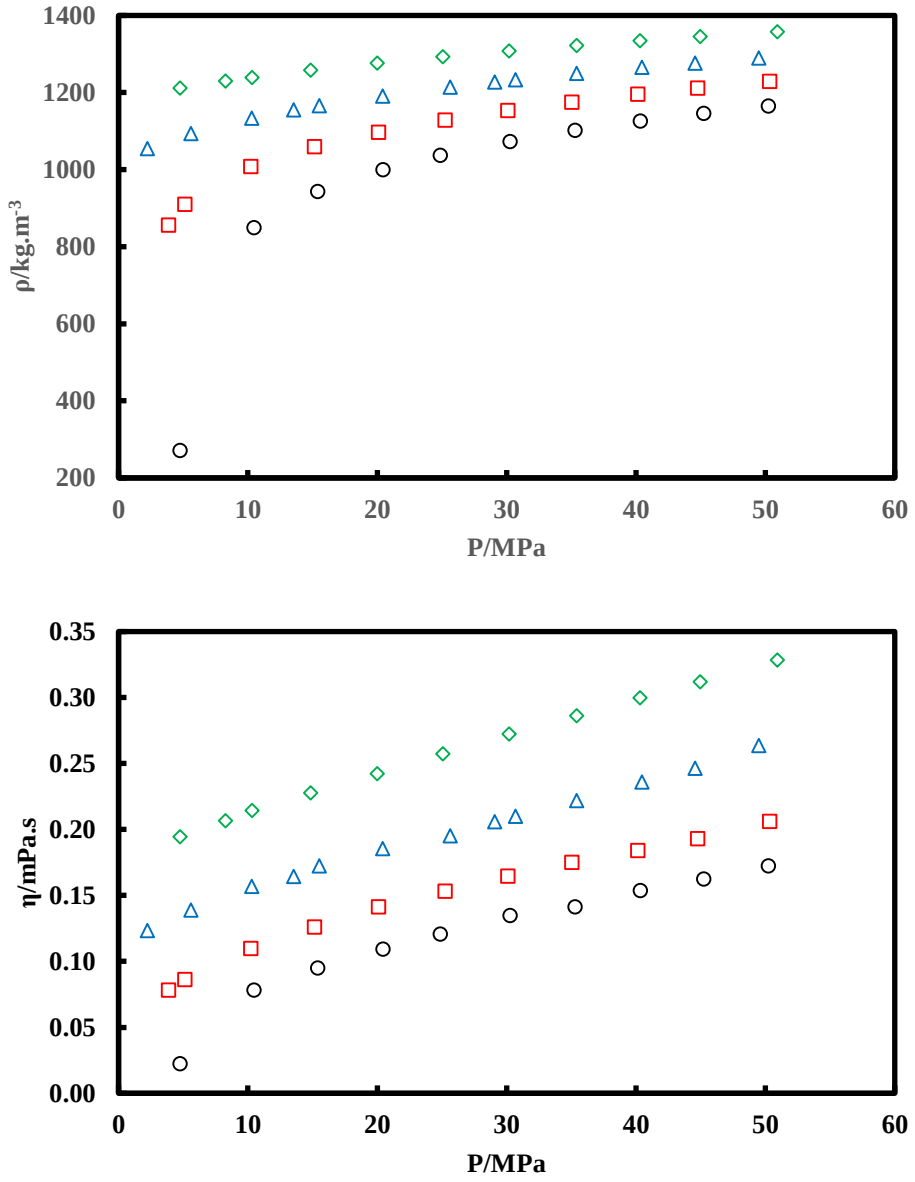

Figure 8.7 Experimental densities and viscosities for the R134a. (◊) 303.67 K; (Δ) 333.27 K; (□) 363.27 K; (○) 393.26 K. U(T) = 0.1 K; U(P) = 0.05 MPa; U(ρ)/ρ = 0.2%; U(η)/η = 2%.

8.4.2. Pure compound R1234yf

The experimental measurements carried out for the R1234yf cover the range of temperatures between 303.15 K and 423.15 K, for pressures up to 50 MPa. The results obtained along with the expanded uncertainties (k = 2) are displayed in *Figure 8.8*. The numerical data can be found in *Table C.5* of Appendix C. We should note that the uncertainties of density and viscosity reported are for the liquid phase. The uncertainties might be higher in the supercritical region.

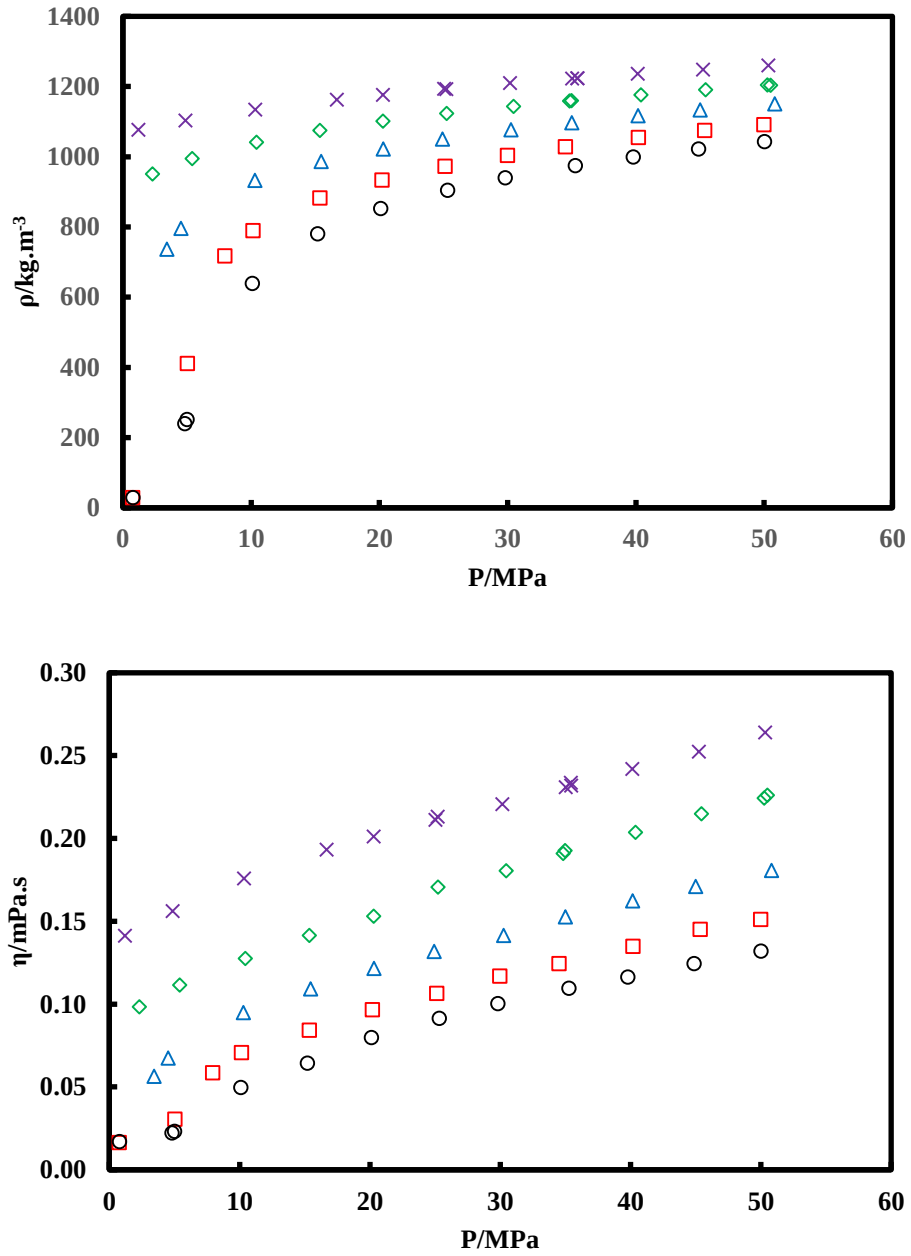

Figure 8.8 Experimental densities and viscosities for the R1234yf. (×) 303.65 K; (◊) 333.20 K; (Δ) 362.71 K; (□) 394.16 K; (○) 423.06 K. U(T) = 0.1 K; U(P) = 0.05 MPa; U(ρ)/ρ = 0.2%; U(η)/η = 2%.

8.4.3. Comparative study

To validate the accuracy of the experimental results obtained using the VWVD, we compared them to some data from the literature and to the results obtained from REFPROP 9.0.

The densities for the R134a are also compared to the results obtained by using the vibrating-tube densimeter (from the experiments carried out at the CTP).

- **Pure compound R134a**

The results obtained for the R134a in comparison with the other experimental and REFPROP data are displayed in *Figure 8.9*.

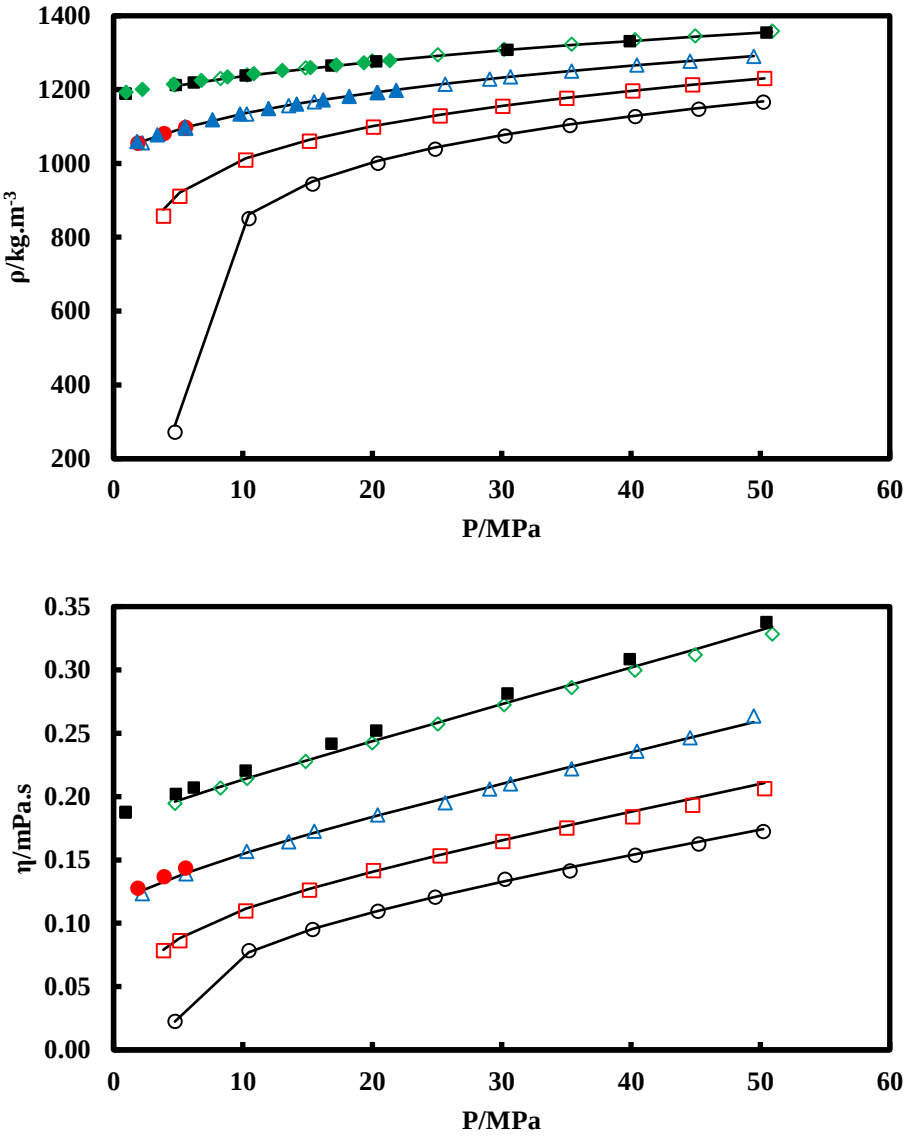

Figure 8.9 Densities and viscosities of the R134a. This work: (◊) 303.67 K; (△) 333.27 K; (□) 363.27 K; (○) 393.26 K. (Oliveira & Wakeham 1993): (■) 303.14 K; (●) 333.15 K. CTP measurements: (♦) 303.21 K; (▲) 333.29 K. (—) REFPROP 9.0 (Lemmon et al. 2010).

From the graphical representation, we can see that the results obtained for both densities and viscosities are in good agreement with the literature data, as well as with REFPROP results.
For the densities of the R134a calculated by REFPROP 9.0, it is reported (in REFPROP 9.0) that "*the typical uncertainties are 0.05%"*, while for the viscosities it is reported (in REFPROP 9.0) that *"the uncertainty is 3% in the liquid phase, 0.5% in the dilute gas, 3-5% in the vapour phase, and 5% in the supercritical region, rising to 8% at pressures above 40 MPa"*.
Also for densities, we can see that the results obtained using the vibrating-tube densimeter (VTD) and the vibrating-wire viscometer-densimeter (VWVD) are similar.

- **Pure compound R1234yf**

The results obtained for the R1234yf in comparison with the other experimental and REFPROP data are displayed in *Figure 8.10*.

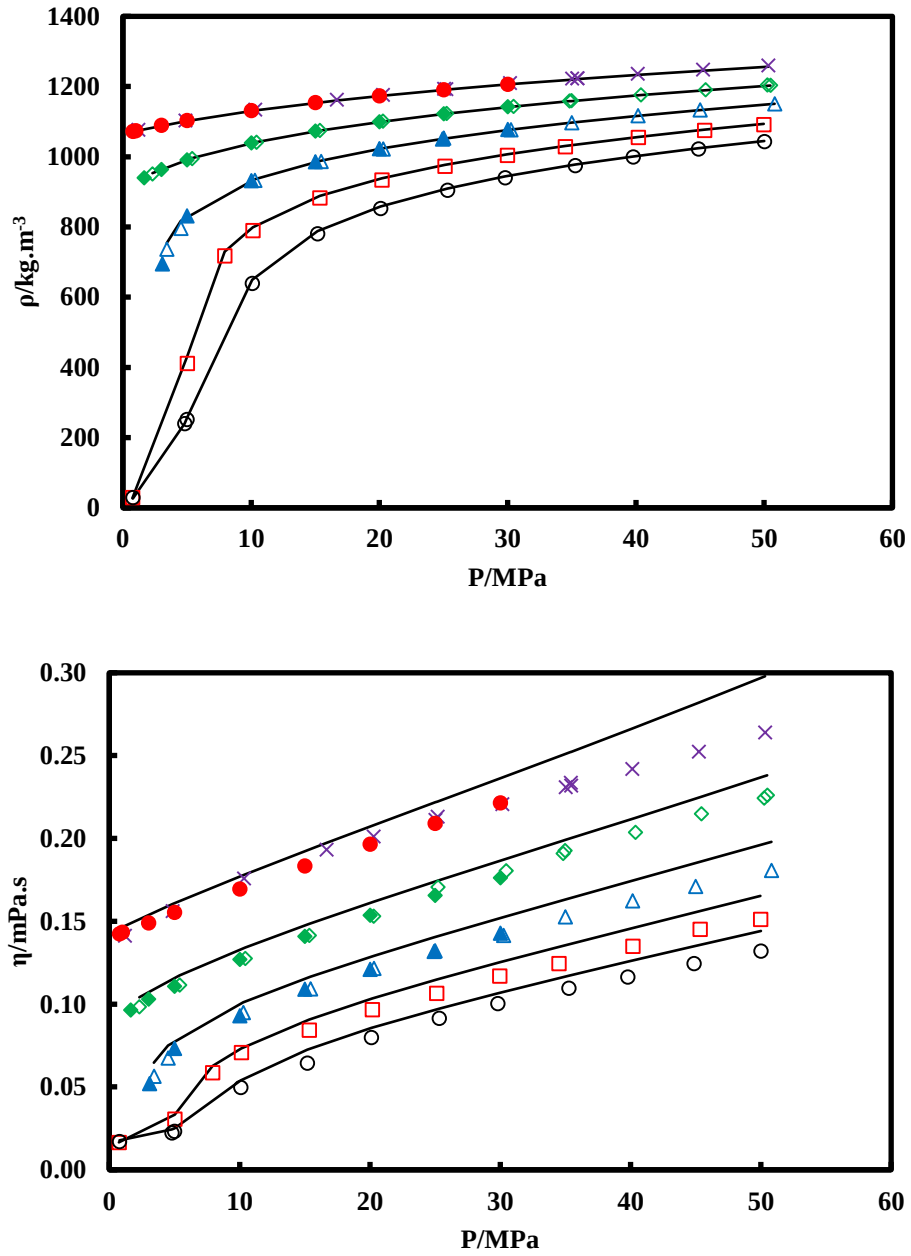

Figure 8.10 Densities and viscosities of the R1234yf. This work: (×) 303.65 K; (◊) 333.20 K; (△) 362.71 K; (□) 394.16 K; (○) 423.06 K. (Meng et al. 2013): (●) 303.15 K; (♦) 333.16 K; (▲) 363.16 K. (——) REFPROP 9.0 (Lemmon et al. 2010).

From the graphical representation of the R1234yf's densities, we can see that the results that we obtained are in good agreement with the literature data as well as with REFPROP's data. For the densities of the R1234yf calculated by REFPROP 9.0, it is reported (in REFPROP 9.0) that *"the uncertainty in density in the liquid phase is 0.1% for temperatures from 240 K to 320 K and pressures up to 10 MPa. The uncertainty increases outside of this region and in the vapour phase to 0.5%, and even higher in the critical region"*.

For the viscosities however, while our results and the literature data are in good agreement, we can notice that REFPROP's results deviate from the experimental ones. This deviation is more significant with higher temperatures. For the viscosities of the R1234yf calculated by REFPROP 9.0, it is reported (in REFPROP 9.0) that *"the estimated uncertainty for viscosity is 10%"*. It is also mentioned (in REFPROP 9.0) that *"the calculations obtained are not of a standard quality"*.

Thus, the results obtained with REFPROP 9.0 for viscosities should be considered carefully, especially for the new refrigerants for which few literature data are available.

8.5. Viscosity modelling

In order to correlate the viscosities data obtained through measurements, we used a model based on the friction theory, inspired from the work of Quiñones-Cisneros and co-workers (Quiñones-Cisneros et al. 2000; Quiñones-Cisneros et al. 2001; Quiñones-Cisneros & Deiters 2006)

8.5.1. Friction theory model

In the friction theory, the viscosity of dense fluids, which characterizes pure shear flow, is approached as a mechanical, rather than as a transport property. Thus, separating the total viscosity (η) into a dilute gas term (η_0) and a friction term (η_f). By using two or three temperature-dependent friction coefficients (κ_r, κ_{rr} and κ_a), this theory links the residual friction term to the Van-der-Waals repulsive and attractive pressure terms; p_r and p_a respectively; (Quiñones-Cisneros et al. 2000; Quiñones-Cisneros et al. 2001; Quiñones-Cisneros & Deiters 2006). The schematic of *Figure 8.11* gives a basic idea about this theory.

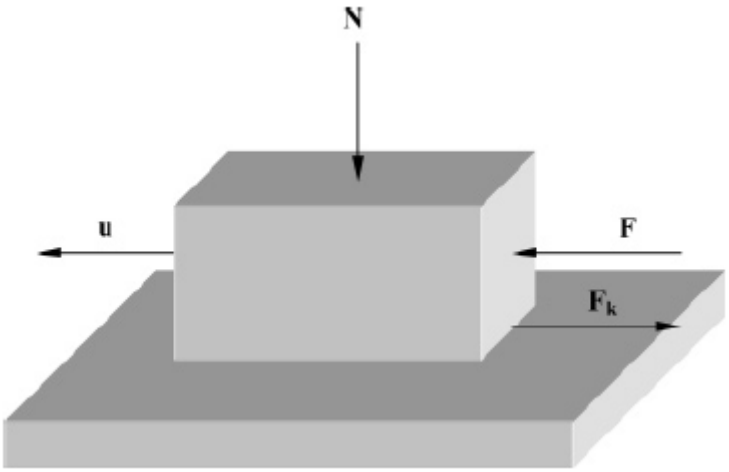

Figure 8.11 Basic forces acting in the case of a block moving under mechanical friction. N: normal force; F: tangential force responsible for movement; F_k: friction force opposing F; u: resulting velocity. (Quiñones-Cisneros & Deiters 2006).

The motivations behind using such a model is that a rather simple cubic equation of state can be used as a basis for obtaining highly accurate modelling of the viscosity of fluids from low to extreme high pressures. Since the cubic equations of state are well tuned for accurate pressure–temperature performance, and pressure is the main mechanical property linked to friction, the obtained accuracy does not depend on the density performance of the equation (Quiñones-Cisneros & Deiters 2006). Also, it is a simple model to correlate the experimental data. In this work the friction theory model is used with the NEoS. The relations describing the friction theory model are illustrated by Eq (8.8).

$$\eta = \eta_0 + \eta_f$$

$$\eta_f = \kappa_r p_r + \kappa_{rr} {p_r}^2 + \kappa_a p_a \qquad (8.8)$$

$$p_r = \frac{RT}{v - b}$$

$$p_a = -\frac{a(T)}{v^2 + ubv + wb^2}$$

The Van-der-Waals repulsive and attractive pressure terms p_r and p_a are calculated from the NEoS. The parameters κ_r, κ_{rr} and κ_a are adjusted on the experimental viscosities we measured, for each temperature independently, by minimising the difference between the experimental viscosities and the calculated ones, according to the following objective function:

$$F_{obj} = \sum_{1}^{N} \left(\eta_{exp} - \eta_{cal}\right)^2 \quad (8.9)$$

with η_{exp} the experimental viscosity and η_{cal} the total viscosity calculated from the friction theory model.

8.5.2. Modelling results

By equating these relations, the results obtained from the friction theory model are displayed in *Figure 8.12* and *Figure 8.13*, for the viscosities of both the R134a and the R1234yf, in comparison with the experimental results.

From the results obtained, we can see that the results of the model are in good agreement with the experimental data. We should however take into account that the model was used by adjusting the parameters on the experimental data, and not in a predictive way. Thus, it does not give an idea about the predictive capacity of such a model. This should be investigated more deeply in order to use the model in a predictive way.

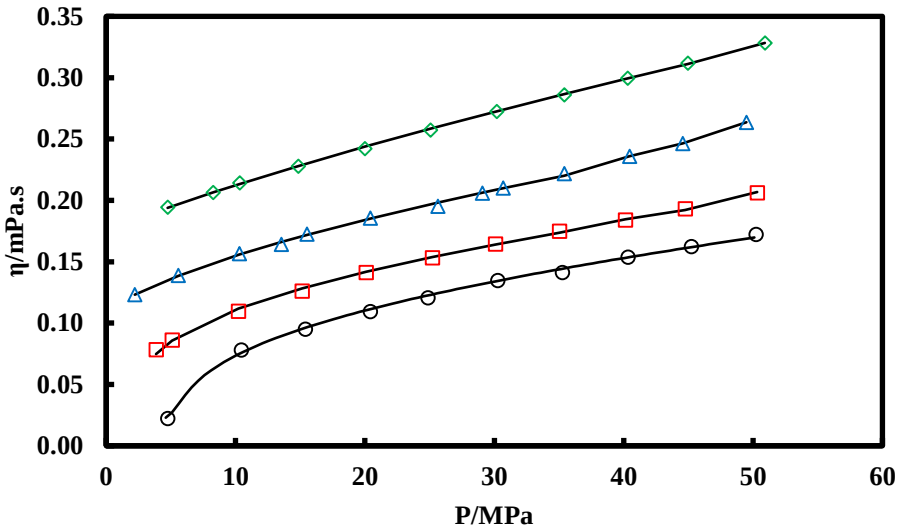

Figure 8.12 Viscosities of the R134a. This work: (◊) 303.67 K; (Δ) 333.27 K; (□) 363.27 K; (○) 393.26 K. (——) Friction theory model.

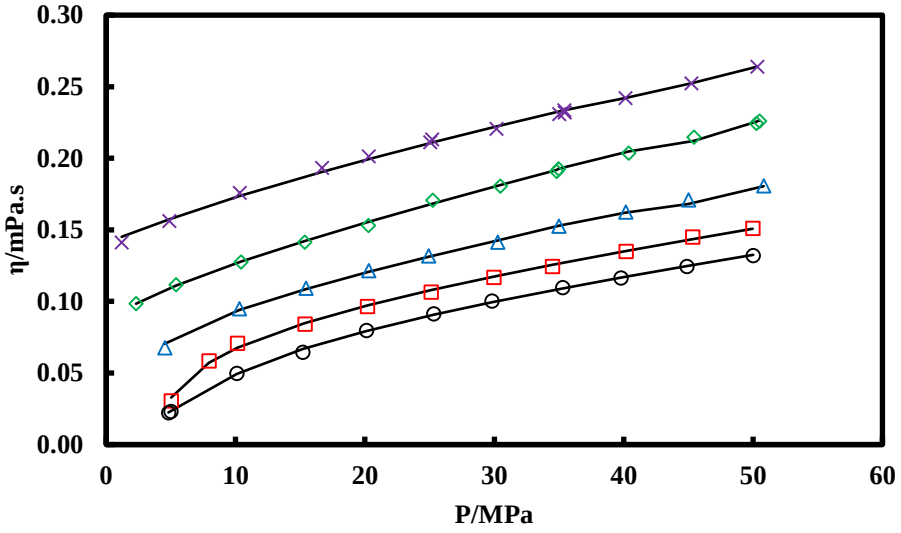

Figure 8.13 Viscosities of the R1234yf. This work: (×) 303.65 K; (◊) 333.20 K; (Δ) 362.71 K; (□) 394.16 K; (○) 423.06 K. (——) Friction theory model.

From the results obtained, we calculated the ARD and the BIAS for the viscosities, as reported in *Table 8.1*.

These results support the previous finding from the graphical representation and show the good capacity of this model to calculate the viscosities.

Table 8.1 ARD and BIAS of the viscosities for the refrigerants R134a and R1234yf.

Refrigerants	*T/K*	*ARD (%)*	*BIAS (%)*
R134a	303.65	0.23	0.00
	333.27	0.41	0.01
	363.27	1.04	0.18
	393.26	1.87	-0.55
R1234yf	303.65	0.77	-0.05
	333.20	0.67	0.00
	362.65	0.89	-0.23
	394.16	1.80	-0.36

8.5.3. Temperature dependency of the parameters κ_r, κ_{rr} and κ_a

Since the adjusted parameters κ_r, κ_{rr} and κ_a are temperature dependent, we tried to see if there is a correlation between these parameters and the temperature.

Thus, for the R134a, we have four sets of parameters, and for the R1234yf, we have five sets of parameters. The values of the parameters κ_r, κ_{rr} and κ_a obtained from the adjustment are reported in *Table 8.2*.

Table 8.2 The values of the parameters κ_r, κ_{rr} and κ_a for refrigerants R134a and R1234yf.

Refrigerants	*T/K*	κ_r	κ_{rr}	κ_a	$ln\|\kappa_r\|$	$ln\|\kappa_{rr}\|$	$ln\|\kappa_a\|$
R134a	303.65	-2818E-10	33E-10	1848E-10	-15.08	-19.53	-15.50
	333.27	-1061E-10	20E-10	1289E-10	-16.06	-20.03	-15.86
	363.27	323E-10	11E-10	1008E-10	-17.25	-20.59	-16.11
	393.26	477E-10	8E-10	922E-10	-16.86	-20.90	-16.20
R1234yf	303.65	-11E-10	26E-10	1583E-10	-20.67	-19.77	-15.66
	333.20	2291E-10	10E-10	1961E-10	-15.29	-20.73	-15.44
	362.65	863E-10	9E-10	1524E-10	-16.27	-20.82	-15.70
	394.16	1642E-10	6E-10	1109E-10	-15.62	-21.18	-16.01
	423.06	1581E-10	5E-10	1081E-10	-15.66	-21.52	-16.04

The graphical representation of these parameters in function of the temperature is displayed in *Figure 8.14*, for the refrigerants R134a and R1234yf.

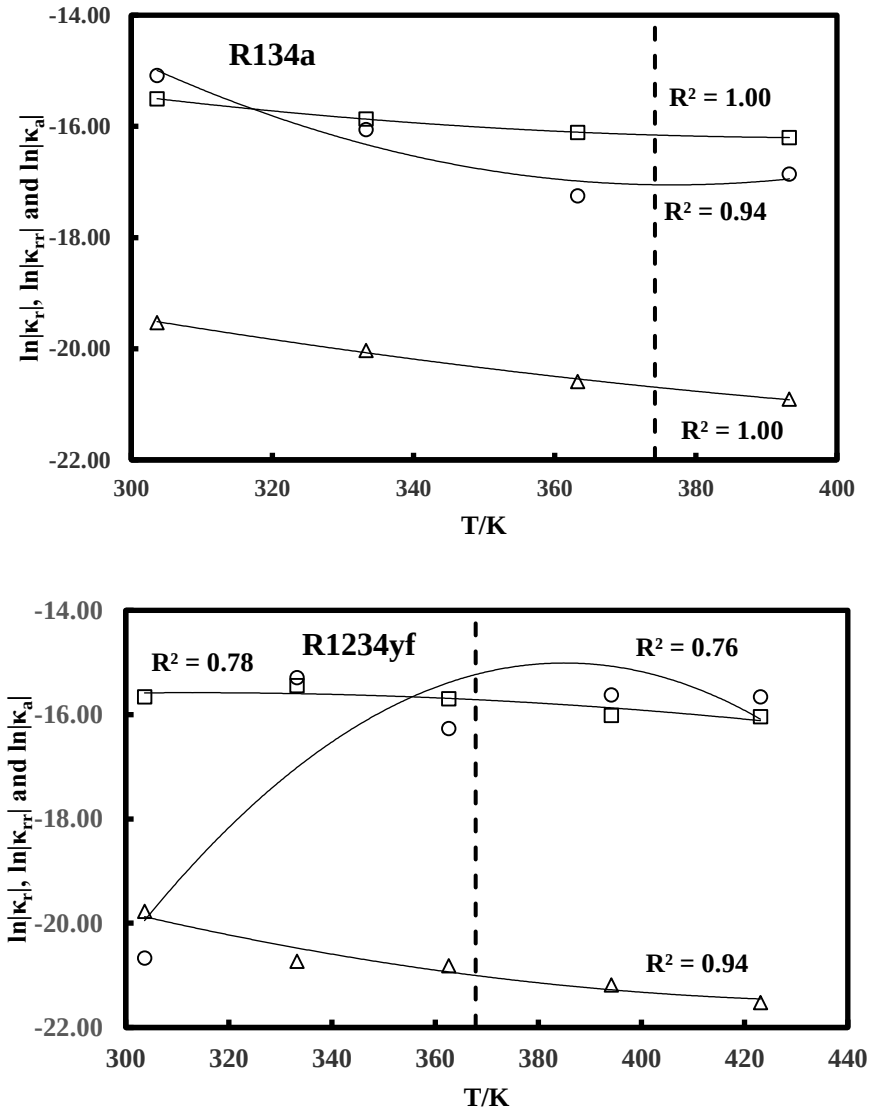

Figure 8.14 Parameters $\ln|\kappa_r|$, $\ln|\kappa_{rr}|$ and $\ln|\kappa_a|$ in function of the temperature. (○) $\ln|\kappa_r|$; (Δ) $\ln|\kappa_{rr}|$; (□) $\ln|\kappa_a|$; (----) Critical temperature: 374.21 K for R134a and 367.85 K for R1234yf.

From this graphical representation, we can see that for the R134a, $\ln|\kappa_r|$, $\ln|\kappa_{rr}|$ and $\ln|\kappa_a|$ depend on the temperature, and a second order polynomial tendency can be deduced.

For the R1234yf, a good second order polynomial tendency can be seen between $\ln|\kappa_{rr}|$ and the temperature, while for $\ln|\kappa_r|$ and $\ln|\kappa_a|$ the tendency is less good.

A further study on more experimental data with more isotherms might be needed in order to fully understand this dependency. Also, it could be interesting to see if there is two behaviours depending if we have subcritical or supercritical temperatures.
This can be a good starting point for generalizing this model for the refrigerants, with the aim of using the model in a predictive way.

Concluding remarks

In this chapter, we presented and described briefly the principle of the vibrating wire and the equipment used along with the experimental procedure. Then we present the results obtained for densities and viscosities of the two pure compounds refrigerants R134a and R1234yf.
The results obtained were in good agreement with other experimental data found in the literature for both the densities and the viscosities of both refrigerants. Also, the densities of the R134a obtained from using the vibrating-tube densimeter and the vibrating-wire viscometer-densimeter were compared, showing that both equipment give similar results. The viscosities of the R1234yf obtained from REFPROP 9.0 show however some deviations to the experimental data. These deviations become more important at higher temperatures.
In order to correlate the data obtained for viscosities, we used a friction theory model with three adjusted parameters. The results obtained from this model were in good accordance with the experimental data.
In the aim of generalizing such a model and be able to use it in a predictive way, a further study would be needed in order to develop correlations for the friction parameters.

9. Conclusions & Perspectives

Les propriétés thermo-physiques des réfrigérants sont extrêmement importantes pour plusieurs applications industrielles. Les mesures expérimentales de ces propriétés est primordial, particulièrement pour les systèmes dont on dispose de peu de données.

En particulier, les mesures d'ELV et de densités nous donnent des informations cruciales sur les diagrammes de phase, le comportement thermodynamique et les propriétés volumétriques du système étudié. Ces propriétés sont nécessaires pour le design et l'optimisation des systèmes thermodynamiques. Les densités peuvent aussi être utilisées pour le calcul des propriétés de transport (les viscosités et les conductivités thermiques à titre d'exemple).

Dans ce manuscrit, les mesures d'ELV et de densités pour les systèmes de réfrigérants (corps purs et mélanges) ont été établies, et les résultats obtenus ont été présenté dans le chapitre 3. Les mesures expérimentales se sont focalisés dur l'étude des systèmes de réfrigérants avec peu de données disponibles, plus particulièrement les systèmes contenant au moins un fluide de nouvelle génération (HFOs et HCFOs).

Les mesures VLE ont été achevées au moyen d'une cellule d'équilibre, basée sur une méthode statique-analytique. Les mesures de densités ont été faites au biais d'un densimètre à tube vibrant, se basant sur une méthode synthétique-dynamique. La présentation et la description des équipements utilisés a été couverte dans le chapitre 2.

Les mesures expérimentales seules ne sont pas suffisantes pour couvrir tous les systèmes de réfrigérants possibles, dans les différentes conditions de mesures, mais restent essentielles pour développer et valider les modèles thermodynamiques, et pour ajuster les paramètres de ces modèles, ce qui les rend une étape essentielle dans le processus de sélection de fluide pour une l'application désirée.

En parallèle avec les mesures expérimentales, il est important d'avoir un bon modèle thermodynamique de prédiction. La NEoS en est un exemple, permettant de bien prédire les propriétés thermodynamiques des corps purs et des mélanges.

La NEoS a été utilisée dans ce travail pour la prédiction des propriétés thermodynamiques des fluides frigorigènes, notamment les ELV et les densités, et les résultats obtenus ont été comparés aux résultats provenant de d'autres équations d'état, telles que l'EdE de PR et PT. Les trois équations d'état considérées ont été associées à la fonction alpha de Mathias-Copeman. Les paramètres de la fonction alpha, ainsi que le facteur critique de compressibilité (dans le cas de NEoS et PT), ont été calculés à partir des corrélations développées dans le chapitre 4.

Pour les mélanges binaires et ternaires, le paramètre d'interaction binaire k_{ij} a été pris nul, dans la plupart des cas, en utilisant les règles de mélanges classiques de van-der-Waals.

Toutefois, il a été nécessaire d'ajuster le k_{ij} pour certains systèmes ayant un comportement thermodynamique assez complexe, comme dans le cas des systèmes azéotropiques. En effet, les fluides frigorigènes se caractérisent par une large hétérogénéité en termes de propriétés moléculaires, puisque certains composés possèdent de forts moments dipolaires et/ou quadripolaires, tandis que d'autres composés ont de faibles moments. Ceci pourrait être l'une des raisons d'avoir à utiliser un k_{ij}.

Il est aussi intéressant de tester d'autres règles de mélanges; comme les règles de mélanges g^E ; pour voir leur effet sur la représentation des propriétés thermodynamiques des mélanges de réfrigérants. Aussi, il pourrait être intéressant d'ajouter un terme polaire dans la NEoS, pour prendre en considération la polarité des réfrigérants.

Une autre voie qui serait intéressante à étudier est la combinaison de la NEoS avec une méthode de contribution de groupes pour calculer le k_{ij}, tout en gardant les règles de mélanges de van-der-Waals, en s'inspirant des travaux sur la PPR78 (Jaubert & Mutelet 2004; Jaubert et al. 2005; Privat et al. 2008; Xu, Jaubert, et al. 2015; Xu, Privat, et al. 2015). Ceci donne à la NEoS la capacité d'être prédictive (puisque le k_{ij} est prédit et non pas ajusté), tout en améliorant les résultats.

Les résultats de la prédiction pour les corps purs et les mélanges; présentés en chapitre 5 et 6; montrent que la NEoS permet une meilleure représentation des densités liquides à saturation et hors saturation, en comparaison avec les résultats obtenus par les EdE PR et PT. Les résultats sont aussi meilleurs dans la région critique, et pour les isothermes supercritiques. La prédiction par la NEoS pourrait toutefois être améliorée pour quelques isothermes subcritiques hors saturation, surtout à basse température.

Les densités dans la région critique sont nettement mieux représentées par la NEoS comparée aux autres équations d'état considérées dans ce travail. Toutefois, il est possible d'améliorer cette prédiction en combinant la NEoS avec une méthode de renormalisation (Wilson 1971; Wilson & Fisher 1972), en utilisant une approche Crossover (Dicko & Coquelet 2011; Janeček et al. 2015) ou la méthode récursive de White (Cai & Prausnitz 2004).

En général, la NEoS permet une meilleure prédiction des densités, ce qui est essentiel pour la prédiction des propriétés de transport (viscosités, conductivités thermiques…), et il serait notamment intéressant de coupler la NEoS avec la méthode TRAPP (Huber et al. 1992; Klein et al. 1997), ou la théorie de friction (Quiñones-Cisneros et al. 2000; Quiñones-Cisneros et al. 2001; Quiñones-Cisneros & Deiters 2006), pour le calcul des viscosités par exemple.

La capacité de prédiction des ELV par la NEoS pour des systèmes complexes (avec un k_{ij} nul) reste limitée. Cependant, les résultats présentés lors de ce travail, la NEoS montre une

meilleure prédiction des densités avec un k_{ij} nul, ce qui rend cette équation d'état intéressante et mérite ainsi d'être testée dans des simulateurs de procédés pour des applications industrielles.

En plus de la NEoS présenté dans ce travail, des corrélations pour le calcul les densités et les tensions superficielles à saturation ont été développées. Les corrélations pour les densités sont basées sur les lois d'échelles, tandis que les corrélations pour les tensions de surface sont inspirées de la théorie du gradient de densité, et sont reliés directement aux densités calculées, via une loi de puissance.

Les calculs obtenus à partir de ces corrélations montrent de très bons résultats pour les densités et les tensions superficielles, et étaient en très bon accord avec les données expérimentales de comparaison. Les résultats détaillés concernant ces corrélations sont présentés dans le chapitre 7.

Finalement, et dans le but d'étudier les propriétés de transport (viscosités) des réfrigérants, j'ai passé cinq mois à l'Imperial College London, au sein du groupe de recherche du Professeur J.P. Martin Trusler. Les mesures expérimentales ont été faites au moyen d'un viscomètre-densimètre à fil vibrant (basé sur une méthode statique-synthétique), permettant la mesure simultanée des densités et des viscosités (comme présenté dans le chapitre 8).

Deux réfrigérants ont été étudiés, le R134a et le R1234yf, pour différentes températures et pressions. Les résultats obtenus ont été comparés aux résultats de REFPROP 9.0, et à d'autres données de la littérature. Tous les résultats comparés étaient en accord, à l'exception des viscosités du R1234yf obtenues de REFPROP 9.0, qui déviaient de nos mesures expérimentales, ainsi que des données de la littérature.

En plus des mesures expérimentales de viscosités, un modèle de calcul a été développé. Ce modèle est basé sur la théorie de friction, et est associé à la NEoS. Les premiers résultats obtenus à partir de ce modèle étaient en très bon accord avec nos mesures expérimentales.

Pour conclure, lors de ce travail de thèse nous avons étudié les propriétés thermo-physiques des fluides frigorigènes, en particulier les réfrigérants de nouvelle génération. L'étude a été faite au moyen de mesures expérimentales et par des outils de modélisation, et nous a permis d'acquérir une bonne connaissance et compréhension des propriétés de ces fluides.

En se basant sur tous les résultats obtenus, à partir des mesures expérimentales et de la modélisation; et dans la continuité de ce travail; il serait intéressant d'utiliser une approche de type « Product design » dans le but de sélectionner et/ou de concevoir un fluide de travail

optimal, répondant aux besoins de différentes applications industrielles. En effet, ceci est l'un des objectifs du projet PREDIREF, et il serait intéressant de pouvoir aboutir à un tel résultat.

The thermophysical properties of refrigerants are extremely important for many industrial applications. The experimental measurements of these properties are mandatory, especially for systems where the data are scarce or unavailable.

In particular, VLE and density measurements give us crucial information about the system phase diagrams, thermodynamic behavior, and volumetric properties. These properties are necessary for the design and optimization of thermodynamic systems. Density properties can also be used for transport property calculations (viscosity and thermal conductivity for instance).

In this work, VLE and density measurements of the refrigerant systems (pure compounds and mixtures) were carried out, and the results obtained were presented in Chapter 3. The experimental measurements focused on the study of new systems of refrigerants not available in the literature, especially systems containing at least one new-generation refrigerant (HFOs and HCFOs).

The VLE measurements were performed using an equilibrium cell, following a static analytic method. The density measurements were achieved using a vibrating tube densimeter, following a synthetic dynamic method. The presentation and description of the equipment used were given in Chapter 2.

The experimental measurements of thermophysical properties -alone- are not sufficient to cover the wide range of refrigerants and thermodynamic conditions to study, but they remain essential to develop and validate thermodynamic models, and fit parameters of these models, making them an essential step of the fluid selection process for a particular application.

In addition to the experimental measurements, having a good predictive model is essential to complete the experimental results. The NEoS is an example of such a model, allowing one to predict accurately the thermodynamic properties of pure compound and mixture of refrigerants.

The NEoS was used to predict the thermodynamic properties of fluid refrigerants, such as the VLE and density properties, and the results obtained were compared to the PT-EoS and PR-EoS ones.

The three EoSs considered were associated with the MC alpha function. The parameters of this alpha function, as well as the optimized critical compressibility factor (for the NEoS and the PT-EoS), were calculated based on the correlations established in Chapter 4.

For the binary and ternary systems, the binary interaction parameters k_{ij} was set to 0, without any fitting to experimental data, while the classical mixing rules of van-der-Waals.

However, for some systems, such as the azeotropic ones, it has been necessary to consider a k_{ij} parameter to accurately represent the VLE behavior of the systems. Indeed, for instance, the

refrigerant compounds are characterized by a large heterogeneity in terms of molecular properties, as some compounds possess strong dipole and/or quadrupole moments and other compounds only weak multipole moments. This may be why a k_{ij} parameter is needed to model some of the binary systems considered.

It would also be interesting to test other mixing rules than the van der Waals ones (used in this work), such as g^E –mixing rules, and also to think about adding a polar term in the NEoS to take into account the polarity of some refrigerant compounds.

An additional path that could be interesting to investigate is the combination of the NEoS with a group contribution method to calculate the k_{ij} of van der Waals mixing rules, as it is done successfully with the PPR78 model (Jaubert & Mutelet 2004; Jaubert et al. 2005; Privat et al. 2008; Xu, Jaubert, et al. 2015; Xu, Privat, et al. 2015).

Together, the results of the predictions for the pure compounds and for the binary and ternary mixtures – presented in Chapters 5 and 6- show that the NEoS provides a better representation of the liquid density at saturation and out of saturation, compared to the results obtained with the PT-EoS and PR-EoS. The results are also better for the density in the critical region and for supercritical isotherms. However, the NEoS prediction for the ternary mixture could be improved for the subcritical temperatures.

The density in the critical region is well represented by using the NEoS, compared to the other EoSs considered in this work. However, this prediction could be improved by combining the NEoS with a renormalization group theory (Wilson 1971; Wilson & Fisher 1972), using a crossover approach (Dicko & Coquelet 2011; Janeček et al. 2015) or the White's recursive method (Cai & Prausnitz 2004).

In overall, the NEoS provides a better representation of the densities, which are essential for the prediction of transport properties (viscosity, thermal conductivity…), and it would be particularly interesting to couple the NEoS with the TRAPP method (Huber et al. 1992; Klein et al. 1997), or the friction theory (Quiñones-Cisneros et al. 2000; Quiñones-Cisneros et al. 2001; Quiñones-Cisneros & Deiters 2006) for instance, for viscosities calculations.

The prediction ability of the VLE (without k_{ij}) for complex systems with the NEoS is limited, however, from the results presented in this work concerning refrigerants, the NEoS shows better density prediction potentialities (without k_{ij}) than the PR-EoS and PT-EoS, and this EoS deserves thus to be tested in process simulators for industrial purpose.

In addition to the NEoS developed, correlations for calculating densities and surface tensions were developed. The correlations developed for densities are based on the scaling laws, while

the correlations for surface tensions are based on the density-gradient theory, and are related directly to the densities calculated.

The calculations using the correlations developed shows very accurate results for densities and satisfactory results for surface tensions. The details about the results obtained are presented in Chapter 7.

Finally, and in order to study the transport properties (viscosities), I spent five months at Imperial College London within the research group of Prof. J.P. Martin Trusler. The experimental measurements were carried out using a vibrating-wire viscometer-densimeter (based on a static-synthetic method), allowing simultaneous measurements of densities and viscosities (as presented in Chapter 8).

Two refrigerants were studied, the R134a and the R1234yf, for a wide range of temperatures and pressures. The results obtained were compared to the results from REFPROP 9.0, and to other literature data, showing a good agreement between all the data, except for the viscosities of the R1234yf obtained from REFPROP 9.0, that showed some deviations to our experimental results as well as to the literature data.

In addition to the experimental measurements of the viscosities, a model based on the friction theory was developed, and associated to the NEoS. The primary results obtained through this model were in good agreement with the experimental measurements.

To sum up, through this thesis, we investigated and studied the thermophysical properties of the refrigerants, with a focus on the new generation fluids. The study was carried out experimentally and through modelling, and allowed us to have a good knowledge and understanding of the properties of these refrigerants.

Based on all the results obtained, both experimentally and through modelling, and in the continuity of this work, it would be very interesting to use a “Product design” approach in order to select and/or design an optimal refrigerant, to respond to the industry demand. This, in fact, is one of the aims of the PREDIREF project, and it would be very interesting to go further in this study and achieve this goal.

Appendices

A. Names of the refrigerants and literature data

Table A.1 Names and formulas of refrigerants.

Type	*Number*	*IUPAC[3] Chemical Name*	*Formula*	*CAS Registry Number*
CFC	R-11	Trichlorofluoromethane	CCl_3F	75-69-4
CFC	R-113	1,1,2-Trichlorotrifluoroethane	$C_2F_3Cl_3$	76-13-1
CFC	R-114	1,2-Dichlorotetrafluoroethane	$C_2F_4Cl_2$	76-14-2
CFC	R-115	Chloropentafluoroethane	C_2F_5Cl	76-15-3
CFC	R-12	Dichlorodifluoromethane	CCl_2F_2	75-71-8
CFC	R-13	Chlorotrifluoromethane	$CClF_3$	75-72-9
HCFC	R-123	2,2-Dichloro-1,1,1-trifluoroethane	$C_2HF_3Cl_2$	306-83-2
HCFC	R-124	2-Chloro-1,1,1,2-tetrafluoroethane	C_2HF_4Cl	2837-89-0
HCFC	R-141b	1,1-Dichloro-1-fluoroethane	$C_2H_3FCl_2$	1717-00-6
HCFC	R-142b	1-Chloro-1,1-difluoroethane	$C_2H_3F_2Cl$	75-68-3
HCFC	R-21	Dichlorofluoromethane	$CHFCl_2$	75-43-4
HCFC	R-22	Chlorodifluoromethane	$CHClF_2$	75-45-6
HCFC	R-244bb	2-Chloro-1,1,1,2-tetrafluoropropane	$C_3H_3F_4Cl$	421-73-8
HCFO	R-1233xf	2-chloro-3,3,3 -trifluoropropène	$C_3F_3H_2Cl$	2730-62-3
HCFO	R-1233zd(E)	trans-1-chloro,3,3,3-trifluoropropene	$C_3F_3H_2Cl$	102687-65-0
HFC	R-23	Trifluoromethane (Fluoroform)	CHF_3	75-46-7
HFC	R-32	Difluoromethane	CH_2F_2	75-10-5
HFC	R-41	Fluoromethane	CH_3F	593-53-3
HFC	R-125	Pentafluoroethane	C_2HF_5	354-33-6
HFC	R-134a	1,1,1,2-Tetrafluoroethane	$C_2H_2F_4$	811-97-2
HFC	R-143a	1,1,1-Trifluoroethane	$C_2H_3F_3$	420-46-2
HFC	R-152a	1,1-Difluoroethane	$C_2H_4F_2$	75-37-6
HFC	R-161	Fluoroethane	C_2H_5F	353-36-6
HFC	R-227ea	1,1,1,2,3,3,3-Heptafluoropropane	C_3HF_7	431-89-0
HFC	R-236ea	1,1,1,2,3,3-Hexafluoropropane	$C_3H_2F_6$	431-63-0
HFC	R-236fa	1,1,1,3,3,3-Hexafluoropropane	$C_3H_2F_6$	690-39-1
HFC	R-245ca	1,1,2,2,3-Pentafluoropropane	$C_3H_3F_5$	679-86-7

[3] IUPAC: International Union of Pure and Applied Chemistry

HFC	R-245fa	1,1,1,3,3-Pentafluoropropane	$C_3H_3F_5$	460-73-1
HFC	R-236fa	1,1,1,3,3,3-hexafluoropropane	$C_3H_2F_6$	690-39-1
HFO	R-1234yf	2,3,3,3-Tetrafluoropropene	$C_3H_2F_4$	754-12-1
HFO	R-1234ze	1,3,3,3-Tetrafluoropropene	$C_3H_2F_4$	1645-83-6
HFO	R-1225ye(z)	1,2,3,3,3-pentafluoroprop-1-ene	C_3HF_5	5528-43-8
HFO	R-1243zf	3,3,3 - Trifluoropropene	$C_3H_3F_3$	677-21-4
HFO	R-1225zc	1,1,3,3,3-pentafluoroprop-1-ene	C_3HF_5	690-27-7
HFO	R-1225yc	1,1,2,3,3-pentafluoroprop-1-ene	C_3HF_5	433-66-9
HFO	R-1234ze(trans)	(1E)-1,3,3,3-tetrafluoroprop-1-ene (1234ze)	$C_3H_2F_4$	29118-24-9
HFO	R-1234yc	1-Propene,1,1,2,3-tetrafluoro	$C_3H_2F_4$	115781-23-2
HFO	R-1225yc	1,1,2,3,3-pentafluoroprop-1-ene	$CHF_2CF=CF_2$	433-66-9
HFO	R-1225ye(E)	(1E)-1,2,3,3,3-pentafluoroprop-1-ene	$CF_3CF=CHF$	5595-10-8
HFO	R-1225zc	1,1,3,3,3-pentafluoroprop-1-ene	$CF_3CH=CF_2$	690-27-7
HFO	R-1234ye(E)	(1E)-1,2,3,3-tetrafluoroprop-1-ene	$CHF_2CF=CHF$	115781-19-6
HFO	R-1234ye(Z)	(1Z)-1,2,3,3-tetrafluoroprop-1-ene	$CHF_2CF=CHF$	730993-62-1
HFO	R-1234zc	1,1,3,3-tetrafluoroprop-1-ene	$CHF_2CH=CF_2$	4556-24-5
HFO	R-1234ze(E)-trans	(1E)-1,3,3,3-tetrafluoroprop-1-ene	$CF_3CH=CHF$	29118-24-9
HFO	R-1234ze(Z)-cis	(1Z)-1,3,3,3-tetrafluoroprop-1-ene	$CF_3CH=CHF$	29118-25-0
HFO	R-1243yc	1,1,2-trifluoroprop-1-ene	$CH_3CF=CF_2$	563-85-9
HFO	R-1243ye(E)	(1E)-1,2,3-trifluoroprop-1-ene	$CH_2FCF=CHF$	1237522-12-1
HFO	R-1243yf	2,3,3-trifluoroprop-1-ene	$CHF_2CF=CH_2$	158664-13-2
HFO	R-1243zc	1,1,3-trifluoroprop-1-ene	$CH_2FCH=CF_2$	58777-31-4
HFO	R-1243ze(E)	(1E)-1,3,3-trifluoroprop-1-ene	$CHF_2CH=CHF$	100922-85-8
PFC	R-14	Tetrafluoromethane	CF_4	75-73-0
PFC	R-116	Hexafluoroethane	C_2F_6	76-16-4
PFC	R-218	Octafluoropropane	C_3F_8	76-19-7
PFC	R-C318	Octafluorocyclobutane (Perfluorocyclobutane)	C_4F_8 or -$(CF_2)_4$-	115-25-3

Table A.2 Molecular structures of some refrigerants used in this work.

Refrigerant number	*Chemical formula*	*Molecular structure*
R-134a	$C_2H_2F_4$	
R-152a	$C_2H_4F_2$	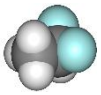
R-245fa	$C_3H_3F_5$	
R-23	CHF_3	
R-1234yf	$C_3H_2F_4$	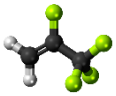
R-1233zd(E)	$C_3F_3H_2Cl$	
R-744	CO_2	
R-290	C_3H_8	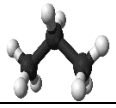

Table A.3 References of the experimental data for pure compounds refrigerants (Last updated 01/10/2016).

PFC	*CFC*	*HCFC*	*HFC*	*HCFO*	*HFO*
RC318 (Lemmon et al. 2010)	R11 (Lemmon et al. 2010)	R21 (Lemmon et al. 2010)	R23 (Lemmon et al. 2010)	R1233xf (Zhang et al. 2013)	R1225ye(E) (Brown et al. 2010b)
R14 (Lemmon et al. 2010)	R12 (Lemmon et al. 2010)	R22 (Lemmon et al. 2010)	R32 (Lemmon et al. 2010; Fu et al. 1995)	R1233zd(E) (Hulse et al. 2012)	R1225ye(z) (Brown et al. 2010b)
R116 (Lemmon et al. 2010)	R13 (Lemmon et al. 2010)	R123 (Lemmon et al. 2010)	R41 (Lemmon et al. 2010)	--	R1225zc (Brown et al. 2010b)
R218 (Lemmon et al. 2010)	R113 (Mastroianni et al. 1978; Lemmon et al. 2010)	R124 (Lemmon et al. 2010)	R125 (Lemmon et al. 2010)	--	R1234ye(E) (Brown et al. 2010b)
--	R114 (Lemmon et al. 2010; Fukuizumi & Uematsu 1991b; Higashi et al. 1985)	R141b (Lemmon et al. 2010)	R134a (Lemmon et al. 2010)	--	R1234yf (Lemmon et al. 2010; Di Nicola et al. 2010; Yang et al. 2014; Brown et al. 2010b; Hu, L. X. Chen, et al. 2013; Tanaka & Higashi 2010b; Klomfar et al. 2012)
--	R115 (Lemmon et al. 2010)	R142b (Lemmon et al. 2010)	R143a (Lemmon et al. 2010; Duan et al. 2004)	--	R1234ze(E)-trans (Brown et al. 2012; Tanaka et al. 2010; Giovanni Di Nicola et al. 2012; Brown et al. 2010b)
--	--	R244bb (Yang et al. 2014)	R152a (Lemmon et al. 2010)	--	R1234ze (trans) (Lemmon et al. 2010)
--	--	--	R161 (Lemmon et al. 2010; Han et al. 2011; Chen et al. 2005; Cui et al. 2006; Xuan & Chen 2005)	--	R1234ze(Z)-cis (Brown et al. 2010b)
--	--	--	R227ea (Lemmon et al. 2010; Hu & Chen 2004; Feng et al. 2010)	--	R1243zf (Brown et al. 2013)
--	--	--	R236ea (Lemmon et al. 2010)	--	R1216 (Coquelet et al. 2010)

--	--	--	R236fa (Lemmon et al. 2010; Duan & Meng 2004; Duan et al. 2004; Feng et al. 2010)	--	--
--	--	--	R245ca (Lemmon et al. 2010)	--	--
--	--	--	R245fa (Lemmon et al. 2010; Sotani & Kubota 1999; Feng et al. 2010)	--	--
--	--	--	R365mfc (Lemmon et al. 2010; Fröba et al. 2004; Bobbo et al. 2004; Klomfar et al. 2013)	--	--

Table A.4 References of the experimental data for mixtures of refrigerants (Last updated 01/10/2016).

Systems	*References*	*Systems*	*References*
R14 - R13 (1)	(Kubic & Stein 1981)	R161 - R227ea (46)	(Wang, Xu, et al. 2010)
R116 - R134a (2)	(Madani et al. 2008b)	R236ea - R32 (47)	(Bobbo et al. 2000)
R116 - R143a (3)	(Madani et al. 2009)	R236ea - R125 (48)	(Bobbo et al. 2000)
R116 - CO_2 (4)	(Valtz et al. 2007)	HFP - R123 (49)	(Nelson et al. 2011)
R12 - R22 (5)	(Higashi et al. 1984)	HFPO - R123 (50)	(Nelson et al. 2011)
R22 - R114 (6)	(Fukuizumi & Uematsu 1991a)	CO_2 - R32 (51)	(Rivollet et al. 2004)
R22 - R134a (7)	(Arita et al. 1991)	CO_2 - R134a (52)	(Duran-Valencia et al. 2002)
R22 - R152a (8)	(Maezawa, Sato, et al. 1991)	CO_2 - R152a (53)	(Madani et al. 2008a)
R23 - R11 (9)	(Chareton et al. 1990)	CO_2 - R227ea (54)	(Valtz et al. 2003)
R23 - R13 (10)	(Stein & Proust 1971)	CO_2 - R1234yf (55)	(Juntarachat et al. 2014)
R23 - R32 (11)	(Lim et al. 2000)	CO_2 - R1234ze(E) (56)	(Juntarachat et al. 2014)
R23 - R125 (12)	(Lim et al. 2000)	CO_2 - HFP (57)	(Nelson et al. 2011)
R23 - R134a (13)	(Lim et al. 2001)	CO_2 - HFPO (58)	(Nelson et al. 2011)
R23 - R143a (14)	(Lim, K. H. Park, et al. 2002)	R290 - R227ea (59)	(Valtz et al. 2002)
R23 - R152a (15)	(Lim, K. H. Park, et al. 2002)	R3110 - R365mfc (60)	(Madani et al. 2013)
R23 - R227ea (16)	(Lim et al. 2001)	R161 - R1234yf (61)	(Chen et al. 2015)
R32 - R125 (17)	(Kobayashi & Nishiumi 1998)	R1234yf - R227ea (62)	(Hu, Chen, Zhu, et al. 2014b)
R32 - R134a (18)	(Chung & Kim 1997; Kobayashi & Nishiumi 1998)	R1234yf - R152a (63)	(Hu, Chen, Zhu, et al. 2014a)
R32 - R143a (19)	(Barley et al. 1997)	R1234yf - R600a (64)	(Hu, Chen & Chen 2014)
R32 - R227ea (20)	(C Coquelet et al. 2003)	R1234yf - R244bb (65)	(Z. Yang et al. 2015)
R32 - R236fa (21)	(Bobbo et al. 1999)	R152a - R134 (66)	(Guo et al. 2012)
R32 - R1234yf (22)	(Kamiaka et al. 2013)	R23 - R116 (67)	[NIST]
R32 - R290 (23)	(Coquelet et al. 2003)	R152a - R245fa (68)	(L. Yang et al. 2015)

R41 - CO_2 (24)	(Di Nicola et al. 2005)	R32 - SO_2 (72)	(Valtz et al. 2004)
R125 - R134a (25)	(Kobayashi & Nishiumi 1998)	R23 - Propane (73)	(Ju et al. 2009)
R125 - R143a (26)	(Barley et al. 1997)	R23 - nButane (74)	(Ju et al. 2009)
R125 - R152a (27)	(Lim et al. 2000)	Isopentane - R365mfc (75)	(ElAhmar et al. 2012)
R125 - R236fa (28)	(Bobbo et al. 1999)	Isopentane - R245fa (76)	(ElAhmar et al. 2012)
R125 - R1234yf (29)	(Kamiaka et al. 2013)	CO_2 - R1233zd(E) (77)	[CD]
R134a - R12 (30)	(Kleiber 1994)	R134a - R1233zd(E) (78)	[CD]
R134a - R142b (31)	(Kleiber 1994)	R152a - R1233zd(E) (79)	[CD]
R134a - R227ea (32)	(Hu, L. X. Chen, et al. 2013)	R404A (80)	(Lemmon et al. 2010)
R134a - R236fa (33)	(Bobbo et al. 1998)	R421A (81)	(Lemmon et al. 2010)
R134a - R245fa (34)	(Bobbo et al. 2001)	R508A (82)	(Lemmon et al. 2010)
R134a - R1234yf (35)	(Kamiaka et al. 2013)	R410A (83)	(Lemmon et al. 2010)
R134a - R1234ze(E) (36)	(Dong et al. 2013)	R161 - R125 - R143a (84)	(Xuan & Chen 2005)
R143a - R134a (37)	(Barley et al. 1997)	R161 - R125 - R32 (85)	(Chen, R.-H. Hong, et al. 2006)
R143a - R161 (38)	(Wang, Gao, et al. 2010)	R32 - R290 - R227ea (86)	(C Coquelet et al. 2004)
R143a - R1234yf (39)	(Hu, L. X. Chen, et al. 2013)	R32 - R125 - R134a (87)	(Nagel & Bier 1995)
R134a - R152a (40)	(Kleiber 1994)	R125 - R143a - R134a (88)	(Nagel & Bier 1996)
R152a - R227ea (41)	(Lim et al. 2001)	R22 - R152a - R142b (89)	(Maezawa, Widiatmo, et al. 1991)
R152a - R1234ze(E) (42)	(Yang et al. 2013)	R290 - R600a - R32 (90)	(Akasaka et al. 2007)
R161 - R32 (43)	(Han et al. 2010)		
R161 - R125 (44)	(Chen, R. Hong, et al. 2006)		
R161 - R134a (45)	(Chen et al. 2011)		

B. Uncertainties calculations and VTD equations

B.1. Uncertainties calculations

The result of an experimental measure is often an approximation of the real value. The difference between the two is the measurement error. It is composed of the random error and the systematic error, as illustrated in Figure B.1.

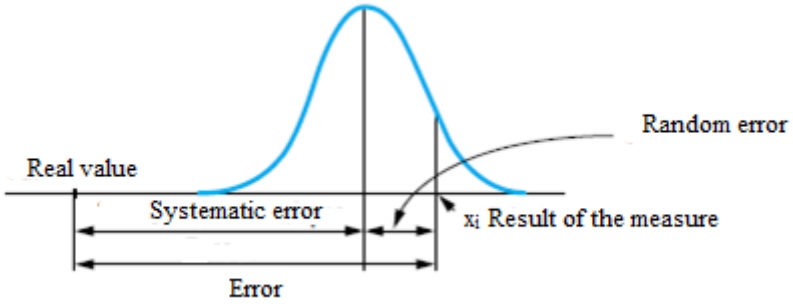

Figure B.1 Random and systematic errors (Zhang 2012).

The measurement error should be minimized in order to have a result as close as possible to the real value. The random error is minimized through repetition of measurements and the systematic error is minimized through corrections (calibration for example). But, even after these corrections, there is still an uncertainty due to the fact that the corrections are not perfect. The uncertainty expresses the interval where the real value exists.

The uncertainties can be classified within two main categories:

- Type A standard uncertainty: this type of uncertainty is evaluated by statistical methods (Taylor 2009).
- Type B standard uncertainty: this type of uncertainty is evaluated by other means (Taylor 2009).

When many sources of uncertainties exist, the global uncertainty is the combination of all the sources of uncertainties (combined standard uncertainty).

B.1.1. Calculation method

B.1.1.1. Type A standard uncertainty

In order to estimate the real value of a measurand θ, N independent observations can be realized at the same conditions of measurements. The values obtained θ_k, (k=1…N) are in the most cases different. The real value of θ is estimated by the mean value of θ_k (Zhang 2012; Taylor 2009):

$$\bar{\theta} = \frac{1}{N}\sum_{k=1}^{N} \theta_k \tag{B.1}$$

The error distribution follows the normal law. The type A uncertainty is calculated as follows (Zhang 2012; Taylor 2009):

$$u(\theta) = \sqrt{\frac{\sigma^2(\theta_k)}{N}} = \sqrt{\frac{1}{N(N-1)}\sum_{k=1}^{N}(\theta_k - \bar{\theta})^2} \tag{B.2}$$

Where σ^2 is the variance of the values obtained.

B.1.1.2. Type B standard uncertainty

When the value θ is not obtained through repetitive observations, its uncertainty is of a type B. The calculated method of a type B uncertainty is based on a scientific judgment using all the available information (previous measurements data, manufacturer specifications, etc.). Consequently, the method of calculations varies depending on the circumstances.

In this work, we suppose that the distribution of probabilities of θ follows a rectangular law, with an upper limit θ^+ and a lower limit θ^-. The probability distribution is uniform inside the interval $[\theta^-, \theta^+]$ and equal to zero outside. The width of the interval is denoted 2a.

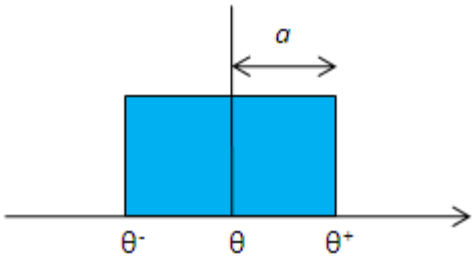

Figure B.2 Rectangular distribution (Zhang 2012).

The type B uncertainty is calculated as follows (Zhang 2012; Taylor 2009):

$$u(\theta) = \frac{(\theta^+ - \theta^-)/2}{\sqrt{3}} = \frac{a}{\sqrt{3}} \tag{B.3}$$

B.1.1.3. Combined standard uncertainty

If the measured value of θ has several sources of uncertainty $u_k(\theta)$ (k=1…N), the combined standard uncertainty u_c, is expressed through the combination of all the sources of uncertainties, following Eq. (B.4) (Zhang 2012; Taylor 2009):

$$u_c(\theta) = \sqrt{\sum_{k=1}^{N} u_k^2(\theta)} \tag{B.4}$$

If θ is calculated with a mathematical relation from other values of independent measurands α_k (k=1…N) according to Eq (B.5), the law of propagation of uncertainty is applied according to Eq. (B.6) (Zhang 2012; Taylor 2009):

$$\theta = f(\alpha_1, \alpha_2, \ldots \alpha_k, \ldots \alpha_N) \tag{B.5}$$

$$u_c(\theta) = \sqrt{\sum_{k=1}^{N} \left(\frac{\partial f}{\partial \alpha_k}\right)^2 u^2(\alpha_k)} \tag{B.6}$$

In some cases, α_k are dependent between them. This dependency should be taken into account in the calculation of u_c, according to Eq. (B.7) (Zhang 2012; Taylor 2009):

$$u_c(\theta) = \sqrt{\sum_{k=1}^{N} \left(\frac{\partial f}{\partial \alpha_k}\right)^2 u^2(\alpha_k) + 2 \sum_{k=1}^{N-1} \sum_{l=k+1}^{N} \frac{\partial f}{\partial \alpha_k} \frac{\partial f}{\partial \alpha_l} u(\alpha_k, \alpha_l)} \quad \text{(B.7)}$$

Where $u(\alpha_k,\alpha_l)$ is the covariance between α_k and α_l. The covariance expresses the dependency between two variables. It is comprised between -1 and +1. It is equal to 0 if the variables are independent.

B.1.2. VLE measurements

While performing VLE measurements, we measure pressure, temperature and composition (P, T, x_i). Therefore, calculations of uncertainties are performed to obtain u(P), u(T) and $u(x_i)$. In this section, we will present the calculation method of these uncertainties.

B.1.2.1. Calculation methods of u(P) and u(T)

u(P) and u(T) are calculated with the same method, so we will treat only the example of u(P) and apply the same method to u(T).

For u(P), we have two sources of uncertainties:

- $u_{rep}(P)$: which is related to the repeatability of measurements.
- $u_{calib}(P)$: which is related to the calibration. $u_{calib}(P)$ is composed of two terms: $u_{ref}(P)$ and $u_{corr}(P)$. $u_{ref}(P)$ is the uncertainty of the calibrator used. It is obtained from a accredited organism (such as LNE: Laboratoire National de métrologie et d'Essais). $u_{corr}(P)$ is the uncertainty related to the polynomial expression established between the values read on the apparatus used for measurement (pressure transducer in this case) and the values of the calibrator.

Then, u(P) is expressed as follows (Zhang 2012; Soo 2011):

$$u(P) = \sqrt{u_{rep}^2(P) + u_{calib}^2(P)} = \sqrt{u_{rep}^2(P) + u_{ref}^2(P) + u_{corr}^2(P)} \quad \text{(B.8)}$$

- **Calculation method of $u_{rep}(P)$**

The uncertainty related to the repeatability is from type A. So, according to Eq (B.2) it is calculated as follows (Zhang 2012; Taylor 2009):

$$u_{rep}(P) = \sqrt{\frac{1}{N(N-1)}\sum_{k=1}^{N}(P_k - \bar{P})^2} \tag{B.9}$$

- **Calculation method of $u_{ref}(P)$**

The uncertainty of the standard given by the manufacturer is in the form of ±a. It is a type B uncertainty, calculated according to Eq (B.3) as follows (Zhang 2012; Soo 2011):

$$u_{calib}(P) = \frac{a}{\sqrt{3}} \tag{B.10}$$

- **Calculation method of $u_{corr}(P)$**

Before using a pressure transducer, it is calibrated first. From this calibration, we develop a polynomial relation (order 2 in general) between the values read on the pressure transducer P_{read_k} (k=1…N) and the values measured by the reference pressure transducer P_{ref_k} (k=1…N):

$$P = a_0 + a_1 P_{read} + a_2 P_{read}^2 \tag{B.11}$$

This expression allows to correct the values read on the pressure transducer during the measurements.

P is in function of the parameters a_0, a_1 and a_2 which are correlated between them. The law of propagation of uncertainty (Eq (B.7)) can be applied to Eq (B.11) to calculate $u_{corr}(P)$ (Zhang 2012):

$$u_{corr}(P) = \sqrt{u^2(a_0) + P_{read}^2 u^2(a_1) + P_{read}^4 u^2(a_2) + 2[P_{read} u(a_0, a_1) + P_{read}^2 u(a_0, a_2) + P_{read}^3 u(a_1, a_2)]} \tag{B.12}$$

To determine the standard uncertainties of the parameters and the covariances between them, we calculate the variance-covariance matrix V of these parameters from P_{read_k} and P_{ref_k} (k=1…N). We define first the matrix X from the P_{read_k} (k=1…N) (Zhang 2012):

$$X = \begin{bmatrix} 1 & P_{read\_1} & P_{read\_1}^2 \\ 1 & P_{read\_2} & P_{read\_2}^2 \\ \vdots & \vdots & \vdots \\ 1 & P_{read\_k} & P_{read\_k}^2 \\ \vdots & \vdots & \vdots \\ 1 & P_{read\_N} & P_{read\_N}^2 \end{bmatrix} \quad \text{(B.13)}$$

We define the residual variance σ^2, which is calculated as follows (Zhang 2012):

$$\sigma^2 = \frac{1}{N - N_{par}} \sum_{k=1}^{N} \varepsilon_k^2 \quad \text{(B.14)}$$

Where N_{par} is the number of parameters (N_{par} = 3 in this example), and ε_k is the residue associated to P_{ref_k} and P_{read_k}. the residue ε_k is calculated as follows (Zhang 2012):

$$\varepsilon_k = P_{ref\_k} - (a_0 + a_1 P_{read\_k} + a_2 P_{read\_k}^2) \quad \text{(B.15)}$$

The variance-covariance matrix V (which is a symmetric matrix) is expressed as follows (Zhang 2012):

$$V = \begin{bmatrix} u^2(a_0) & u(a_0, a_1) & u(a_0, a_2) \\ u(a_0, a_1) & u^2(a_1) & u(a_1, a_2) \\ u(a_0, a_2) & u(a_1, a_2) & u^2(a_2) \end{bmatrix} \quad \text{(B.16)}$$

The matrix V is calculated from Eq (B.17) (Zhang 2012) as follows:

$$V = \sigma^2 (X^T X)^{-1} \quad \text{(B.17)}$$

The terms of V allow to calculate $u_{corr}(P)$ from Eq (B.12).

B.1.2.2. Calculation methods of u(x_i)

In this example, we will treat the case of a binary system. The molar fraction is determined from the number of moles of each compound in the analyzed sample, given by the relation:

$$x_1 = \frac{n_1}{n_1 + n_2} \tag{B.18}$$

The calculation method is the same for the two compounds, so we will treat the example of the compound 1, and apply the same method to compound 2.

For $u(x_1)$, we have three sources of uncertainties:

- $u_{rep}(x_1)$: which is the uncertainty related to the repeatability of the measurements.
- $u(n_1)$: which is the uncertainty related to the calibration. $u(n_1)$ is composed of two terms: $u_{inj}(n_1)$ and $u_{corr}(n_1)$. $u_{inj}(n_1)$ is the uncertainty of the number of moles n1 injected. $u_{corr}(n_1)$ is the uncertainty related to the polynomial expression established between the surface area of the pic obtained S_1 and the number of moles n_1.
- $u(n_2)$: is defined the same as $u(n_1)$ but for n_2.

$u(n_1)$ and $u(n_2)$ are calculated following the same method, so we will treat only the case of $u(n_1)$ and apply it to $u(n_2)$. $u(n_1)$ is expressed as follows (Zhang 2012):

$$u(n_1) = \sqrt{u_{inj}^2(n_1) + u_{corr}^2(n_1)} \tag{B.19}$$

Then, $u(x_1)$ is expressed according to Eq. (B.6) as follows (Zhang 2012):

$$u(x_1) = \sqrt{u_{rep}^2(x_1) + \left(\frac{1 - x_1}{n_1 + n_2}\right)^2 u^2(n_1) + \left(\frac{x_1}{n_1 + n_2}\right)^2 u^2(n_2)} \tag{B.20}$$

- **Calculation method of $u_{rep}(x_1)$**

$u_{rep}(x_1)$ is due to repeatability, so it is a type A uncertainty. Then, according to Eq (B.2) it is calculated as follows (Soo 2011; Zhang 2012):

$$u_{rep}(x_1) = \sqrt{\frac{1}{N(N-1)}\sum_{k=1}^{N}(x_{1\_k} - \bar{x}_1)^2} \tag{B.21}$$

- **Calculation method of $u_{inj}(n_1)$**

The number of moles injected is usually determined from the volume injected. The calculation method of $u_{inj}(n_1)$ varies depending on the compound studied. Here, we will limit to compounds in gas state at room temperature (1 atm, 25°C). In this case, n_1 is determined from ideal gas law:

$$n_1 = \frac{PV_1}{RT} \tag{B.22}$$

According to Eq (B.6), $u_{inj}(n_1)$ is expressed in function of u(P), u(T) and $u(V_1)$ as follows (Soo 2011):

$$u_{inj}(n_1) = n_1\sqrt{\frac{u^2(P)}{P^2} + \frac{u^2(T)}{T^2} + \frac{u^2(V_1)}{V_1^2}} \tag{B.23}$$

u(P) and u(T) are determined from the methods described before (Appendix B.1.2.1), if the same measurement apparatus are used. If not, u(P) and u(T) are determined according to the available information. In general, P and T are constant during the calibration.

In our measurements, the gas is injected through an automatic injector eVol®, allowing more precise injections. The volume uncertainty is related to the injector precision and the human error. As proposed by Soo (Soo 2011), we take ±2% of the volume read as error. $u(V_1)$ is a type B uncertainty, so it is calculated through Eq. (B.3) as follows (Soo 2011):

$$u(\theta) = \frac{0.02 \times V_1}{\sqrt{3}} = 0.012 V_1 \quad \text{(B.24)}$$

- **Calculation method of $u_{corr}(n_1)$**

During the calibration of the gas chromatograph, we establish a polynomial expression between the surface area of the peak obtained S_1 and the number of moles injected n_1:

$$n_1 = a_0 + a_1 S_1 + a_2 S_1^2 \quad \text{(B.25)}$$

This relation allows us to convert the surface area of the peak to number of moles during the measurements.

$u_{corr}(n_1)$ is determined following the same method as for $u_{corr}(P)$ before (Appendix B.1.2.1).

B.2. VTD equations

The calibration method of the vibrating-tube densimeter using a forced path mechanical calibration (FPMC) model for the Anton Parr DMA 512 densimeter were well described by (Bouchot & Richon 2001; Nazeri et al. 2016). The U-tube of the DMA 512 densimeter cell can be modelled by a linear hollow vibrating system whose internal volume is $V_i = V_i(T,P)$ and its total vibrating mass is $(M_0+\rho V_i)$ (Bouchot & Richon 1998a; Bouchot & Richon 2001). M_0 is the proper mass of the tube under vacuum and ρ is the density of the inner fluid to be determined. This system has a natural transversal stiffness K = K (T, P) and is vibrating with a period (τ) in an undamped harmonic way under the effect of a mechanical excitation (Nazeri et al. 2016; Bouchot & Richon 1998a; Bouchot & Richon 2001).
The relation between these quantities can be written in the following general form:

$$\rho = \left(\frac{M_0}{V_i}\right)\left(\left(\frac{K}{K_0}\right)\left[\frac{\tau^2}{\tau_o^2}\right]-1\right) \tag{B.26}$$

where K_0 and τ_0 are the transversal stiffness and the vibrating period of the evacuated tube, respectively.

The term K/K_0 is expressed as follows (Nazeri et al. 2016):

$$\frac{K}{K_0} = \frac{I}{I_0}\left(\frac{L_0}{L}\right)^3 \tag{B.27}$$

The first term in Eq. (B.27) is expressed as follows (Nazeri et al. 2016):

$$\frac{I}{I_0} = \frac{\Delta r^4}{\Delta r_0^4} = \frac{r_e^4 - r_i^4}{r_{e0}^4 - r_{i0}^4} \tag{B.28}$$

The second term of Eq. (B.27) is the relative inverse cubic length change expressed as follows (Nazeri et al. 2016):

$$\left(\frac{L_0}{L}\right)^3 = \exp\left(-3\gamma_T P\right) \tag{B.29}$$

The term (M_0/V_i) is expressed as follows (Nazeri et al. 2016):

$$\frac{M_0}{V_i(T,P)} = \frac{M_0}{\pi r_i^2 L} = \frac{M_0}{L_{00}}\left(\frac{1}{\pi r_i^2 \delta L}\right) \tag{B.30}$$

The complete FPMC model can be expressed as follows:

$$\rho(T,P) = \frac{M_0}{L_{00}}\left(\frac{1}{\pi r_i^2(T,P)\delta L(T,P)}\right)\left\{\left(\frac{\Delta r^4(T,P)}{\Delta r_0^4(T)}\right)\exp\left(-3\gamma_T P\right)\left[\frac{\tau^2(T,P)}{\tau_o^2(T)}\right]-1\right\} \tag{B.31}$$

The two parameters γ_T and (M_0/L_{00}) are adjusted using the density data of the calibration fluid used from REFPROP 9.0 (Lemmon et al. 2010) (for example R134a in this work) at the desired pressure ranges and for each measured isotherm.

C. Experimental measurements

C.1. Experimental data

Table C.1 Vapour pressures for the pure compound R1234yf.

R1234yf	
T/K	*P/MPa*
275.81	0.3445
275.82	0.3446
278.21	0.3727
278.21	0.3727
283.03	0.4355
283.04	0.4353
287.94	0.5065
287.94	0.5064
292.76	0.5846
292.82	0.5857
297.70	0.6736
297.71	0.6740
302.59	0.7717
302.60	0.7719
307.39	0.8780
307.43	0.8789
312.22	0.9951
312.25	0.9961
317.25	1.1298
322.11	1.2720
322.12	1.2727
327.00	1.4286
327.00	1.4288
331.82	1.5970
331.83	1.5971
336.65	1.7793
336.67	1.7800

Expanded uncertainties are: U(T) = 0.08 K; U(P) = 0.0004 MPa; (k = 2).

Table C.2 VLE data of the system CO_2 (1) + R1234yf (2).

P/MPa	x_1	y_1
	T = 283.21 K	
0.8387	0.1123	0.4701
1.1510	0.1963	0.6223
1.7922	0.3678	0.7796
2.4729	0.5402	0.8606
3.4865	0.7809	0.9362
3.9283	0.8779	0.9614
	T = 293.18 K	
0.8150	0.0569	0.2687
1.0563	0.1162	0.4350
1.5732	0.2438	0.6341
2.1195	0.3649	0.7496
2.7107	0.4904	0.8160
3.4338	0.6340	0.8772
4.3171	0.7904	0.9281
4.9250	0.8860	0.9583
5.3107	0.9418	0.9768
	T = 298.11 K	
0.9894	0.0681	0.2873
1.8041	0.2407	0.6187
2.5793	0.3922	0.7490
3.1769	0.5044	0.8103
3.6932	0.5979	0.8493
4.2563	0.6926	0.8838
4.9018	0.7942	0.9160
5.5476	0.8851	0.9496
5.9520	0.9378	0.9706
	T = 308.20 K	
1.0196	0.0255	0.1155
2.3810	0.2879	0.6321
3.6035	0.4933	0.7739
4.4994	0.6257	0.8348
5.4709	0.7514	0.8808
5.9288	0.8067	0.9009
6.4431	0.8612	0.9209
6.7199	0.8877	0.9313
6.9229	0.9084	0.9393
7.0909	0.9244	0.9456
7.2107	0.9360	0.9498
	T = 323.18 K	
1.5040	0.0340	0.1216
1.7424	0.0738	0.2354
2.4990	0.1953	0.4634
3.5137	0.3459	0.6203
4.5007	0.4776	0.7053
5.4434	0.5919	0.7589
5.9935	0.6521	0.7800
6.4076	0.6957	0.7934
6.6800	0.7261	0.7985
6.8637	0.7478	0.7973
6.9530	0.7615	0.7926
	T = 338.24 K	
2.1404	0.0440	0.1216
2.6175	0.1111	0.2637
3.0326	0.1676	0.3543

3.7317	0.2589	0.4628
4.4293	0.3444	0.5361
5.2081	0.4362	0.5920
5.6055	0.4825	0.6099
5.9611	0.5252	0.6170
6.1185	0.5471	0.6148
	T = 353.25 K	
2.8266	0.0393	0.0821
3.1869	0.0849	0.1615
3.5196	0.1264	0.2220
3.9990	0.1861	0.2900
4.3959	0.2343	0.3314
4.7327	0.2814	0.3557
4.9029	0.3005	0.3606
4.9582	0.3113	0.3581
4.9840	0.3173	0.3557
5.0083	0.3320	0.3433

Expanded uncertainties are: U(T) = 0.06 K; U(P) = 0.0008 MPa; $U(x_1) = 0.008$; $U(y_1) = 0.008$; (k = 2).

Table C.3 VLE experimental results for R23 (1) + Propane (2).

P/MPa	x_1	y_1
	T = 293.18 K	
0.8368	0	0
1.3538	0.0534	0.3409
1.8594	0.1204	0.5080
2.8118	0.3216	0.6701
3.1979	0.4532	0.7167
3.6002	0.6252	0.7686
3.7345	0.6865	0.7916
3.9258	0.7763	0.8303
4.1419	0.9061	0.9146
4.1703	0.9368	0.9404
4.1769	0.9476	0.9493
4.1800	0.9544	0.9551
4.1774	-	0.9549
4.1797	0.9592	0.9597
4.1819	0.9663	0.9666
4.1823	0.9695	0.9695
4.1821	0.9738	0.9736
4.1822	0.9774	0.9769
4.1805	0.9817	0.9815
4.1790	0.9863	0.9857
4.1787	0.9917	0.9913
4.1717	1	1
	T = 298.15 K	
0.9508	0	0
1.6831	0.0747	0.3871
3.0651	0.3140	0.6478
2.3621	0.1700	0.5502
3.6164	0.4843	0.7090
3.9604	0.6096	0.7469
4.2464	0.7204	0.7877
4.4949	0.8194	0.8408
4.5411	0.8395	0.8542
4.5644	0.8495	0.8622
4.6067	0.8710	0.8780
4.6287	0.8826	0.8877
4.6686	0.9058	0.9059
4.6944	0.9268	0.9270
4.7180	0.9572	0.9571
4.7191	0.9637	0.9640
4.7206	0.9680	0.9683
4.7184	-	0.9620
4.7217	0.9795	0.9792
4.7208	0.9878	0.9878
4.7093	1.0000	1.0000
	T = 313.15 K	
1.3801	0	0
2.0388	0.0572	0.2738
3.0674	0.1733	0.4814
3.7409	0.2782	0.5582
4.1408	0.3542	0.5917
4.6054	0.4595	0.6225
4.8038	0.5119	0.6292
4.9324	0.5501	0.6304
5.0006	0.5763	0.6229
	T = 323.15 K	

1.7130	0	0
2.4390	-	0.2369
3.1572	0.1283	0.3739
3.5130	-	0.4178
2.2264	0.0396	0.1822
2.8503	0.0971	0.3266
3.5541	0.1722	0.4307
4.0748	-	0.4849
2.4525	0.0597	0.2393
4.1810	0.2566	0.4909
4.4982	0.3066	0.5052
4.8326	0.3657	0.5230
5.0287	0.4063	0.5297
5.1504	0.4372	0.5274
5.1895	0.4470	0.5233
	T = 353.15 K	
3.1354	0	0
3.5010	0.0247	0.0625
3.7949	0.0457	0.1040
4.0015	0.0617	0.1329
4.2831	0.0849	0.1629
4.3708	0.0921	0.1698
4.4198	0.0960	0.1733
4.5218	0.1052	0.1820
3.4204	0.0179	0.0480
4.6256	0.1150	0.1891
4.7208	0.1254	0.1949

Expanded uncertainties are: U(T) = 0.08 K; U(P) = 0.0008 MPa; U(x_1) = 0.009; U(y_1) = 0.009; (k = 2).

Table C.4 Experimental densities and viscosities of R134a.

P/MPa	*ρ/kg.m^{-3}*	*η/mPa.s*	*P/MPa*	*ρ/kg.m^{-3}*	*η/mPa.s*
	T = 303.67			*T = 363.27*	
4.74	1212.06	0.19458	3.85	856.61	0.07838
8.26	1229.92	0.20666	5.10	910.09	0.08618
10.31	1239.39	0.21442	10.22	1008.09	0.10977
14.83	1258.23	0.22780	15.13	1059.90	0.12618
19.99	1277.05	0.24234	20.08	1097.69	0.14143
25.06	1293.59	0.25730	25.22	1128.59	0.15325
30.19	1308.55	0.27250	30.08	1153.80	0.16462
35.39	1322.60	0.28623	35.03	1175.56	0.17509
40.31	1334.57	0.29976	40.12	1196.15	0.18407
44.95	1345.36	0.31192	44.75	1212.35	0.19312
50.91	1358.39	0.32834	50.32	1229.53	0.20623
	T = 333.27			*T = 393.26*	
2.21	1055.35	0.12341	4.74	271.48	0.02245
5.57	1094.36	0.13894	10.45	850.17	0.07829
10.30	1133.47	0.15681	15.39	943.33	0.09510
13.53	1155.58	0.16434	20.42	999.95	0.10939
15.51	1166.02	0.17254	24.87	1037.73	0.12067
20.41	1191.20	0.18561	30.25	1073.54	0.13485
25.63	1214.49	0.19526	35.26	1102.28	0.14139
29.07	1227.84	0.20594	40.32	1126.08	0.15379
30.68	1233.77	0.21008	45.23	1146.68	0.16243
35.40	1249.90	0.22192	50.22	1165.79	0.17244
40.45	1265.69	0.23591			
44.56	1276.79	0.24650			
49.48	1289.69	0.26366			

Expanded uncertainties are: U(T) = 0.1 K; U(P) = 0.05 MPa; U(ρ)/ρ = 0.2%; U(η)/η = 2%; (k = 2).

Table C.5 Experimental densities and viscosities of R1234yf.

P/MPa	*ρ/kg/m^{-3}*	*η/mPa.s*	*P/MPa*	*ρ/kg/m^{-3}*	*η/mPa.s*
	T = 303.65			*T = 394.16*	
1.19	1077.22	0.14127	0.74	29.12	0.01638
4.86	1103.86	0.15620	5.02	411.41	0.03055
10.32	1134.38	0.17591	7.93	717.82	0.05853
16.67	1162.67	0.19324	10.14	789.62	0.07069
20.28	1176.92	0.20129	15.35	882.59	0.08421
25.02	1193.55	0.21130	20.18	933.84	0.09657
25.20	1193.51	0.21315	25.12	973.47	0.10657
30.16	1210.31	0.22067	29.97	1004.26	0.11689
35.01	1223.58	0.23091	34.49	1028.52	0.12441
35.41	1223.95	0.23370	40.18	1054.96	0.13489
35.43	1224.45	0.23201	45.34	1075.64	0.14513
40.13	1237.06	0.24205	49.97	1092.25	0.15117
45.23	1248.96	0.25242			
50.32	1260.29	0.26399			
	T = 333.20			*T = 423.06*	
2.30	951.23	0.09847	0.78	29.32	0.01697
5.39	995.24	0.11160	4.81	240.46	0.02228
10.42	1042.12	0.12762	5.00	252.14	0.02322
15.34	1075.21	0.14144	10.09	639.49	0.04969
20.27	1101.51	0.15303	15.18	781.09	0.06444
25.22	1123.55	0.17064	20.10	852.76	0.07982
30.45	1143.99	0.18050	25.31	905.08	0.09146
34.81	1159.14	0.19088	29.81	940.07	0.10028
34.97	1160.37	0.19269	35.27	975.03	0.10966
40.38	1176.46	0.20368	39.78	999.35	0.11638
45.43	1191.07	0.21490	44.88	1022.23	0.12443
50.24	1204.49	0.22441	50.01	1043.46	0.13199
50.49	1204.09	0.22605			
59.88	1227.51	0.23437			
	T = 362.71				
3.42	737.21	0.05654			
4.52	796.26	0.06755			
10.29	933.13	0.09501			
15.44	986.79	0.10927			
20.29	1023.00	0.12162			
24.91	1050.60	0.13175			
30.26	1077.60	0.14140			
34.99	1097.77	0.15262			
40.15	1117.41	0.16237			
44.99	1134.02	0.17099			
50.81	1151.25	0.18077			

Expanded uncertainties are: U(T) = 0.1 K; U(P) = 0.05 MPa; U(ρ)/ρ = 0.2%; U(η)/η = 2%; (k = 2).

C.2. Experimental data of the R1233zd(E)

Additional experimental measurements of the densities of the R1233zd(E) at high temperatures have been recently performed, using the vibrating-tube densimeter. The temperatures covered are 354.08 K, 373.60 K, 392.84 K and 413.05 K, for pressures up to 12 MPa.

The results obtained for the vapor densities are displayed in *Figure C.1*, representing the experimental data and the modelling results obtained using the NEoS.

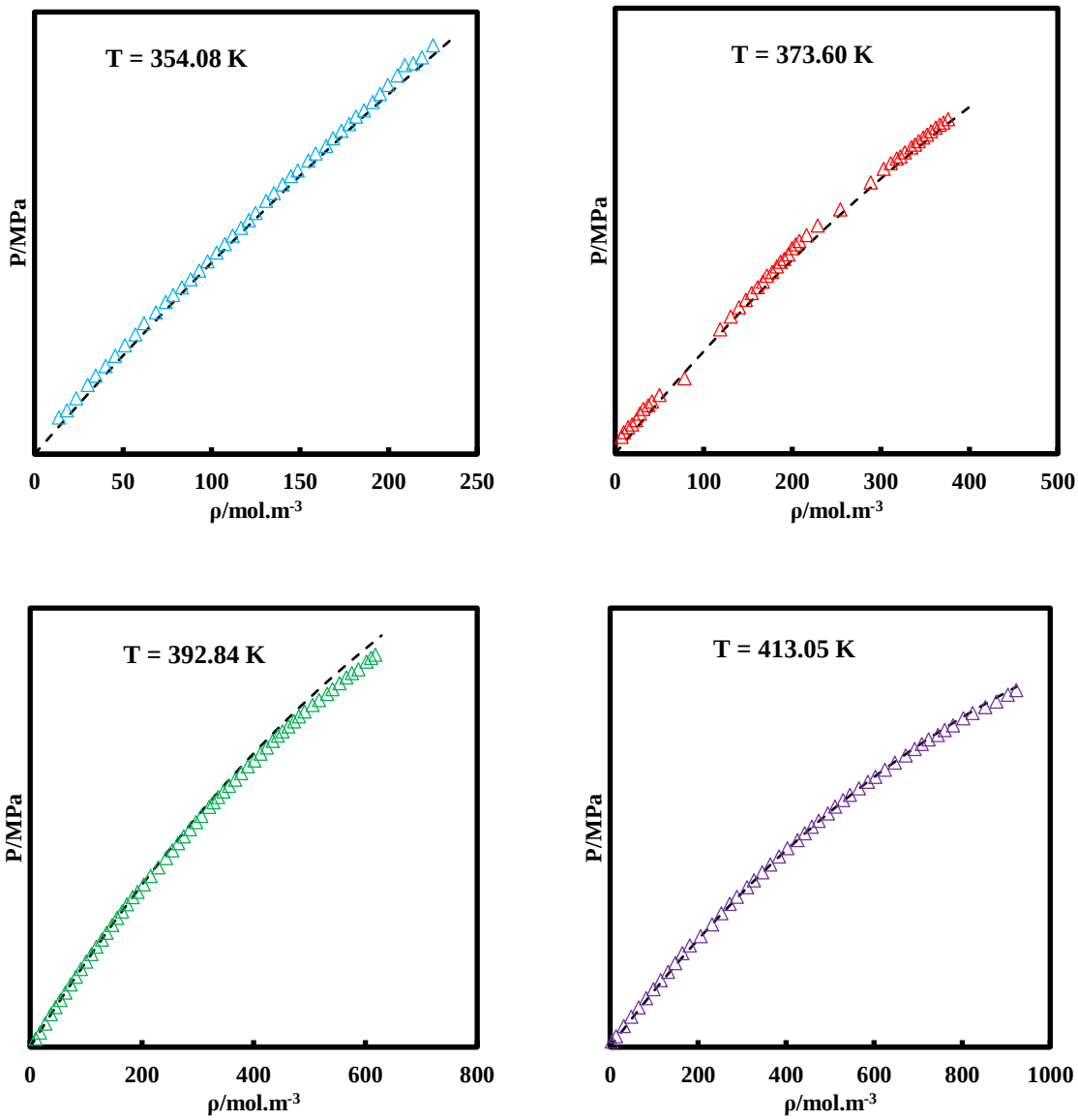

Figure C.1 Vapour densities of pure compound R1233zd(E) at high temperatures. (Δ) Experimental data; (- - - -) NEoS.

We can see from this graphical representation that the results obtained from the NEoS are in good agreement with the experimental vapour densities, for all the temperatures studied.

The results obtained for the liquid densities are displayed in *Figure C.2*, representing the experimental data and the modelling results obtained using the NEoS.

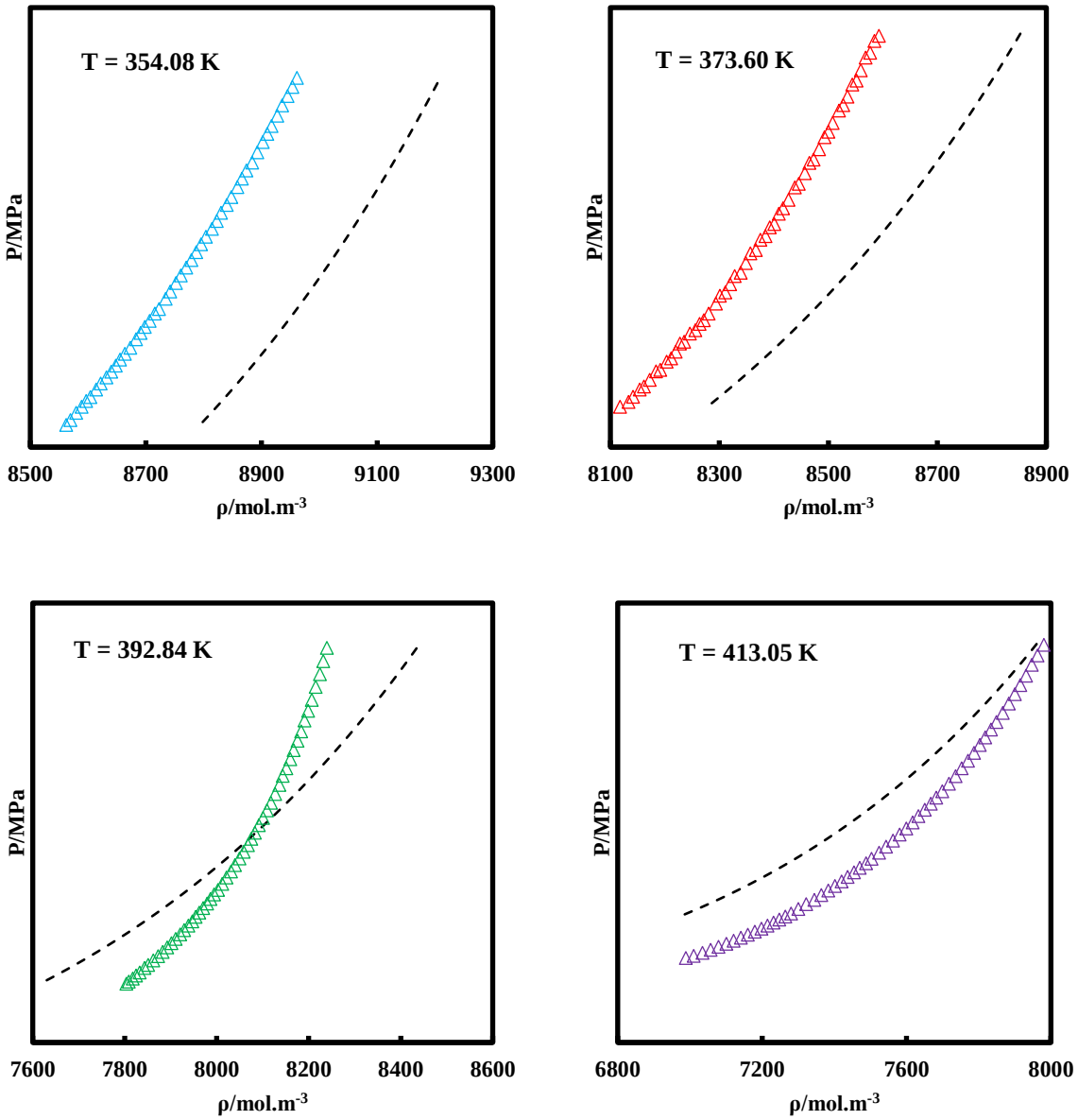

Figure C.2 Liquid densities of pure compound R1233zd(E) at high temperatures.
(Δ) Experimental data; (- - - -) NEoS.

We can see from this graphical representation that the results obtained with the NEoS have some deviations for representing the liquid densities. We can also notice that the curve obtained with the NEoS K is crossing the curve of the experimental densities at 392.94.

From the densities measured out of saturation using the vibrating-tube densimeter, the densities at saturation for the temperatures studied have been determined using a graphical method. The full details about this graphical determination method can be found in (Bouchot & Richon 1998b).

In addition to that, the densities near the critical point have been measured using a "Critical point determination" apparatus, via a static-synthetic method. The full details about this apparatus can be found in our recently published paper (Williams-Wynn et al. 2017).

The results obtained are displayed in *Figure C.3*, representing the experimental data measured, the data obtained using the graphical method and the modelling results obtained using the NEoS.

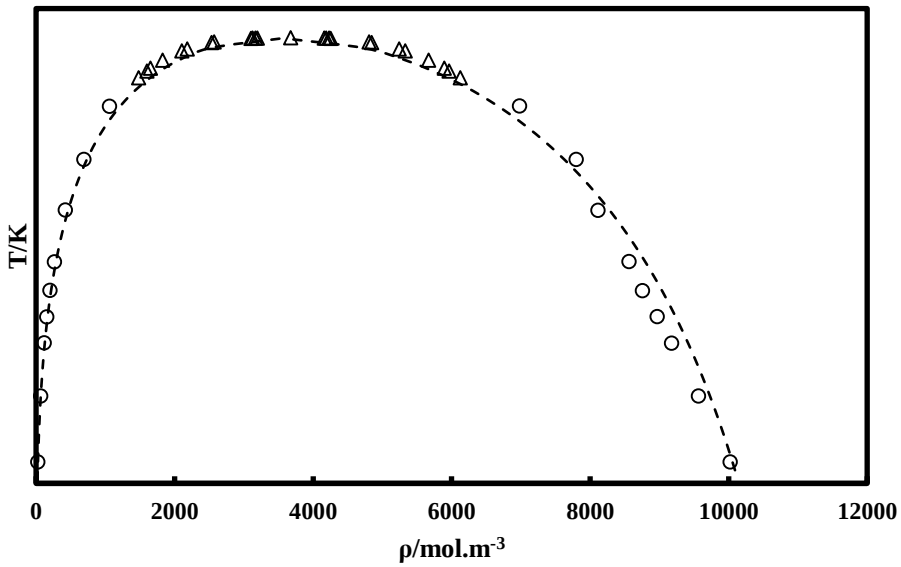

Figure C.3 Densities of pure compound R1233zd(E) at saturation. (Δ) Experimental data; (○) Data obtained using the graphical method; (- - - -) NEoS.

We can see from this graphical representation that the results obtained from the NEoS are in good agreement with the experimental data. We can also notice some little deviations of the densities determined at 392.84 K and 413.05 K compared to the other experimental points.

D. Complements to the modelling

D.1. Patel-Teja EoS

In *Table D.1* are reported the alpha function parameters and the critical compressibility factor adjusted from vapour pressure and saturated liquid density of pure compounds, obtained using PT-EoS associated with the MC alpha function.

Table D.1 Experimental and PT-EoS adjusted parameters for several refrigerant families (with m_2 = -0.01 and m_3 = 0.4). ω is the acentric factor, m_1 the alpha function parameter, and $Z_{c,opt}$ and Z_c the optimized and the experimental critical compressibility factors, respectively.

Families	*Compounds*	*ω*	m_1	$Z_{c,opt}$	Z_c
PFC	R-C318	0.35530	0.90709	0.31295	0.27751
	R-14	0.17850	0.67555	0.31954	0.27883
	R-116	0.25660	0.77577	0.31510	0.28151
	R-218	0.31720	0.84300	0.31391	0.27553
CFC	R-11	0.18875	0.65407	0.31346	0.27901
	R-12	0.17948	0.63489	0.31310	0.27643
	R-13	0.17230	0.63476	0.31484	0.27685
	R-113	0.25253	0.74834	0.31080	0.28019
	R-114	0.25230	0.74764	0.30981	0.27563
	R-115	0.25000	0.75177	0.31374	0.26779
	R-22	0.22082	0.66722	0.30519	0.26825
	R-123	0.28192	0.76770	0.30627	0.26806
	R-124	0.28810	0.77740	0.30741	0.26865
	R-141b	0.21950	0.69075	0.30842	0.27057
HFC	R-125	0.30520	0.80551	0.30706	0.26844
	R-134a	0.32684	0.79532	0.29871	0.26004
	R-143a	0.26150	0.67484	0.29264	0.25502
	R-152a	0.27521	0.67453	0.28916	0.25233
	R-161	0.21700	0.62261	0.29548	0.25979
	R-227ea	0.35700	0.88229	0.30851	0.26849
	R-23	0.26300	0.67957	0.29438	0.25821
	R-236ea	0.37940	0.92944	0.31120	0.27578
	R-236fa	0.37721	0.90641	0.30662	0.26664
	R-245ca	0.35360	0.87946	0.30986	0.27003
	R-245fa	0.37760	0.90658	0.30630	0.26702
	R-32	0.27690	0.61931	0.27683	0.24291
	R-365mfc	0.38000	0.90970	0.30914	0.26686
	R-41	0.20040	0.52412	0.27968	0.24036
HFO	R-1234yf	0.27600	0.74045	0.30169	0.26519
	R-1234ze(E)	0.31300	0.80128	0.30522	0.26651
HCFO	R-1233zd(E)	0.34137	0.82034	0.30811	0.27884

Based on this adjustment, correlations were established, relating the alpha function parameters to the acentric factor ω, and the optimized critical compressibility factor to the experimental one. The results are reported in Eq. (D.1).

$$\begin{gathered} m_1 = 3.6410\omega^2 - 0.5673\omega + 0.6142 \\ m_2 = -0.01 \\ m_3 = 0.4 \\ \mathrm{Z_{c,opt}} = -11.356\mathrm{Z_c}^2 + 6.8984\mathrm{Z_c} - 0.7266 \end{gathered} \tag{D.1}$$

In *Figure D.1* are displayed the correlations relating the alpha function parameter m_1 to the acentric factor ω, and the optimized critical compressibility factor to the experimental one.

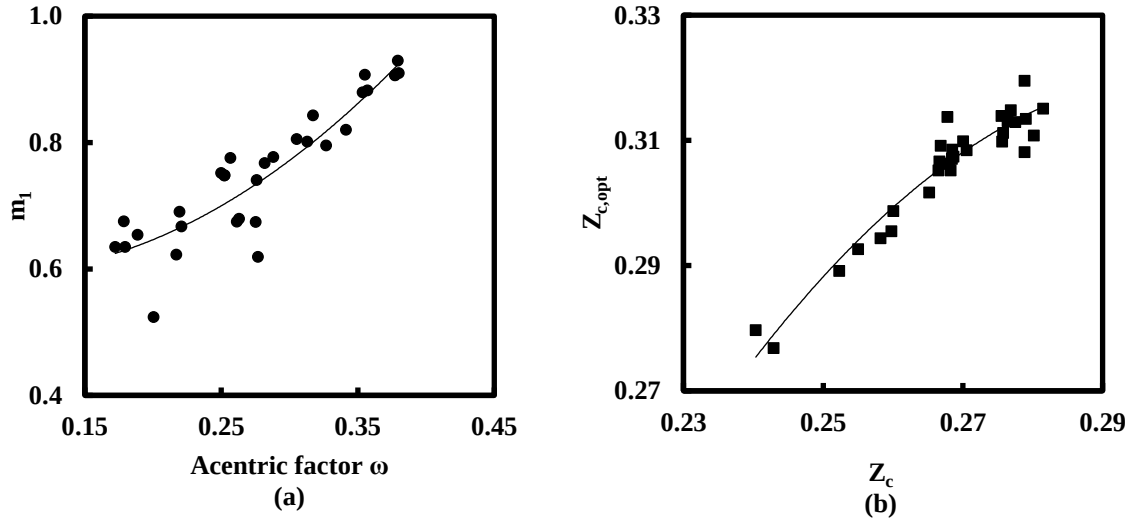

Figure D.1 Correlations obtained with PT-EoS. (a): the parameter m_1 as a function of the acentric factor ω (coefficient of determination R^2 = 0.83). (b): the optimized critical compressibility factor $Z_{c,opt}$ as a function of the experimental critical compressibility factor Z_c (coefficient of determination R^2 = 0.92).

D.2. Peng-Robinson EoS

In *Table D.2* are reported the alpha function parameters adjusted from vapour pressure of pure compounds, obtained using PR-EoS associated with the MC alpha function.

Table D.2 Experimental and PR-EoS adjusted parameters for several refrigerant families (with $m_2 = 0$ and $m_3 = 0.49$). ω is the acentric factor, m_1 the alpha function parameter, and $Z_{c,opt}$ and Z_c the optimized and the experimental critical compressibility factors, respectively.

Families	*Compounds*	ω	m_1
PFC	R-C318	0.35530	0.87504
	R-14	0.17850	0.61886
	R-116	0.25660	0.73579
	R-218	0.31720	0.80385
CFC	R-11	0.18875	0.61810
	R-12	0.17948	0.59947
	R-13	0.17230	0.59317
	R-113	0.25253	0.72610
	R-114	0.25230	0.73275
	R-115	0.25000	0.71730
HCFC	R-21	0.20610	0.65949
	R-22	0.22082	0.66061
	R-123	0.28192	0.75902
	R-124	0.28810	0.76343
	R-141b	0.21950	0.67316
	R-142b	0.23210	0.68115
HFC	R-125	0.30520	0.79991
	R-134a	0.32684	0.82270
	R-143a	0.26150	0.72686
	R-152a	0.27521	0.73535
	R-161	0.21700	0.65300
	R-227ea	0.35700	0.86570
	R-23	0.26300	0.71889
	R-236ea	0.37940	0.90565
	R-236fa	0.37721	0.90003
	R-245ca	0.35360	0.85944
	R-245fa	0.37760	0.89974
	R-32	0.27690	0.72710
	R-365mfc	0.38000	0.89465
	R-41	0.20040	0.61788
HFO	R-1234yf	0.27600	0.76202
	R-1234ze(E)	0.31300	0.80066
HCFO	R-1233zd(E)	0.34137	0.80854
NATURAL FLUIDS	CO_2	0.22394	0.69219

Based on this adjustment, a correlation was established, relating the alpha function parameters to the acentric factor ω. The results are reported in Eq. (D.2).

$$m_1 = -0.0944\omega^2 + 1.5012\omega + 0.3417$$
$$m_2 = 0 \qquad \text{(D.2)}$$
$$m_3 = 0.49$$

In *Figure D.2* is displayed the correlation relating the alpha function parameter m_1 to the acentric factor ω.

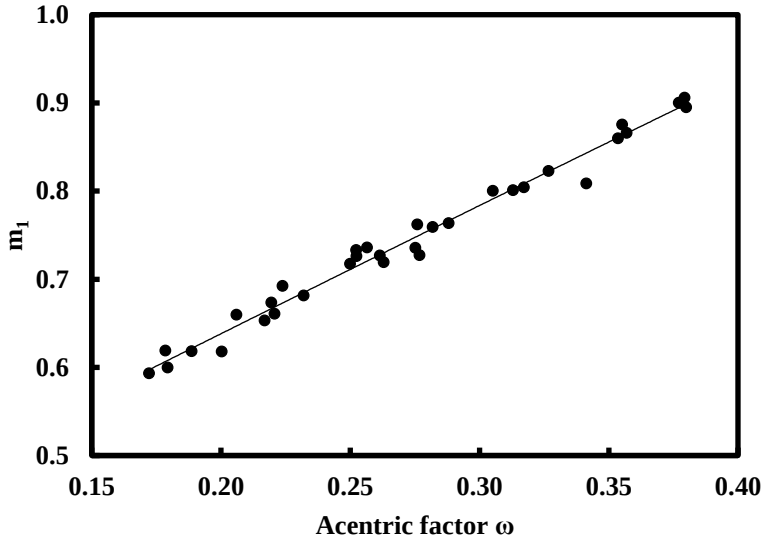

Figure D.2 Correlation obtained with PR-EoS. Parameter m_1 as a function of the acentric factor ω (coefficient of determination $R^2 = 0.98$).

D.3. Fugacity coefficient calculation for the NEoS

- **Pure compounds**

The formulas for fugacity coefficient calculations for a pure compound are given according to (Ji & Lempe 1998).

Formula for fugacity coefficient calculation for $w < u^2/4$:

$$\ln \varphi^* = z - 1 - \ln\left(z - \frac{pb}{RT}\right) - \frac{a(T)}{RTb\sqrt{u^2 - 4w}} \ln \frac{2z + \left(u - \sqrt{u^2 - 4w}\right)\frac{pb}{RT}}{2z + \left(u + \sqrt{u^2 - 4w}\right)\frac{pb}{RT}} \tag{D.3}$$

Formula for fugacity coefficient calculation for $w > u^2/4$:

$$\ln \varphi^* = z - 1 - \ln\left(z - \frac{pb}{RT}\right) - \frac{a(T)}{RTb\sqrt{w - u^2/4}} \left[\arctan\left(\frac{z + \frac{upb}{2RT}}{\frac{pb}{RT}\sqrt{w - u^2/4}}\right) - \frac{\pi}{2}\right] \tag{D.4}$$

- **Mixtures**

From writing the NEoS in the following generalized formula:

$$P = \frac{RT}{v - b} - \frac{a(T)}{(v + c)(v + d)} \tag{D.5}$$

where the parameters c and d are expressed as follows:

$$c = b\left(\frac{u - \sqrt{u(u + 4)}}{2}\right)$$
$$d = b\left(\frac{u + \sqrt{u(u + 4)}}{2}\right) \tag{D.6}$$

We can express the formula for fugacity coefficient calculations for mixtures as follows (Ji et al. 2007):

$$\ln \varphi_i^* = -\ln\left\{\frac{p(v-b)}{RT}\right\} + z - 1 + \frac{1}{v-b}\left[n\frac{\partial b}{\partial n_i}\right] - \frac{1}{RT(c-d)}\left(a + \left[n\frac{\partial a}{\partial n_i}\right]\right)\ln\frac{v+c}{v+d} + \frac{a}{RT(c-d)^2}\left\{\left[n\frac{\partial c}{\partial n_i}\right]\left(\ln\frac{v+c}{v+d} - \frac{c-d}{v+c}\right) - \left[n\frac{\partial d}{\partial n_i}\right]\left(\ln\frac{v+c}{v+d} - \frac{c-d}{v+d}\right)\right\} \tag{D.7}$$

in which the derivatives are calculated as follows:

$$\left[n\frac{\partial b}{\partial n_i}\right] = b_{ii} - \sum_k x_k b_{kk}$$
$$\left[n\frac{\partial c}{\partial n_i}\right] = c_{ii} - \sum_k x_k c_{kk} \tag{D.8}$$
$$\left[n\frac{\partial d}{\partial n_i}\right] = d_{ii} - \sum_k x_k d_{kk}$$

The calculation of the derivative of a depends on the mixing rules used.

We should note that theses formulas can be applied with any cubib equation of state and not only with the NEoS.

D.4. Enthalpy and heat capacities properties prediction

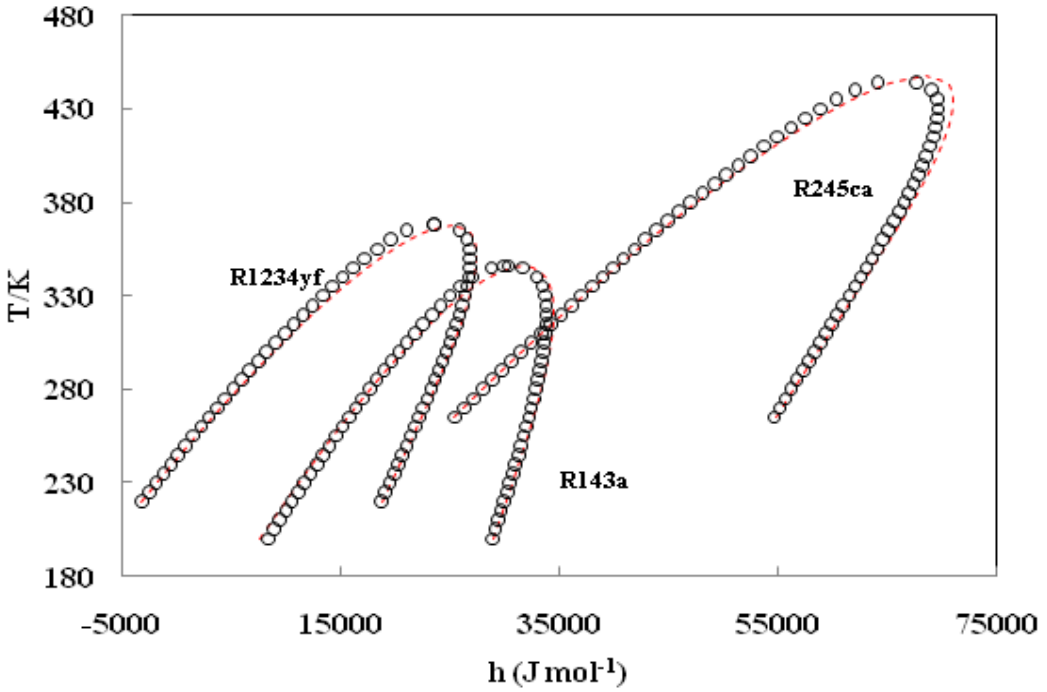

Figure D.3 Residual enthalpies of saturated phases. (○) REFPROP. (- - - -) NEoS.

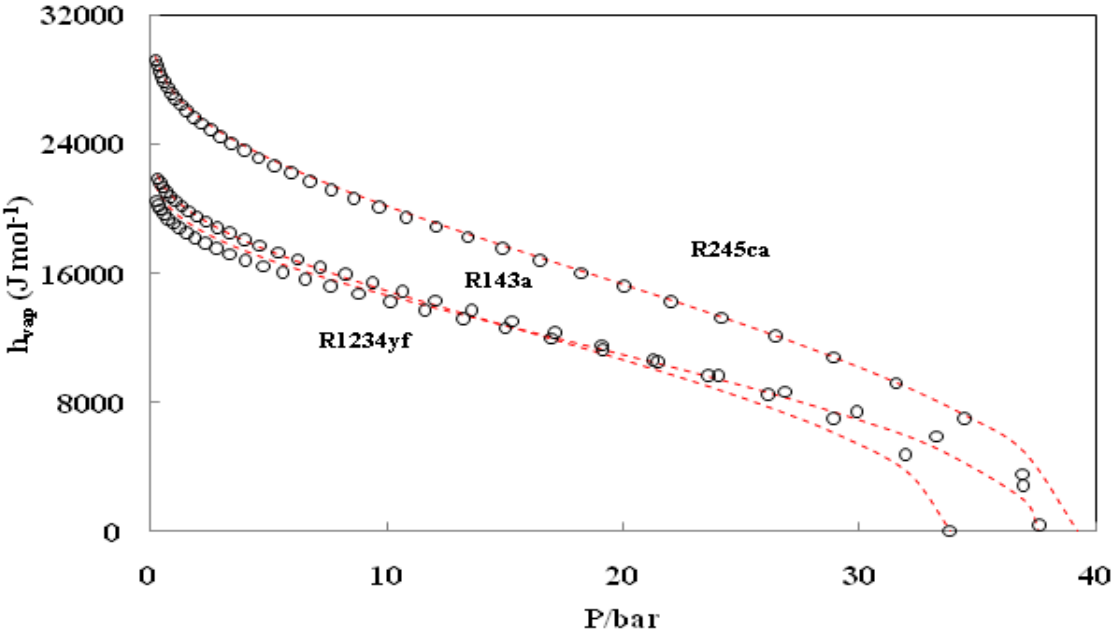

Figure D.4 Residual enthalpies of vaporization. (○) REFPROP; (- - - -) NEoS.

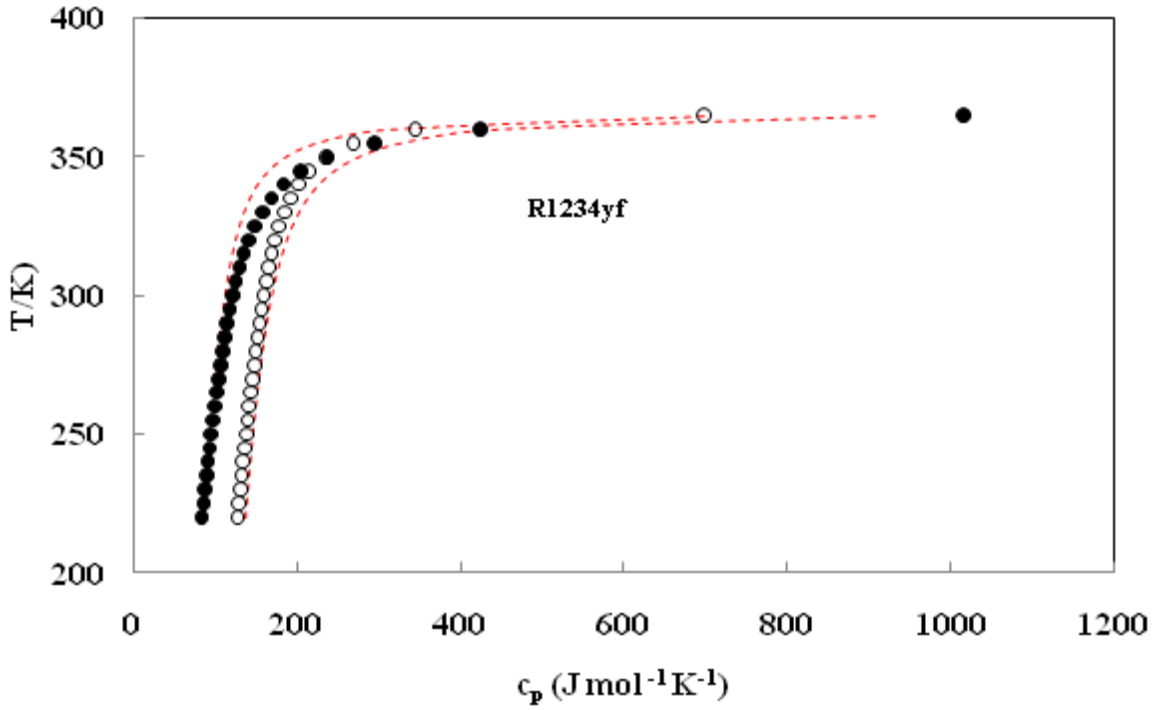

Figure D.5 Residual isobaric heat capacities of saturated phases. (○) Liquid, (●) Vapor – REFPROP; (- - - -) NEoS.

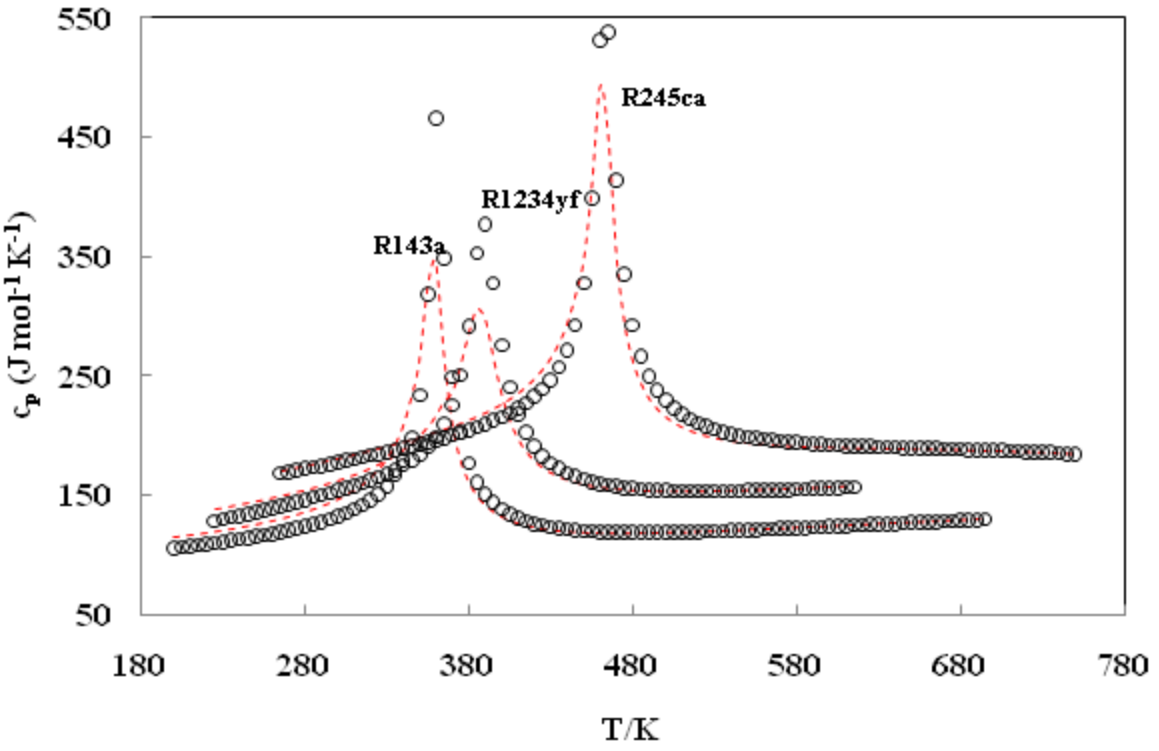

Figure D.6 Residual isobaric heat capacities at P = 5 MPa. (○) REFPROP; (- - - -) NEoS.

E. List of publications

➢ Papers

- Mark D. Williams-Wynn, **Jamal El Abbadi**, Alain Valtz, Elodie Kovacs, Céline Houriez, Paramespri Naidoo, Christophe Coquelet, Deresh Ramjugernath, *"Experimental determination of the critical loci for R-23 + (n-propane or n-hexane) and R-116 + n-propane binary mixtures"*, Journal of Chemical Thermodynamics. vol. 108, pp. 84–96, December 25, 2016

- Christophe Coquelet, **Jamal El Abbadi**, Céline Houriez, "Prediction of thermodynamic properties of refrigerant fluids with a new three-parameter cubic equation of state" Int. J. Refrig., vol. 69, pp. 418–436, September 2016.

- Hakim Madani, Alain Valtz, Fan Zhang, **Jamal El Abbadi**, Céline Houriez, Patrice Paricaud, Christophe Coquelet, *"Isothermal vapor–liquid equilibrium data for the trifluoromethane (R23) + 2,3,3,3-tetrafluoroprop-1-ene (R1234yf) system at temperatures from 254 to 348 K"* Fluid Phase Equilib., vol. 415, pp. 158–165, May 2016.

➢ Oral communications

- Patrice Paricaud, Olivier Baudouin, Christophe Coquelet, Abdelatif Baba-Ahmed, Louis Campagnolo, Johnny Deschamps, Laurent Catoire, Jiri Janecek, Julien Glorian, Celine Houriez, **Jamal El Abbadi**, Gilbert Fuchs, *"Experimental Measurements and Predictions of the Properties of Refrigerant Fluids Using Ab-Initio, SAFT-VR Mie and COSMO Calculations"*, AIChE Annual Meeting, November 13-18, 2016, San Francisco, United States.

- Julien Glorian, **Jamal El Abbadi**, Jiri Janecek, Patrice Paricaud, Johnny Deschamps, Laurent Catoire, Céline Houriez, Christophe Coquelet, Olivier Baudouin, Abdelatif Baba-Ahmed, Gilbert Fuchs, *"Experimental measurements and predictions of the*

properties of refrigerant fluids using ab-initio, SAFT-VR Mie and COSMO calculations", 14th PPEPPD, May 2016, Porto, Portugal.

- **Jamal El Abbadi**, Céline Houriez, Christophe Coquelet, *"Experimental aspects: VLE and density measurements"*. Seminar on refrigerants, 10th March, 2016, Paris, France.

- **Jamal El Abbadi**, Céline Houriez, Fan Zhang, Alain Valtz, Christophe Coquelet, Patrice Paricaud, Johnny Deschamps, Olivier Baudouin, Abdelatif Baba-Ahmed, *"Prediction of the physical properties of next-generation refrigerant fluids"*, ECCE10 Conference (10th European Congress of Chemical Engineering), 27th September – 1st October, 2015, Nice, France.

➢ **Posters**

- **Jamal El Abbadi**, Céline Houriez, Jiri Janecek, Michel Masella, Patrice Paricaud, Johnny Deschamps, Christophe Coquelet, *"Prediction of thermodynamic properties of refrigerant fluids by molecular simulation and equation of state"*, June 2016, Lyon, France.

- **Jamal El Abbadi**, Céline Houriez, Christophe Coquelet, *"Prediction of the thermodynamic properties of refrigerant fluids"*, Equations of State Congress: From cubic equations of state to the equations issued from molecular thermodynamic, 26th – 27th October, 2015, Toulouse, France.

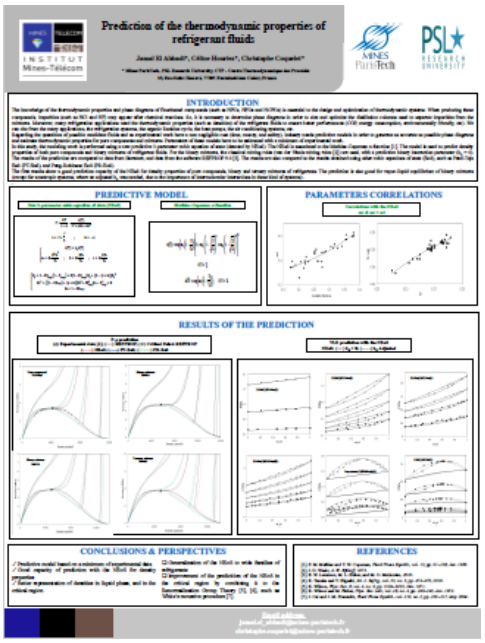

- Julien Glorian, **Jamal El Abbadi**, Jiri Janecek, Patrice Paricaud, Laurent Catoire, Céline Houriez, Christophe Coquelet, Olivier Baudouin, Abdelatif Baba-Ahmed, Gilbert Fuchs, *"Experimental measurements and predictions of the properties of refrigerant fluids using ab-initio, SAFT-VR Mie and COSMO calculations"*, ECCE10 Conference (10th European Congress of Chemical Engineering), 27th September – 1st October, 2015, Nice, France.

- **Jamal El Abbadi**, Céline Houriez, Christophe Coquelet, *"Prediction of the physical properties of refrigerant fluids"*. PhD Students Workshop, 24th - 25th June, 2015, Paris, France.

➢ **Professional reports**

- **Jamal El Abbadi**, Céline Houriez, Christophe Coquelet, *"Thermodynamic properties of new refrigerants"*, 2nd year PhD report, September, 2015.

- **Jamal El Abbadi**, Céline Houriez, Alain Valtz, Christophe Coquelet, *"Experimental measurements"*, PREDIREF project, June 2015.

- **Jamal El Abbadi**, Céline Houriez, Alain Valtz, Christophe Coquelet, *"Bibliographic review and data treatment"*, PREDIREF project, March 2015.

- **Jamal El Abbadi**, Céline Houriez, Alain Valtz, Christophe Coquelet, *"Bibliographic review and experimental measurements"*, PREDIREF project, March 2015.

- **Jamal El Abbadi**, Céline Houriez, Christophe Coquelet, *"Thermodynamic properties of new refrigerants"*, 1st year PhD report, September, 2014.

➢ **Professional presentations**

- **Jamal El Abbadi**, Céline Houriez, Christophe Coquelet, J.P. Martin Trusler, *"Thermophysical properties of new refrigerants"*, Group meeting, 15th September, 2016, London, United Kingdom.

- **Jamal El Abbadi**, Céline Houriez, Christophe Coquelet, *"Prediction of the physical properties of next-generation refrigerant fluids - Task 4: Experimental measurements"*, PREDIREF project, 2nd September, 2016, Lyon, France.

- **Jamal El Abbadi**, Céline Houriez, Christophe Coquelet, *"Prediction of the physical properties of next-generation refrigerant fluids - Task 4: Experimental measurements"*, PREDIREF project, 28th October, 2015, Toulouse, France.

- **Jamal El Abbadi**, Céline Houriez, Christophe Coquelet, *"Thermodynamic properties of new refrigerants"*, 2nd year PhD evaluation, 24th September, 2015, Paris, France.

- **Jamal El Abbadi**, Céline Houriez, Christophe Coquelet, *"Prediction of the physical properties of next-generation refrigerant fluids - Task 4: Experimental measurements"*, PREDIREF project, 16th December, 2014, Palaiseau, France.

- **Jamal El Abbadi**, Céline Houriez, Christophe Coquelet, *"Thermodynamic properties of new refrigerants"*, 1st year PhD evaluation, 25th September, 2014, Paris, France.

- **Jamal El Abbadi**, Céline Houriez, Christophe Coquelet, *"Prediction of the physical properties of next-generation refrigerant fluids - Task 4: Experimental measurements"*, PREDIREF project, 19th June, 2014, Palaiseau, France.

EXECUTIVE SUMMARY

Of the PhD Thesis entitled

"Thermodynamic properties of new refrigerants"

By

Jamal EL ABBADI

Supervised by

Dr. Céline HOURIEZ, MINES ParisTech

Pr. Christophe COQUELET, HDR, MINES ParisTech

MINES ParisTech
Centre Thermodynamique des Procédés (CTP)
35 Rue Saint-Honoré, 77300 Fontainebleau

F. Executive summary

Introduction

For several years, new-generation refrigerants are proposed, in order to reduce the overall emission of greenhouse gases (Kyoto protocol, 1997) and to respect the environmental regulations issued by the European Union (F-gas regulations) (Lasserre et al. 2014). In particular, due to their low global warming potential (GWP), hydrofluoroolefins (HFOs), such as R-1234yf (2,3,3,3-tetrafluoropropene) and R-1234ze (trans-1,3,3,3-tetrafluoropropene), arouse interest and have been proposed as replacements for some previous-generation fluids such as the 1,1,1,2-tetrafluoroethane (R-134a) (Minor & Spatz 2008). However, the use of pure component fluid may not be suitable for some refrigeration applications, due to performance and safety concerns. Thus, blends of refrigerants are often considered, including for instance a HFO, a hydrofluorocarbon (HFC), and CO_2, such as the R-445A blend.

The detailed knowledge of the thermodynamic properties of refrigerants, and particularly of their vapor-liquid equilibrium (VLE) behavior, is essential to design and optimize thermodynamic systems involving working fluids, from the production and separation units to the refrigerant-based systems (such as air-conditioning systems, organic Rankine cycles, heat pumps etc.). In the field of refrigeration, there is a strong need for thermophysical data of fluids, either to retrofit existing equipments with alternative refrigerants or to replace these equipments. In particular, when developing an alternative refrigerant, the list of possible mixtures is very large, and to obtain detailed experimental data for all the promising candidates can become rapidly time-consuming and expensive. The selection of these fluids requires predictive tools that are fast and less expensive. Examples of such tools are the equations of state.

In fact, equations of state (EOSs) are one of the most convenient tools to correlate, extrapolate and predict thermodynamic properties and phase behavior for pure fluids and mixtures. For instance, they can be very useful to screen possible fluid candidates for their suitability in a particular application. Since van der Waals introduced his famous equation of state (EoS) in 1873 (Waals 1873), cubic EoSs (CEoSs) have been subject to active research and improvements, and were widely used in industrial process design and optimization, due to their accuracy, generality, simplicity and speed of computation (Sengers et al. 2000), (Valderrama 2003).

The Soave-Redlich-Kwong (SRK) and Peng-Robinson (PR) equations are among the most popular cubic EoSs and are used for many applications, in which thermodynamic and VLE properties are required.

Concerning the vapor pressures, the capacity of prediction of the cubic EoSs is related to the model chosen for the temperature-dependent alpha function, while the prediction of volumetric properties depends on the volume function (Valderrama 2003; Wei & Sadus 2000; Twu et al. 1992; Twu et al. 1991). For instance, in the PR-EoS, the modification of the volume dependency of attractive term represents an improvement upon SRK-EoS, and allows one to obtain better results for liquid densities and better representation of VLE for many mixtures (Valderrama 2003; Wei & Sadus 2000; Orbey & Sandler 1998).

One of the drawbacks of the two-parameter cubic EoSs is that they involve a critical compressibility factor Z_c whose value is constant, regardless of the substance, providing saturated liquid densities and critical densities different from the experimental ones (Twu et al. 1992; Ji & Lempe 1998).

The use of a substance-dependent critical parameter instead of a fixed value of Z_c has been proposed to overcome this deficiency (Abbott 1973). However, it has been shown that the optimal value of the critical compressibility factor is generally different from the experimental one (Schmidt & Wenzel 1980; Abbott 1973).

One of the well-known three-parameter equation of state is the Patel-Teja (PT) EoS and its generalized form (Patel & Teja 1982; Valderrama 1990), which has been successfully applied to correlate mixture VLE data (Danesh et al. 1991).

The three-parameter cubic equation of state proposed in this work (denoted by NEoS), which is a modification of the PT-EoS, is based on the use of an optimized substance-dependent critical compressibility factor, yielding better representation of liquid densities. The NEoS is associated with the Mathias-Copeman alpha function.

By applying the NEoS to pure compound refrigerants, we were able to develop correlations relating the alpha function parameters to the acentric factor, and the optimized critical compressibility factor to the experimental one. As a result, the NEoS can be used for a wide range of refrigerants for which no experimental data are available. Furthermore, in this work, we show that by only calculating for pure compounds the alpha function parameters and the optimized critical compressibility factor, from the correlations developed, we can extend the prediction to mixtures. This has been done without need of VLE experimental data, and with no adjustment of the binary interaction parameter k_{ij} (as we worked with $k_{ij} = 0$).

In this work, the NEoS is used along with other cubic EoSs (PT-EoS and PR-EoS), in order to compare their respective prediction results with REFPROP and experimental data.

I.State of the art

In order to have a complete public database of refrigerant systems, the collection of existing experimental data was performed.

The data presented were collected from articles and reviews available in the literature, as well as from the NIST Reference Database software REFPROP[4] 9.0 (data in this software are based on correlations) (Lemmon et al. 2010). This software contains data of several systems of pure compounds and some well-known mixtures.

The thermodynamic data concerning the systems of refrigerants are very scarce in the literature, and few publications are available for the VLE data of the new generation refrigerants (for both pure compounds and mixtures).

The software REFPROP 9.0 contains data of a limited number of refrigerants. Most of them are from the old-generation fluids, such as PFCs (perfluorocarbons), CFCs (chlorofluorocarbons), HCFCs (hydrochlorofluorocarbons) and HFCs (hydrofluorocarbons).

Only two HFOs (hydrofluoroolefins) data are available in this database, concerning the R-1234yf and R-1234ze(trans). The data for the other refrigerants, HFOs and HCFOs (hydrochlorofluoroolefins), were collected from papers and reviews available in the literature.

For the mixtures, few publications are available and in most of the cases with systems not containing the new-generation fluids.

The systems of pure compounds and mixtures collected are respectively reported in *Table F.1* and *Table F.2*.

[4] REFPROP: Reference Fluid Properties

Table F.1 Pure compounds refrigerants with available data.

PFC	*CFC*	*HCFC*	*HFC*	*HCFO*	*HFO*
RC318	R11	R21	R23	R1233xf	R1225ye(E)
R14	R12	R22	R32	R1233zd(E)	R1225ye(z)
R116	R13	R123	R41	--	R1225zc
R218	R113	R124	R125	--	R1234ye(E)
--	R114	R141b	R134a	--	R1234yf
--	R115	R142b	R143a	--	R1234ze(E)-trans
--	--	R244bb	R152a	--	R1234ze (trans)
--	--		R161	--	R1234ze(Z)-cis
--	--		R227ea	--	R1243zf
--	--		R236ea	--	R1216
--	--		R236fa	--	--
--	--	--	R245ca	--	--
--	--	--	R245fa	--	--
--	--	--	R365mfc	--	--

Table F.2 Mixtures of refrigerants with available data.

Systems			
R14 - R13	R161 - R227ea	R32 - R290	R23 - Propane
R116 - R134a	R236ea - R32	R41 - CO_2	R23 - nButane
R116 - R143a	R236ea - R125	R125 - R134a	Isopentane - R365mfc
R116 - CO_2	HFP - R123	R125 - R143a	Isopentane - R245fa
R12 - R22	HFPO - R123	R125 - R152a	CO_2 - R1233zd(E)
R22 - R114	CO_2 - R32	R125 - R236fa	R134a - R1233zd(E)
R22 - R134a	CO_2 - R134a	R125 - R1234yf	R152a - R1233zd(E)
R22 - R152a	CO_2 - R152a	R134a - R12	R161 - R125 - R143a
R23 - R11	CO_2 - R227ea	R134a - R142b	R161 - R125 - R32
R23 - R13	CO_2 - R1234yf	R134a - R227ea	R32 - R290 - R227ea
R23 - R32	CO_2 - R1234ze(E)	R134a - R236fa	R32 - R125 - R134a
R23 - R125	CO_2 - HFP	R134a - R245fa	R125 - R143a - R134a
R23 - R134a	CO_2 - HFPO	R134a - R1234yf	R22 + R152a + R142b
R23 - R143a	R290 - R227ea	R134a - R1234ze(E)	R290 - R600a - R32
R23 - R152a	R3110 - R365mfc	R143a - R134a	R404A
R23 - R227ea	R161 - R1234yf	R143a - R161	R421A
R32 - R125	R1234yf - R227ea	R143a - R1234yf	R421B
R32 - R134a	R1234yf - R152a	R134a - R152a	R508A
R32 - R143a	R1234yf - R600a	R152a - R227ea	R410A
R32 - R227ea	R1234yf - R244bb	R152a - R1234ze(E)	R410B
R32 - R236fa	R152a - R134	R161 - R32	
R32 - R1234yf	R23 - R116	R161 - R125	
R161 - R134a	R152a - R245fa	R32 - SO_2	

II.Experimental measurements

In order to complete the data available in literature, experimental measurements were performed for refrigerant systems, at the CTP (Centre Thermodynamique des Procédés) laboratory, with systems containing the new generation refrigerants.

The experimental work concerns mainly the vapor-liquid equilibrium (VLE) and density measurements.

VLE measurements are performed through a static-analytic method, by means of an equilibrium cell, with vapor and liquid phases sampling, using a capillary sampler (ROLSI^{TM}, ARMINES Patent) (Juntarachat et al. 2014).

Density measurements are performed through a synthetic-dynamic method using a vibrating tube densimeter (Khalil et al. 2007; Khalil 2006).

In addition to the VLE and density measurements, viscosity measurements were performed, as part of visit period held at the *Thermophysics Laboratory* (*Imperial College London*) within the research group of *Professor J. P. Martin Trusler*.

The viscosity measurements were performed using a vibrating-wire viscometer-densimeter, based on a static-synthetic method.

In

Table F.3, we give examples of the systems that have been experimentally measured, for VLE and density measurements, with the range of temperatures covered.

Table F.3 Experimental measurements.

Systems	*T/K*	*Type of measurements*
R134a + R1233zd(E)	303.07, 333.23	VLE
R152a + R1233zd(E)	303.10, 333.23	VLE
R1234yf + R1233zd(E)	303.22, 333.27	VLE
R134a + R1233xf	298.30, 323.38, 348.27	VLE
R1234yf + R1233xf	298.31, 323.27, 348.25	VLE
CO_2 + R1234yf	283.21, 293.18, 298.11, 308.20, 323.18, 338.24, 353.25	VLE
CO_2 + R1233zd(E)	278.28, 302.59, 333.17	VLE
R1234yf + R134a	278.17, 303.16, 333.17	VLE
R1234yf + R152a	278.18, 303.16, 333.29	VLE
R245fa + R1233xf	323.40, 353.27	VLE
R245fa + R1233zd(E)	323.23, 353.27	VLE
R23 + Propane	293.18, 298.15, 313.15, 323.15, 353.15	VLE
R1233xf	260.48, 273.43, 292.65, 312.44, 332.42	Density
R1233zd(E)	278.15, 303.15, 323.15, 333.15, 343.15	Density
R1234yf + R134a	278.15, 303.15, 333.15	Density
R1234yf + R152a	278.15, 303.15, 333.15	Density
R134a + R152a + R1234yf	278.15, 303.15, 333.15	Density
R134a	303.67, 333.27, 363.27, 393.26	Viscosity
R1234yf	303.65, 333.20, 362.71, 394.19, 423.06	Viscosity

Examples of the results obtained for some refrigerant systems measured experimentally are displayed in Figure F.1.

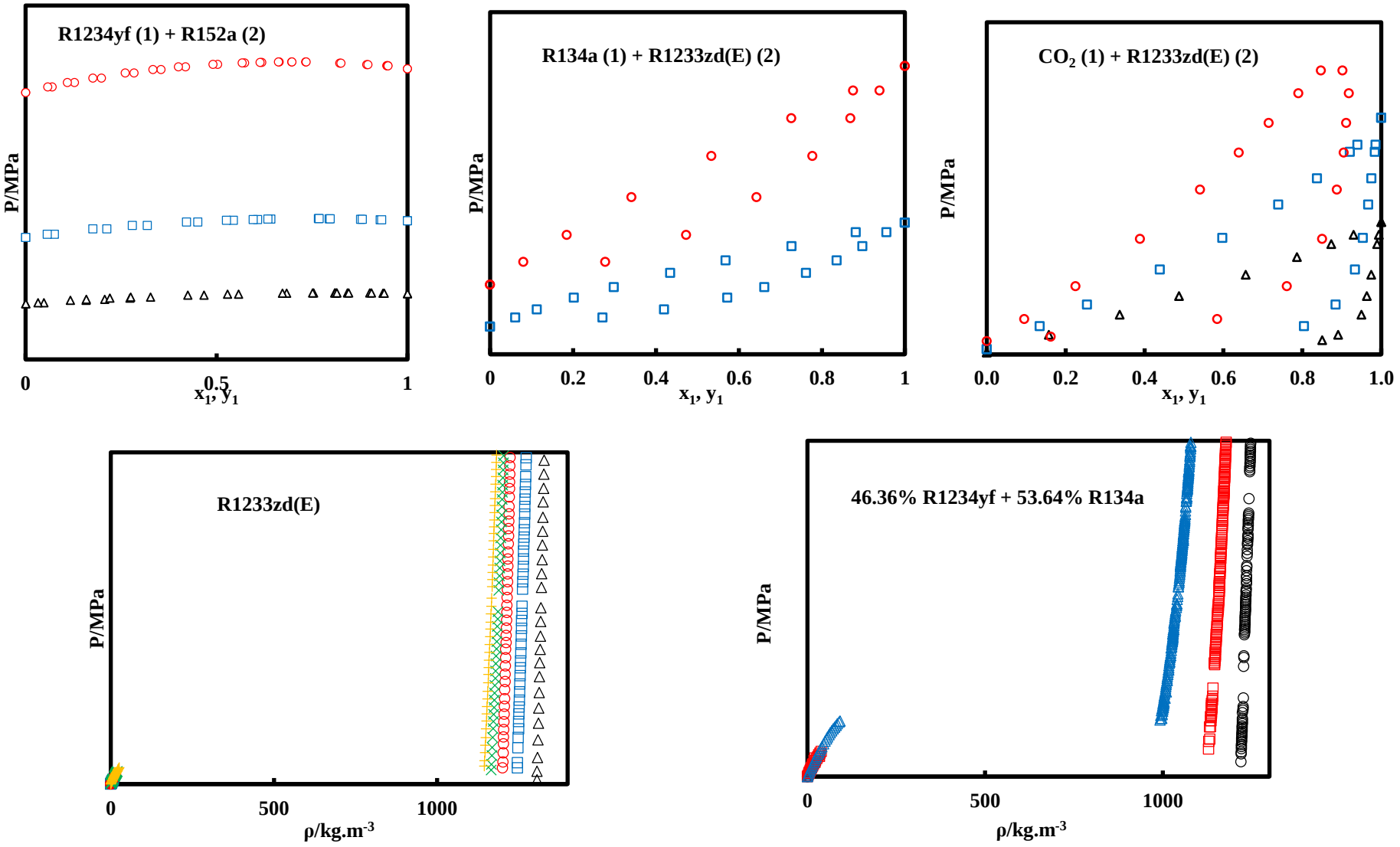

Figure F.1 Experimental VLE and density measurements.

III.Thermodynamic modeling

In order to predict accurately the thermodynamic properties of refrigerants (both pure compounds and mixtures), a new EoS (denoted by NEoS) was developed, based on the modification of the well-known PT-EoS (Patel & Teja 1982).

The NEoS is a three-parameter cubic EoS and is defined by the following relation:

$$P = \frac{RT}{v - b} - \frac{a(T)}{v^2 + ubv + wb^2} \tag{F.1}$$

where P is the pressure, T the temperature, v the volume, and R the universal constant for ideal gases. b is the volumetric parameter and a(T) the cohesive energy parameter.

u and w are two parameters defined in order to have: u + w = 0, which was shown to be the optimal combination for liquid-density calculations by cubic EoSs (Ji & Lempe 1998).

Here, u and w are defined as follows:

$$u = 1 + \frac{c}{b}$$
$$w = -u \tag{F.2}$$

While the PT-EoS (Patel & Teja 1982), (Forero G. & Velásquez J. 2012; Ji & Lempe 1998) and the NEoS have the same definition for u, a different definition for w is chosen in the NEoS in order to fulfil the conditions defined by Ji and Lempe (Ji & Lempe 1998), i.e. u + w = 0 (note that in the case of the PT-EoS, u + w = 1).

The cohesive energy parameter a(T) depends on the temperature and is defined as follows:

$$a(T) = a_c \alpha(T) \tag{F.3}$$

α(T) is the alpha function that will be defined below, and which depends on both the temperature and the substance.

The parameters a_c, b and c of Eq. (F.1)-(F.3) are obtained from the thermodynamic conditions at the critical point, defined as follows:

$$\left(\frac{\partial P}{\partial v}\right)_{T_c} = \left(\frac{\partial^2 P}{\partial^2 v}\right)_{T_c} = 0 \; ; \; at \; T_c, P_c, and \; v_c \tag{F.4}$$

T_c, P_c and v_c are respectively the critical temperature, the critical pressure and the critical volume. The parameters a_c, b and c are calculated according to the relations:

$$a_c = \Omega_a \frac{R^2 {T_c}^2}{P_c}$$

$$b = \Omega_b \frac{RT_c}{P_c} \tag{F.5}$$

$$c = \Omega_c \frac{RT_c}{P_c}$$

Ω_a, Ω_b and Ω_c are factors depending on the substance, and calculated from the following relations (Forero G. & Velásquez J. 2012):

$$\Omega_a = 1 - 3Z_{C,opt}\left(1 - Z_{c,opt}\right) + 3(1 - 2\mathrm{Z_{c,opt}})\Omega_b + [2 - (u + w)]{\Omega_b}^2$$

$${\Omega_b}^3 + \left[\left(1 - 3Z_{c,opt}\right) + (u + w)\right]{\Omega_b}^2 + 3Z_{c,opt}^2\Omega_b - Z_{c,opt}^3 = 0 \tag{F.6}$$

$$\Omega_c = 1 - 3Z_{c,opt}$$

$Z_{c,opt}$ is an apparent optimized critical compressibility factor. It is different from the experimental critical compressibility factor Z_c, and adjusted from the experimental VLE data (Ji et al. 2007; Ji & Lempe 1998), in order to improve the prediction of liquid densities.
Here, as u + w = 0, we can simplify Eq. (F.6) to obtain:

$$\Omega_a = 1 - 3Z_{C,opt}\left(1 - Z_{c,opt}\right) + 3(1 - 2\mathrm{Z_{c,opt}})\Omega_b + 2{\Omega_b}^2$$

$${\Omega_b}^3 + (1 - 3Z_{c,opt})\,{\Omega_b}^2 + 3Z_{c,opt}^2\Omega_b - Z_{c,opt}^3 = 0 \tag{F.7}$$

By including the critical compressibility factor in the calculations, better results can be obtained, even though the apparent critical compressibility factor $Z_{c,opt}$ is larger than the experimental one, Z_c.

The NEoS is associated with the Mathias-Copeman (MC) alpha function (Mathias & Copeman 1983), which is defined as follows:

$$\alpha(T) = \left[1 + m_1\left(1 - \sqrt{\frac{T}{T_c}}\right) + m_2\left(1 - \sqrt{\frac{T}{T_c}}\right)^2 + m_3\left(1 - \sqrt{\frac{T}{T_c}}\right)^3\right]^2 ; \quad if\ T < T_c$$
$$\alpha(T) = \left[1 + m_1\left(1 - \sqrt{\frac{T}{T_c}}\right)\right]^2 ; \quad if\ T > T_c \tag{F.8}$$

The parameters of the alpha function, m_1, m_2, and m_3, and the optimized critical compressibility factor $Z_{c,opt}$ were adjusted from data of 34 pure compounds obtained by using REFPROP 9.0 (Lemmon et al. 2010).

The objective function (in the case of NEoS and PT-EoS) contains vapor pressures and liquid densities and is defined as follows:

$$F_{obj} = \frac{100}{N}\left[\sum_1^N \left(\frac{P_{exp} - P_{cal}}{P_{exp}}\right)^2 + \sum_1^N \left(\frac{\rho^L_{exp} - \rho^L_{cal}}{\rho^L_{exp}}\right)^2\right] \tag{F.9}$$

In the case of PR-EoS, the objective function contains vapor pressures and is as follows:

$$F_{obj} = \frac{100}{N}\left[\sum_1^N \left(\frac{P_{exp} - P_{cal}}{P_{exp}}\right)^2\right] \tag{F.10}$$

N is the number of data points, P_{exp} is the experimental vapor pressure, P_{cal} the calculated vapor pressure, ρ^L_{exp} the experimental saturated liquid density and ρ^L_{cal} is the calculated saturated liquid density.

To estimate the parameters, we need the values of the critical pressure P_c, the critical temperature T_c, the experimental critical compressibility factor Z_c (in the case of PR-EoS, Z_c is fixed at 0.3074), and the acentric factor ω. We need also the data of the vapor pressures P^{sat}, as

well as the saturated liquid densities ρ^L for different temperatures (for the NEoS and PT-EoS; for PR-EoS, only the data of vapor pressures are required).

In this work, the temperatures range from the triple point temperature to the critical temperature (T_c), with a step of 1 K.

For the NEoS, PT-EoS, and PR-EoS, we estimate the alpha function parameter m_1, while the parameters m_2 and m_3 were set to constant values. For the NEoS and PT-EoS, the optimized critical compressibility factor $Z_{c,opt}$ is also estimated, while the Z_c value is 0.3074 for the PR-EoS.

For the three EoSs, we carried out the parameter determination by associating each EoS with the MC alpha function, leading to three different sets of parameters.

Based on these adjusted parameters, we established a correlation between the alpha function parameter m_1 and the acentric factor ω, as well as a correlation between the optimized critical compressibility factor $Z_{c,opt}$ and the experimental one Z_c.

In this way, we can calculate the alpha parameters and the optimized critical compressibility factor for other compounds, whose thermodynamic properties are not known experimentally, allowing us to predict their thermodynamic behavior.

The correlations obtained with the NEoS are shown in *Figure F.2* and given in Eq. (F.11).

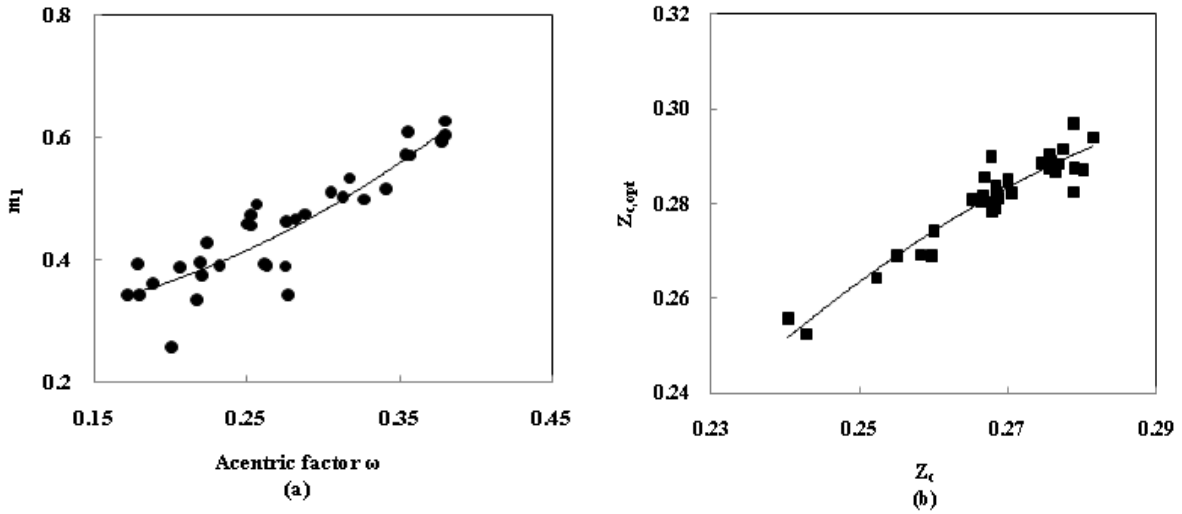

Figure F.2 Correlations obtained with the NEoS. (a): the parameter m_1 as a function of the acentric factor ω (coefficient of determination R^2 = 0.82); (b): the optimized critical compressibility factor $Z_{c,opt}$ as a function of the experimental critical compressibility factor (coefficient of determination R^2 = 0.89).

$$m_1 = 2.7868\omega^2 - 0.2376\omega + 0.3007$$
$$m_2 = 0.47$$
$$m_3 = -0.08$$
$$Z_{c,opt} = -7.4737 Z_c^{\,2} + 4.8824 Z_c - 0.4900 \quad \text{(F.11)}$$

The model was applied to predict density properties at saturation and out of saturation for pure compounds and mixtures, and phase diagrams for mixtures.

For the mixtures, the NEoS was associated to the van der Waals mixing rules (Waals 1873), and the binary interaction parameter was set to zero ($k_{ij} = 0$), and not fitted to experimental data. The results of the model were compared to the experimental results, and also to the results obtained using other cubic equations of state, such as PT-EoS and PR-EoS.

In *Figure F.3* to *Figure F.5* are displayed the results of the prediction obtained respectively for the pure compound R-1234yf, the binary mixture R-508A, and the ternary mixture R-404A.

From the results of the prediction, the average relative deviation (ARD) and the BIAS were calculated, leading to the results obtained in *Table F.4*.

The ARD and BIAS are calculated according to Eq. (F.12), as follows:

$$ARD(X)\ \% = \left| \frac{100}{N} \sum_{1}^{N} \frac{X_{exp} - X_{cal}}{X_{exp}} \right| \quad \text{(F.12)}$$
$$BIAS\ (X)\ \% = \frac{100}{N} \sum_{1}^{N} \frac{X_{exp} - X_{cal}}{X_{exp}}$$

Table F.4 ARD and BIAS for the R-1234yf.

		ARD (%)			*BIAS (%)*		
Compounds	*CEoS*	*P*	ρ^L	ρ^V	*P*	ρ^L	ρ^V
R-1234yf	NEoS	1.4	2.2	2.9	-1.4	-0.6	-2.8
	PT-EoS	2.2	3.9	2.0	-2.2	1.9	-1.8
	PR-EoS	1.9	3.9	1.6	-1.9	3.4	-1.3
R-508A	NEoS	1.0	1.7	1.7	-0.4	-1.1	1.0
	PT-EoS	1.9	2.7	5.3	1.0	0.4	4.9
	PR-EoS	2.9	2.8	8.6	2.9	-0.4	8.6
R-404A	NEoS	1.6	2.3	5.8	-1.6	-1.1	-5.8
	PT-EoS	2.6	3.7	5.3	-2.6	1.3	-5.3
	PR-EoS	4.7	5.4	6.6	-4.7	5.4	-6.6

The results obtained show a good prediction capacity of the NEoS, especially for liquid density, and in the vicinity of the critical region, better than the prediction with PT-EoS and PR-EoS.
In *Figure F.7* to *Figure F*.9, are displayed examples of VLE results obtained using the NEoS. We can notice that the VLE prediction with a null k_{ij}, gives good results for simple systems, however, it is limited for systems presenting an azeotropic behavior, or under critical conditions, where a k_{ij} is needed to accurately represent these systems.
The experimental data used were collected from literature (Tanaka & Higashi 2010b; Lim, J.-Y. Park, et al. 2002; Hu, L. X. Chen, et al. 2013; Rivollet et al. 2004; Zhang et al. 2008).

The NEoS was also used to predict the residual enthalpies, the enthalpies of vaporization, and the residual heat capacities of pure compound refrigerants (R-1234yf, R-245ca and R-143a).
The results of the prediction were compared to REFPROP 9.0 data, as displayed in *Figure F.10* to *Figure F.13*.
We can see from the graphical representation that the prediction is in good agreement with REFPROP 9.0 results.

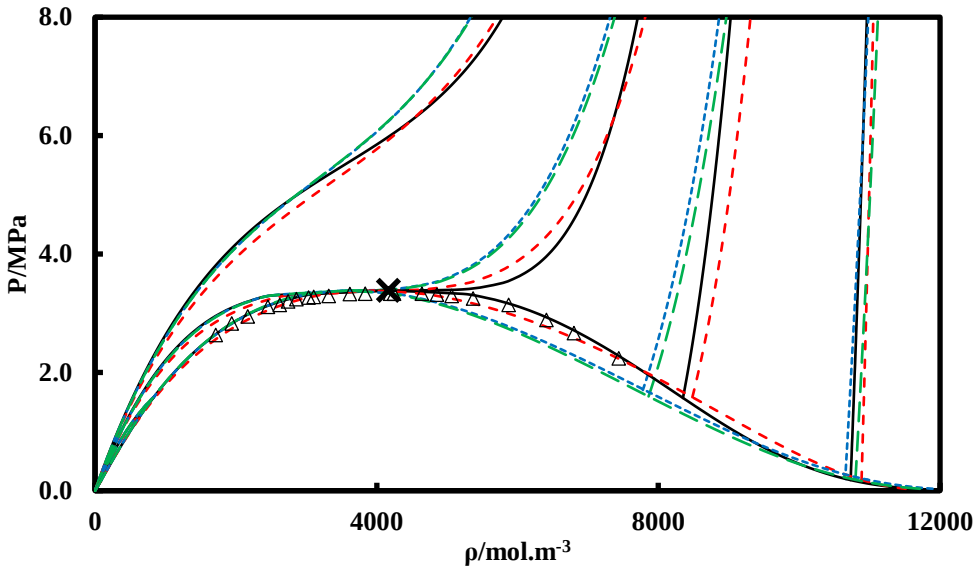

Figure F.4 P-ρ diagram for pure compound R-1234yf. (Δ) (Tanaka & Higashi 2010b); (——) REFPROP; (×) Critical Point: REFPROP (T_c = 367.85K); (- - - -) NEoS; (……) PT-EoS;(— — —) PR-EoS. Out of saturation: T_r = 0.7, 0.9, 1.0, 1.1.

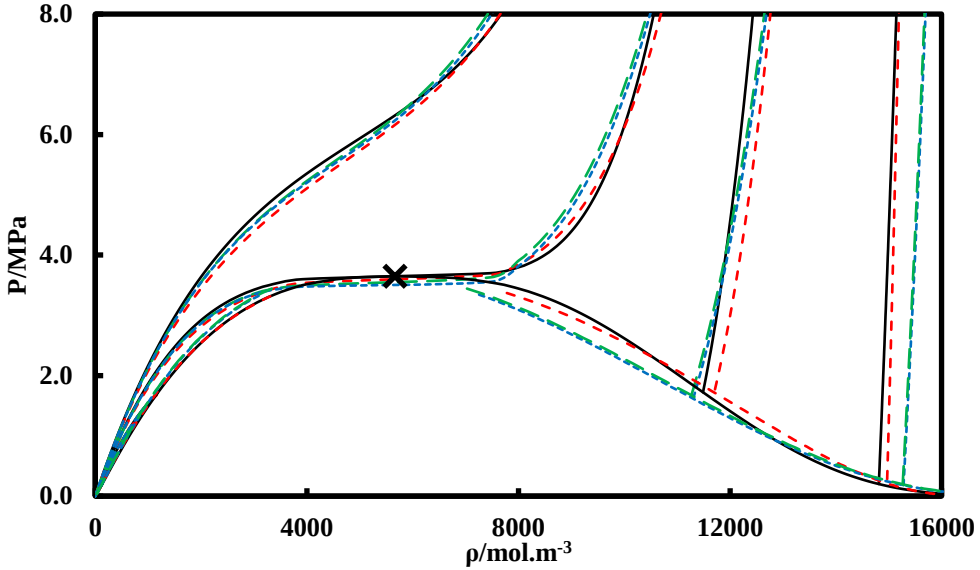

Figure F.3 P-ρ diagram for binary mixture R-508A. (——) REFPROP; (×) Critical Point: REFPROP (T_c = 283.34K); (- - - -) NEoS; (……) PT-EoS; (— — —) PR-EoS. Out of saturation: Tr = 0.7, 0.9, 1.0, 1.1.

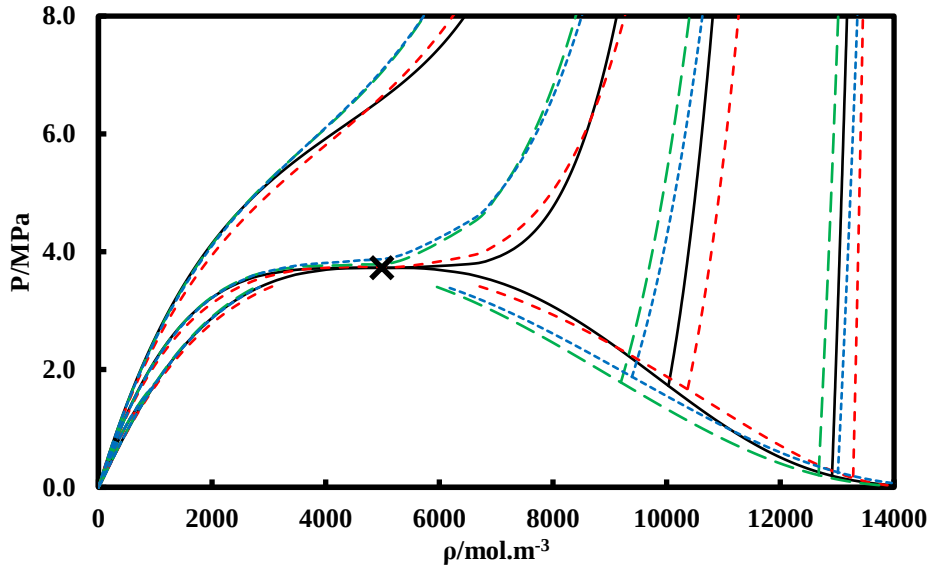

Figure F.5 P-ρ diagram for ternary mixture R-404A. (——) REFPROP; (×) Critical Point: REFPROP (T_c=345.2K); (- - - -) NEoS; (……) PT-EoS; (— — —) PR-EoS. Out of saturation: T_r = 0.7, 0.9, 1.0, 1.1.

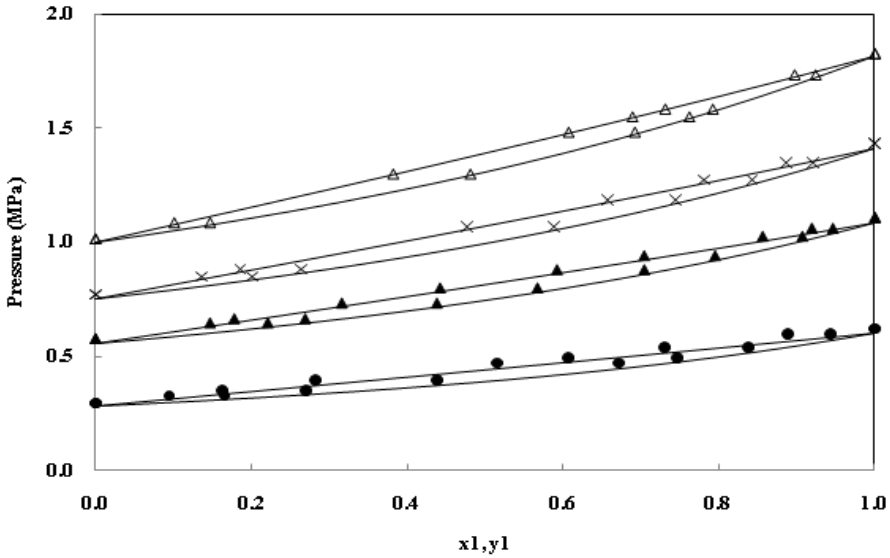

Figure F.7 VLE prediction for R-143a (1) + R-134a (2). (Lim, J.-Y. Park, et al. 2002): (●) 273.15K; (▲) 293.15K; (×) 303.15 K; (Δ) 313.15 K. NEoS: (—) $k_{ij} = 0$.

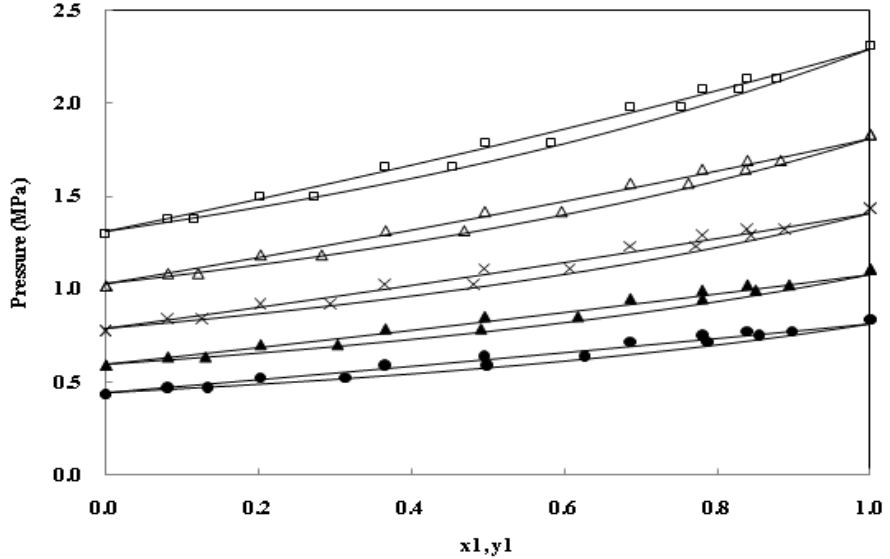

Figure F.6 VLE prediction for R-143a (1) + R-1234yf (2). (Hu, L. X. Chen, et al. 2013): (●) 283.15 K; (▲) 293.15 K; (×) 303.15 K; (Δ) 313.15 K; (□) 323.15 K. NEoS: (—) $k_{ij} = 0$.

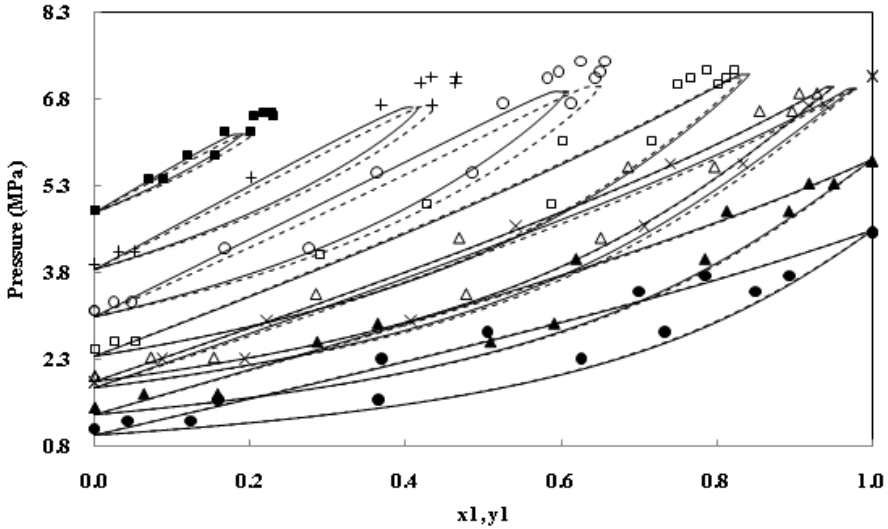

Figure F.9 VLE prediction for CO_2 (1) + R-32 (2). (Rivollet et al. 2004): (●) 283.12 K; (▲) 293.11 K; (×) 303.13 K; (Δ) 305.15 K; (□) 313.30 K; (○) 323.34 K; (+) 333.33 K; (■) 343.23 K. NEoS: (- - - -) $k_{ij} = 0$; (—) k_{ij} adjusted.

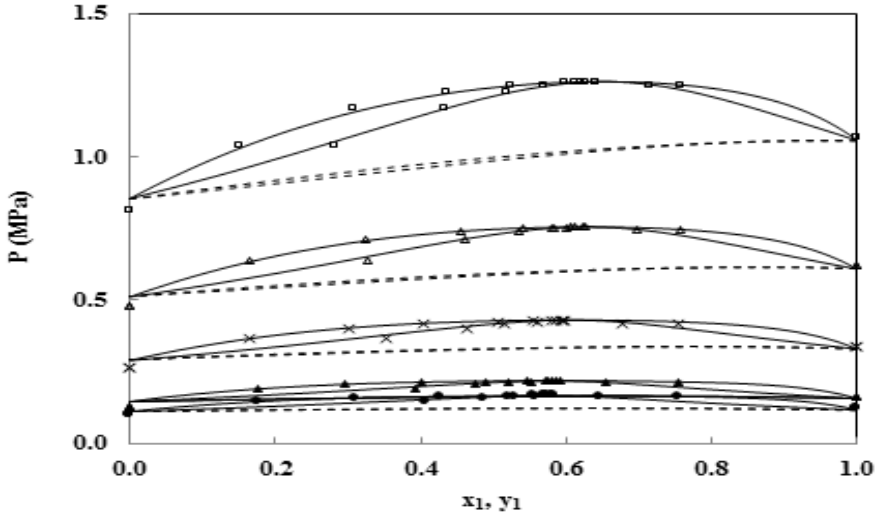

Figure F.8 VLE prediction for R-23 (1) + R-116 (2). (Zhang et al. 2008): (●) 194.33 K; (▲) 199.71 K; (×) 214.19 K; (Δ) 229.63 K; (□) 244.94 K. NEoS: (- - - -) $k_{ij} = 0$; (—) k_{ij} adjusted.

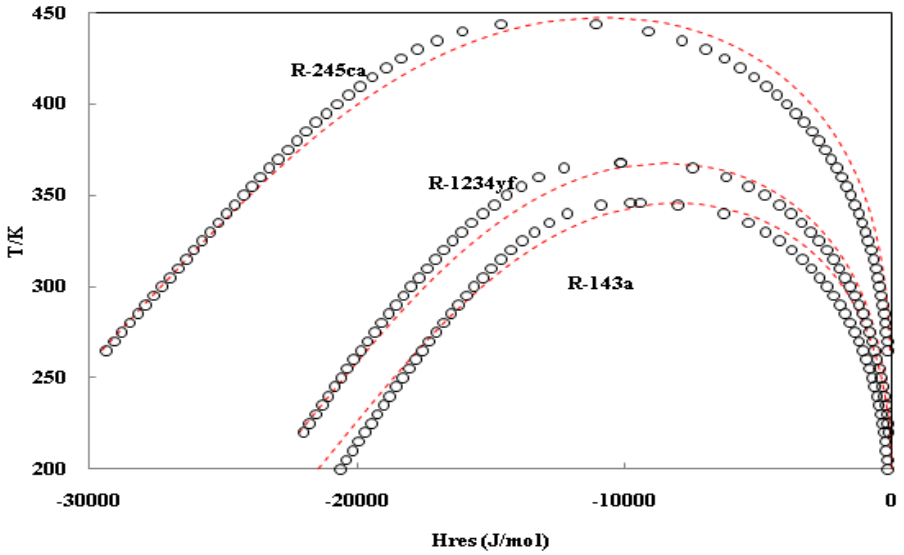

Figure F.10 Residual enthalpies of saturated phases. (○) REFPROP. (- - - -) NEoS.

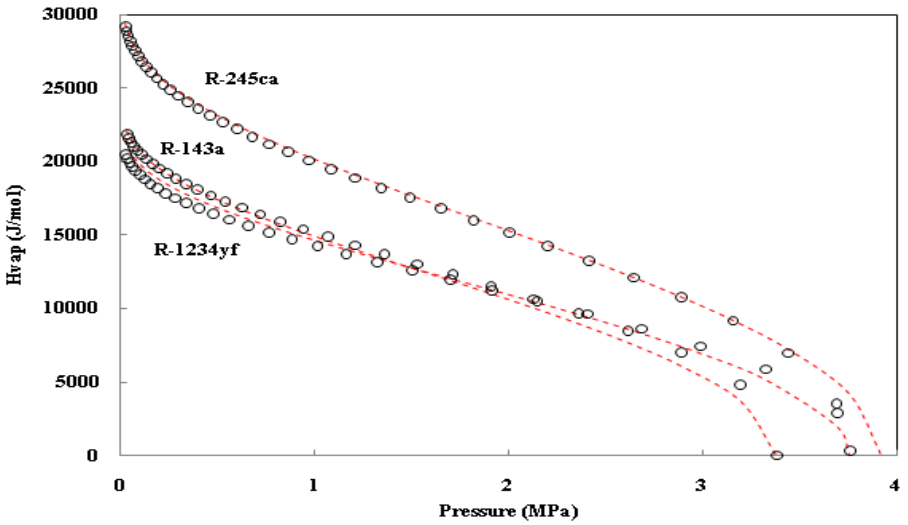

Figure F.11 Enthalpies of vaporization. (○) REFPROP. (- - - -) NEoS.

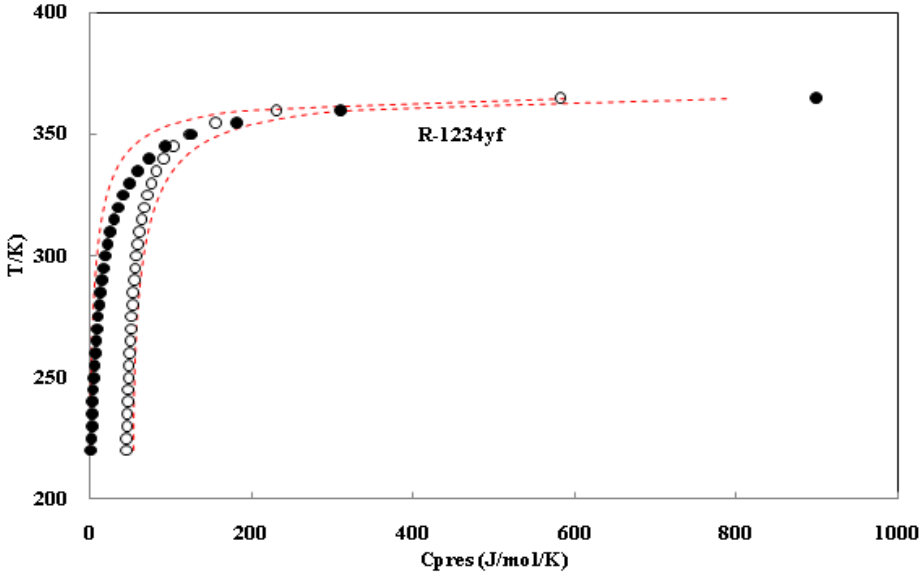

Figure F.13 Residual isobaric heat capacities of saturated phases. (○) Liquid, (●) Vapor – REFPROP. (- - - -) NEoS.

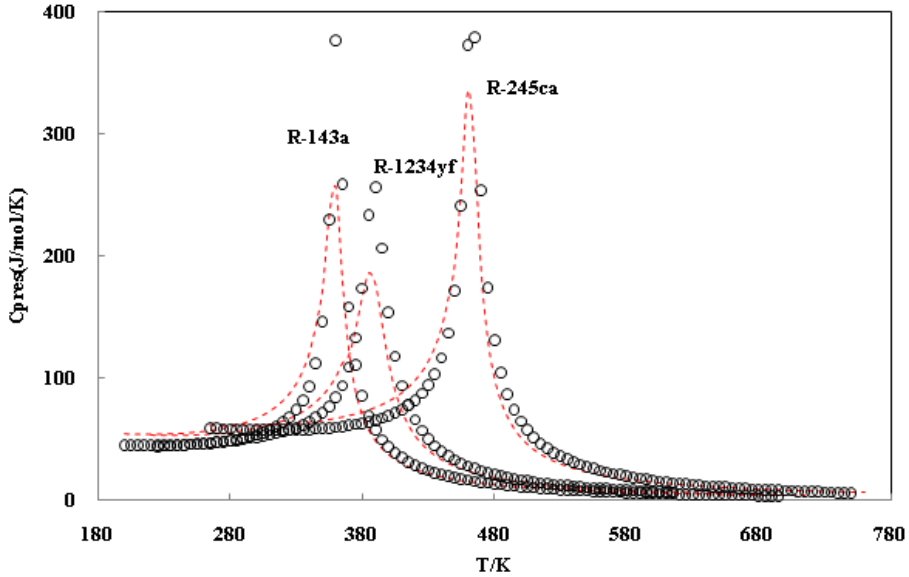

Figure F.12 Residual isobaric heat capacities at P = 5 MPa. (○) REFPROP. (- - - -) NEoS.

Conclusions

The thermophysical properties of working fluids are extremely important for many industrial applications. The experimental measurements of these properties are mandatory, especially for systems where the data are scarce or unavailable.

In particular, VLE and density measurements give us crucial information about the system phase diagrams, thermodynamic behaviour, and volumetric properties. These properties are necessary for the design and optimization of thermodynamic systems. Density properties can also be used for transport property calculations (viscosity and thermal conductivity for instance).

In this work, VLE and density measurements of the refrigerant systems studied were presented. The experimental measurements focused on the study of new systems of refrigerants not available in the literature, especially systems containing the new-generation refrigerants (HFOs and HCFOs).

Viscosity measurements were performed as part of a visiting period held at the *Thermophysics Laboratory* (*Imperial College London*) within the research group of *Professor J. P. Martin Trusler*.

The experimental measurements of thermophysical properties -alone- are not sufficient to cover the wide range of refrigerants and thermodynamic conditions to study, but they remain essential to develop and validate thermodynamic models, and fit parameters of these models, making them an essential step of the fluid selection process for a particular application.

In addition to the experimental measurements, having a good predictive model is essential to complete the experimental results. The NEoS is an example of such a model, allowing one to predict accurately the thermodynamic properties of pure compound and mixture refrigerants.

The NEoS was used to predict the thermodynamic properties of fluid refrigerants, such as the pressure-x-y and pressure-density diagrams, and the results obtained were compared to the PT-EoS and PR-EoS ones.

The three EoSs considered were associated with the MC alpha function. The parameters of this alpha function, as well as the optimized critical compressibility factor (for the NEoS and the PT-EoS), were calculated based on the correlations established in the present work.

For the binary and ternary systems, the binary interaction parameters k_{ij} was set to 0, without any fitting to experimental data.

However, for some systems, such as the azeotropic ones, it has been necessary to consider a k_{ij} parameter to accurately represent the VLE behavior of the systems. Indeed, for instance, the refrigerant compounds are characterized by a large heterogeneity in terms of molecular properties, as some compounds possess strong dipole and/or quadrupole moments and other compounds only weak multipole moments. This may be why a k_{ij} parameter is needed to model some of the binary systems considered.

It would also be interesting to test other mixing rules than the van der Waals ones, such as g^E – mixing rules, or to add a polar term in the NEoS to take into account the polarity of some refrigerant compounds.

An additional path that could be interesting to investigate is the combination of the NEoS with a group contribution method to calculate the k_{ij} of van der Waals mixing rules, as it is done successfully with the PPR78 model (Jaubert & Mutelet 2004; Jaubert et al. 2005; Privat et al. 2008; Xu, Jaubert, et al. 2015; Xu, Privat, et al. 2015).

Together, the results of the predictions for the pure compounds and for the binary and ternary mixtures show that the NEoS provides a better representation of the liquid density at saturation and out of saturation, compared to the results obtained with the PT-EoS and PR-EoS. The results are also better for the density in the critical region. However, the NEoS prediction concerning the ternary mixture could be improved for the subcritical temperatures.

The density in the critical region is well represented by using the NEoS, compared to the other EoSs considered in this work. However, this prediction could be improved by combining the NEoS with a renormalization group theory (Wilson 1971; Wilson & Fisher 1972), using a crossover approach (Dicko & Coquelet 2011; Janeček et al. 2015) or the White's recursive method (Cai & Prausnitz 2004). Such a study will be carried out in a future work.

In overall, the NEoS provides a better representation of the densities, which are essential for the prediction of transport properties (viscosity, thermal conductivity…), and it would be particularly interesting to couple the NEoS with the TRAPP method (Huber et al. 1992; Klein et al. 1997), for instance.

The prediction ability of VLE (without k_{ij}) for complex systems with the NEoS is limited, however, from the results presented in this work concerning refrigerants, the NEoS shows better density prediction potentialities (without k_{ij}) than the PR-EoS and PT-EoS, and this EoS deserves thus to be tested in process simulators for industrial purpose.

References

Abbott, M.M., 1973. Cubic equations of state. *AIChE Journal*, 19(3), pp.596–601.

Akasaka, R. et al., 2007. Vapor–liquid equilibrium measurements and correlations for the binary mixture of difluoromethane+isobutane and the ternary mixture of propane+isobutane+difluoromethane. *Fluid Phase Equilibria*, 261(1–2), pp.286–291.

Arita, K. et al., 1991. Vapour—liquid equilibrium of the non-azeotropic refrigerant mixture formed by chlorofluoromethane and 1,1,1,2-tetrafluoroethane. *Fluid Phase Equilibria*, 63(1–2), pp.151–156.

Attard, P. & Moule, G.A., 1993. A force-balance Monte Carlo simulation of the surface tension of a hard-sphere fluid. *http://dx.doi.org/10.1080/00268979300100631*.

Ball, S.J., 2003. Thermodynamics of compressed liquids from the speed of sound.

Barley, M.H. et al., 1997. Vapour-liquid equilibrium data for binary mixtures of some new refrigerants. *Fluid Phase Equilibria*, 140(1–2), pp.183–206.

Bobbo, S. et al., 1998. A recirculation apparatus for vapor–liquid equilibrium measurements of refrigerants. Binary mixtures of R600a, R134a and R236fa. *Fluid Phase Equilibria*, 150–151, pp.343–352.

Bobbo, S. et al., 2004. Compressed liquid densities and saturated liquid densities of HFC-365mfc. In *Fluid Phase Equilibria*. pp. 291–296.

Bobbo, S. et al., 2001. Isothermal VLE measurements for the binary mixtures HFC-134a + HFC-245fa and HC-600a + HFC-245fa. *Fluid Phase Equilibria*, 185(1–2), pp.255–264.

Bobbo, S. et al., 2000. Vapor+Liquid Equilibrium Measurements and Correlation of the Binary Refrigerant Mixtures Difluoromethane (HFC-32)+1,1,1,2,3,3-Hexafluoropropane (HFC-236ea) and Pentafluoroethane (HFC-125)+1,1,1,2,3,3-Hexafluoropropane (HFC-236ea) at 288.6, 303.2, and 318. *International Journal of Thermophysics*, 21(3), pp.781–791.

Bobbo, S., Camporese, R. & Stryjek, R., 1999. Vapor−Liquid Equilibria for Difluoromethane (R32) + and Pentafluoroethane (R125) + 1,1,1,3,3,3-Hexafluoropropane (R236fa) at 303.2 and 323.3 K. *Journal of Chemical & Engineering Data*, 44(2), pp.349–352.

Bouchot, C. & Richon, D., 2001. An enhanced method to calibrate vibrating tube densimeters. *Fluid Phase Equilibria*, 191(1–2), pp.189–208.

Bouchot, C. & Richon, D., 1998a. Direct Pressure−Volume−Temperature and Vapor−Liquid Equilibrium Measurements with a Single Equipment Using a Vibrating Tube Densimeter up to 393 K and 40 MPa: Description of the Original Apparatus and New Data. *Industrial & Engineering Chemistry Research*, 37(8), pp.3295–3304.

Bouchot, C. & Richon, D., 1998b. Direct Pressure−Volume−Temperature and Vapor−Liquid Equilibrium Measurements with a Single Equipment Using a Vibrating Tube Densimeter up to 393 K and 40 MPa: Description of the Original Apparatus and New Data.

Brown, J. et al., 2012. Vapor Pressure of Hydrofluoroolefins: Critical Review of Experimental Data and Models. *International Refrigeration and Air Conditioning Conference*.

Brown, J.S. et al., 2013. Saturated pressure measurements of 3,3,3-trifluoroprop-1-ene (R1243zf) for reduced temperatures ranging from 0.62 to 0.98. *Fluid Phase Equilibria*, 351, pp.48–52.

Brown, J.S., Zilio, C. & Cavallini, A., 2010a. Thermodynamic properties of eight fluorinated olefins. *International Journal of Refrigeration*, 33(2), pp.235–241.

Brown, J.S., Zilio, C. & Cavallini, A., 2010b. Thermodynamic properties of eight fluorinated olefins. *International Journal of Refrigeration*, 33(2), pp.235–241.

Cahn, J.W. & Hilliard, J.E., 1958. Free Energy of a Nonuniform System. I. Interfacial Free Energy. *The Journal of Chemical Physics*, 28(2), p.258.

Cai, J. & Prausnitz, J.M., 2004. Thermodynamics for fluid mixtures near to and far from the vapor–liquid critical point. *Fluid Phase Equilibria*, 219(2), pp.205–217.

Caudwell, D.R. et al., 2004. The Viscosity and Density of n-Dodecane and n-Octadecane at Pressures up to 200 MPa and Temperatures up to 473 K. *International Journal of Thermophysics*, 25(5), pp.1339–1352.

Caudwell, D.R. et al., 2009. Viscosity and Density of Five Hydrocarbon Liquids at Pressures up to 200 MPa and Temperatures up to 473 K †. *Journal of Chemical & Engineering Data*, 54(2), pp.359–366.

Caudwell, D.R., 2004. *Viscosity of dense fluid mixtures*. Imperial College London (University of London).

Chae, H.B., Schmidt, J.W. & Moldover, M.R., 1990. Surface tension of refrigerants R123 and R134a. *Journal of Chemical & Engineering Data*, 35(1), pp.6–8.

Chareton, A. et al., 1990. Bubble pressures and saturated liquid molar volumes of binary and ternary refrigerant mixtures. *Journal of Chemical & Engineering Data*, 35(2), pp.162–165.

Chen, L.-X. et al., 2015. Vapor–liquid equilibria of fluoroethane (HFC-161) + 2,3,3,3 - tetrafluoroprop - 1 - ene (HFO-1234yf). *Fluid Phase Equilibria*.

Chen, Q. et al., 2011. Gas phase PVTx properties for binary mixtures of HFC-161 and HFC-134a. *Fluid Phase*

Equilibria, 304(1–2), pp.61–63.
Chen, Q., Hong, R.-H. & Chen, G.-M., 2006. Measurements of gas phase PVTx properties for the ternary HFC-161/125/32 system. *Fluid Phase Equilibria*, 249(1–2), pp.92–96.
Chen, Q., Hong, R. & Chen, G., 2006. PVTx properties in the gas phase for binary HFC-161/125 system. *Fluid Phase Equilibria*, 240(1), pp.63–66.
Chen, Q., Hong, R. & Chen, G., 2005. Vapor Pressure Measurements of Ethyl Fluoride. *Journal of Chemical & Engineering Data*, 50(5), pp.1586–1588.
Chung, E.-Y. & Kim, M.S., 1997. Vapor−Liquid Equilibria for the Difluoromethane (HFC-32) + 1,1,1,2-Tetrafluoroethane (HFC-134a) System. *Journal of Chemical & Engineering Data*, 42(6), pp.1126–1128.
Ciotta, F. et al., 2009. Viscosity and Density of Carbon Dioxide + 2,6,10,15,19,23-Hexamethyltetracosane (Squalane) †. *Journal of Chemical & Engineering Data*, 54(9), pp.2436–2443.
Ciotta, F., 2010. *Viscosity of Asymmetric Liquid Mixtures under Extreme Conditions*. Imperial College London.
Ciotta, F. & Trusler, J.P.M., 2010. Improved Understanding of Vibrating-Wire Viscometer−Densimeters. *Journal of Chemical & Engineering Data*, 55(6), pp.2195–2201.
Coquelet, C. et al., 2010. Experimental Measurement of Vapor Pressures and Densities of Pure Hexafluoropropylene. *Journal of Chemical & Engineering Data*, 55(6), pp.2093–2099.
Coquelet, C. et al., 2003. Vapor−Liquid Equilibrium Data for the Azeotropic Difluoromethane + Propane System at Temperatures from 294.83 to 343.26 K and Pressures up to 5.4 MPa. *Journal of Chemical & Engineering Data*, 48(2), pp.317–323.
Coquelet, C. et al., 2003. Vapour–liquid equilibrium data for the difluoromethane+1,1,1,2,3,3,3-heptafluoropropane system at temperatures from 283.20 to 343.38 K and pressures up to 4.5 MPa. *International Journal of Refrigeration*, 26(5), pp.559–565.
Coquelet, C., El Abbadi, J. & Houriez, C., 2016. Prediction of thermodynamic properties of refrigerant fluids with a new three-parameter cubic equation of state. *International Journal of Refrigeration*, 69, pp.418–436.
Coquelet, C., Chapoy, A. & Richon, D., 2004. Development of a New Alpha Function for the Peng–Robinson Equation of State: Comparative Study of Alpha Function Models for Pure Gases (Natural Gas Components) and Water-Gas Systems. *International Journal of Thermophysics*, 25(1).
Coquelet, C., Chareton, A. & Richon, D., 2004. Vapour–liquid equilibrium measurements and correlation of the difluoromethane (R32) + propane (R290) + 1,1,1,2,3,3,3-heptafluoropropane (R227ea) ternary mixture at temperatures from 269.85 to 328.35K. *Fluid Phase Equilibria*, 218(2), pp.209–214.
Cui, X. et al., 2006. Experimental vapor pressure data and a vapor pressure equation for fluoroethane (HFC-161). *Fluid Phase Equilibria*, 245(2), pp.155–157.
Danesh, A., Xu, D.-H. & Todd, A.C., 1991. Comparative study of cubic equations of state for predicting phase behaviour and volumetric properties of injection gas-reservoir oil systems. *Fluid Phase Equilibria*, 63(3), pp.259–278.
Dicko, M., Belaribi-Boukais, G., et al., 2011. Experimental Measurement of Vapor Pressures and Densities at Saturation of Pure Hexafluoropropylene Oxide: Modeling Using a Crossover Equation of State. *Industrial & Engineering Chemistry Research*, 50(8), pp.4761–4768.
Dicko, M. & Coquelet, C., 2011. Application of a new crossover treatment to a generalized cubic equation of state. *Fluid Phase Equilibria*, 302(1–2), pp.241–248.
Dicko, M., Valtz, A. & Coquelet, C., 2011. Reply to "Comments on 'Experimental Measurement of Vapor Pressures and Densities at Saturation of Pure Hexafluoropropylene Oxide: Modeling Using a Crossover Equation of State.'" *Industrial & Engineering Chemistry Research*, 50(15), pp.9476–9477.
Dix, M. et al., 1991. A vibrating-wire densimeter for measurements in fluids at high pressures. *International Journal of Thermophysics*, 12(2), pp.357–370.
Dohrn, R., Peper, S. & Fonseca, J.M.S., 2010. High-pressure fluid-phase equilibria: Experimental methods and systems investigated (2000–2004). *Fluid Phase Equilibria*, 288(1), pp.1–54.
Dong, X. et al., 2013. Measurements of isothermal (vapour+liquid) equilibria data for {1,1,2,2-Tetrafluoroethane (R134)+trans-1,3,3,3-tetrafluoropropene (R1234ze(E))} at T=(258.150 to 288.150)K. *The Journal of Chemical Thermodynamics*, 60, pp.25–28.
Duan, Y.-Y. et al., 2004. Vapor pressure measurements of 1,1,1-trifluoroethane (HFC-143a) and 1,1,1,3,3,3-hexafluoropropane (HFC-236fa). *Fluid Phase Equilibria*, 225, pp.101–106.
Duan, Y.-Y. & Meng, L., 2004. Gaseous PVT properties of 1,1,1,3,3,3-hexafluoropropane (HFC-236fa). *Fluid Phase Equilibria*, 226, pp.313–320.
Duran-Valencia, C. et al., 2002. Vapor−Liquid Equilibrium (VLE) Data for the Carbon Dioxide (CO 2) + 1,1,1,2-Tetrafluoroethane (R134a) System at Temperatures from 252.95 K to 292.95 K and Pressures up to 2 MPa. *Journal of Chemical & Engineering Data*, 47(1), pp.59–61.
ElAhmar, E. et al., 2012. Vapour–liquid equilibrium of binary systems containing pentafluorochemicals from 363 to 413 K: Measurement and modelling with Peng–Robinson and three SAFT-like equations of states. *International Journal of Refrigeration*, 35(8), pp.2297–2310.

Evans, R., 1979. The nature of the liquid-vapour interface and other topics in the statistical mechanics of non-uniform, classical fluids. *http://dx.doi.org/10.1080/00018737900101365*.

Feng, X. et al., 2010. Vapor pressures of 1,1,1,2,3,3,3-heptafluoropropane, 1,1,1,3,3,3-hexafluoropropane and 1,1,1,3,3-pentafluoropropane. *Fluid Phase Equilibria*, 290(1–2), pp.127–136.

Fonseca, J.M.S., Dohrn, R. & Peper, S., 2011. High-pressure fluid-phase equilibria: Experimental methods and systems investigated (2005–2008). *Fluid Phase Equilibria*, 300(1), pp.1–69.

Forero G., L.A. & Velásquez J., J.A., 2012. The Patel–Teja and the Peng–Robinson EoSs performance when Soave alpha function is replaced by an exponential function. *Fluid Phase Equilibria*, 332, pp.55–76.

Fröba, A.P., Krzeminski, K. & Leipertz, A., 2004. Thermophysical properties of 1,1,1,3,3-pentafluorobutane (R365mfc). *International Journal of Thermophysics*, 25(4), pp.987–1004.

Fu, Y.-D., Han, L.-Z. & Zhu, M.-S., 1995. PVT properties, vapor pressures and critical parameters of HFC-32. *Fluid Phase Equilibria*, 111(2), pp.273–286.

Fukuizumi, H. & Uematsu, M., 1991a. Bubble pressures and saturated liquid densities of R 22 + R 114 mixtures in the range 310?400 K. *International Journal of Thermophysics*, 12(2), pp.371–379.

Fukuizumi, H. & Uematsu, M., 1991b. Densities of liquid R 114 at temperatures from 310 to 400 K and pressures up to 10 MPa. *International Journal of Thermophysics*, 12(3), pp.541–548.

Gloor, G.J. et al., 2005. Test-area simulation method for the direct determination of the interfacial tension of systems with continuous or discontinuous potentials. *The Journal of Chemical Physics*, 123(13), p.134703.

Le Guennec, Y. et al., 2016. A consistency test for α-functions of cubic equations of state. *Fluid Phase Equilibria*, 427, pp.513–538.

Guggenheim, E.A., 1945. The Principle of Corresponding States. *The Journal of Chemical Physics*, 13(7), p.253.

Guo, H. et al., 2012. (Vapour+liquid) equilibrium data for the azeotropic {1,1-difluoroethane (R152a)+1,1,2,2-Tetrafluoroethane (R134)} system at various temperatures from (258.150 to 288.150)K. *The Journal of Chemical Thermodynamics*, 54, pp.129–133.

Haile, J.M., Gray, C.G. & Gubbins, K.E., 1976. Theory of surface tension for molecular liquids. II. Perturbation theory calculations. *The Journal of Chemical Physics*, 64(6), p.2569.

Han, X. et al., 2010. Isothermal vapor–liquid equilibrium data for the binary mixture difluoromethane (HFC-32)+ethyl fluoride (HFC-161) over a temperature range from 253.15K to 303.15K. *Fluid Phase Equilibria*, 299(1), pp.116–121.

Han, X.H. et al., 2011. Density Data for the Refrigerant Ethyl Fluoride (HFC-161) over a Temperature Range from (230 to 344) K. *Journal of Chemical & Engineering Data*, 56(7), pp.3038–3042.

Higashi, Y. et al., 1984. Measurements of the vapor-liquid coexistence curve for the binary R12 + R22 system in the critical region. *Journal of Chemical & Engineering Data*, 29(1), pp.31–36.

Higashi, Y., Uematsu, M. & Watanabe, K., 1985. Measurements of the Vapor-liquid Coexistence Curve and Determination of the Critical Parameters for Refrigerant 114. *Bulletin of JSME*, 28(246), pp.2968–2973.

Hu, P., Chen, L.-X., Zhu, W.-B., et al., 2014a. Isothermal VLE measurements for the binary mixture of 2,3,3,3-tetrafluoroprop-1-ene (HFO-1234yf)+1,1-difluoroethane (HFC-152a). *Fluid Phase Equilibria*, 373, pp.80–83.

Hu, P., Chen, L.-X., Zhu, W.-B., et al., 2014b. Vapor−liquid equilibria for the binary system of 2,3,3,3-tetrafluoroprop-1-ene (HFO-1234yf)+1,1,1,2,3,3,3-heptafluoropropane (HFC-227ea). *Fluid Phase Equilibria*, 379, pp.59–61.

Hu, P., Chen, L.-X. & Chen, Z.-S., 2014. Vapor–liquid equilibria for binary system of 2,3,3,3-tetrafluoroprop-1-ene (HFO-1234yf) +isobutane (HC-600a). *Fluid Phase Equilibria*, 365, pp.1–4.

Hu, P., Chen, L.-X. & Chen, Z.-S., 2013. Vapor–liquid equilibria for the 1,1,1,2-tetrafluoroethane (HFC-134a)+1,1,1,2,3,3,3-heptafluoropropane (HFC-227ea) and 1,1,1-trifluoroethane (HFC-143a)+2,3,3,3-tetrafluoroprop-1-ene (HFO-1234yf) systems. *Fluid Phase Equilibria*, 360, pp.293–297.

Hu, P., Chen, L.X. & Chen, Z.S., 2013. Vapor-liquid equilibria for the 1,1,1,2-tetrafluoroethane (HFC-134a)+1,1,1,2,3,3,3-heptafluoropropane (HFC-227ea) and 1,1,1-trifluoroethane (HFC-143a)+2,3,3,3-tetrafluoroprop-1-ene (HFO-1234yf) systems. *Fluid Phase Equilibria*, 360, pp.293–297.

Hu, P. & Chen, Z.-S., 2004. Saturated densities and critical properties of HFC-227ea. *Fluid Phase Equilibria*, 221(1–2), pp.7–13.

Huber, M.L., Friend, D.G. & Ely, J.F., 1992. Prediction of the thermal conductivity of refrigerants and refrigerant mixtures. *Fluid Phase Equilibria*, 80, pp.249–261.

Hulse, R.J. et al., 2012. Physical Properties of HCFO-1233zd(E). *Journal of Chemical & Engineering Data*, 57(12), pp.3581–3586.

IPCC report, 2016. IPCC - Intergovernmental Panel on Climate Change. Available at: https://www.ipcc.ch/.

Janeček, J. et al., 2015. A generalized Kiselev crossover approach applied to Soave–Redlich–Kwong equation of state. *Fluid Phase Equilibria*, 401, pp.16–26.

Jaubert, J.-N. et al., 2005. Extension of the PPR78 model (predictive 1978, Peng–Robinson EOS with temperature dependent kij calculated through a group contribution method) to systems containing aromatic compounds.

Fluid Phase Equilibria, 237(1–2), pp.193–211.
Jaubert, J.-N. et al., 2016. Note on the properties altered by application of a Péneloux–type volume translation to an equation of state. *Fluid Phase Equilibria*, 419, pp.88–95.
Jaubert, J.-N. & Mutelet, F., 2004. VLE predictions with the Peng–Robinson equation of state and temperature dependent kij calculated through a group contribution method. *Fluid Phase Equilibria*, 224(2), pp.285–304.
Ji, W.-R. et al., 2007. Extrapolation of VLE data and simultaneous representation of caloric and volumetric properties by means of a cubic 3-parameter equation of state. *Fluid Phase Equilibria*, 260(1), pp.113–125.
Ji, W.-R. & Lempe, D.A., 1998. A systematic study of cubic three-parameter equations of state for deriving a structurally optimized PVT relation. *Fluid Phase Equilibria*, 147(1–2), pp.85–103.
Ju, M. et al., 2009. (Vapour+liquid) equilibria of the {trifluoromethane (HFC-23)+propane} and {trifluoromethane (HFC-23)+n-butane} systems. *The Journal of Chemical Thermodynamics*, 41(12), pp.1339–1342.
Juntarachat, N. et al., 2014. *Experimental measurements and correlation of vapor-liquid equilibrium and critical data for the CO2 + R1234yf and CO2 + R1234ze(E) binary mixtures*,
Kamiaka, T., Dang, C. & Hihara, E., 2013. Vapor-liquid equilibrium measurements for binary mixtures of R1234yf with R32, R125, and R134a. *International Journal of Refrigeration*, 36(3), pp.965–971.
Khalil, W., 2006. Développement d'un appareil automatisé de mesure simultanée d'équilibres de phases et de propriétés volumétriques. Exploitation des données volumétriques pour le calcul prédictif de grandeurs thermodynamiques dérivées.
Khalil, W., Coquelet, C. & Richon, D., 2007. High-Pressure Vapor−Liquid Equilibria, Liquid Densities, and Excess Molar Volumes for the Carbon Dioxide + 2-Propanol System from (308.10 to 348.00) K. *Journal of Chemical & Engineering Data*, 52(5), pp.2032–2040.
Kim, C.-N. & Park, Y.-M., 1999. Vapor–Liquid Equilibrium of HFC-32/134a And HFC-125/134a Systems. *International Journal of Thermophysics*, 20(2), pp.519–530.
Kim, S.Y., Kim, S.S. & Lee, B., 2009. Prediction of the surface tension of binary systems based on the partial least squares method. *Korean Journal of Chemical Engineering*, 26(2), pp.349–353.
Kleiber, M., 1994. Vapor-liquid equilibria of binary refrigerant mixtures containing propylene or R134a. *Fluid Phase Equilibria*, 92, pp.149–194.
Klein, S.., McLinden, M.. & Laesecke, A., 1997. An improved extended corresponding states method for estimation of viscosity of pure refrigerants and mixtures. *International Journal of Refrigeration*, 20(3), pp.208–217.
Klomfar, J., Součková, M. & Pátek, J., 2012. Liquid-Phase p –ρ– T Data for 2,3,3,3-Tetrafluoroprop-1-ene (R-1234yf) and 1,1,2,3,3,3-Hexafluoroprop-1-ene (R-1216) at Temperatures from (208 to 353) K under Pressures up to 40 MPa. *Journal of Chemical & Engineering Data*, 57(11), pp.3283–3289.
Klomfar, J., Součková, M. & Pátek, J., 2013. Surface Tension and p –ρ– T Data for 1,1,1,3,3-Pentafluorobutane (HFC-365mfc) and 1,1,1,2,2,3,3-Heptafluoro-3-methoxy-propane (HFE-347mcc). *Journal of Chemical & Engineering Data*, 58(8), pp.2316–2325.
Kobayashi, M. & Nishiumi, H., 1998. Vapor–liquid equilibria for the pure, binary and ternary systems containing HFC32, HFC125 and HFC134a. *Fluid Phase Equilibria*, 144(1–2), pp.191–202.
Kondou, C. et al., 2015. Surface tension of low GWP refrigerants R1243zf, R1234ze(Z), and R1233zd(E). *International Journal of Refrigeration*, 53, pp.80–89.
Konynenburg, P.H. Van & Scott, R.L., 1980. Critical Lines and Phase Equilibria in Binary Van Der Waals Mixtures. *Philosophical Transactions of the Royal Society of London A: Mathematical, Physical and Engineering Sciences*, 298(1442).
Kubic, W.L. & Stein, F.P., 1981. An experimental and correlative study of the vapor-liquid equilibria of the tetrafluoromethane-chlorotrifluoromethane system. *Fluid Phase Equilibria*, 5(3–4), pp.289–304.
Kwak, T.Y. & Mansoori, G.A., 1986. Van der waals mixing rules for cubic equations of state. Applications for supercritical fluid extraction modelling. *Chemical Engineering Science*, 41(5), pp.1303–1309.
Lasserre, V. et al., 2014. le règlement F-Gas, objectifs et impacts. *Revue Générale du Froid et du Conditionnement d'Air*.
Lemmon, E.W., Huber, M.L. & McLinden, M.O., 2010. REFPROP, Reference Fluid Thermodynamic and Transport Properties.
Len, C.W., 2003. Viscosity of heavy hydrocarbon liquids with dissolved gases.
Lim, J.S., Park, J.-Y., et al., 2002. Phase equilibria of 1,1,1-trifluoroethane (HFC-143a) + 1,1,1,2-tetrafluoroethane (HFC-134a), and + 1,1-difluoroethane (HFC-152a) at 273.15, 293.15, 303.15, and 313.15 K. *Fluid Phase Equilibria*, 193(1–2), pp.29–39.
Lim, J.S. et al., 2001. Phase Equilibria of CFC Alternative Refrigerant Mixtures. Binary Systems of Trifluoromethane (HFC-23) + 1,1,1,2-Tetrafluoroethane (HFC-134a) and Trifluoromethane (HFC-23) + 1,1,1,2,3,3,3-Heptafluoropropane (HFC-227ea) at 283.15 and 293.15 K. *Journal of Chemical & Engineering Data*, 46(6), pp.1580–1583.
Lim, J.S., Park, J.-Y. & Lee, B.-G., 2000. Vapor–Liquid Equilibria of CFC Alternative Refrigerant Mixtures:

Trifluoromethane (HFC-23)+Difluoromethane (HFC-32), Trifluoromethane (HFC-23)+Pentafluoroethane (HFC-125), and Pentafluoroethane (HFC-125)+1,1-Difluoroethane (HFC-152a). *International Journal of Thermophysics*, 21(6), pp.1339–1349.

Lim, J.S., Park, K.H. & Lee, B.G., 2002. Phase Equilibria of HFC Mixtures: Binary Mixtures of Trifluoromethane + 1,1-Difluoroethane and Trifluoromethane + 1,1,1-Trifluoroethane at 283.15 and 293.15 K. *Journal of Chemical & Engineering Data*, 47(3), pp.582–586.

Lin, H. & Duan, Y.Y., 2003. Surface Tension of 1,1,1-Trifluoroethane (HFC-143a), 1,1,1,2,3,3,3-Heptafluoropropane (HFC-227ea), and Their Binary Mixture HFC-143a/227ea. *International Journal of Thermophysics*, 24(6), pp.1495–1508.

Macleod, D.B., 1923. On a relation between surface tension and density. *Transactions of the Faraday Society*, 19(July), p.38.

Madani, H. et al., 2008a. (Vapor+liquid) equilibrium data for (carbon dioxide+1,1-difluoroethane) system at temperatures from (258 to 343)K and pressures up to about 8MPa. *The Journal of Chemical Thermodynamics*, 40(10), pp.1490–1494.

Madani, H. et al., 2016. Isothermal vapor–liquid equilibrium data for the trifluoromethane (R23) + 2,3,3,3-tetrafluoroprop-1-ene (R1234yf) system at temperatures from 254 to 348 K. *Fluid Phase Equilibria*, 415, pp.158–165.

Madani, H. et al., 2009. Vapor–liquid equilibria of the (hexafluoroethane+1,1,1-trifluoroethane) binary system from 258 to 343K up to 3.89MPa. *International Journal of Refrigeration*, 32(6), pp.1396–1402.

Madani, H. et al., 2008b. Vapor–liquid equilibrium data for the (hexafluoroethane +1,1,1,2-tetrafluoroethane) system at temperatures from 263 to 353K and pressures up to 4.16MPa. *Fluid Phase Equilibria*, 268(1–2), pp.68–73.

Madani, H., Valtz, A. & Coquelet, C., 2013. Isothermal vapor–liquid equilibrium data for the decafluorobutane (R3110)+1,1,1,3,3-pentafluorobutane (R365mfc) system at temperatures from 333K to 441K. *Fluid Phase Equilibria*, 354, pp.109–113.

Maezawa, Y., Widiatmo, J. V., et al., 1991. Saturated liquid densities and bubble point pressures of the ternary HCFC-22/HFC-152a/HCFC-142b system. *Fluid Phase Equilibria*, 67, pp.203–212.

Maezawa, Y., Sato, H. & Watanabe, K., 1991. Saturated liquid densities and bubble-point pressures of the binary HCFC 22 + HFC 152a system. *Fluid Phase Equilibria*, 61(3), pp.263–273.

Mahmoodi, P. & Sedigh, M., 2016. Second derivative of alpha functions in cubic equations of state. *The Journal of Supercritical Fluids*.

Malami, M. & Trusler, J.P.M., 2014. *Standard Operating Procedure (SOP) for 2 kbar vibrating-wire viscometer-densimeter (VWVD)*,

Mastroianni, M.J., Stahl, R.F. & Sheldon, P.N., 1978. Physical and thermodynamic properties of 1,1,2-trifluorotrichloroethane (R-113). *Journal of Chemical & Engineering Data*, 23(2), pp.113–118.

Mathias, P.M. & Copeman, T.W., 1983. Extension of the Peng-Robinson equation of state to complex mixtures: Evaluation of the various forms of the local composition concept. *Fluid Phase Equilibria*, 13, pp.91–108.

May, E.F. et al., 2014. Physical apparatus parameters and model for vibrating tube densimeters at pressures to 140 MPa and temperatures to 473 K. *Review of Scientific Instruments*, 85(9), p.95111.

Meng, X. et al., 2013. Viscosity measurements for 2,3,3,3-tetrafluoroprop-1-ene (R1234yf) and trans-1,3,3,3-tetrafluoropropene (R1234ze(E)). *The Journal of Chemical Thermodynamics*, 63, pp.24–30.

Minor, B. & Spatz, M., 2008. HFO-1234yf Low GWP Refrigerant Update. *International Refrigeration and Air Conditioning Conference*.

Miqueu, C. et al., 2000. An extended scaled equation for the temperature dependence of the surface tension of pure compounds inferred from an analysis of experimental data. *Fluid Phase Equilibria*, 172(2), pp.169–182.

Miqueu, C. et al., 2003. Modelling of the surface tension of pure components with the gradient theory of fluid interfaces: a simple and accurate expression for the influence parameters. *Fluid Phase Equilibria*, 207(1), pp.225–246.

Nagel, M. & Bier, K., 1996. Vapour-liquid equilibrium of ternary mixtures of the refrigerants R125, R143a and R134a. *International Journal of Refrigeration*, 19(4), pp.264–271.

Nagel, M. & Bier, K., 1995. Vapour-liquid equilibrium of ternary mixtures of the refrigerants R32, R125 and R134a. *International Journal of Refrigeration*, 18(8), pp.534–543.

Nazeri, M. et al., 2016. Densities and derived thermophysical properties of the 0.9505 CO2+0.0495 H2S mixture from 273 K to 353 K and pressures up to 41 MPa. *Fluid Phase Equilibria*, 423, pp.156–171.

Nelson, W.M. et al., 2011. Vapor−Liquid Equilibrium Data for Binary Systems Consisting of Either Hexafluoropropene (HFP) or 2,2,3-Trifluoro-3-(trifluoromethyl)oxirane (HFPO) with Carbon Dioxide (R-744) or 2,2-Dichloro-1,1,1-trifluoroethane (R-123). *Journal of Chemical & Engineering Data*, 56(1), pp.74–78.

Di Nicola, G. et al., 2005. PVTx Measurements for the R116 + CO 2 and R41 + CO 2 Systems. New Isochoric

Apparatus. *Journal of Chemical & Engineering Data*, 50(2), pp.312–318.
Di Nicola, G. et al., 2012. PVTx Measurements of the Carbon Dioxide + 2,3,3,3-Tetrafluoroprop-1-ene Binary System. *Journal of Chemical & Engineering Data*, 57(2), pp.450–455.
Di Nicola, G. et al., 2012. Saturated Pressure Measurements of trans -1,3,3,3-Tetrafluoroprop-1-ene (R1234ze(E)) for Reduced Temperatures Ranging from 0.58 to 0.92. *Journal of Chemical & Engineering Data*, 57(8), pp.2197–2202.
Di Nicola, G., Polonara, F. & Santori, G., 2010. Saturated Pressure Measurements of 2,3,3,3-Tetrafluoroprop-1-ene (HFO-1234yf). *Journal of Chemical & Engineering Data*, 55(1), pp.201–204.
Niesen, V.G. et al., 1994. Coexisting densities and vapor pressures of refrigerants R-22, R-134a, and R-124 at 300–395 K. *Fluid Phase Equilibria*, 97, pp.81–95.
Oliveira, C.M.B.P. & Wakeham, W.A., 1993. The viscosity of liquid R134a. *International Journal of Thermophysics*, 14(1), pp.33–44.
Orbey, H. & Sandler, S.I., 1998. *Modeling Vapor-Liquid Equilibria: Cubic Equations of State and Their Mixing Rules, Volume 1*, Cambridge University Press.
Patel, N.C. & Teja, A.S., 1982. A new cubic equation of state for fluids and fluid mixtures. *Chemical Engineering Science*, 37(3), pp.463–473.
PREDIREF website, 2016. Project PREDIREF (Prediction of the physical properties of next-generation refrigerant fluids) | ANR - Agence Nationale de la Recherche. Available at: http://www.agence-nationale-recherche.fr/?Project=ANR-13-CDII-0008.
Privat, R., Jaubert, J.-N. & Mutelet, F., 2008. Use of the PPR78 Model To Predict New Equilibrium Data of Binary Systems Involving Hydrocarbons and Nitrogen. Comparison with Other GCEOS. *Industrial & Engineering Chemistry Research*, 47(19), pp.7483–7489.
Quiñones-Cisneros, S.E. & Deiters, U.K., 2006. Generalization of the Friction Theory for Viscosity Modeling.
Quiñones-Cisneros, S.E., Zéberg-Mikkelsen, C.K. & Stenby, E.H., 2001. One parameter friction theory models for viscosity. *Fluid Phase Equilibria*, 178(1), pp.1–16.
Quiñones-Cisneros, S.E., Zéberg-Mikkelsen, C.K. & Stenby, E.H., 2000. The friction theory (f-theory) for viscosity modeling. *Fluid Phase Equilibria*, 169(2), pp.249–276.
Retsina, T., Richardson, S.M. & Wakeham, W.A., 1986. The theory of a vibrating-rod densimeter. *Applied Scientific Research*, 43(2), pp.127–158.
Retsina, T., Richardson, S.M. & Wakeham, W.A., 1987. The theory of a vibrating-rod viscometer. *Applied Scientific Research*, 43(4), pp.325–346.
Rivollet, F. et al., 2004. Vapor–liquid equilibrium data for the carbon dioxide (CO2) + difluoromethane (R32) system at temperatures from 283.12 to 343.25 K and pressures up to 7.46 MPa. *Fluid Phase Equilibria*, 218(1), pp.95–101.
Rowlinson, J.S., 1979. Translation of J. D. van der Waals' ?The thermodynamik theory of capillarity under the hypothesis of a continuous variation of density? *Journal of Statistical Physics*, 20(2), pp.197–200.
Schmidt, G. & Wenzel, H., 1980. A modified van der Waals type equation of state. *Chemical Engineering Science*, 35(7), pp.1503–1512.
Schmidt, K.A.G. et al., 2015. New Experimental Data and Reference Models for the Viscosity and Density of Squalane. *Journal of Chemical & Engineering Data*, 60(1), pp.137–150.
Scott, J.D. & Steven, R.A., 1993. Chemical process.
Scott, R.L. & van Konynenburg, P.H., 1970. Static properties of solutions. Van der Waals and related models for hydrocarbon mixtures. *Discussions of the Faraday Society*, 49(0), p.87.
Segura, H. et al., 2008. An accurate direct technique for parameterizing cubic equations of state. *Fluid Phase Equilibria*, 265(1–2), pp.155–172.
Sengers, J.V. et al., 2000. *Equations of State for Fluids and Fluid Mixtures*, Elsevier.
Smith, G.J. et al., 2003. Correlation of liquid viscosity at the normal boiling point. In *Proceedings of the 15th Symposium on Thermophysical Properties, Boulder, CO, USA.*
Soo, C.-B., 2011. Experimental thermodynamic measurements of biofuel-related associating compounds and modeling using the PC-SAFT equation of state.
Sotani, T. & Kubota, H., 1999. Vapor pressures and PVT properties of 1,1,1,3,3-pentafluoropropane (HFC-245fa). *Fluid Phase Equilibria*, 161(2), pp.325–335.
Stein, F.P. & Proust, P.C., 1971. Vapor-liquid equilibiriums of the trifluoromethane-trifluorochloromethane system. *Journal of Chemical & Engineering Data*, 16(4), pp.389–393.
Sugden, S., 1924a. CXLI.—The influence of the orientation of surface molecules on the surface tension of pure liquids. *J. Chem. Soc., Trans.*, 125(0), pp.1167–1177.
Sugden, S., 1924b. VI.—The variation of surface tension with temperature and some related functions. *J. Chem. Soc., Trans.*, 125(0), pp.32–41.
Tanaka, K. & Higashi, Y., 2010a. Thermodynamic properties of HFO-1234yf (2,3,3,3-tetrafluoropropene). *International Journal of Refrigeration*, 33(3), pp.474–479.

Tanaka, K. & Higashi, Y., 2010b. Thermodynamic properties of HFO-1234yf (2,3,3,3-tetrafluoropropene). *International Journal of Refrigeration*, 33(3), pp.474–479.

Tanaka, K., Takahashi, G. & Higashi, Y., 2010. Measurements of the Vapor Pressures and p ρ T Properties for trans -1,3,3,3-Tetrafluoropropene (HFO-1234ze(E)). *Journal of Chemical & Engineering Data*, 55(6), pp.2169–2172.

Taylor, B.N., 2009. *Guidelines for Evaluating and Expressing the Uncertainty of NIST Measurement Results (rev. Ed.)*, DIANE Publishing.

Toxvaerd, S., 1972. Surface Structure of a Square-Well Fluid. *The Journal of Chemical Physics*, 57(10), p.4092.

Twu, C.H. et al., 1991. A cubic equation of state with a new alpha function and a new mixing rule. *Fluid Phase Equilibria*, 69, pp.33–50.

Twu, C.H., Coon, J.E. & Cunningham, J.R., 1992. A new cubic equation of state. *Fluid Phase Equilibria*, 75, pp.65–79.

Valderrama, J.O., 1990. A generalized Patel-Teja equation of state for polar and nonpolar fluids and their mixtures. *JOURNAL OF CHEMICAL ENGINEERING OF JAPAN*, 23(1), pp.87–91.

Valderrama, J.O., 2003. The State of the Cubic Equations of State. *Industrial & Engineering Chemistry Research*, 42(8), pp.1603–1618.

Valtz, A. et al., 2003. Vapor–liquid equilibrium data for the CO2 + 1,1,1,2,3,3,3,-heptafluoropropane (R227ea) system at temperatures from 276.01 to 367.30 K and pressures up to 7.4 MPa. *Fluid Phase Equilibria*, 207(1–2), pp.53–67.

Valtz, A. et al., 2002. Vapor–liquid equilibrium data for the propane+1,1,1,2,3,3,3-heptafluoropropane (R227ea) system at temperatures from 293.16 to 353.18 K and pressures up to 3.4 MPa. *Fluid Phase Equilibria*, 202(1), pp.29–47.

Valtz, A., Coquelet, C. & Richon, D., 2007. Vapor–liquid equilibrium data for the hexafluoroethane+carbon dioxide system at temperatures from 253 to 297K and pressures up to 6.5MPa. *Fluid Phase Equilibria*, 258(2), pp.179–185.

Valtz, A., Coquelet, C. & Richon, D., 2004. Vapor–Liquid Equilibrium Data for the Sulfur Dioxide (SO 2) + Difluoromethane (R32) System at Temperatures from 288.07 to 403.16 K and at Pressures up to 7.31 MPa. *International Journal of Thermophysics*, 25(6), pp.1695–1711.

Vega, C. & de Miguel, E., 2007. Surface tension of the most popular models of water by using the test-area simulation method. *The Journal of Chemical Physics*, 126(15), p.154707.

Waals, J.D., 1873. *Over de continuiteit van den gas- en vloeistoftoestand*, A. W. Sijthoff.

Wang, Q., Xu, Y.-J., et al., 2010. Isothermal vapor–liquid equilibrium data for the binary mixture ethyl fluoride (HFC-161)+1,1,1,2,3,3,3-heptafluoroproane (HFC-227ea) over a temperature range from 253.15K to 313.15K. *Fluid Phase Equilibria*, 297(1), pp.67–71.

Wang, Q., Gao, Z.J., et al., 2010. Isothermal Vapor−Liquid Equilibrium Data for the Binary Mixture Trifluoroethane (HFC-143a) + Ethyl Fluoride (HFC-161) over the Temperature Range (253.15 to 303.15) K. *Journal of Chemical & Engineering Data*, 55(9), pp.2990–2993.

Website 1, 2016. How Air Conditioners Work. Available at: https://www.archtoolbox.com/materials-systems/hvac/how-air-conditioners-work.html.

Website 2, 2016. POWER AND REFRIGERATION CYCLES. Available at: http://machineryequipmentonline.com/hydraulics-and-pneumatics/power-and-refriger-a-tion-cyclesthe-ideal-vapor-compression-refrigeration-cycle/.

Wei, Y.S. & Sadus, R.J., 2000. Equations of state for the calculation of fluid-phase equilibria. *AIChE Journal*, 46(1), pp.169–196.

Weinaug, C.F. & Katz, D.L., 1943. Surface Tensions of Methane-Propane Mixtures.

Williams-Wynn, M.D. et al., 2017. Experimental determination of the critical loci for R-23+(n-propane or n-hexane) and R-116+n-propane binary mixtures. *The Journal of Chemical Thermodynamics*, 108, pp.84–96.

Wilson, K., 1971. Renormalization Group and Critical Phenomena. II. Phase-Space Cell Analysis of Critical Behavior. *Physical Review B*, 4(9), pp.3184–3205.

Wilson, K. & Fisher, M., 1972. Critical Exponents in 3.99 Dimensions. *Physical Review Letters*, 28(4), pp.240–243.

Winkelmann, J., 1994. Density functional theory: Prediction of ellipsometric parameters and structural behaviour of pure fluid vapour-liquid interfaces. *Berichte der Bunsengesellschaft für physikalische Chemie*, 98(10), pp.1308–1316.

Winkelmann, J., Brodrecht, U. & Kreft, I., 1994. Density functional theory: Modelling of surface tensions for molecular fluids. *Berichte der Bunsengesellschaft für physikalische Chemie*, 98(7), pp.912–919.

Wright, F.J., 1961. Correlation between surface tension and other physical properties. *Journal of Applied Chemistry*, 11(6), pp.193–196.

Xu, X., Jaubert, J.-N., et al., 2015. Predicting Binary-Interaction Parameters of Cubic Equations of State for Petroleum Fluids Containing Pseudo-components. *Industrial & Engineering Chemistry Research*, 54(10),

pp.2816–2824.

Xu, X., Privat, R. & Jaubert, J.-N., 2015. Addition of the Sulfur Dioxide Group (SO 2), the Oxygen Group (O 2), and the Nitric Oxide Group (NO) to the E -PPR78 Model. *Industrial & Engineering Chemistry Research*, 54(38), pp.9494–9504.

Xuan, Y. & Chen, G., 2005. Experimental study on HFC-161 mixture as an alternative refrigerant to R502. *International Journal of Refrigeration*, 28(3), pp.436–441.

Yang, L. et al., 2015. (Vapour+liquid) equilibrium data for the {1,1-difluoroethane (R152a)+1,1,1,3,3-pentafluoropropane (R245fa)} system at temperatures from (323.150 to 353.150)K. *The Journal of Chemical Thermodynamics*, 91, pp.414–419.

Yang, Z. et al., 2014. Experimental Study of Saturated Pressure Measurements for 2,3,3,3-Tetrafluoropropene (HFO-1234yf) and 2-Chloro-1,1,1,2-Tetrafluoropropane (HCFC-244bb). *Journal of Chemical & Engineering Data*, 59(1), pp.157–160.

Yang, Z. et al., 2015. Isothermal Vapor–Liquid Equilibrium for the Binary System of 2,3,3,3-Tetrafluoropropene and 2-Chloro-1,1,1,2-tetrafluoropropane. *Journal of Chemical & Engineering Data*, p.150311152143003.

Yang, Z. et al., 2013. Phase equilibrium for the binary mixture of {1,1-difluoroethane (R152a)+trans-1,3,3,3-tetrafluoropropene (R1234ze (E))} at various temperatures from 258.150 to 288.150K. *Fluid Phase Equilibria*, 355, pp.99–103.

Zhang, F., 2012. Développement d'un dispositif expérimental original et d'un modèle prédictif pour l'étude thermodynamique des composés soufrés.

Zhang, W. et al., 2013. Vapor Pressures of 2-Chloro-3,3,3-trifluoropropene (HCFO-1233xf). *Journal of Chemical & Engineering Data*, 58(8), pp.2307–2310.

Zhang, Y., Gong, M. & Wu, J., 2008. Vapor-liquid equilibrium measurement and correlation for R23 + R116 system. *Journal of Chemical Industry and Engineering*, 59, pp.269–275.

Zhao, G. et al., 2014. Liquid Viscosity and Surface Tension of R1234yf and R1234ze Under Saturation Conditions by Surface Light Scattering. *Journal of Chemical & Engineering Data*, 59(4), pp.1366–1371.

Zhao, G. et al., 2010. Surface Tension of Propane (R-290) + 1,1-Difluoroethane (R-152a) from (248 to 328) K. , 55 (9), pp.3077–3079.

Zuo, Y.-X. & Stenby, E.H., 1997. Corresponding-states and parachor models for the calculation of interfacial tensions. *The Canadian Journal of Chemical Engineering*, 75(6), pp.1130–1137.

Résumé

La connaissance des propriétés thermodynamiques et des diagrammes de phases des composés fluorés est indispensable pour le dimensionnement et l'optimisation des systèmes thermodynamiques. Les applications sont nombreuses : réfrigération, récupération de chaleur (ORC), pompe à chaleur, climatisation automobile. Du fait des contraintes environnementales (la F-gaz pour l'UE) liées au fait que les fluides actuellement utilisés doivent être inoffensifs vis-à-vis de la couche d'ozone mais aussi posséder un pouvoir de réchauffement climatique bas (GWP CO_2=1, valeur de référence), les chimistes doivent développer de nouvelles molécules qui répondent à ce nouveau cahier des charges. Actuellement, ils ont mis au point des fluides de la famille des HFO dont le plus célèbre est le HFO1234yf. Son GWP est faible (4) tout comme celui de ses principaux isomères le HFO1234ze et le HFO1234zd. Si le fluide pur ne convient pas pour les applications souhaitées, des mélanges doivent être élaborés.

L'objectif de cette thèse est d'étudier plusieurs fluides HFOs en corps purs et en mélanges et de développer/comparer des modèles thermodynamiques permettant de prédire les diagrammes de phases et les densités de ces fluides. Ces modèles doivent pouvoir être transposables vers l'industrie. Le CTP dispose de plusieurs équipements permettant d'acquérir des données expérimentales. Le densimètre à tube vibrant sera utilisé pour acquérir des données de masse volumique, et une cellule d'équilibre entre phase (technique statique-analytique) pour acquérir des données d'équilibre liquide-vapeur. Les équations d'état cubiques seront utilisées pour le traitement des données. Une nouvelle équation d'état plus précise pour la prédiction des masses volumiques sera présentée. Une comparaison en termes de description des diagrammes de phases et des propriétés volumétriques sera également effectuée.

Mots Clés

Mesures expérimentales, modélisation, équations d'état, diagrammes de phases, densités

Abstract

The knowledge of the thermodynamic properties and phase diagrams of fluorinated compounds is essential for the design and optimization of thermodynamic systems. There are many applications: refrigeration, organic Rankine cycle (ORC), heat pump, and air conditioning systems.

Due to the environmental constraints (F-gas for the EU) related to the fact that the fluids being used must be harmless to the ozone layer, but also with a low global warming potential (GWP CO_2=1, reference value), the chemists must develop new molecules responding to these constraints. Today, they have developed fluids called HFOs whose most famous is the HFO1234yf, with a low GWP (4), along with his isomers HFO1234ze and HFO1234zd. If the pure fluid is not suitable for the applications, blends should be developed instead.

The objective of this thesis is to study several HFOs, in pure compounds and mixtures and develop/compare thermodynamic models in order to predict the phase diagrams and density of these fluids. These models should be transferable to industry.

The CTP has several equipments to acquire experimental data. The vibrating-tube densimeter will be used to acquire density data and the equilibrium cell (static-analytic method) to acquire vapour-liquid equilibrium data.

The cubic equations of state will be used for data treatment. A new equation of state more accurate for density prediction will be presented. A comparison in terms of phase diagrams and density prediction will be carried out.

Keywords

Experimental measurements, modelling, equations of state, phase diagram, density